

ZnO Nanorods-Based Piezoelectric Energy Harvesters

Nimra Jalali

**Submitted in partial fulfilment of the
requirements of the Degree of Doctor of
Philosophy**



**School of Engineering and Materials Science,
Queen Mary, University of London
London, United Kingdom
13th July 2015**

Declaration

I, Nimra Jalali, confirm that the research included within this thesis is my own work or that where it has been carried out in collaboration with, or supported by others, that this is duly acknowledged below and my contribution indicated. Previously published material is also acknowledged below.

I attest that I have exercised reasonable care to ensure that the work is original, and does not to the best of my knowledge break any UK law, infringe any third party's copyright or other Intellectual Property Right, or contain any confidential material.

I accept that the College has the right to use plagiarism detection software to check the electronic version of the thesis.

I confirm that this thesis has not been previously submitted for the award of a degree by this or any other university.

The copyright of this thesis rests with the author and no quotation from it or information derived from it may be published without the prior written consent of the author.

A handwritten signature in black ink, appearing to read 'Nimra', with a stylized flourish at the end.

Nimra Jalali

13th July 2015.

Abstract

Piezoelectric nanostructures of ZnO were employed for development of vibration energy harvesters. Columnar nanorod structures of ZnO, incorporated into various heterojunction-based device prototypes, were strained to generate voltage signals. The fabricated devices' prototypes were based on different top electrodes such as: p-n junction-type Poly(3,4-ethylenedioxythiophene) Polystyrene sulfonate (PEDOT:PSS)/ZnO devices, metal-insulator-semiconductor type Poly(methyl methacrylate) (PMMA)/ZnO devices. Similarly, various bottom electrode materials based prototypes were also assembled: ZnO/indium tin oxide (ITO), ZnO/silver (Ag) and ZnO/zinc (Zn). The overall device design was based on flexible electrodes and substrates, due to which low temperature (below 100 °C) fabrication processes were implemented. Device performance measurement and characterisation techniques were explored and implemented to improve the reliability of results. These techniques included open-circuit voltage and short-circuit current output measurement, resistive load matching and impedance analysis. The analysed performance of energy harvester was assessed in relation to its constituent material properties.

The parameters which affect the energy harvester performance were investigated and for this p-n junction-based (PEDOT:PSS/ZnO) devices were used. It was analysed that devices with optimum shunt (R_{sh}) and series resistance (R_s), which were in the ranges of 0.08 – 0.17 k Ω and 0.5 – 1.65 k Ω respectively, generated the highest peak open-circuit voltage (V_{oc}) and peak power density (P_L) of 90 – 225 mV and 36 – 54 $\mu\text{W cm}^{-2}$. However, the p-n junction-based devices with low shunt resistance (R_{sh}), ranged between 0.2 – 0.3 k Ω , were considered to be affected with leakage losses, such as short-circuits. Therefore, these devices generated lower V_{oc} and P_L in the range of 20 - 60 mV and 2 - 16 $\mu\text{W cm}^{-2}$. Similarly, the p-n junction-based devices with higher R_s , ranged between 0.3 – 0.6 k Ω , were adversely affected by I^2R losses and therefore their generated power density was also dropped to 0.22 - 0.25 $\mu\text{W cm}^{-2}$. In addition to parasitic resistance losses, the most significant phenomenon investigated in ZnO energy harvesters was, screening of polarisation

charges in ZnO. The polarisation screening effects were observed to be related to the electrical properties of device components like electrode material type and conductivity of ZnO.

Hence, the effect of electrode electrical properties on electric field screening was investigated. In this regard, device electrodes were varied and their effect on energy harvesting efficiency was studied. A comparison based on the performance of bottom electrodes like indium tin oxide (ITO), silver (Ag) and zinc foil on device performance was made. It was observed that due to lower screening effects of ITO, the ITO-based devices generated voltage output which was two orders of magnitude higher than the zinc foil-based devices.

Similarly, the screening effects of top electrode materials, like PEDOT:PSS and PMMA, on device output generation were investigated. The PMMA-based devices generated average 135 mV which was higher than average 100 mV generation of PEDOT:PSS-based devices; which indicated that the PMMA-based devices had slower screening rate. On the contrary, the PMMA-based devices' 7 times higher series resistance than PEDOT:PSS-based devices caused the P_L of PMMA-based devices to be $0.4 \mu W cm^{-2}$, which was two orders of magnitude lower than $54 \mu W cm^{-2}$ generated by PEDOT:PSS-based devices.

Further to electrode materials study, polarisation screening caused by electrical properties of ZnO was also analysed. In this regard, the surface-induced conductivity of ZnO was decreased by using surface coating of copper thiocyanate (CuSCN). The reduction in ZnO conductivity was considered to reduce the screening of polarisation charges. Consequently, the power density of ZnO devices was enhanced from $54 \mu W cm^{-2}$ to $434 \mu W cm^{-2}$.

Dedication

This thesis is lovingly dedicated to my mother and father, Zakia Jalali and Qasim Jalali. Their support, encouragement, and constant love have sustained me throughout my life.

Acknowledgement

I would like to thank my supervisor, Steve Dunn, for his guidance and advices which have helped me to constantly improve my performance. He kept me motivated to achieve my project goals and his advices considerably improved my research and reporting skills. I have been very lucky to be supervised by Joe Briscoe, who improved my laboratory skills, helped me to resolve experimental issues and provided ideas to support my research. I am very grateful to Markys Cain, Paul Weaver, Mark Stewart and Peter Woolliams at National Physical Laboratory, for supporting this project and providing brilliant meteorological ideas for device characterisation.

I want to express my deepest gratitude to all the staff at School of Engineering and Materials Science (QMUL) and Nanoforce for their support and encouragement. I am very thankful to Dr. Zofia Luklinska for her generous help and friendliness.

My friends have been my greatest strength throughout my PhD. I would like to say thanks to Yongfei Cui, Pelin Yilmaz, Shuqun Chen, Chen Chen, Alex Wibawa, Eric Asare, Zhu Xiaojing, Yaqiong Wang and Yejiao Shi for making my every day lovely and delightful. They have encouraged my efforts and always motivated me to achieve the best results. Many thanks to the M. Eng and Undergraduate project students, Lokeshwari Mohan, Yanzhi Tan, Shyam Sikotra and Sophia for their incredible team work and meaningful contribution to this research work.

I would like to express my deepest gratitude to my family, especially to my parents and my uncle, whose endless love and care keeps me strong. I truly appreciate my uncle Meer, who had been my greatest support during my stay in London. Many thanks to my mum and dad for being my inspiration. I am very thankful to my brother and sisters who believed in me and supported me in every way. A special thanks to my eldest sister, Uzma, whose guidance keeps me positive and incredible sense of humour lifts my spirit. Sincere appreciation to my brother Babras and sister Beenish who keep on motivating me to learn and achieve beyond my expectations.

Publications and Presentations

Journal Publications

Jalali N, Woolliams P, Stewart M, Weaver P M, Cain M G, Dunn S and Briscoe J 2014 Improved performance of p–n junction-based ZnO nanogenerators through CuSCN-passivation of ZnO nanorods J. Mater. Chem. A 2 10945

Briscoe J, Jalali N, Woolliams P, Stewart M, Weaver P M, Cain M and Dunn S 2013 Measurement techniques for piezoelectric nanogenerators Energy Environ. Sci. 6 3035

Conference Proceedings

Jalali N, Briscoe J, Tan Y Z, Woolliams P, Stewart M, Weaver P M, Cain M G and Dunn S 2014 ZnO nanorod surface modification with PDDA/PSS Bi-layer assembly for performance improvement of ZnO piezoelectric energy harvesting devices J. Sol-Gel Sci. Technol.

Jalali N, Briscoe J, Woolliams P, Stewart M, Weaver P M, Cain M and Dunn S 2013 Passivation of Zinc Oxide Nanowires for Improved Piezoelectric Energy Harvesting Devices J. Phys. Conf. Ser. 476 012131

Briscoe J, Jalali N, Loh L, Shoaee S, Woolliams P, Stewart M, Cain M, Weaver P M, Durrant J R and Dunn S 2013 ZnO Nanostructured Diodes - Enhancing Energy Generation through Scavenging Vibration MRS Proc. 1556 mrs13-1556 – w04-01

Briscoe J, Jalali N, Woolliams P, Stewart M, Cain M, Weaver P M and Dunn S 2013 ZnO nanogenerators: energy generation through scavenging vibration, advantages of using a diode SPIE Microtechnologies ed U Schmid, J L Sánchez de Rojas Aldavero and M Leester-Schaedel (International Society for Optics and Photonics) p 876308

Oral Presentations

Passivation of Zinc Oxide Nanorods for Improved Piezoelectric Energy Harvesting Devices, PowerMEMS (London), 2013

Passivation of Zinc Oxide Nanorods for Improved Piezoelectric Energy Harvesting Devices, QMUL, 2013

Poster Presentations

Alternating Current Nanogenerators with p-n Junction, QMUL, 2012

Enhanced Peak Power Density with CuSCN-Passivated Zinc Oxide Nanogenerators, QMUL, 2013

Performance Optimisation of ZnO Nanorods Based Energy Harvesters, Energy Harvesting Event (London), 2014

Performance Optimisation of ZnO Nanogenerators By Nanorod-Passivation, EMRS (Lille), 2014

Performance Optimisation of ZnO Nanogenerators By Nanorod-Passivation, QMUL, 2014

Awards

Best Poster Presentation, EMRS (2014): Performance Optimisation of ZnO Nanogenerators By Nanorod-Passivation

Best Poster Presentation, Energy Harvesting Event (2014): Performance Optimisation of ZnO Nanorods Based Energy Harvesters

Table of Contents

1. Introduction.....	1
1.1. Background – Energy Harvesting	1
1.2. Piezoelectric Energy Harvesting	2
1.3. Aims and Objectives	5
1.4. References	7
2. Literature Review	9
2.1. Dielectric Materials	9
2.2. Non-Centrosymmetric Functional Materials	10
2.2.1. Ferroelectric Materials	10
2.2.2. Pyroelectric Materials	12
2.2.3. Piezoelectricity	13
2.3. Functional Materials Used In Piezoelectric Devices.....	16
2.3.1. Zinc Oxide.....	16
2.3.2. Lead Zirconate Titanate (PZT).....	17
2.3.3. Quartz.....	18
2.4. Piezoelectric Energy Harvesting	20
2.4.1. Concepts in Energy Harvester’s Performance Characterisation	20
2.5. Concepts In Semiconductor Piezoelectric Material-Based Energy Harvesters.....	26
2.5.1. Semiconductor Junctions	26
2.6. Piezoelectric Energy Harvesting Devices	28
2.6.1. Bulk and Thin Film PZT Based Energy Harvesters	28
2.6.2. ZnO-Based Piezoelectric Energy Harvesters	34
2.7. Summary	45

2.8. References	47
3. Experimental and Methodology	53
3.1. ZnO Seed Layer Deposition on Bottom Electrode.....	53
3.1.1. Substrate Cleaning	54
3.1.2. Zinc Acetate-Based Seed Solution Deposition	54
3.1.3. Sputter Deposition.....	55
3.1.4. ZnO Nanoparticle Seed Deposition	56
3.2. Nanorods Growth on Bottom Electrode: Aqueous Solution Growth Technique	58
3.2.1. 25 mM Equimolar Solution Growth Condition	58
3.2.2. 50 mM Equimolar Solution Growth Condition	59
3.3. Surface Passivation of ZnO Nanorods	60
3.3.1. CuSCN Passivation	61
3.4. Top Electrode Fabrication	61
3.4.1. Spin Coating of PEDOT:PSS.....	61
3.4.2. Spin Coating of PMMA	63
3.5. Wiring Device Terminals and Fabrication of Mechanical Structure Suitable for Bend-Release Test	66
3.5.1. Masking and Electrode Sputtering.....	66
3.5.2. Wiring and Mounting of Device on Base Substrate.....	67
3.6. Bend Release Measurements.....	71
3.7. Measurement of Device Output	71
3.8. References	73
4. Nucleation and Growth of ZnO Nanorod Arrays.....	74
4.1. Aqueous Solution Growth Technique	74
4.1.1. ZnO Nanorods Grown on Zinc Acetate-Based Seed Layer	76
4.1.2. ZnO Nanorods on Sputtered ITO	78
4.1.3. ZnO Nanorods Grown from Nanoparticles Seed Layer.....	80

4.2.	Summary	87
4.3.	References	89
5.	Analysis of Mechanical and Electrical Performance Parameters of Devices	90
5.1.	Analysis of Electromechanical Response.....	90
5.1.1.	Simultaneous Voltage and Displacement Measurements	91
5.2.	Analysis of Electrical Parameters.....	98
5.2.1.	Series (R_s) and Shunt Resistances (R_{sh})	99
5.3.	Analysis of Electrical Output	110
5.3.1.	Peak Open-Circuit Voltage (V_{oc}) and Peak Short-Circuit Current Density (J_{sc}).....	112
5.3.2.	Peak Power Delivered to the Load (P_L) and Electrical Impedance Spectroscopy	116
5.3.3.	Energy Delivered (E_L) to the Load	121
5.3.4.	Charge Transferred (Q_L) to the Load	123
5.4.	Repeatability of Device Output and Long-term Stability	126
5.4.1.	Measurement Repeatability.....	126
5.4.1.	Long-term Stability	126
5.5.	Summary	128
6.	Effects of Electrode Materials on Device Performance.....	133
6.1.	Effects of Bottom Electrode Materials	134
6.1.1.	Overview of Device types based on Bottom Electrode Materials	136
6.2.	Comparative Analysis on the Bottom Electrode Materials	146
6.3.	Effects of Top Electrode Materials	149
6.3.1.	Overview of Device types based on Electrode Materials	149
6.3.2.	PEDOT:PSS-based p-n Junction-type Devices.....	153
6.3.3.	PMMA-based Insulator-type Device	160

6.4. Comparative Analysis on the PEDOT:PSS-based and PMMA-based Devices	181
6.5. Summary	186
6.6. References	188
7. Surface Modified ZnO-based Devices.....	190
7.1. CuSCN-coated Nanorod-Based Devices	190
7.1.1. Current-Voltage Electrical Characterisation	195
7.1.2. Performance Evaluation and Comparison with non-coated Devices	199
7.2. A Theoretical Approach to Understand the Effect of ZnO Surface Passivation on Device Internal Screening	215
7.3. Summary	218
7.4. References	220
8. Conclusion	222
8.1. Future Work	224
8.1.1. Surface Passivation	224
8.1.2. Impedance Matching	224
8.1.3. Doping of Nanorods	224
8.1.4. Nanorods Aspect Ratio	225
8.1.1. p-n-p Device Design	225

List of Figures

Figure 1. Yearly consumption of energy sources from 1988 to 2013.....	1
Figure 2. The relationship of ferroelectric, pyroelectric and piezoelectric materials relative to 21 non-centrosymmetric functional materials (excluding 432 point groups).	9
Figure 3. DC electric field poling of ferroelectric material ⁸	10
Figure 4. P-E loop of ferroelectric material showing spontaneous polarisation as P_s and E_c coercive electric field ¹¹	12
Figure 5. Crystal lattice of a pyroelectric material having permanent dipole moment δ . The dipole changes when an external temperature change is applied.	12
Figure 6. Piezoelectric effect: dislocation of centres of gravity of positive and negative charges upon application of mechanical stress. ¹⁹	14
Figure 7. Crystal structure of ZnO: Coordination of Zn^{+2} (black) and O^{-2} (white) ions along (a) 0001 direction and (b) 0001 direction ²⁴ , (c) tetrahedron coordination of Zn^{+2} and O^{-2} ions ²⁷	17
Figure 8. Crystal structure of perovskite PZT having Pb in the corners, O atoms as face centred and Zr/Ti as body centred ⁹	18
Figure 9. Crystal structure of Quartz showing tetrahedron coordination of O^{-2} ⁴²	19
Figure 10. Open-circuit voltage output measurement condition, when no load is connected across the device and the output is measured across infinite (ideally) resistance.	20
Figure 11. Short-circuit current output measurement condition, when no load is connected across the device and the output is measured across zero (ideally) resistance.	21
Figure 12. (a) General circuit diagram showing voltage source E_1 , impedances Z_1 , Z_2 and load impedance Z_L (b) Thevenin equivalent of the circuit after removal of voltage source and load impedance ⁴⁷	22
Figure 13. Resistive load matching across a piezoelectric energy harvester showing maximum power transfer to occur across load resistance of 1.5 k Ω	23
Figure 14. Nyquist plot of perfect parallel RC circuit ⁴⁹	25
Figure 15. Schottky contact and band bending between metal and semiconductor ⁵¹ . Φ_M and Φ_S represents the work function of metal and semiconductor, Φ_s is the schottky barrier.	26
Figure 16. Ohmic contact and band bending between metal and semiconductor ⁵¹	27
Figure 17. Model of internal and external screening effect in a semiconducting material ⁵⁴	28
Figure 18 Various configurations of PZT energy harvesters (a)cantilever structure ⁶⁶ (b)cymbal-type structure ⁶¹ (c)stack-type structure ⁶⁷	29
Figure 19. (a) Peak open-circuit voltage output across load resistance, (b) average power output across load resistances showing optimum load of 6 k Ω , (c) peak open-circuit voltage	

output at varying vibration frequency, (d) average power density at varying vibration frequency ⁵⁹	30
Figure 20. Proposed models for broadband tuning of PZT MEMS cantilever devices ⁶³	31
Figure 21. Buck converter circuit used for matching the impedance of energy harvester ⁷³ . 33	
Figure 22. (a) Complex impedance matching for the buck converter in Figure 21. (b) Design of cymbal-type MEMS device ⁷³	33
Figure 23. (a) Schematic of a typical piezoelectric biomorph device ⁷⁶ . Inset showing top view of actual device reported by Sodano et al. (2004) ^{74,75} . (b) Micro Fibre Composite (MFC) device assembly ⁷⁴	34
Figure 24. (a) SEM image of ZnO nanowire, (b) C-AFM measurement showing lateral bending of ZnO nanowire using AFM tip ⁷⁷	35
Figure 25. Various Schottky-type device configurations (a) flexible Au/ZnO device ⁸⁰ , (b) and (c) rows of Au/ZnO devices connected in series ^{81,83}	37
Figure 26. (a) PEDOT:PSS/ZnO device band diagram, showing: (b) internal carrier screening, (c) fast screening effect from ITO/ZnO junction and (d) slow screening effect from PEDOT:PSS/ZnO junction ⁵⁴	40
Figure 27. Series connected insulator-type device ⁸⁵	41
Figure 28. Correlation of resistivity to piezoelectric response in ZnO nanorods ⁹²	44
Figure 29. 0.3 x 1 cm ² of the area from the edge of the substrate was masked with kapton polyimide tape.....	55
Figure 30. Substrate attached to the surface of a glass slab and immersed facing down in a jar containing precursor solution.....	60
Figure 31. (a) As-grown ZnO nanorods, (b) CuSCN solution spray-coated on the surface of ZnO nanorods.....	61
Figure 32. (a) ZnO nanorods before top electrode, (b) Top electrode spin-deposited on top of the nanorods.	63
Figure 33. Step by step processes involved in the fabrication of ZnO energy harvester.	68
Figure 34. Block diagram of experimentations carried out on ITO substrates to fabricate ITO-based devices.	69
Figure 35. Block diagram of experimentations carried out on Ag and Zn substrates to fabricate ITO-based devices.	70
Figure 36. Bend-release measurement kit with motor/cam assembly used to bend the device.	72
Figure 37. (a) 187 nm wide densely packed nanorods grown on ITO substrate spin-coated with zinc acetate-based seed solution. (b) Uneven coverage of the seed layer on ITO forming island-like patches where nanorods grew.	76

Figure 38. Zinc acetate seed layer spin-deposition on ethanol-treated ITO substrate: (a) nanorods grew in densely packed fashion similar to the rods on non-treated ITO (b) The coverage of the seed layer on ethanol treated-ITO improved when compared to non-treated ITO but non-seeded voids and gaps were present.....	78
Figure 39. Contact angle of water droplets measured using sessile method: (a) 78.8° contact angle on non-treated ITO substrate, (b) 58.7° contact angle on ethanol-treated ITO surface	78
Figure 40. (a) Surface of ITO coated on PET substrate. (b) ZnO seed layer sputtered onto ITO.....	79
Figure 41. (a) ZnO nanorods grown on sputtered ITO-coated PET substrate using 25 mM precursor solution concentration. (b) 5 μm magnification image showing even coverage of nanorods on ITO surface.....	79
Figure 42. (a) ZnO nanorods grown on sputtered ITO-coated PET substrate using 50 mM precursor solution concentration. (b) 10 μm magnification image showing even coverage of nanorods on ITO surface.....	80
Figure 43. (a) Surface of ITO coated on PET substrate. (b) ZnO nanoparticle seed layer spray-coated onto ITO.	81
Figure 44. (a) C-axis oriented nanorods grown from spray-coated nanoparticle seeds on ITO-coated PET substrate. (b) 10 μm magnified image confirming the even coverage of the seed layer and nanorods on the substrate.	83
Figure 45(a) C-axis oriented nanorods grown from spray-coated nanoparticle seeds on Ag-coated kapton polyimide substrate. (b) 10 μm magnified image confirming the even coverage of the seed layer and nanorods on the substrate.	83
Figure 46. (a) C-axis oriented nanorods grown from spray-coated nanoparticle seeds on Zn foil substrate. (b) 10 μm magnified image confirming the even coverage of the seed layer and nanorods on the substrate.	84
Figure 47. XRD analysis of ZnO on various substrates showing 002 peak positioned at 34.4°. ZnO nanorods grown on (a) ITO, (b) zinc foil and (c) Ag (silver).	86
Figure 48. Displacement profile of device showing bend and release of the device by the cam rotating at 1 Hz.....	92
Figure 49. Peak open-circuit voltage of the device measured along with its displacement, showing generation of voltage signal when the device was released	92
Figure 50. The displacement plot in Figure 49 was time derivated to obtain device's velocity profile. When the cam released the device, its output voltage attained a peak value of 125 mV at a peak motion velocity of 1.5 m/sec.....	93
Figure 51. Screening model in a polarised piezoelectric material, showing bound charges screened out by the flow of mobile free-charge carriers.....	96

Figure 52. Measurement of peak open circuit voltage of PDOT-A4 when bent and released by a cam rotating at (a) 1 Hz, (b) 2 Hz and (c) 3 Hz.....	97
Figure 53. Band diagram showing p-n junction formation between n-type ZnO and p-type PEDOT:PSS.....	99
Figure 54. J-V characteristic plot of PDOT-A2 device demonstrating non-linear diode curve due to formation of p-n junction between ZnO and PEDOT:PSS. The inverse slope of forward bias and reverse bias region determines the R_s and R_{sh} , respectively.....	100
Figure 55. J-V characteristic curves of devices in groups: (a) PDOT-Shorted, (b) PDOT-2K/A, (c) PDOT-2K/B and (d) PDOT-1K.....	101
Figure 56. Cross-section images showing PEDOT:PSS layers coated onto ZnO nanorods at (a) 1000 RPM and forming 3 μm thick final layer (b) 2000 RPM and forming 1 μm thick final layer.	103
Figure 57. Schematic of ITO/ZnO/PEDOT:PSS/Au heterojunction, showing the series connection among the stacked materials.....	104
Figure 58. Non-ideal diode characteristic curve having (a) linearity in the forward bias region due to series resistance and (b) linearity in the reverse bias region due to shunt resistance ²⁷	104
Figure 59. SEM image of PDOT-Sh1 device showing areas of PEDOT:PSS having voids and gaps which caused short-circuits in the device.	105
Figure 60. (a) Schematic showing short-circuit condition due to pin-holes, voids or gaps in PEDOT:PSS layer and ZnO nanorod arrays. (b) Resistive circuit model showing short-circuit fault ($R_{sh} \approx 0$) causing output voltage to drop.....	106
Figure 61. SEM image showing the thickness of PEDOT:PSS near the edges of the substrate to be as low as 300 nm – 500 nm.	108
Figure 62. (a) Insufficient PEDOT:PSS layer thickness causing underlying nanorods to be exposed, (b) Homogeneously nucleated ZnO microrods settled on the surface of heterogeneously nucleated nanorods during synthesis. These microrods are 5 – 10 μm long and 2-4 μm wide, due to which they are not fully coated by 1 μm thick PEDOT:PSS layer.	108
Figure 63. SEM image of PEDOT:PSS coated on nanorods at 2000 RPM and 1000 RPM. (a) PDOT-B3 device having microrods and ZnO residue not coated sufficiently by 1 μm thick PEDOT:PSS coated at 2000 RPM. (b) PDOT-1K device having lesser exposed microrods and ZnO residue than PDOT-B3. This demonstrated that 3 μm PEDOT:PSS coating at 1000 RPM had better coverage of the non-homogeneously nucleated matter.	109
Figure 64. Cracking-off of PEDOT:PSS layer during gold sputtering process in vacuum..	110

Figure 65. Measured peak open-circuit voltage plots of devices in groups: (a) PDOT-2K/A, (b) PDOT-2K/B and (c) PDOT-1K.....	115
Figure 66. Measured peak short-circuit current plots of devices in groups PDOT-2K/A....	116
Figure 67. Resistive load matching plots for devices in groups: (a) PDOT-2K/A, (b) PDOT-2K/B and (c) PDOT-1K.	119
Figure 68. Impedance plots for devices in groups PDOT-2K/A.....	120
Figure 69. Impedance plots for devices in groups PDOT-2K/B.....	121
Figure 70. Device PDOT-A4 output voltage cycle measured across its optimum load.....	122
Figure 71. Measured voltage across optimum load (R_L) for devices in groups: (a) PDOT-2K/A, (b) PDOT-2K/B.....	123
Figure 72. peak open-circuit voltage output of PEDOT:PSS-based device named CuSCN-20-1, recorded for 10 cycles of mechanical excitation ³	126
Figure 73. Long-term performance stability test on PDOT-A4 device ³	127
Figure 74. (a) Schottky contact between n-type semiconductor and metal when work function of metal (ϕ_M) is higher than work function of semiconductor (ϕ_s). (b) Proposed Ohmic contact between Zn metal and ZnO, when Zn of marginally higher ϕ_M of 4.3 eV ϕ_M is contacted with ZnO having 4.2 eV ϕ_M	134
Figure 75. SEM images of nanorods grown on ITO: (a) Cross-section view, (b) top view.	138
Figure 76. J-V characteristic curve of PDOT-Sm devices. Inset: JV curve of PDOT-Sm-2, for clarity.....	138
Figure 77. Open-Circuit voltage output of PDOT-Sm devices.....	140
Figure 78. SEM images of nanorods grown on Ag electrode: (a) Cross-section view, (b) top view.....	141
Figure 79. Delamination of ZnO nanorods from Ag electrode due to insufficient adhesion between electrode and ZnO seed layer.	142
Figure 80. (a) J-V characteristic curve of PDOT-Ag devices. (b) J-V characteristic curve of PDOT-Ag-1, plotted to highlight the non-linear curves.	142
Figure 81. SEM images of nanorods grown on Zinc metal electrode: (a) Cross-section view, (b) top view.....	143
Figure 82. J-V characteristic curves of PDOT-Zn devices.	144
Figure 83. Open-circuit voltage output of PDOT-Zn devices.....	145
Figure 84. (a) Schottky contact between ITO and ZnO, having an Schottky barrier (ϕ_B) at the interface. (b) Polarised ZnO under strain, causing depolarisation field (E_{dep}) to develop and allow free-charge carriers to flow from within material and from the ITO contact. (c) The negative polarisation charges completely screening by the external and internal screening effect.	148

Figure 85. (a) Ohmic contact between Zn and ZnO, causing no energy barrier at the interface. (b) Polarised ZnO under strain, causing depolarisation field (E_{dep}) to develop and allow free-charge carriers from within material and from the ITO contact to flow. (c) The negative polarisation charges completely screening by the external and internal screening effect.	149
Figure 86. (a) Au/PMMA/ZnO metal-insulator semiconductor heterojunction. (b) Au/ZnO Schottky junction.	150
Figure 87. p-n junction between ZnO and PEDOT:PSS showing depletion region.	151
Figure 88. SEM image of 1 μ m PEDOT:PSS layer coated on top of nanorods. (b) Schematic of ITO/ZnO/PEDOT:PSS/Au heterojunction	154
Figure 89. J-V characteristics curve of PDOT-2K/A devices.....	154
Figure 90. Measured peak open-circuit voltage plots of devices in groups: (a) PDOT-2K/A, (b) PDOT-2K/B and (c) PDOT-1K.....	156
Figure 91. Measured peak short-circuit current plots of devices in groups: (a) PDOT-2K/A.	157
Figure 92. SEM images of (a) 3.5 μ m thick PMMA layer coated on top of ZnO nanorods (b) 1 μ m thick PMMA layer coated on top of ZnO nanorods. (c) Schematic of ITO/ZnO/PMMA/Au heterojunction device.....	161
Figure 93. J-V characteristic curve of (a) PMA-2K and (b) PMA-3K devices. Inset showing J-V curve of PMA-3K-3 for clarity.....	162
Figure 94. Metal insulator semiconductor (n-type) junction at (a) equilibrium, (b) under reverse bias condition, (c) under forward bias condition.	163
Figure 95. J-V characteristic curves of PMMA-based devices right after fabrication demonstrating the change in device characteristics due to incomplete evaporation of solvent. J-V characteristics of devices after 1 week of storage, showing change in behaviour after solvent evaporation.	165
Figure 96. JV Characteristic curve of PMA-3K devices, right after fabrication.	166
Figure 97. SEM images of (a) homogeneously nucleated nanorods adhered onto the surface of heterogeneously nucleated nanorods, (b) 30 nm PMMA coating on nanorods near the edge of the device substrate.	167
Figure 98. Measured peak open-circuit voltage output of PMA-2K devices.....	170
Figure 99. Resistive load matching for power density calculation of PMA-2K devices the impedance plot contained higher noise points near the optimum load resistance (R_L) (due to incomplete solvent evaporation effects). Therefore, the R_L is marked for clarity.	171
Figure 100. Nyquist plots from impedance analysis of PMA-2K devices.....	173
Figure 101. Measured peak open-circuit voltage of PMA-3K devices.....	176

Figure 102. Nyquist plots from the impedance analysis of PMA-3K devices.	178
Figure 103. Resistive load matching for PMA-3K devices. For PMA-3K-2 and PMA-3K-3, the impedance plot contained higher noise points near the optimum load resistance (R_L) (due to incomplete solvent evaporation effects). Therefore, the R_L is marked for clarity.	179
Figure 104. (a) PEDOT:PSS/ZnO p-n junction at equilibrium. (b) Polarised ZnO causing free carriers to move toward positive polarisation and holes in PEDOT:PSS drifting away from depletion region. (c) Complete screening of positive polarisation caused by accumulated charges at the junction and internal flow of carriers. Assumed partial screening of negative polarisation.	183
Figure 105. (a) Au (gold)/PMMA/ZnO metal-insulator-semiconductor junction at equilibrium. (b) Polarised ZnO causing free carriers to move toward positive polarisation (c) Partial screening (representing slower screening <i>rate</i>) of positive polarisation caused by accumulated internal carriers at the PMMA/ZnO junction only. Assumed partial screening of negative polarisation.	184
Figure 106. SEM image showing (a) non-coated and as-grown ZnO nanorods, (b) nanorods after 2 steps spray deposition of CuSCN, (c) nanorods after 10 steps spray deposition of CuSCN (d) nanorods after 20 steps spray deposition of CuSCN ²	193
Figure 107. SEM image of nanorods in different regions of CuSCN-20-1 sample: (a) showing rods heavily coated with CuSCN, (b) showing area where rods were not thickly coated with CuSCN. (Images sharpened to observe details).	193
Figure 108. SEM image of PEDOT:PSS layer coated on top of nanorods. This type of top electrode configuration was chosen for both non-coated and CuSCN-coated nanorod devices. (b) Schematic of (i) non-coated PEDOT:PSS-based and (ii) CuSCN-coated PEDOT:PSS-based device.	196
Figure 109. SEM image of CuSCN layer coated on top of nanorods in CuSCN-full device. (b) Schematic of (i) CuSCN-full device showing ITO/ZnO/CuSCN/Au heterojunction. ...	196
Figure 110. J-V characteristic curve of PDOT-A1, A2 and CuSCN-full devices.	197
Figure 111. JV characteristic curves of (a) CuSCN-2, (b) CuSCN-10-1, 10-2 and (c) CuSCN-20-1, 20-2 devices.	198
Figure 112. Measured peak open-circuit voltage output of (a) PDOT-2K/A and (b) CuSCN-2 devices.	200
Figure 113. Measured peak short circuit current density of (a) PDOT-2K/A and (b) CuSCN-2 devices.	200
Figure 114. Resistive load matching of (a) PDOT-2K/A and (b) CuSCN-2 devices across optimum R_L	201
Figure 115. Measured peak open-circuit voltage output of (a) CuSCN-10 and (b) CuSCN-20 devices.	202

Figure 116. Measured peak short-circuit current density output of (a) CuSCN-10 and (b) CuSCN-20 devices.....	203
Figure 117. Resistive load matching across optimum load resistance for (a) CuSCN-10, (b) CuSCN-20 devices.....	203
Figure 118. Nyquist plots of impedance analysis of PDOT-A1 and A2 devices.....	208
Figure 119. Nyquist plots of impedance analysis of CuSCN-2 devices.	209
Figure 120. Nyquist plots of impedance analysis of CuSCN-10 devices.	211
Figure 121. Nyquist plots of impedance analysis of CuSCN-20 devices.	212
Figure 122. Modelling of piezoelectric voltage source.....	216
Figure 123. Correlation between device voltage output and its time constant (τ_{RC}).....	218

List of Tables

Table 1. Group names of the ITO, zinc and silver substrates seeded using various methods.	57
Table 2. ZnO nanorods grown using different final solution concentrations and on various substrates. These nanorod samples were grouped as follows:	59
Table 3. PEDOT:PSS-based device groups based on the top electrode fabrication method, bottom electrode and nanorod fabrication method and surface modification.	65
Table 4. PMMA-based device groups based on the top electrode fabrication method, bottom electrode and nanorod fabrication method and surface modification.	65
Table 5. Group names of the ITO-coated PET, zinc foil and silver (Ag)-coated kapton substrates seeded using various methods.	75
Table 6. Group names and electrode fabrication method (from Chapter 3) for PEDOT:PSS- based devices, used in this chapter for analysis of electrical losses, characterisation and performance evaluation.....	98
Table 7. Calculated series (R_s) and shunt (R_{sh}) resistances of devices in groups (a) PDOT- 2K/A, (b) PDOT-2K/B and PDOT-1K	103
Table 8. Peak open-circuit voltage and short-circuit current density of fabricated devices.	113
Table 9. Peak power density, optimum load and resistive impedance of fabricated devices.	117
Table 10. Overall performance parameters of all the fabricated devices in groups: PDOT- 2K/A and PDOT 2K/B.....	124
Table 11. Overall performance parameters of all the fabricated devices in group PDOT-1K.	125
Table 12. Calculated series (R_s) and shunt (R_{sh}) resistances of devices in groups (a) PDOT- 2K/A, (b) PDOT-2K/B and PDOT-1K	136
Table 13. Group names and electrode fabrication method (from Chapter 3) for the ITO, zinc and silver based device used for the analysis of bottom electrode screening effects.....	137
Table 14. Comparison between PDOT-2K/A and PDOT-Sm devices.	140
Table 15. Calculated R_s and R_{sh} and measured V_{oc} of PDOT-Zn devices.	146
Table 16. Group names and names of devices used for analysis on top electrode materials.	152
Table 17. Performance parameters of PDOT-2K/A and PDOT-2K/B devices from Chapter 5.	158
Table 18. Performance parameters of PDOT-1K devices from Chapter 5.	159
Table 19. Calculated R_s and R_{sh} of PMA-2K and PMA-3K devices.	164

Table 20. V_{oc} , J_{sc} and P_L of PMA-2K devices.....	172
Table 21. Performance parameters of PMA-2K devices.	174
Table 22. J_{sc} and V_{oc} and P_L of PMA-3K devices.	176
Table 23. Performance parameters of PMA-3K devices.	180
Table 24. Measured and calculated performance parameters of the PMMA and PEDOT:PSS devices ¹⁶	181
Table 25. List of devices and their respective group titles, used for analysis on surface passivation.....	194
Table 26. V_{oc} , J_{sc} and P_L of PDOT-A1, A2, CuSCN-2, CuSCN-10 and CuSCN-20 devices.	204
Table 27. Performance parameters of best selected devices from each group.....	205
Table 28. Devices' critical frequency and time constants derived from their Nyquist plots.	210
Table 29. Performance parameters of PDOT-A1, A2 and CuSCN-2 devices.	213
Table 30. Performance parameters of CuSCN-10 and CuSCN-20 devices.	214

1. Introduction

1.1. Background – Energy Harvesting

Fossil fuels remain the world's most dominant energy sources according to world energy consumption statistics reported by British Petroleum (2014) ¹. Furthermore, the global energy consumption is projected to rise from 13 bn toe (tons of oil equivalent) in 2014 to 22 bn toe by 2050 ². If fossil fuel usage is pursued at the present rate, then it is estimated for energy prices to rise by 30-35% and carbon emissions to increase to 50 Gt/year ³ by 2050. Therefore, a widely considered issue is how to provide affordable, clean, efficient and sustainable energy solutions. In this regard, carbon-neutral, carbon capture and storage (CCS) and energy harvesting (renewable and sustainable resources) technologies are significant options to resolve energy crisis ³.

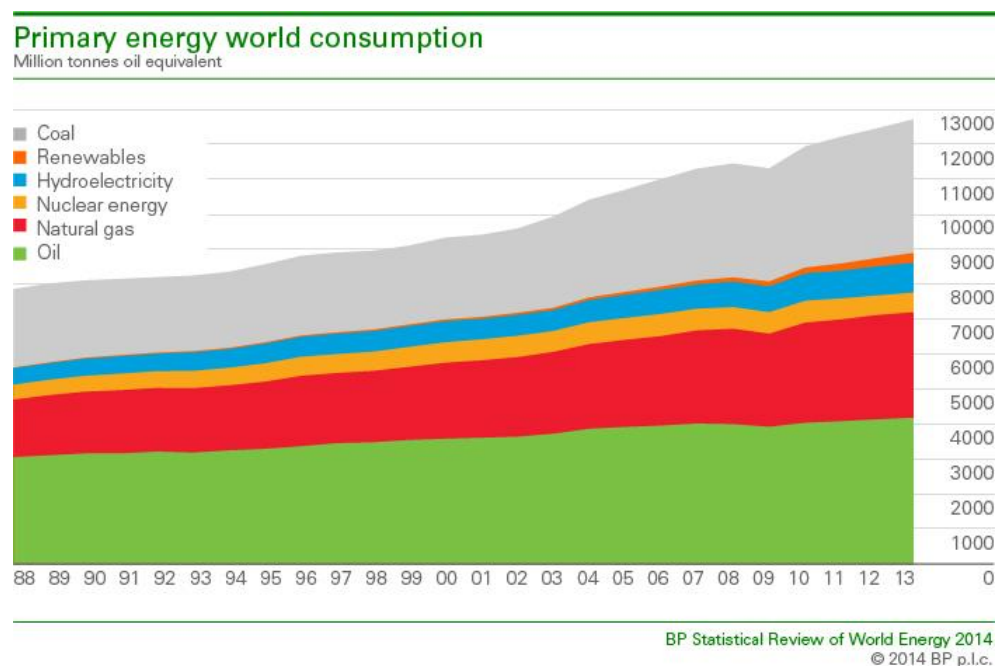


Figure 1. Yearly consumption of energy sources from 1988 to 2013

Energy harvesting involves capturing energy from ambient sources which would otherwise be dissipated as heat. The aim of harvesting energy from alternative resources is to enhance energy savings on the demand side and use of carbon-neutral fuels. Solar, wind, hydrothermal, thermoelectric and bio-mass are sustainable energy resources which can be harvested through specifically designed and integrated systems, and mega-watt ranged power can be generated from the environment. However, these systems are significant for outdoor power generation. For indoor energy scavenging, specifically for powering milli-watt ranged portable electronics and sensing devices, these systems are either not compatible or not sufficiently efficient. For instance, an outdoor solar cell efficiently generates 15 mW cm^{-3} of power density but, for indoor applications its power density drops to $15\text{-}20 \text{ }\mu\text{W cm}^{-3}$ ⁴. Therefore, for the application of energy harvesting to portable electronics and sensing, at indoor as well as outdoor ambience, vibration energy harvesting is considered to be the most applicable alternative. Since, vibration energy harvesting technology suits the type and amount of available ambient energy as well as size limitations.

Hence, using vibration energy harvesting, kinetic energy from wind, human motion, bridges, household goods, buildings, aircrafts, vehicles, engines and industrial machineries can be converted into electrical energy by the use of a transducer which may be piezoelectric, electromagnetic or electrostatic^{5,6}.

1.2. Piezoelectric Energy Harvesting

The most widely researched and implemented principles to convert vibration energy into electrical energy are electromagnetic induction, electrostatic generation and piezoelectricity. Piezoelectricity refers to a phenomenon according to which, when stress is applied on a piezoelectric material an electric field is induced in it.

Amongst the mainly focussed vibration-to-electrical energy conversion techniques, piezoelectric based transduction has obtained consideration in miscellaneous applications. Piezoelectric materials have found a large number of applications in our day-to-day lives and are used in printers, fuel injectors and pumps⁷. MEMS (Micro-Electro-Mechanical Systems) piezoelectric systems are commercially applied as sensors and detectors for navigation, automotive and smartphones^{8,9}. They have

gained wide attention in wireless sensing and monitoring for remote operations of systems on which wired connections are impractical^{10,11}. For energy harvesting applications, piezoelectric devices combine the ability of being self-powered with size compactness⁷. In addition, scaling piezoelectric materials such as ZnO and GaAs to nanostructured level has provided a significant impact on research on self-powered nanoscaled devices.

The most widely researched and commercially used material for piezoelectric MEMS devices is lead zirconate titanate (PZT). Owing, to its attractive electromechanical properties such as for PZT-5H, electromechanical coupling coefficient (k_{33}) is 0.75¹², strain coefficients d_{33} and d_{31} are 593 pC N⁻¹¹³ and -274 pC N⁻¹¹³; PZT has attained commercial applications as actuators and sensors. However, the main problem associated with PZT is brittleness and it raises challenges related to stress-induced cracking and fracture¹⁴. This limits the applications of PZT at kHz-ranged high frequency and cyclic loading at high accelerations¹⁵. To meet these challenges, polymer PVDF (Polyvinylidene fluoride), has been researched as a flexible and easy-to-shape piezoelectric material for sensing applications^{16,17}. The electromechanical coupling coefficient (k_{33}) of 0.21¹² for PVDF is the main drawback, which is why it cannot be substituted for PZT for energy harvesting and energy generation applications. Hence, flexibility along with appreciable electromechanical and strain coefficient is the main concern in piezoelectric systems which demands new materials exploration.

ZnO has been researched for photosensors, solar cells and LEDs. For piezoelectric applications, ZnO gained wide attention because of its readiness to form wide variety of nanostructures at low temperature (below 100 °C). Therefore, ZnO nanostructures combine the idea of vibration energy harvesting with size miniaturisation. Moreover, ZnO has appreciable mechanical stability and electromechanical properties. The electromechanical k_{33} and k_{31} coefficients of ZnO have been reported as 0.47 and 0.18¹⁸ while the strain coefficients d_{33} and d_{31} are 12 pC/N and 5 pC/N¹⁹. Moreover, the Young's Modulus of ZnO (bulk) has been measured to be 140 GPa²⁰. The nanostructured-ZnO can be incorporated into devices which have proposed applications as self-powered wireless sensors and vibration energy harvesters (often termed as nanogenerators). From 2006-2012, ZnO-based piezoelectric energy harvesters have been researched extensively. Pillar-like columnar structures of ZnO,

termed as nanorods, have been embedded into flexible and rigid devices and demonstrated to generate piezoelectric response to sound vibration and human motion such as tapping, rubbing and stepping. Moreover, energy harvesting circuits were used to power LED ²¹, wrist-watch ²² and wireless transmitter ²³ which showed the compatibility of these systems with energy available in the ambience. However, a rigorous system for device measurement and characterisation was required to establish the fundamental understanding on device electrical characteristics such as, electrical losses.

Device flexibility has been regarded as a feasible solution for vibration to energy conversion, since the higher the mechanical flexibility the more is the electrical sensitivity. In this regard, reported fabrication processes have been focussed on low temperature (below 100 °C) criteria; such as aqueous solution growth of ZnO, spin coating, RF magnetron sputtering and photo resist etching. In addition to low temperature fabrication techniques, research on ZnO-based piezoelectric energy harvesters has been focussed on material optimisation and device improvement. In this regard, electrical properties of ZnO have been optimised using doping techniques and surface modification and thereby, the performance of energy harvesters has been improved.

To sum up, the research on nanostructured-ZnO energy harvesters have been based on fabrication techniques, materials processing and performance optimisation. In such literature, there was not enough evidence on how the underlying piezoelectric mechanism was affected when devices' electrical properties and constituent materials were varied. One of the main reasons behind this lack of evidence and understanding was limited device characterisation. The ZnO energy harvesters were only measured for their current-voltage characterisation, open-circuit voltage output and short-circuit current density. These parameters were not enough to elaborate the electrical characteristics of an energy harvester. To elaborate this gap in research, let us take the example of PZT-based and PVDF-based energy harvesters. Most of the research in PZT-based and PVDF-based piezoelectric energy harvesters had focussed impedance load matching and resonance frequency matching characterisation for understanding the effects of electrical and mechanical properties on device's output power generation. Further to this, impedance analysis was used to study the device internal impedance and its effects on device output

performance. On the contrary, in the case of ZnO-devices the measurement of open-circuit voltage and short-circuit current alone were not enough to calculate device power generation, to understand its impedance-related losses and screening effects.

Hence, this report presents ZnO energy harvesters fabricated and optimised using low temperature (below 100 °C) processes. It analyses the stress-induced voltage generation from devices and investigates its dependence on polarisation screening caused by electrode interfaces and ZnO surface properties. Similarly, this thesis analyses the dependence of power generation of devices on their electrical losses. The overall investigation and analysis was established through implementation of detailed measurement and characterisation techniques such as, voltage and current output, impedance matching for power density calculation and impedance analysis.

1.3. Aims and Objectives

The aim of this study was to develop a nanostructured material based energy harvester with optimised output power generation and to develop a repeatable and reliable method of its measurement and characterisation.

The initial motivation of the project was to fabricate a basic energy harvesting device structure using synthesised piezoelectric nanorods of ZnO. Through successful fabrication, the target was to develop measurement and characterisation techniques on these devices, which would assist in understanding the device transduction mechanism and electrical losses.

After achieving the understanding on device mechanism and losses, the next set aim was to demonstrate proof-of-concept for the internal and external screening losses in piezoelectric polarisation in ZnO. Approaches were undertaken to reduce the screening effect, which resultantly enhanced the power generation from the energy harvesters.

To achieve the above-mentioned aims the following objectives were outlined:

1. Fabricate a basic device architecture comprising of a p-n junction diode based device. These device types were planned to be used for establishing characterisation techniques such as current-voltage characterisation, impedance analysis and resistive load matching for power density calculation

across optimum load. It was considered to establish device parasitic losses analysis, such as series and shunt resistance, through the mentioned characterisation techniques.

2. Implement the quantitative analysis and characterisation techniques learnt through the basic p-n junction device on various other prototypes. The planned prototypes involved ZnO nanorods sandwiched between various electrode types. Actually, the objective of this design approach was to study the screening effects of electrode types on device performance. Therefore, different electrode material types such as metal, metal-oxide, insulators and semiconductors were planned to be studied.
3. Investigate the internal screening of polarisation charges in ZnO. This study was planned to be approached by reducing the surface-induced free-charge carriers in ZnO and examining its impact on the induced-electric field.

1.4. References

1. British Petroleum. *Review by energy type: Primary energy*. Available at: <http://www.bp.com/en/global/corporate/about-bp/energy-economics/statistical-review-of-world-energy/review-by-energy-type/primary-energy.html>. [Accessed 02 February 2015].
2. H.-W. Schiffer, *Energy Policy*, 2008, **36**, 2464–2470.
3. L. Vallejo, C. Tim, G. Ajay, A. Heyes, T. Hills, M. Jennings, O. Jones, N. Kalas, J. Keirstead, C. Khor, C. Mazur, T. Napp, A. Strapasson, D. Tong, and J. Woods, *Halving global CO₂ by 2050: technologies and costs*, 2013.
4. S. Priya and D. J. Inman, *Energy Harvesting Technologies*, Springer, 2008.
5. S. P. Beeby, M. J. Tudor, and N. M. White, *Meas. Sci. Technol.*, 2006, **17**, R175–R195.
6. G. Poulin, E. Sarraute, and F. Costa, *Sensors Actuators A Phys.*, 2004, **116**, 461–471.
7. K. Uchino, in *Piezoelectricity SE - II*, Springer Berlin Heidelberg, 2008, vol. 114, pp. 257–277.
8. J. Marek, in *Proceedings of 2011 International Symposium on VLSI Technology, Systems and Applications*, IEEE, 2011, pp. 1–2.
9. H. J. Lim, R. P. Singh, K. C. T. Chuan, D. Nuttman, and M. Je, in *2011 International Symposium on Integrated Circuits*, IEEE, 2011, pp. 571–574.
10. E. P. James, M. J. Tudor, S. P. Beeby, N. R. Harris, P. Glynne-Jones, J. N. Ross, and N. M. White, *Sensors Actuators A Phys.*, 2004, **110**, 171–176.
11. M. Lallart, D. Guyomar, Y. Jayet, L. Petit, E. Lefeuvre, T. Monnier, P. Guy, and C. Richard, *Sensors Actuators A Phys.*, 2008, **147**, 263–272.
12. E. Lefeuvre, G. Sebald, D. Guyomar, M. Lallart, and C. Richard, *J. Electroceramics*, 2007, **22**, 171–179.
13. E. Lefeuvre, G. Sebald, D. Guyomar, M. Lallart, and C. Richard, *J. Electroceramics*, 2007, **22**, 171–179.
14. I. Chopra and J. Sirohi, *Smart Structures Theory*, Cambridge University Press, 2013.
15. T. Proulx, *MEMS and Nanotechnology, Volume 2: Proceedings of the 2010 Annual Conference on Experimental and Applied Mechanics*, Springer, 2011.
16. S. R. Anton and H. A. Sodano, *Smart Mater. Struct.*, 2007, **16**, R1–R21.
17. Q. Mao and S. Pietrzko, *Control of Noise and Structural Vibration: A MATLAB®-Based Approach*, Springer, 2013.
18. J. Dargahi, S. Sokhanvar, S. Najarian, and S. Arbatani, *Tactile Sensing and Display: Haptic Feedback For Minimally Invasive Surgery And Robotics*, Wiley, 2012.
19. K. Ellmer, A. Klein, and B. Rech, Eds., *Transparent Conductive Zinc Oxide*, Springer Berlin Heidelberg, Berlin, Heidelberg, 2008, vol. 104.

20. C. F. Klingshirn, B. K. Meyer, A. Waag, A. Hoffmann, and J. Geurts, *Zinc Oxide: From Fundamental Properties Towards Novel Applications*, Springer Berlin Heidelberg, Berlin, Heidelberg, 2010, vol. 120.
21. F. Xu, Q. Qin, A. Mishra, Y. Gu, and Y. Zhu, *Nano Res.*, 2010, **3**, 271–280.
22. G. Zhu, R. Yang, S. Wang, and Z. L. Wang, *Nano Lett.*, 2010, **10**, 3151–3155.
23. Y. Hu, L. Lin, Y. Zhang, and Z. L. Wang, *Adv. Mater.*, 2012, **24**, 110–4.
24. Y. Hu, Y. Zhang, C. Xu, L. Lin, R. L. Snyder, and Z. L. Wang, *Nano Lett.*, 2011, **11**, 2572–7.
25. S. Priya and S. Nahm, Eds., *Lead-Free Piezoelectrics*, Springer New York, New York, NY, 2012.
26. S. R. Anton and H. A. Sodano, *Smart Mater. Struct.*, 2007, **16**, R1–R21.
27. E. Dallago, D. Miatton, G. Venchi, G. Frattini, and G. Ricotti, in *2007 IEEE International Symposium on Circuits and Systems*, IEEE, 2007, pp. 1633–1636.
28. Z. L. Wang and W. Wu, *Angew. Chem. Int. Ed. Engl.*, 2012, **51**, 11700–21.

2. Literature Review

2.1. Dielectric Materials

An ideal dielectric material is defined as a non-conductor of electricity which possesses permittivity to intensify electrostatic and magnetic fields ¹⁻³. Dielectric materials are classified as polar and non-polar materials. The polar materials have centres of positive and negative charge pairs separated by a distance which creates a dipole moment. These dipoles are randomly oriented in a crystal, which is why the net dipole moment is zero. The non-polar dielectrics do not possess any charge pair separation and therefore there is no dipole moment between them ¹.

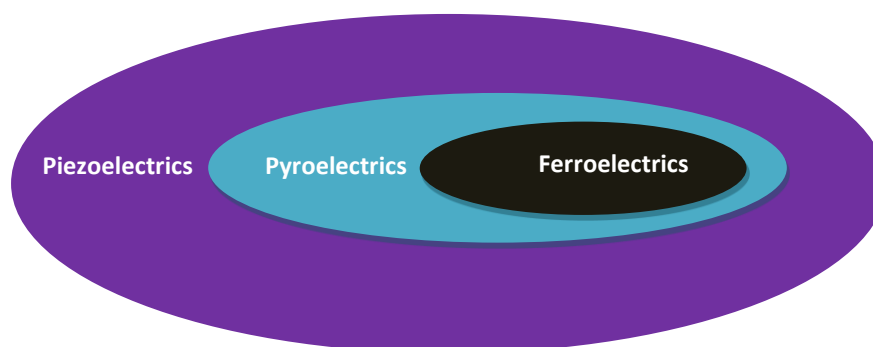


Figure 2. The relationship of ferroelectric, pyroelectric and piezoelectric materials relative to 21 non-centrosymmetric functional materials (excluding 432 point groups).

Out of 32 crystal classes, 11 possess a centre of symmetry and are non-polar. The remaining 21 classes do not possess centre of symmetry (centre of inversion) ⁴, 20 of which exhibit direct piezoelectricity. 10 of these are polar and possess electric dipole moment in the absence of electric field (spontaneous polarisation). If the spontaneous polarisation changes with the temperature then these crystals are said to be pyroelectric, however in some crystals this spontaneous polarisation can be permanently switched or reversed upon application of electric field. These materials are said to be ferroelectric ^{5,6}. The non-centrosymmetric class which does not exhibit piezoelectricity is point group 432.

The spontaneous polarization P_s arises due to surface charge density in non-centrosymmetric pyroelectric and ferroelectric crystals ⁷:

$$P_s = \frac{Q_s}{A}$$

Where $\frac{Q_s}{A}$ is the density of surface charges ⁷.

2.2. Non-Centrosymmetric Functional Materials

2.2.1. Ferroelectric Materials

Ferroelectric materials exhibit spontaneous polarization which can be re-oriented between two crystallographically equivalent configurations by an external field. Hence, it is not only spontaneous polarisation but also the re-orientability of polarization which describes a ferroelectric material ⁷.

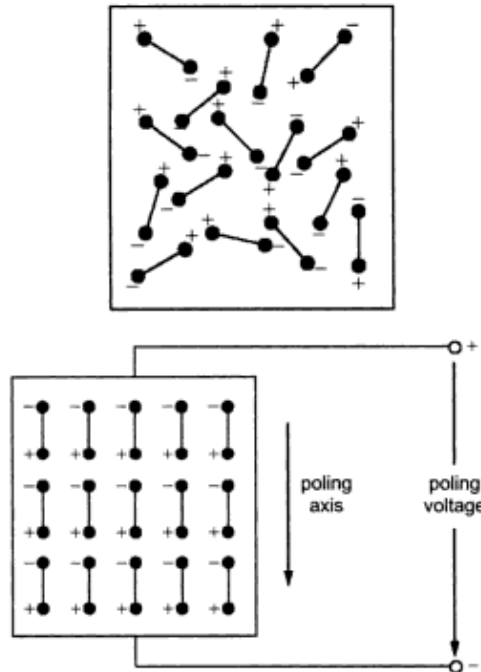


Figure 3. DC electric field poling of ferroelectric material ⁸.

Ferroelectric domain is described as a microscopic region in which all electric dipoles are arranged in same direction because of interaction of internal electric

fields. For a ferroelectric material, these domains are in large quantity and they have oriented in a specific direction. This random orientation of domains causes the net polarisation to be zero in the absence of an external electric field. When an external field is applied to the ferroelectric material then these domains align according to the direction of the electric field ⁹.

The application of electric field on the ferroelectric material and the consequent change in domain orientation is described in Figure 4. Initially in the absence of external electric field, the net polarisation is zero (point A). As the applied field is increased, the domains get oriented in the direction of the applied field, and resultantly the polarisation increases linearly as indicated by the curve AB. When the field is further increased, the number of aligned domains increases and the polarisation increases non-linearly and attains a point C at which maximum domains are aligned according to the direction of applied field. This point C is the saturation point, which if extrapolated then the corresponding value on the y-axis is called spontaneous polarisation (P_S). If at the saturation limit, the applied field is removed then it leaves a remnant polarisation (P_R), which is slightly less than the P_S . To reduce P_R , it is required to reduce the electric field in negative direction. The applied field which reduces developed remnant polarisation to zero is called coercive field ($-E_C$). A further reduction in electric field will cause reverse spontaneous polarisation ($-P_S$) to develop. When the field is then removed then it will leave behind negative remnant polarisation ($-P_R$). The electric field is required to increase in positive direction and when it is equal to coercive field, the negative remnant polarisation ($-P_R$) becomes zero. Further increase in electric field will trace the path $E_C C$ and close the loop. This closed loop is referred to as hysteresis loop ^{9,10}.

The domains of ferroelectric materials are aligned in one direction upon application of a strong electric field across the material and this process is called poling. As a result of poling, the ferroelectric material exhibits piezoelectricity. Since in ferroelectric materials the spontaneous polarisation is reversible, the direction of domains can be reversed by the application of a reversed electric field. ⁸.

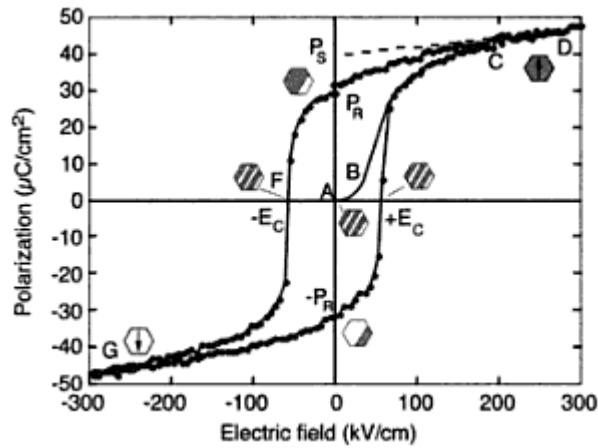


Figure 4. P-E loop of ferroelectric material showing spontaneous polarisation as P_S and E_C coercive electric field ¹¹.

2.2.2. Pyroelectric Materials

If a pyroelectric material is held at a constant temperature for a period of time, it becomes electrically neutral due to the flow of free carrier charges through the material. If the temperature of material is changed, the electrical polarisation changes and a voltage is developed ¹²⁻¹⁴.

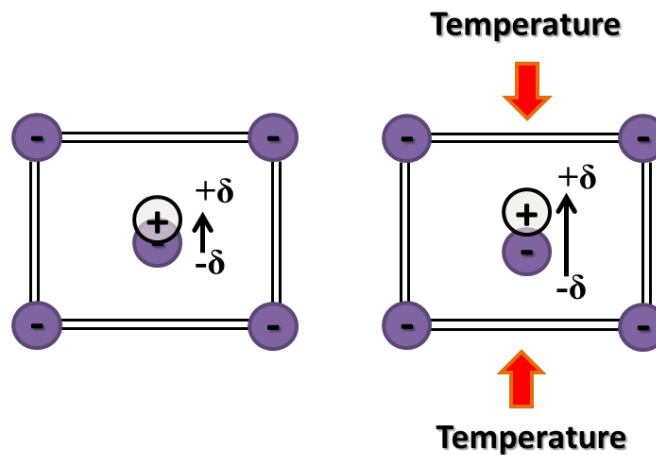


Figure 5. Crystal lattice of a pyroelectric material having permanent dipole moment δ . The dipole changes when an external temperature change is applied.

Pyroelectric materials exhibit spontaneous polarization which unlike ferroelectric materials is not re-orientable by the application of electric field. At a constant temperature, this polarization is compensated by the free-charge carriers. However,

if the temperature of the material is varied ΔT at a rate faster than the redistribution of free-carriers then an electric signal ΔP is obtained ^{7,15,16}.

$$\Delta P = p_{py} \cdot \Delta T$$

Where p_{py} describes pyroelectric coefficient ⁷. The unit of p_{py} is charge per unit area per unit temperature change or coulomb/m²K ¹⁴.

All pyroelectric materials are also piezoelectric but all piezoelectric materials are not pyroelectric. For example, GaAs (Gallium Arsenide) and Quartz are both piezoelectric but not pyroelectric. Pyroelectric effect is exhibited by solids which have a certain crystallographic orientation ¹⁷:

- (a) The crystal lattice should be non-centrosymmetric.
- (b) The crystal must have no more than one axis of rotation ¹⁷.

2.2.3. Piezoelectricity

When stress is applied on a certain materials, an electric polarisation is produced proportional to the stress applied. This phenomenon is called piezoelectricity and it is exhibited by piezoelectric materials.

The mechanism producing piezoelectric effect is based on dislocation of the centres of gravity of positive and negative charges. This displacement of ions cause a dipole moment and the material is polarised. The polarisation change corresponds to charge build-up that can be measured as generated voltage across the terminals.

All polar crystals exhibit direct and converse piezoelectricity. Direct piezoelectricity means that a mechanical strain induces polarisation due to displacement of charge centres of the anions and cations. On the contrary, converse piezoelectric effect produces strain in piezoelectric material when an electric field is applied across it ⁷. Hence the electric polarisation P is related to applied mechanical stress T ($= \frac{F}{A}$) by a piezoelectric coefficient d or d^t , mechanical strain S and applied electric field E ¹⁸.

The relation for direct piezoelectric effect is demonstrated as follows ^{7,18}:

$$\mathbf{P} = \mathbf{d} \cdot \mathbf{T}$$

The relation for converse piezoelectric effect is illustrates as follows ^{7,18}:

$$\mathbf{S} = \mathbf{d}^t \cdot \mathbf{E}$$

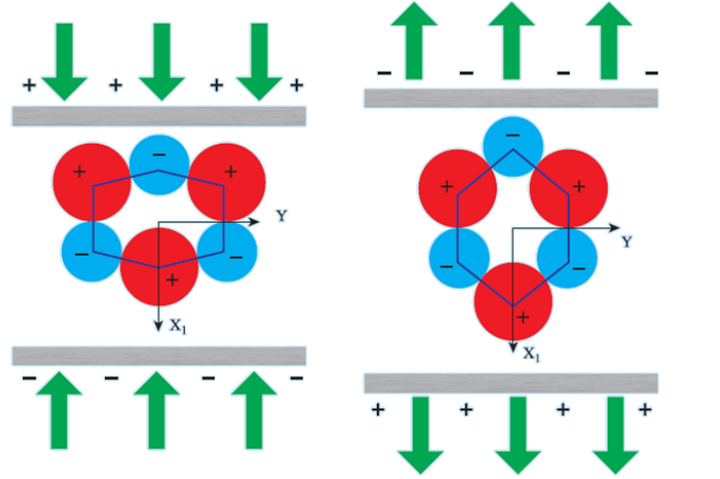


Figure 6. Piezoelectric effect: dislocation of centres of gravity of positive and negative charges upon application of mechanical stress. ¹⁹

“t” denotes the transposed matrix. The subscripts T indicate that stress is constant; subscript E indicates that electric field is constant.

2.2.3.1. Constitutive Equations of Piezoelectric Materials

The constitutive equations of piezoelectric materials define the relationship between applied stress and induced electric field in the material and vice versa.

In an unstressed dielectric material, the dielectric displacement \mathbf{D} is the charge per unit area, and it is related to electric field as ^{7,18,20–22}:

$$\mathbf{D} = \epsilon \mathbf{E} \quad \text{Equation 1}$$

Where, ϵ is the permittivity of dielectric medium.

Similarly, if a dielectric material is placed in a zero electric field then the applied stress and strain on it can be related as ^{7,18,20–22}:

$$\mathbf{S} = \mathbf{s}\mathbf{T} \quad \text{Equation 2}$$

Where, s is the mechanical compliance.

According to principle of conservation of energy, the two electrical and mechanical constitutive equations (Equation 1 and 2) are coupled and written as^{7,18,20–22}:

$$\mathbf{S} = \mathbf{s}_E \mathbf{T} + \mathbf{d}^t \mathbf{E}$$

$$\mathbf{D} = \mathbf{d} \mathbf{T} + \boldsymbol{\epsilon}_T \mathbf{E}$$

s_E is the mechanical compliance measured at zero electric field, d^t and d are the piezoelectric coupling between electrical and mechanical variable and ϵ_T is the dielectric constant measured at zero mechanical stress^{7,18,20–22}.

2.3. Functional Materials Used In Piezoelectric Devices

2.3.1. Zinc Oxide

Zinc oxide is pyroelectric material with wurtzite crystal structure. Having a hexagonal lattice structure, ZnO is asymmetrical and belongs to $P6_3mc$ space group. The absence of centre of inversion in ZnO structure can be observed from the alternating planes of Zn^{+2} and O^{-2} ions in tetrahedron coordination along the c-axis²³. Along the c-axis, the lattice of ZnO has distinct atom termination at the alternating surfaces; the $[0001]$ surface is terminated by Zn atoms and $[000\bar{1}]$ surface is terminated by O atoms²⁴. Therefore, due to distinct polar surfaces on both ends, ZnO has dipole moment along the c-axis and the 0001 surface has the highest energy and fastest growth when compared to other fast growth non-polar surfaces $[2\bar{1}\bar{1}0]$ and $[01\bar{1}0]$ ²³. Therefore, being $[0001]$ as the fastest growth axis, ZnO usually exhibits columnar/pillar like nanostructure growth called nanowire and nanorods²⁵.

Nanostructures of ZnO have attained wide attention due to material's functional properties, such as wide band gap (3.37 eV), pyroelectric and piezoelectric nature. Therefore, as a semiconducting wide band gap material, it has been employed in solar cells, photodiodes and photodetectors. The piezoelectric nature of ZnO has proposed applications in self-powered vibration sensors and vibration energy harvesters. Additionally, ZnO possesses attractive piezoelectric properties. The d_{33} , c_{33} and ϵ_{33}/ϵ_0 for bulk material were measured as 10-12 pC/N, 200-300 GPa and 9-11. The electromechanical coupling coefficient of ZnO is 0.23²⁶.

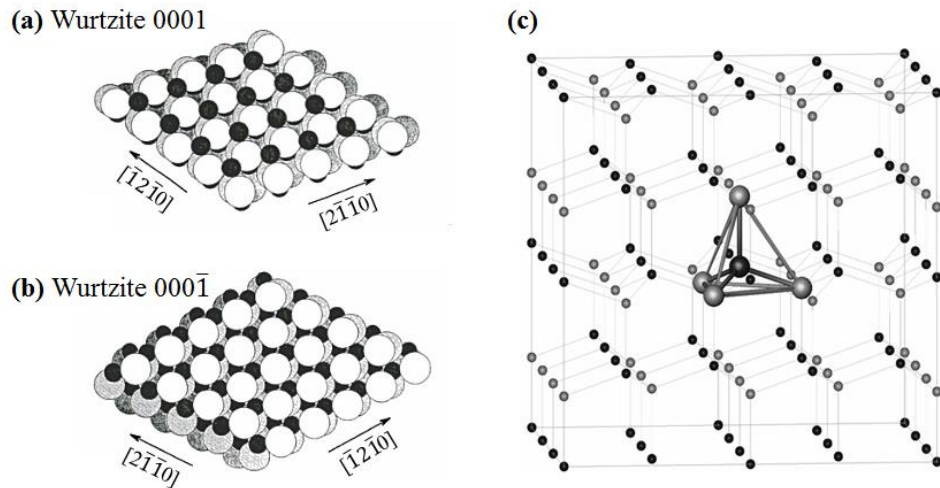


Figure 7. Crystal structure of ZnO: Coordination of Zn^{+2} (black) and O^{-2} (white) ions along (a) 0001 direction and (b) $000\bar{1}$ direction ²⁴, (c) tetrahedron coordination of Zn^{+2} and O^{-2} ions ²⁷.

Several experimental and theoretical approaches have been applied to study the Young's modulus of ZnO and reports have identified the existence of nanorod size dependence on their Young's Modulus. Reportedly, the Young's Modulus increases as the diameter decreases ^{28,29}. It was reported that the Young's Modulus of ZnO nanorods of 80 nm diameter, under different loading modes (tension and buckling), was close to its bulk modulus of 140 GPa ³⁰.

In addition to electromechanical properties, the surface properties of ZnO have been studied extensively for their defects and surface states. The surface properties of ZnO are vital topic for research because they affect its conductivity and interface with other materials. Hence, unintentional doping from surface states causes ZnO to be an n-type semiconductor. The most commonly reported native defects are oxygen vacancies, oxygen interstitials, zinc vacancies and zinc interstitials ^{31–36}. These surface species interact with abundant gases in the environment such as oxygen, CO_2 , hydrogen and moisture and form impurities on its surface. One of the donor-type impurity highlighted in research work is hydroxyl radicals ^{33,37}. Moreover, it is highly debatable whether Zn interstitial or oxygen vacancies act as donor defects on ZnO surface ³⁸. To sum up, the surface properties of ZnO tune its electrical properties and therefore they play a major role in affecting the performance of ZnO-based electronic devices. In addition, they are reported to change the interfacial properties of ZnO by allowing charges to be trapped at junctions ³⁹.

2.3.2. Lead Zirconate Titanate (PZT)

Lead zirconate titanate $\text{Pb}(\text{Zr.Ti})\text{O}_3$ is a ferroelectric polycrystal which is poled with high DC electric field and the domains align to create a net piezoelectric effect. PZT has a perovskite structure, which is defined as a structure with non-centrosymmetry in microscale and anisotropy in macroscale ⁴⁰. The unit cell of PZT is shown in Figure 8, the Pb form its corners, O atoms arranged as face centred, and Ti and Zr atoms are body centred. The Curie temperature of PZT is 350 °C at which it forms paraelectric cubic structure ⁹. PZT has relative permittivity (constant strain) ϵ_{33}^s of 1300 – 3400 ⁴¹, d_{33} coefficient of 289 – 593 pm/V ⁴¹ and k_{33} coefficient of 0.68 –

0.78⁴¹. Due to these excellent piezoelectric properties, it is commercially available in sensors, actuators and resonators.

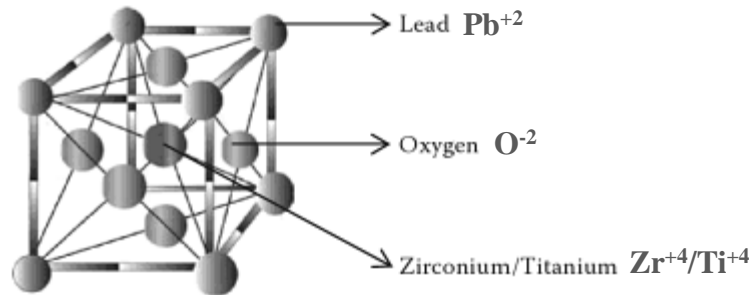


Figure 8. Crystal structure of perovskite PZT having Pb in the corners, O atoms as face centred and Zr/Ti as body centred⁹.

2.3.3. Quartz

Quartz (SiO_2) is a piezoelectric material with a crystal structure comprising of one Si^{+4} ion in the centre of four tetrahedrally oriented oxygen ions O^{-2} (Figure 9)⁴². Quartz has been a favoured material in various piezoelectric applications because of its underlying properties. Quartz crystal has aging stability and durability as compared to other piezoelectric materials. It is monocrystal therefore unlike PZT it does not require unidirectional polarization. Its mechanical quality factor Q_m lies in the range of 10^4 - 10^6 due to which it has considerable sensitivity and has been frequently used in sensing applications. In addition, it has also been used in resonators. Quartz lacks electromechanical applications because its longitudinal k_{33} and transverse k_{31} electromechanical coupling coefficients are 0.15 and 0.1⁴³, which are not sufficient for energy harvesting and actuation applications.

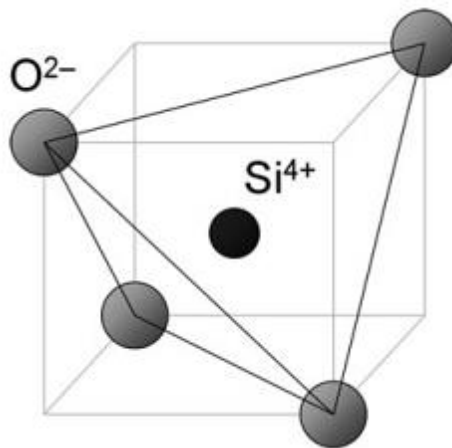


Figure 9. Crystal structure of Quartz showing tetrahedron coordination of O^{2-} ⁴²

2.4. Piezoelectric Energy Harvesting

2.4.1. Concepts in Energy Harvester's Performance Characterisation

2.4.1.1. Open-Circuit Voltage (V_{oc})

Direct piezoelectric effect refers to the situation when a piezoelectric material is subjected to mechanical force, which results in a change in polarisation. This change in polarisation corresponds to charge build-up that can be measured as generated voltage. Open-circuit voltage is the term commonly used to describe generated voltage from a device when a load is not connected across its terminals. During open-circuit voltage measurement, the current passing through the device circuitry is minimum (ideally zero current) ⁴⁴.

Open-Circuit Voltage

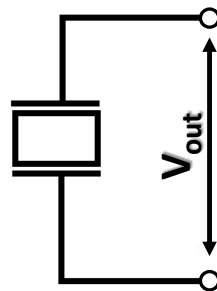


Figure 10. Open-circuit voltage output measurement condition, when no load is connected across the device and the output is measured across infinite (ideally) resistance.

2.4.1.2. Short-Circuit Current (I_{sc})

Schmidt et al. (2014) ⁴⁵ explained that the strain-induced charge displacement in piezoelectric material causes voltage output generation. Moreover, the current output from the piezoelectric material or device depends on the conductivity of material. Therefore, the current flows due to free-charge carriers present in the piezoelectric material. The flow of current is measured across the device terminals. The condition at which the current is measured across minimum impedance (ideally zero impedance) is called short-circuit current. At short-circuited condition a load is not

connected across device terminals and the terminals are effectively connected across a short-circuit ⁴⁴.

Short-circuit Current

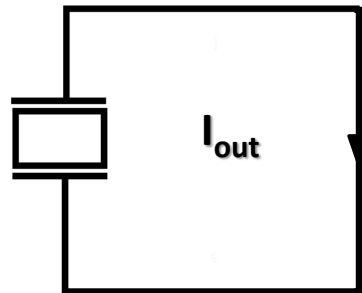


Figure 11. Short-circuit current output measurement condition, when no load is connected across the device and the output is measured across zero (ideally) resistance.

2.4.1.3. Impedance Load Matching and Maximum Power Output

In most of the reported energy harvesting applications the maximum power is obtained using load matching between the source and the load. In photovoltaic applications the DC source is matched with resistive load to obtain the optimal load at which the maximum deliverable power is obtained. Similarly, for highly capacitive sources like piezoelectric generators, the impedance is usually matched using reactive and resistive loads ⁴⁶. The concept of impedance load matching is based on the maximum power transfer theorem, which states that ⁴⁷:

“In an active network, maximum power transfer to the load takes place when the load impedance is the complex conjugate of an equivalent impedance of the network as viewed from the terminals of the load.”

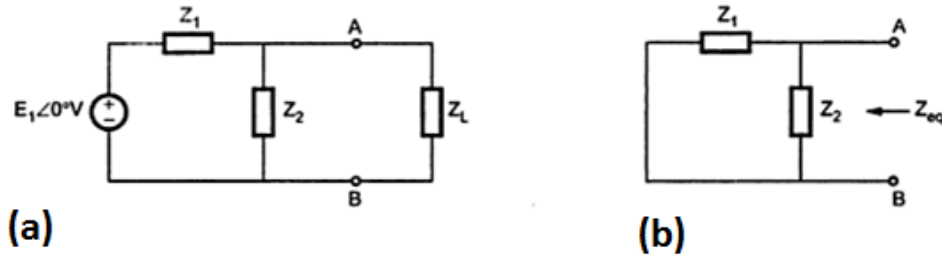


Figure 12. (a) General circuit diagram showing voltage source E_1 , impedances Z_1 , Z_2 and load impedance Z_L (b) Thevenin equivalent of the circuit after removal of voltage source and load impedance⁴⁷.

In Figure 12(a), if the voltage source E_1 and load Z_L is removed then the equivalent impedance of the network is represented in Figure 12 (b), and the equivalent impedance is given as⁴⁷:

$$Z_{eq} = R + jX$$

According to the theorem, the maximum power can be transferred if the Z_L is the complex conjugate of Z_{eq} ⁴⁷:

$$Z_L = Z_{eq}^* = R - jX$$

For piezoelectric generators, the mechanical resonance frequency is the characteristic frequency at which the optimum power is harvested. However, in a condition when excitation vibrational frequencies are different from the resonance frequency then the generator would not generate optimum power output. In this situation, the power generation is optimized using the impedance load matching technique⁴⁶. For this, the impedance of piezoelectric generator is matched with a load circuit so that maximum power is transferred to the load. This impedance matching can be achieved by using energy harvesting circuits such as, DC-DC buck converters.

A simple demonstration of impedance load matching using maximum power transfer theorem is illustrated in Figure 13. Figure 13 basically illustrates the particular case of optimised power delivered by semiconducting piezoelectric material-based energy harvester of 1.5 k Ω resistive internal impedance. Across this energy harvester, load resistances were connected from 100 Ω to 1 M Ω . The power delivered across each resistor was calculated and plotted. It was observed that the maximum power transfer

from this device was observed to occur across a load of 1.5 k Ω . This load resistance of 1.5 k Ω matched with the resistive internal impedance of the energy harvester. Hence, in the illustrated way, the energy harvester was optimised to generate its maximum power across 1.5 k Ω .

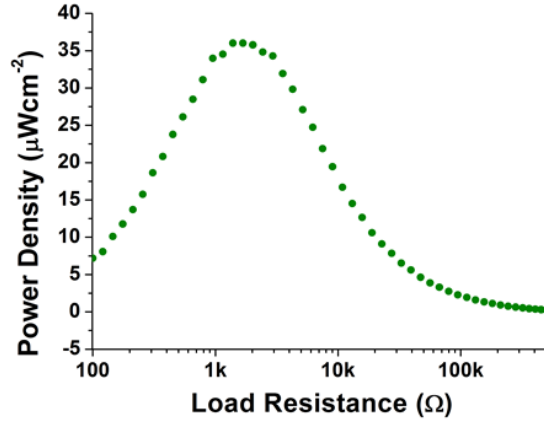


Figure 13. Resistive load matching across a piezoelectric energy harvester showing maximum power transfer to occur across load resistance of 1.5 k Ω .

For the case of an insulating material (PZT) based piezoelectric energy harvesters operating at resonance frequency, it has been demonstrated by Harris (2014)⁴⁸ that $\omega R_L C_P$ equals to unity; which enabled determination of R_L using $R_L = (\omega C_P)^{-1}$. Where, ω is the resonant frequency subjected to the piezoelectric device.

2.4.1.4. Impedance Analysis

Impedance analysis is an important tool of dielectric spectroscopy which has been used to analyse the response of impedance components in an electric circuit. Impedance analysis provides information on the ability of an electrical circuit to resist the flow of electric current, which is indicated as the real resistive impedance and the ability of an electric circuit to store electrical energy which is represented as the imaginary reactive impedance⁴⁹. Therefore, impedance is represented by a complex number which is a vector sum of real impedance R and imaginary impedance X , as follows⁵⁰:

$$Z^* = R + jX$$

The impedance is measured by the application of a sinusoidal voltage signal of amplitude V_A and frequency f (usually expressed in Hertz (Hz)). The voltage signal $V(t)$ is expressed as ⁴⁹:

$$V(t) = V_A \sin(2\pi ft) = V_A \sin(\omega t)$$

In response to a sinusoidal input voltage, the current is phase shifted which is determined by the ratio between the capacitive and resistive components in the circuit. The output current $I(t)$ with amplitude I_A and phase Φ is defined as ⁴⁹:

$$I(t) = I_A \sin(\omega t + \varphi)$$

The impedance being the ratio between input voltage $V(t)$ and output current $I(t)$ according to Ohm's Law can be expressed as ⁴⁹:

$$Z^* = \frac{V(t)}{I(t)} = \frac{V_A \sin(\omega t)}{I_A \sin(\omega t + \varphi)} = \frac{V_A e^{j\omega t}}{I_A e^{j\omega t - j\varphi}}$$

$$\text{Or, } Z^* = \frac{V(t)}{I(t)} = Z_A \frac{\sin(\omega t)}{\sin(\omega t + \varphi)}$$

Therefore as per the definition, impedance is the vector sum of “real” or “in-phase” part Z_{REAL} and “imaginary” or “out-of-phase” part Z_{IMG} ⁴⁹:

$$Z^* = Z_A e^{j\varphi} = Z_A (\cos \varphi + j \sin \varphi) = Z_{REAL} + jZ_{IMG}$$

The phase shift is defined by the ratio of imaginary and real impedance components ⁴⁹:

$$\tan \varphi = \frac{Z_{IMG}}{Z_{REAL}} \text{ or } \varphi = \tan^{-1} \left(\frac{Z_{IMG}}{Z_{REAL}} \right)$$

The impedance response to the frequency variation is often represented as Nyquist plots. Through this technique the relationship between frequency-dependent reactive impedance is plotted against the frequency-independent resistive impedance. The shape of the response determines the possible conduction mechanism in the circuit. Figure 14 shows the semicircular Nyquist shape response for a perfect RC parallel circuit. In real-circuits this response is often different; for instance, a depressed semicircle which corresponds to more than one charge-transfer process ⁴⁹. Two or

three semi-circles are often observed in heterojunction devices where multiple layers of materials have their respective capacitive contribution ⁴⁹.

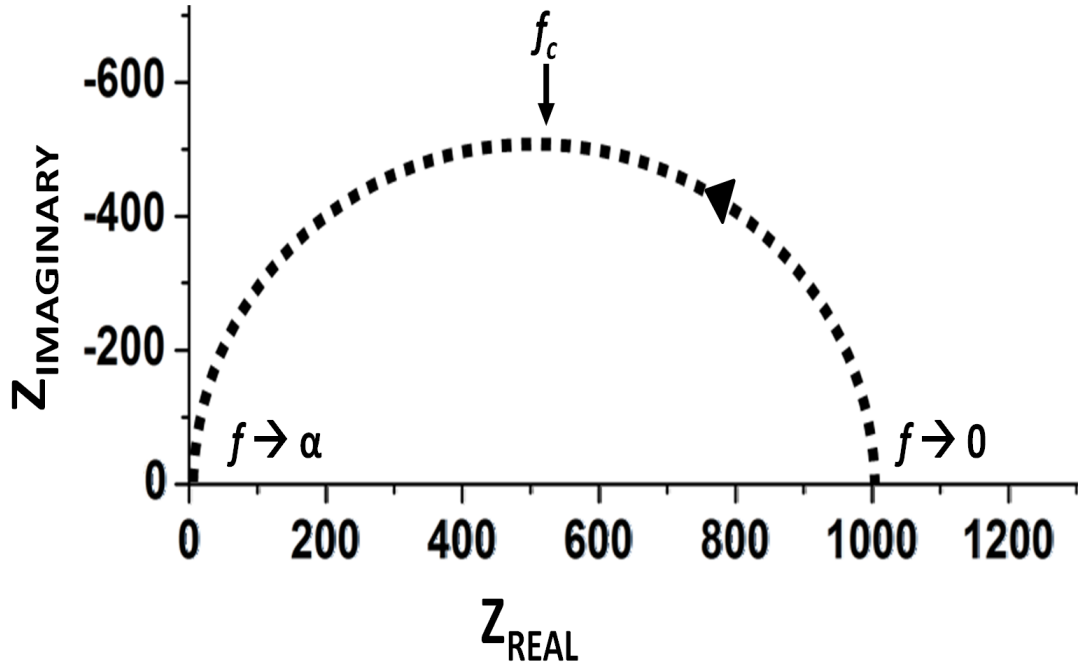


Figure 14. Nyquist plot of perfect parallel RC circuit ⁴⁹.

The Nyquist representation in Figure 14 demonstrates the response of current passing through an ideal RC circuit; the reactive impedance is dependent on the inverse of applied AC signal frequency ω , and the resistive impedance is frequency-independent. At very low frequency ($f \rightarrow 0$), the impedance is completely resistive whereas at very high frequency ($f \rightarrow \infty$), the impedance is completely capacitive. The phase angle Φ approaches -90° at high frequencies and 0° at low frequencies. At a phase angle of -45° , the $Z_{\text{IMG}} = Z_{\text{REAL}}$ and this point is known as the “critical frequency” f_c . The critical frequency f_c is associated with the circuit parameter called “time constant” $\tau = \frac{1}{f_c} = 2\pi RC$. The time constant relates to the time required to charge or discharge the capacitor, this value can be changed by adjusting the values of R and C in a circuit. In real systems the Nyquist plots demonstrate either multiple loops or depressed semicircular shapes, there are more than one time constant associated with the charge transfer process ⁴⁹.

2.5. Concepts In Semiconductor Piezoelectric Material-Based Energy Harvesters

2.5.1. Semiconductor Junctions

2.5.1.1. Schottky Contact in n-type Semiconductor

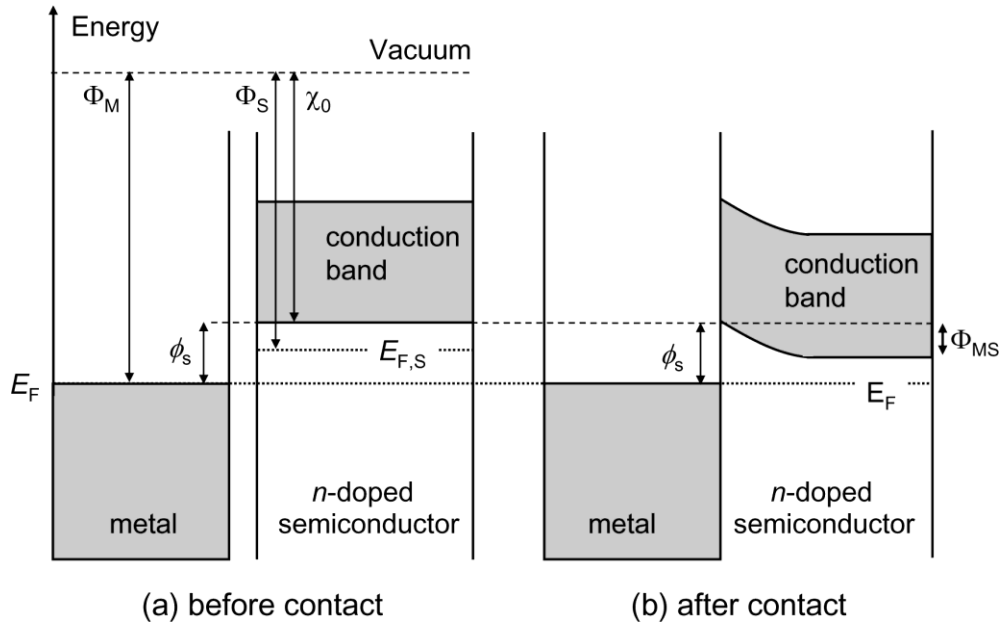


Figure 15. Schottky contact and band bending between metal and semiconductor⁵¹. Φ_M and Φ_S represents the work function of metal and semiconductor, Φ_s is the schottky barrier.

Figure 15 shows a contact of n-type semiconductor with a metal. If the work function Φ_M of electrons in the metal is greater than the semiconductor electron affinity χ_0 then the electrons transfer from the semiconductor to the metal, forming a depletion region called Schottky barrier Φ_S . The Fermi levels are aligned as the electron energy is lowered in semiconductor^{51–53}. The Schottky barrier provides rectifying properties to metal-semiconductor junction, and its height is defined as⁵¹:

$$\Phi_S = \Phi_M - \chi_0$$

2.5.1.2. Ohmic Contact in n-type Semiconductor

Figure 16 shows an n-type semiconductor in contact with a metal of lower work function Φ_M than the electron affinity of the semiconductor χ_0 . In this case, the electrons from the metal lower their energy by moving in the semiconductor conduction band. Upon obtaining the electrons from the metal, the Fermi levels align

and an accumulation region of low resistance is formed between the metal and semiconductor^{51–53}.

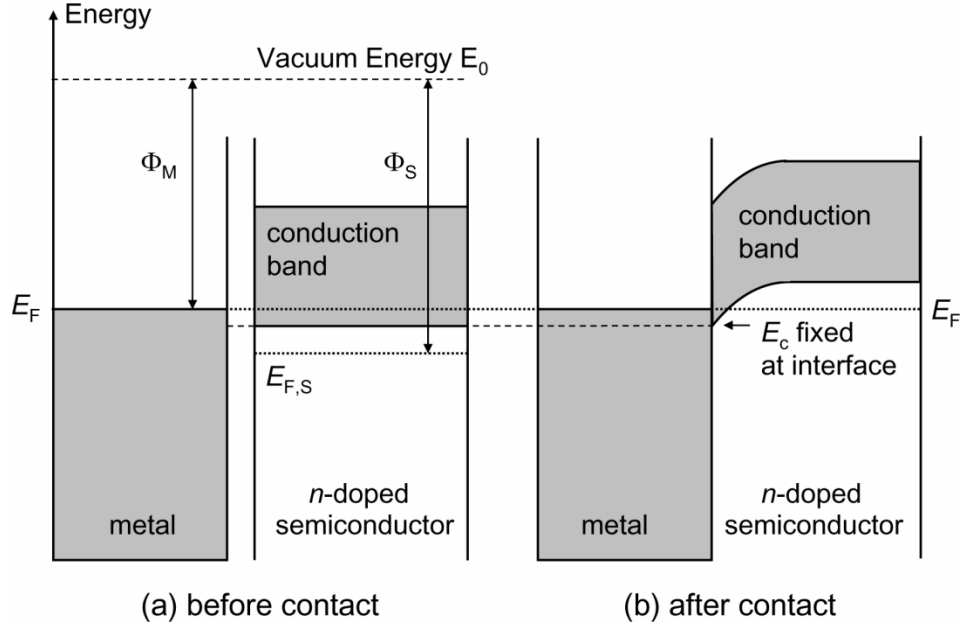


Figure 16. Ohmic contact and band bending between metal and semiconductor⁵¹.

2.5.1.3. Electric Field Screening

Semiconducting materials contain free-charge carriers associated with unintentional doping by impurities and surface defects. Due to strain-induced piezoelectric polarisation, the charge carriers are free to flow through the material under the induced electric field. The polarisation-induced electric field (E_{dep}) is believed to be suppressed by the screening field (E_{scr}) of the free-charge carriers, causing an effect called internal screening^{54–57}. In addition, an application of external electric field to the piezoelectric material through the use of Schottky, ohmic or p-n junction contact allows free-charges to be transferred from the contact to the material. These carriers induced by external contacts suppress the polarisation field and this effect is called external screening^{54–57}.

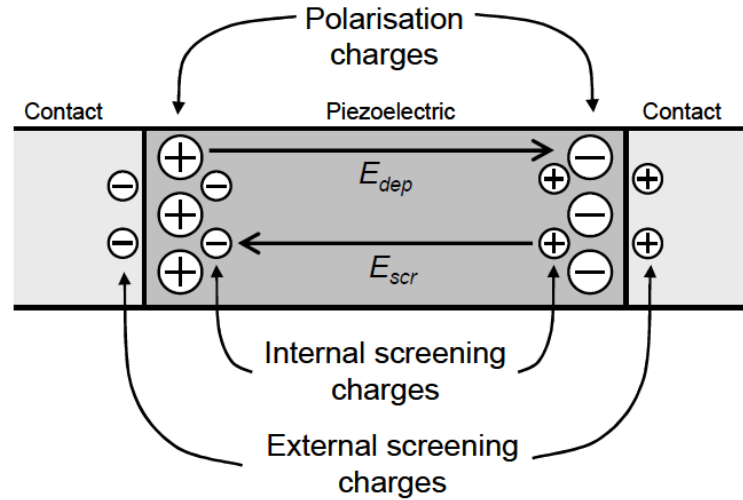


Figure 17. Model of internal and external screening effect in a semiconducting material ⁵⁴.

2.6. Piezoelectric Energy Harvesting Devices

2.6.1. Bulk and Thin Film PZT Based Energy Harvesters

Lead zirconate titanate $\text{Pb}(\text{Zr.Ti})\text{O}_3$ is widely employed in sensors, actuators and resonators due to its attractive piezoelectric properties such as electromechanical coupling coefficient $k_{33} > 0.7$ and piezoelectric coefficient $d_{33} > 350 \text{ pm/V}$ ⁵⁸. Amongst many applications, thin films and bulk structures of PZT have been widely used in microelectromechanical systems (MEMS) for sensing in automobiles and actuation in fuel injectors and printheads. In addition, they are gaining wide interests for energy harvesting applications. This section provides an overview on the development of PZT energy harvesters and the purpose of this discussion is to analyse the device measurement and characterisation techniques reported by the authors. For PZT devices, the impedance analysis was reported in many research literatures ^{59–65}. By analysing impedance results, the critical electrical frequency at resonance was matched with critical mechanical frequency at resonance under dynamic strain. These results were the key to characterise and verify electrical-mechanical transduction in PZT devices. In addition, impedance load matching was performed which provided measure of device's maximum power generation across an optimum load. Therefore, the frequency matching and impedance matching results confirmed that these characterisation techniques were useful to determine

reliability of device output. Hence, this verified that the observed output signals were piezoelectric and not electrostatic artefact.

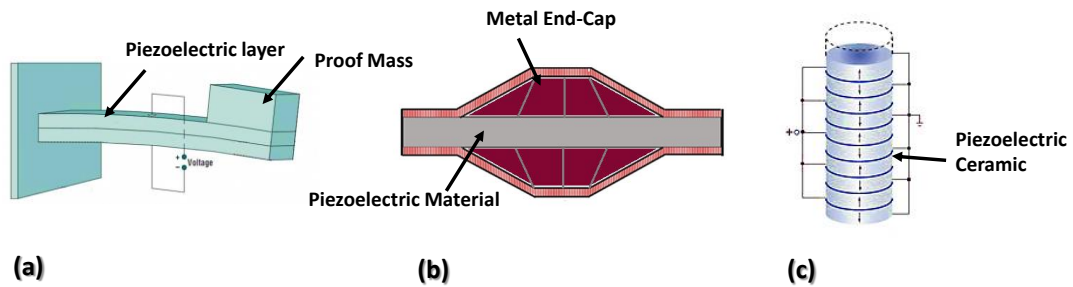


Figure 18 Various configurations of PZT energy harvesters (a)cantilever structure⁶⁶ (b)cymbal-type structure⁶¹ (c)stack-type structure⁶⁷.

PZT MEMS energy harvesters have been frequently configured into cantilevers, cymbal-type and stack-type structures. A cantilever beam generally composed of one or two piezoelectric films, known as unimorph and bimorph respectively, are the simplest structures used for piezoelectric energy harvesting. These devices generate alternating voltage output when subjected to dynamic stress loading using a vibrational host for e.g. electrodynamical shaker. They can be designed for d_{33} and d_{31} modes, however mostly d_{31} mode is implemented because higher strain is induced in the device when it is bent in lateral mode⁶⁸.

Shen et al. (2008) fabricated a MEMS cantilever device using 1 μm thick PZT thin film in a multilayer structure of Pt/PZT/Pt/Ti/SiO₂. This device was designed for optimum operation at low frequency (hundreds of Hertz) and high amplitude (>1 g) vibrations. The impedance analysis was performed and the electrical resonant frequency of the PZT device was measured to be 462.5 Hz. Figure 19 shows the peak voltage output and average power density plotted against a sweep of resistive load, when the device was subjected to vibrations at variable frequency, acceleration and amplitude using electromagnetic shaker controlled by external function generator⁶⁰. The maximum average power delivered was 3272 $\mu\text{W cm}^{-3}$ across a 6 k Ω optimum load at 2g. The optimum load resistance increased with the increase in acceleration because the mechanical stress on device increased which increased the device mechanical damping; consequently the electrical damping required for mechanical compensation also increased. The voltage and power density output were

also analysed as a function of excitation frequency (Figure 8(c-d)). The devices were observed to attain mechanical resonance at the frequency range of 461 – 461.5 Hz, which matched with the electrical resonant frequency observed using impedance analysis⁵⁹. This research work carried important device measurement and characterisation techniques. The electrical and mechanical resonant frequencies were shown to compensate each other with the use of resistive load matching, which confirmed that the device was generating piezoelectric output which was not interfered by the measurement artefacts. Moreover, the device performance was evaluated at varied accelerations, which indicated the significance of self-powered systems as accelerometers.

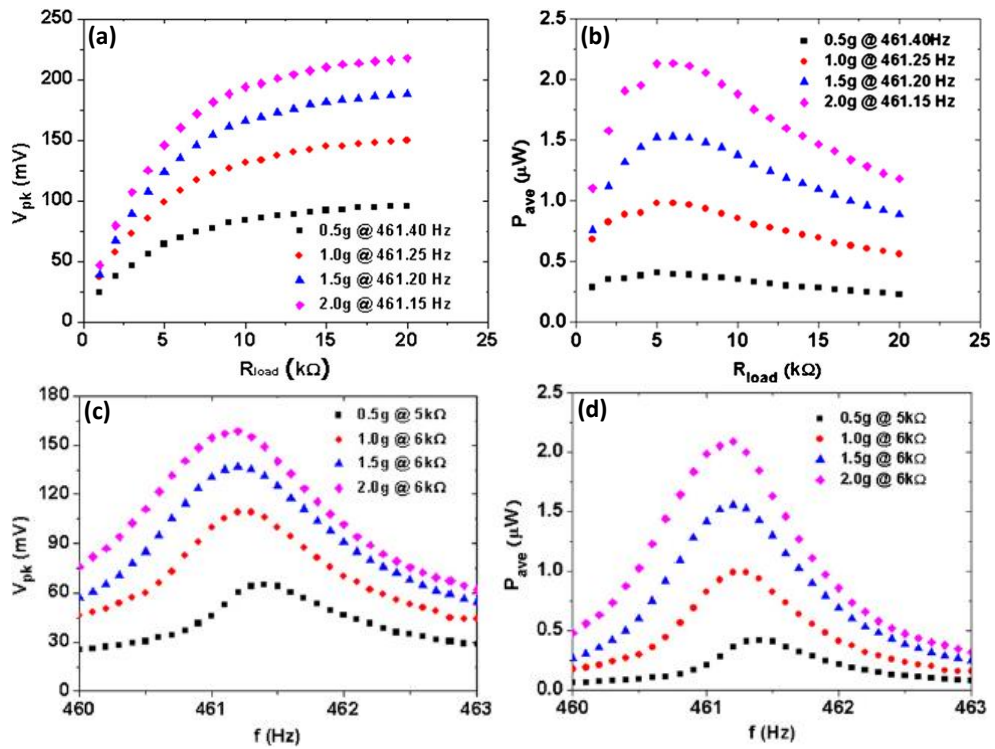


Figure 19. (a) Peak open-circuit voltage output across load resistance, (b) average power output across load resistances showing optimum load of 6 $k\Omega$, (c) peak open-circuit voltage output at varying vibration frequency, (d) average power density at varying vibration frequency⁵⁹.

Cantilever piezoelectric MEMS structures are simple in geometry and fabrication but their scaling poses design limitations, e.g., in case of anisomeric scaling, if the length of a beam is shortened by a factor S then the stiffness and resonant frequency of the

beam increases by S^3 and S^2 respectively. This reduces the deflection of cantilever beam, and when strained it allows shear deformation to the device which is complex to be modelled⁷¹. Secondly for thin films, the higher d_{31} coefficients of ~ 120 pC/N were found for PZT with thickness around 200 nm. For this range of PZT thickness, the cantilever beam can only be minimized to a limit of 2 μm thickness⁷¹.

Moreover, for maximum power conversion efficiency the cantilever resonant frequency is matched with the ambient vibrations frequency. If the beam departs from the resonant frequency then there is a considerable drop in piezoelectric power generation. In order to address this issue, a few designs for wide bandwidth frequency range were suggested: tapered cantilever beam with PZT blocks attached on maximum stress locations (Figure 20(a)), multiple cantilever with varying size and tip mass connected in series (Figure 20(b)), multiple beams of PZT with varying dimensions connected in parallel (Figure 20(c))⁶³. In the proposed designs shown in Figure Figure 20(a), more than one piezoelectric material blocks were arranged at various locations on the tapered cantilever. This was considered to cause each PZT block to be tuned at a different resonant frequency. Hence, this type of system was assumed to be capable of scavenging optimum power at multiple input frequencies. Similarly in Figure 20 (b) and (c), multiple beams were arranged in a specific manner and size, so that each of the beam could be tuned to a different resonant frequency. Hence, these systems were proposed to increase the frequency bandwidth of piezoelectric transducers.

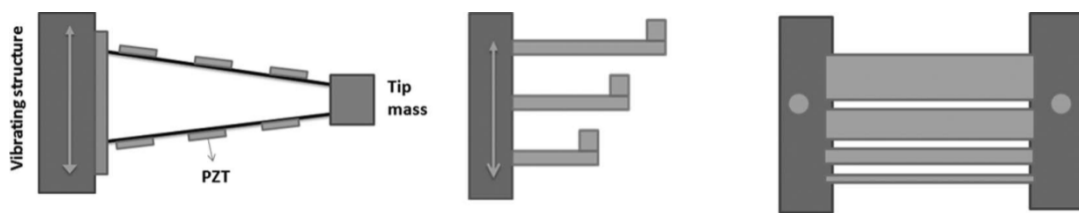


Figure 20. Proposed models for broadband tuning of PZT MEMS cantilever devices⁶³.

Cymbal-type MEMS consist of a piezoelectric material sandwiched between two electrodes and they produce considerable strain when subjected to transverse force⁶². Kim et al. (2005) demonstrated fabrication and performance measurement of a

cymbal-type MEMS energy harvester (Figure 22(b)). The device was mechanically excited by a force of 7.8 N at 100 Hz using an amplitude vibrator. The device generated maximum power of 39 mW and its load was matched at 400 k Ω after the rectification circuit ⁷². The research on cymbal device became more interesting when its impedance was matched with energy harvesting circuit called DC-DC buck converter. In this way, the concept of maximum power transfer was applied to demonstrate efficient power transfer from the capacitive piezoelectric power source to a complex load. To elaborate, a DC-DC buck converter circuit was used and its impedance was matched with the impedance of the piezoelectric device. The output of this DC-DC buck converter was used to charge a battery which had an internal impedance of few hundred ohms. For efficient energy harvesting load was matched with the internal resistive and reactive impedance of the energy harvester. In case of buck converter, the inductor L (Figure 21) was tuned to match the reactive impedance of the piezoelectric source. Figure 22(a) shows the power density output of the piezoelectric cymbal device across varying resistive load in DC-DC buck converter, with the inductance fixed for each measurement. The optimum efficiency was obtained at an inductive load of 470 μ H ⁷³.

Generally, a cymbal-type device is an example of piezoelectric MEMS on which an impulsive force is usually applied. These devices are not necessarily designed to operate at mechanical resonance frequency, instead they are designed with metal-ceramic composite to withstand high mechanical loading ⁷³ under cyclic stress. In addition, they have a high effective strain coefficient d_{eff} ⁷³, such as ~15,000 pC/N as reported by Kim et al. (2007) ⁷³. In the research work reported by Kim et al. (2007) ⁷³ the device impedance was matched with a complex load ($R + jX_L$) of the DC-DC converter circuit whereas, Shem et al. (2008) ⁵⁹ performed impedance matching using resistive load only. It is worth considering that unlike resistive load matching, complex load matching increases the bandwidth of operation and allows the energy harvester to have a broader range of optimum load resistances (as shown in Figure 22(a)).

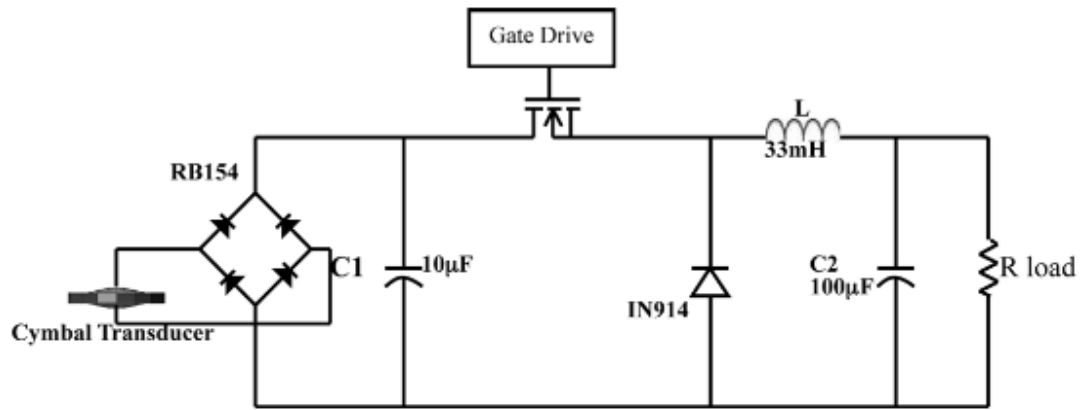


Figure 21. Buck converter circuit used for matching the impedance of energy harvester ⁷³.

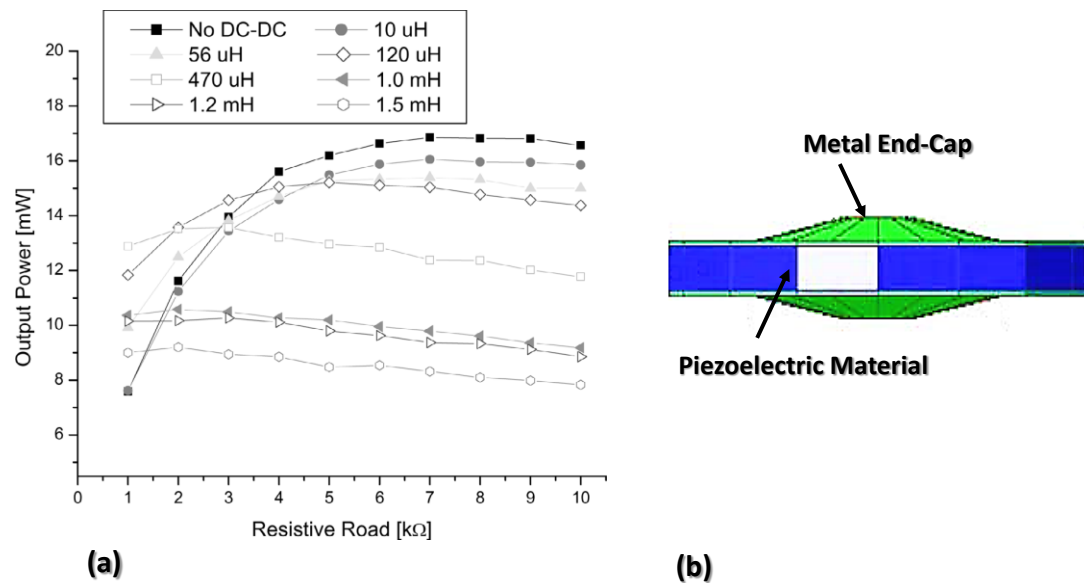


Figure 22. (a) Complex impedance matching for the buck converter in Figure 21. (b) Design of cymbal-type MEMS device ⁷³.

The effect of energy harvester's internal impedance on the power output performance was investigated by Sodano et al. (2004). A PZT-based Micro Fibre Composite (MFC) MEMS, originally designed by NASA Langley Research, was fabricated and its performance was compared with a biomorph piezoelectric device. The biomorph was fabricated using monolithic PZT embedded in epoxy composite. The MFC design comprised of PZT microfibres also embedded in epoxy composite

and they were contacted with interdigitated copper electrodes (Figure 23(b)). For comparison, the surface area of PZT and the measurement conditions for both devices were kept same. The MFC device generated open-circuit voltage higher than the bimorph device but, due to interdigitated electrode (IDE) design it possessed higher internal impedance than the later. The IDE were designed to connect multiple PZT fibres in series which increased the series resistance of the device and therefore its current density decreased. Owing to this reason, the MFC device did not produce enough current to charge a 200 mA h nickel metal hydride battery whereas, the biomorph device was able to charge the same in 4 hours^{74,75}.

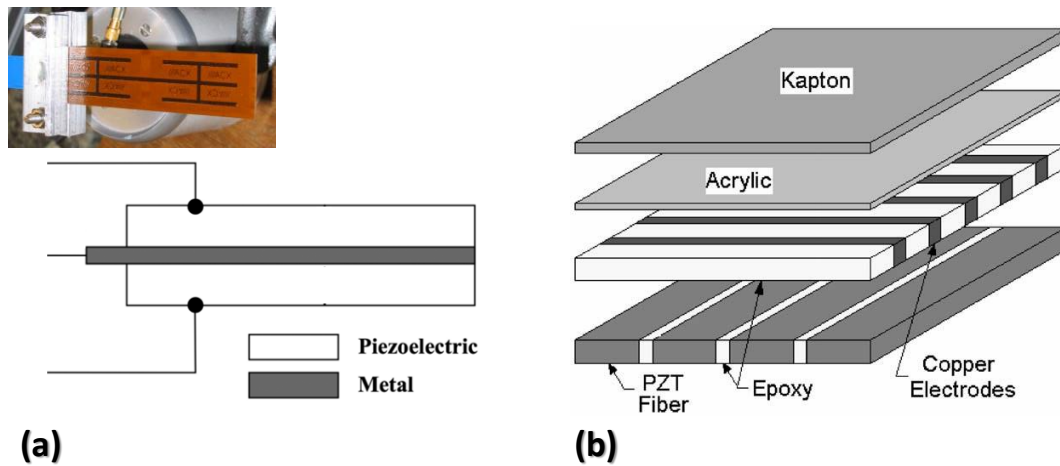


Figure 23. (a) Schematic of a typical piezoelectric biomorph device⁷⁶. Inset showing top view of actual device reported by Sodano et al. (2004)^{74,75}. (b) Micro Fibre Composite (MFC) device assembly⁷⁴.

2.6.2. ZnO-Based Piezoelectric Energy Harvesters

ZnO nanostructures are considered for applications in gas sensors, solar cells, photo sensors, vibration sensors and vibration energy harvesters. The piezoelectric property of ZnO nanorods and nanowires is widely used in nanostructure-based vibration energy harvesters (also called nanogenerator). The nanorods and nanowire provide benefit of vertical alignment which is believed to facilitate longitudinal, transverse and shear modes of strain distribution. This section provides a brief overview on the

development of nanostructured-ZnO energy harvesters with the main focus on their fabrication, measurement and characterisation. The piezoelectric charge generation from ZnO nanowires was first observed using conductive atomic force microscopy (c-AFM) technique. 0.2 – 0.5 μm long nanowire arrays were fabricated on $\alpha\text{-Al}_2\text{O}_3$ substrate using vapour-liquid solid (VLS) method. Voltage peaks of 2 mV - 8.5 mV across load resistance R_L of 500 $\text{M}\Omega$ were observed when nanowire tips were laterally bent 66 nm - 149 nm using platinum (Pt) coated AFM tip in contact mode while maintaining a constant force of 5 nN between the tip and ZnO surface⁷⁷.

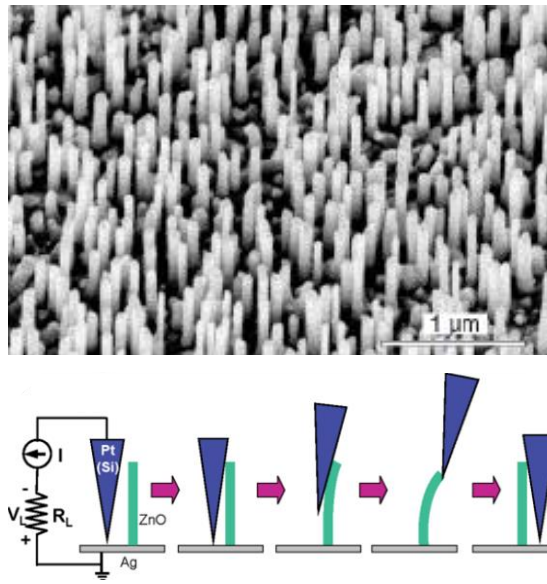


Figure 24. (a) SEM image of ZnO nanowire, (b) C-AFM measurement showing lateral bending of ZnO nanowire using AFM tip⁷⁷.

Due to electron affinity (E_a) of 4.5 eV for ZnO and work function (ϕ) of 6.1 eV for Pt, ZnO-Pt contact formed a Schottky barrier. As explained by Wang and Song (2006)⁷⁷, when scanned on the tensile positive surface, the AFM tip made a reverse biased Schottky contact with ZnO which facilitated *piezoelectric charge accumulation* in the nanowire volume. Thereafter, a forward biased Schottky contact was formed when the AFM tip contacted the compressed negative surface and the discharge of the *piezoelectric charges* occurred through the AFM tip. Therefore, Schottky barrier was described to be essential for piezoelectric charge generation⁷⁷. However, the concept of *piezoelectric charge accumulation* under reverse bias

Schottky contact is arguable. Firstly, the concept of *piezoelectric charge* is considered as fundamentally invalid. As explained by Abu-Faraj (2012)¹⁸, in a piezoelectric material stress-induced polarisation is caused by its crystal's ionic separation. This polarisation change is measured as voltage output. The measured voltage is therefore not developed due to movement or discharge of charges, but it is built-up by retention of polarised immobile charges⁷⁸. Hence, the reported concept of generation or flow of *piezoelectric charges* under polarisation field was fundamentally incorrect.

To further elaborate the necessity of Schottky barrier as an essential element for piezoelectric response measurement, we consider the concept of screening. The voltage generation of piezoelectric material or device is affected by external and internal screening. As explained previously, screening refers to damping of polarisation charges by free mobile carriers. These mobile carriers are said to cause internal screening, when they are generated due to material carrier concentration. Therefore, internal screening effect increases with the increase in material conductivity. When the flow of free-charge carriers is caused by external contacts on the piezoelectric material, then the resulting screening is called external screening⁵⁴. In the case of AFM measurement, the probe of AFM was considered to be an external contact on ZnO and therefore, the measurement of piezoelectric response was affected by external screening.

A Schottky contact between metal and semiconductor forms a Schottky barrier. This energy barrier at metal/semiconductor interface is considered to reduce the flow of external charges from measurement circuit to the semiconductor. As the rate of flow of free-charge carriers is reduced, the retention of polarisation charges is increased and this causes a measureable voltage to be built-up across the material. Therefore, it was considered that the presence of Schottky contact between ZnO and Pt was responsible in reducing the screening effect and causing voltage to be measured.

This effect of a barrier between piezoelectric material and external contact was later elaborated to be essential for reducing external screening⁷⁹. Additionally, Schottky contacts were used in device fabrication and the first devices fabricated for vibration energy harvesting with ZnO nanostructures were based on ZnO and metal contacts

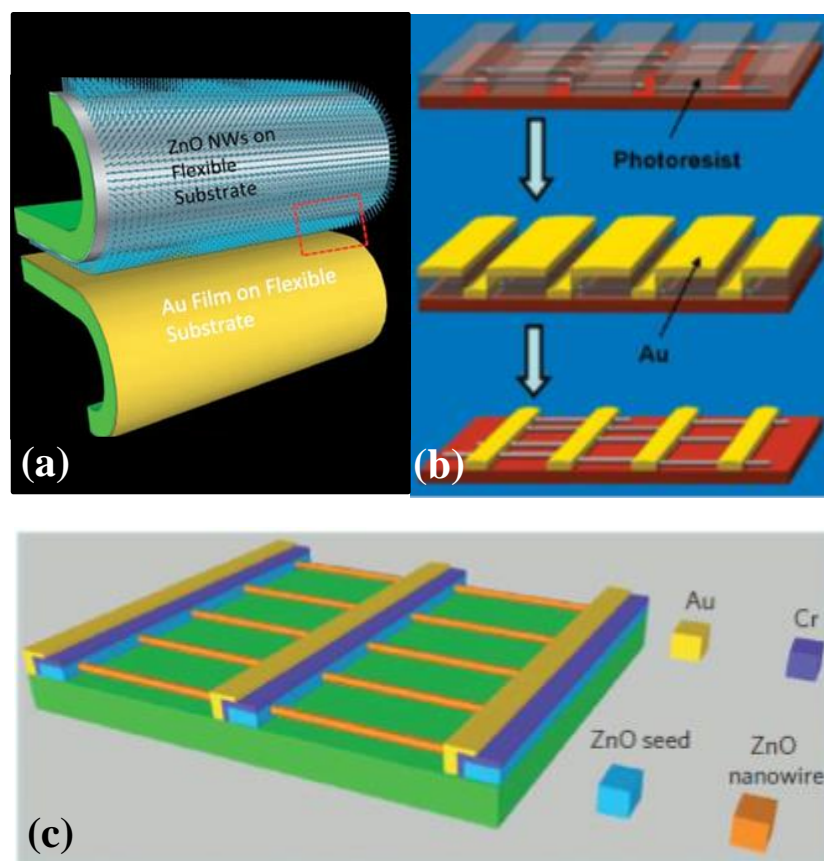


Figure 25. Various Schottky-type device configurations (a) flexible Au/ZnO device⁸⁰, (b) and (c) rows of Au/ZnO devices connected in series^{81,83}.

The research on ZnO-based devices from 2006-2012 was focused on material processing and fabrication techniques. The research focus was not majorly on measurement and characterisation of devices. Due to this, understanding effects of device components, such as electrode material, on its performance were not clear.

As a concept established through research work on metal contact-based ZnO piezoelectric energy harvesters, Schottky barrier provided separation of interfacial charges at metal-semiconductor junction and prevented the screening of ZnO polarisation charges by the carriers moving from the external contacts^{77,79}. Hence, initially Schottky contact was considered to be essential for devices to work. Moreover, it was observed that the peak voltage generation from Schottky-type devices was limited to few hundred millivolts⁵⁴. The only method used for improving voltage generation was through devices' series connection.

As demonstrated by Lee et al. (2011)⁸⁰, the highest peak voltage generation of a Schottky-type ZnO nanowires-based energy harvester was 350 mV and 125 nA cm⁻². The nanowires were vertically grown on ZnO-seeded indium tin oxide/kapton polyimide substrate using aqueous solution of Zn(NO₃)₂ and Hexamethylenetetramine (HMT). They were spin-coated with poly(methyl methacrylate) (PMMA) and the tips were etched using oxygen plasma treatment in order to form Schottky contact with a metal top contact. A mechanical vibration system, operated at 10 Hz excitation frequency, was used to generate voltage response of 350 mV. Thereafter, 10 devices of this configuration were stacked in series to increase the peak voltage output and current density to 2.1 V and 105 nA⁸⁰.

Similarly, as reported by Zhu et al. (2010), voltage output for Schottky junction-based ZnO energy harvester was achieved by integrating 600 rows of ZnO devices in electrical series connection (Figure 25). The nanowires were laterally assembled on 125 µm thick kapton polyimide substrate. 600 rows of 300 nm thick gold electrodes were sputtered on top of the nanowires (Figure 25(b)). The completed device was encapsulated in Polydimethylsiloxane (PDMS). This device was mechanically stretched and released using force applied by a linear motor. At the maximum applied excitation frequency of 0.33 Hz, peak voltage and peak current density of 2 V and 107 nA/cm² was obtained⁸³. A similar approach of connecting 700 devices was reported by Xu et al. (2010), where 700 laterally aligned nanowire-based devices were connected in series⁸¹ (Figure 25(c)). This series connected device generated 1.2 V output.

From the analysis of results reported by Zhu et al. (2010)⁸³ and Xu et al. (2010)⁸¹ it was certain that if 600 - 700 devices connected in series generated peak open-circuit voltage of 1.2 V to 2 V, then each device was generating 1 – 2 mV voltage output. It was considered that there were losses in Schottky-type devices which were not addressed and analysed; instead rows and stacks of devices were connected in series to increase the final output. In any case, connecting multiple Schottky-type devices was not a solution to reduce device losses. Losses caused by device electrodes were later explained by Briscoe et al. (2012)⁵⁴ by considering external screening effect caused by electrode types. For experimental analysis, A p-n junction-type device comprising of semiconducting top electrode was reported to generate peak open-circuit voltage of 10 mV and short-circuit current density of 10 µA cm⁻² by bending

the device at a rate of ~ 2 Hz. In this device, n-type ZnO nanorods were coated with a film of p-type semiconductor Poly(3,4-ethylenedioxythiophene) Polystyrene sulfonate (PEDOT:PSS). The open-circuit voltage output and short-circuit current density of this device was higher than the individual Schottky-type devices reported by Zhu et al. (2010)⁸³ and Xu et al. (2010)⁸¹. This increase in voltage output was described to be caused by reduced screening effect of semiconducting top electrode. It was reported that free-charge carrier transport into ZnO was higher from metal electrodes than semiconducting PEDOT:PSS top electrode. This was because metals have carrier concentration in the range of $\sim 10^{28} \text{ m}^{-3}$ ⁸⁴, which is higher than PEDOT:PSS carrier concentration of 10^{19} cm^{-3} ⁵⁴. Additionally, interfacial charges were also considered to be higher in metal/ZnO contact, due to higher carrier mobility at metal surface. Hence, the rate of external screening of polarisation charges was higher in metal contacts than semiconducting contacts.

The slower rate of screening in p-n junction-type device was further elaborated using band diagrams (Figure 26). An understanding of piezoelectric polarisation and its screening was developed using the band positions of ZnO/PEDOT:PSS. The bands of polarised ZnO were demonstrated to be tilted due to depolarisation field (E_{dep}), which drives the compensating free-carriers present within the material and transported from the contacts (Figure 26(b)). The internal screening of the polarisation field is dependent on the conductivity of ZnO. Hence, increase in ZnO conductivity increases the rate of internal screening. It was analysed that, when carrier concentration of ZnO increases to 10^{18} cm^{-3} , the energy harvester voltage output is completely screened before getting measured. However in the presented report, the carrier concentration of ZnO was $\sim 10^{17} \text{ cm}^{-3}$ which did not completely internally screen the polarisation field. The faster screening was demonstrated to occur due to interfacial charges between ZnO and ITO (Figure 26(c)). The bound charges were shown to be partially screened. Thereafter, the screening due to hole accumulation at the ZnO/PEDOT:PSS interface occurred at a slower screening rate due to semiconducting properties of PEDOT:PSS, which allowed generated voltage to be measured before it was completely compensated (Figure 26(d))⁵⁴. Hence, this study highlighted the importance of using semiconducting external electrodes with piezoelectric material. It effectively explained the losses due to metal external electrodes and the resulting short-comings in the devices fabricated with them.

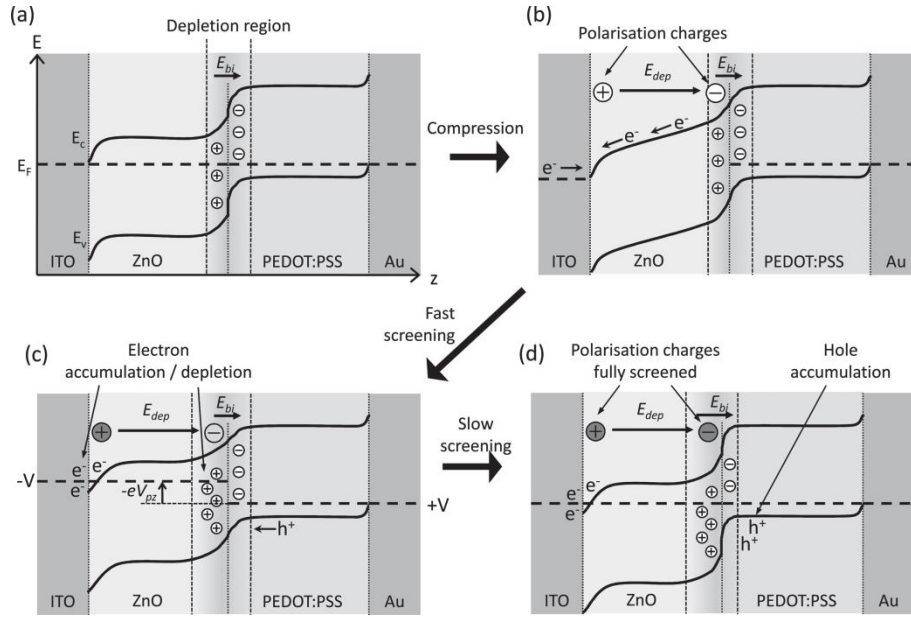


Figure 26. (a) PEDOT:PSS/ZnO device band diagram, showing: (b) internal carrier screening, (c) fast screening effect from ITO/ZnO junction and (d) slow screening effect from PEDOT:PSS/ZnO junction⁵⁴.

The external screening issue was also addressed by introducing an insulating layer, most commonly poly(methyl methacrylate) (PMMA), as a top contact with nanowires⁸⁵. This insulator-type device was first integrated with two series connected devices (as shown in Figure 27). ZnO nanowires using hydrothermal method were synthesized on the two surfaces of the ZnO seeded polystyrene (PS) substrate. PMMA layer was spin coated on the nanowires on both surfaces. The PMMA layers filled the interspaces of the nanowire arrays and covered their tips. A Cr/Au electrode was deposited on top of the PMMA. 2 series connected insulator-type devices generated 10 V which was an order of magnitude higher than hundreds of series connected Schottky-type devices reported Zhu et al. (2010)⁸³ and Xu et al. (2010)⁸¹. The current density also increased to $10 \mu\text{A cm}^{-2}$ ⁸⁵. It was interesting to note that although the peak open-circuit voltage output of the insulator-type device was also an order of magnitude higher than the p-n junction-type device reported by Briscoe et al. (2012)⁵⁴ but the short-circuit current density was in the same range. This indicated that although the insulator-type device's open-circuit voltage output was enhanced but there were factors which reduced its voltage-driven current density. Therefore, this result required further consideration and study. Hence,

determination of differences between p-n junction-type and insulator-type device performance became one of the motivations of study presented in this report.

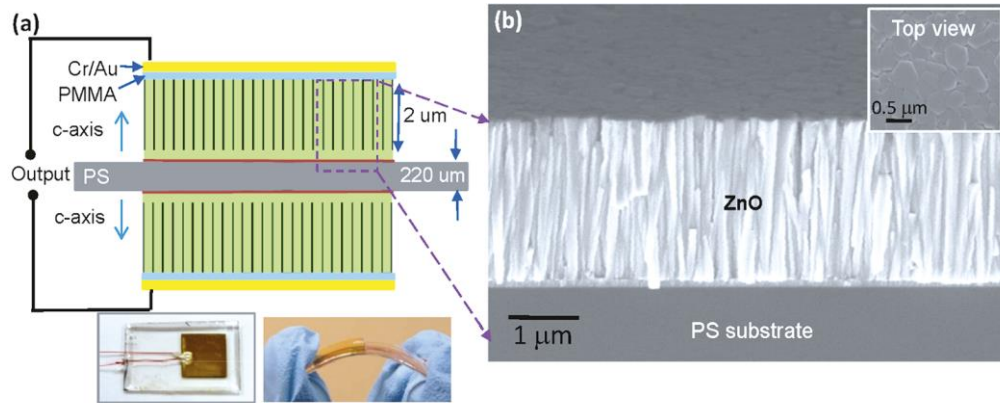


Figure 27. Series connected insulator-type device ⁸⁵.

Adverse effect of internal screening of polarisation charges is as substantial as that of external screening. The improvement in ZnO energy harvester's performance is linked with minimising both external and internal screening effects. The internal screening effect in ZnO is caused by its conductivity which is enhanced due to: (1) increase in donor type impurities, (2) increase in carrier concentration upon UV illumination (band gap 3.37 eV) ⁵⁴. ZnO has intrinsic surface donor defects such as oxygen vacancies and zinc interstitials ^{35,36}. The interaction of the material surface with moisture creates hydroxyl OH⁻ ions which were also identified as donor species ⁸⁶. The surface states unintentionally dope ZnO by injecting carriers. Therefore, this increases the n-type conductivity of ZnO and consequently, the rate of internal screening of polarisation field increases ^{36,87}.

In order to suppress the effects of surface species, ZnO surface was modified using thermal and chemical treatments. These treatments are considered to modify material surface by suppressing their defects and impurities. Consequently, the carrier-induced conductivity of ZnO reduces, which reduces the internal screening effect. Three types of treatments were carried out by Hu et al. (2012) ³⁶: oxygen plasma treatment, thermal annealing and chemical coating. The top electrode material and configuration of this treated-nanorod based device was similar to PMMA-based

device⁸⁵, however ZnO nanorods in this case was surface treated for performance optimisation. The oxygen plasma treatment was applied to reduce the oxygen related defects on ZnO surface. Therefore, this resulted in the generation of 5 V and 300 nA cm². The device performance was observed to be further enhanced with ZnO surface thermally annealed at 350°C. This treatment was considered to eradicate the surface adsorbed species and non-stoichiometric defects which resulted in ZnO energy harvester to produce 8 V and 900 nA cm⁻². Oxygen plasma treatment and thermal annealing were the treatments which passivated ZnO surface, but did not form any permanent coat on it. Due to this, the oxygen plasma treated ZnO-based energy harvester was exposed to the environment for stability study. It was observed that the performance of oxygen plasma treated ZnO device deteriorated after 2 weeks, which indicated instability of oxygen plasma treatment under atmospheric conditions. In order to resolve this issue, a permanent coating of polyelectrolyte solutions of Polydiallyldimethylammonium chloride (PDADMAC) and Polystyrene sulfonate (PSS) were coated on ZnO surface. Due to adhesion of coating onto ZnO surface, the suppression of surface states was more effective as compared to oxygen plasma and thermal treatment. The device generated peak open-circuit voltage of 20 V and short-circuit current density of 6 $\mu\text{A cm}^{-2}$ ³⁶.

Another method commonly adopted to reduce donor concentration in ZnO is by doping it with acceptor ions of lithium (Li+) and silver (Ag+). This approach was adopted to reduce the rate of internal free-carrier screening in ZnO nanowires. In doped ZnO, the rate of internal screening was successfully reduced; but the reported devices of doped ZnO were fabricated with Schottky-type contacts which could have increased the external screening losses. The voltage output of the devices were therefore an order of magnitude less than that of the insulator-type ZnO surface treated devices reported by Hu et al. (2012)³⁶. Sohn et al. (2013) reported growth of 2.5 μm long ZnO nanowires on ZnO-seeded p-type Si substrate using chemical bath method with aqueous solutions of Zn(NO₃)₂, HMT and dopant precursor Lithium Nitrate (LiNO₃). The ITO-coated PES substrate was contacted on top of the nanowires and they were mechanically excited using sonic waves of 100 dB at 100 Hz. The doped nanowire devices generated ~900 mV with the optimum addition of Li ions. In another device, the surface of doped nanowires was treated with oleic acid and the voltage output was further increased to 2.9 V⁸⁸. Similarly, the ZnO

nanowires were doped with Ag ions during wet chemical bath growth technique. ZnO nanowires were grown on ZnO-seeded gold (Au)-coated polyester fibres using $\text{Zn}(\text{NO}_3)_2$, HMT and silver nitrate (AgNO_3) precursor solutions. The Ag dopants were ions generated by AgNO_3 which act as shallow acceptor in ZnO nanowires. Another gold (Au)-coated polyester was used as the electrode layer on top of the nanowire arrays. The device generated 4 V peak-to-peak and $0.1 \mu\text{A cm}^{-2}$ peak-to-peak⁸⁹.

2.6.2.1. Impedance Matching in ZnO-based Piezoelectric Energy Harvesters

For optimised power generation, the impedance of ZnO energy harvesters was matched using energy harvesting circuits such as: simple bridge rectifier with storage capacitor⁸³ and buck converter³⁶. The energy harvesters were demonstrated to electrically energise the circuit to power an LED⁸³, wrist watch³⁶, wireless transmitter³⁶, etc. These demonstrations were useful in highlighting the benefits of ZnO energy harvesters as self-powered source. However, unlike the reported knowledge in PZT energy harvesters, the literature on ZnO devices did not provide details and procedures of impedance matching with energy harvesting circuits. Secondly, not only it is important for energy harvester to drive an electronic circuit but also to charge the capacitor of energy harvesting circuits in sufficient time. The best performing devices for insulator-type devices generated short-circuit current density of 300 nA cm^{-2} to $10 \mu\text{A cm}^{-2}$, were reported to charge a capacitor and deliver stored power to light an LED. But, to charge capacitor, number of input vibration cycles and duration taken to charge the capacitor was not specified.

2.6.2.2. Study of Screening Effects using Piezoelectric Force Microscopy

The semiconductor piezoelectric nanorods of ZnO have reportedly been synthesised by Pulsed Layer Deposition (PLD), Chemical Vapour Deposition (CVD), Chemical Bath and Electrochemical methods⁹⁰. The growth parameters and procedures affect the crystallinity, defects, surface-states and carrier concentration of ZnO nanorods which affect its piezoelectric behaviour. A considerable variation in the piezoelectric

behaviour of ZnO nanorods is caused by the screening effects of free-electron carriers which are influenced by its electron transport properties, surface-states, native defects and doping concentration^{29,90,91}.

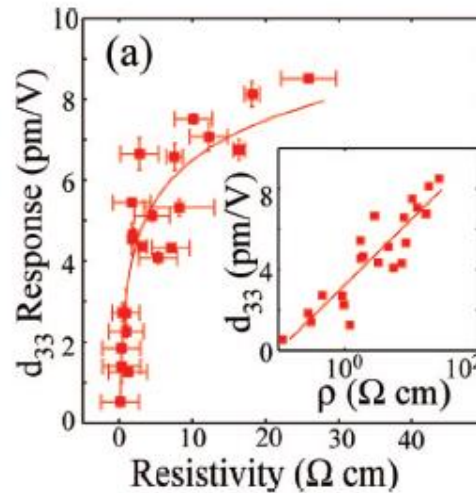


Figure 28. Correlation of resistivity to piezoelectric response in ZnO nanorods⁹².

Piezoelectric Force Microscopy (PFM) technique has been used to determine the piezoelectric response of nanostructured-ZnO in association with its electrical properties such as, surface defects and carrier concentration. The PFM technique is essentially based on Scanning Probe Microscopy (SPM) with an AC signal applied between the conductive tip of a probe and the substrate. The displacement in the material, normally expressed in picometer per volt, is detected by a photo diode sensor and transmitted to the lock-in amplifier^{93,94}. This technique was implemented to measure piezoelectric coefficient of ZnO nanostructures; for instance d_{33} of ZnO nanorods was measured and a correlation between d_{33} properties and resistivity of ZnO nanorods was observed⁹². It was reported that as the resistivity of the nanorods was increased from 0.1 to 155 Ωcm the corresponding piezoelectric coefficient increased from 0.4 to 9.5 pm/V (Figure 28). This effect was explained using free-charge carrier screening phenomenon. It has been established that conductivity of ZnO governs the flow of internal free-charge carriers in its polarised state. Therefore due to higher carrier conductivity in 0.1 Ωcm nanorod sample, the internal screening rate was considered to be higher and therefore the piezoelectric response of the nanorod reduced, causing the measured d_{33} value of 0.4 pm/V^{29,92}.

Hussain et al.⁹⁵ demonstrated a reduction in the defect level of ZnO using oxygen plasma treatment. The consequent reduction in ZnO free-carrier density improved the voltage output from individual nanorods bent using AFM tip. Before oxygen plasma treatment, the average output voltage was 78 mV and after oxygen plasma treatment it increased to 122.7 mV⁹⁵.

2.7. Summary

This section was aimed to provide an overview on the dielectric materials which are classed as non-centrosymmetric crystals and due to their functional properties they are used for energy harvesting applications. Piezoelectricity is a widely employed phenomenon in sensors, actuators and resonators, nevertheless it is considered vital for self-powered energy harvesting systems. In order to develop a piezoelectric energy harvester, it is very important to evaluate its performance using standardised characterisation and measurement techniques such as impedance analysis. Impedance analysis is an effective tool which studies the behaviour of reactive and resistive impedance in piezoelectric energy harvesters. Thus it provides the resonant frequency at which the power generation of the piezoelectric source can be maximised. Secondly, it indicates the impedance offered by resistive and capacitive elements in piezoelectric source and therefore identifies the importance of complex load matching ($R + jX$) with it. Piezoelectric energy harvesters/generators are capacitive sources and their power generation is optimised using load matching. This concept is based on maximum power transfer theorem and is aimed to obtain the load impedance to which the energy harvester delivers maximum power output.

For the purpose of piezoelectric energy harvesting, materials like Barium Titanate (BaTiO_3) and Aluminium Nitride (AlN) have been considered, but PZT has been the most frequently used. The piezoelectric energy harvesters were mainly fabricated using bulk and thin film materials and in this regard PZT gained popularity in microelectromechanical systems (MEMS) due to its excellent piezoelectric properties such as electromechanical coupling coefficient $k_{33} > 0.7$ and piezoelectric coefficient $d_{33} > 350 \text{ pm/V}$. MEMS energy harvesters have been fabricated as simple cantilever-type, cymbal-type and stack-type structures. Each structure has its own advantages and disadvantages and is implemented according to applications and requirements. The significance of studying PZT MEMS devices not only lies in their

designs but, also in the methods used to measure and characterise them. PZT MEMS devices have been fabricated and operated at mechanical as well as electrical resonance⁵⁹ which was a very useful demonstration of optimising power generation of piezoelectric devices. The main issue with piezoelectric devices is narrow frequency bandwidth of operation. Therefore, methods were developed to address this problem and the concept of inductive load matching⁷³ was reported which tuned the piezoelectric device to operate across a bandwidth of load. Secondly, for mechanical frequencies, the same problem was approached by using MEMS devices with more than one PZT sources tuned to operate at different frequencies⁶³. In addition to power generation optimisation and broadband tuning techniques, energy harvesting converter circuits were also developed and the impedance of piezoelectric generators was experimentally matched with circuit impedance⁷³. These techniques were significant in understanding the fundamentals of piezoelectric device output performance and its evaluation.

ZnO gained wide interest as a piezoelectric energy harvesting material due to its growth below 100°C on flexible polymer substrates. However, the research focused from 2006-2012 on ZnO energy harvesters was mainly based on materials processing and device fabrication techniques. The electrical characterisation of devices such as impedance matching and impedance analysis were not developed, therefore, it was difficult to understand the role of materials, for e.g., conducting and non-conducting top electrodes, in the device output performance. Some of the research work however aimed at understanding the polarisation field screening effects due to external contacts and internal carriers in semiconductor piezoelectric material. Another critical factor was the reported power density, which was calculated as the product of open-circuit voltage and short-circuit current density. This method of power density calculation did not provide the power delivered to the load, because it was multiplication of current and voltage at no load conditions. A better approach to analyse power delivered to load was by performing impedance analysis. Therefore, fundamental analysis such as impedance analysis, impedance load matching were the gaps in the nanostructured ZnO-based energy harvesters, which became the motivation of the research conducted and reported here.

2.8. References

- (1) Raju, G. S. N. *Electromagnetic Field Theory and Transmission Lines*. New Delhi: Dorling Kindersley, 2006.
- (2) Darbyshire, A. *Mechanical Engineering: BTEC National Option Units*; Newnes, 2003.
- (3) Cleveland, C. J.; Morris, C. G. *Dictionary of Energy: Expanded Edition*; Elsevier Science, 2009.
- (4) Vilarinho, P. M.; Rosenwaks, Y.; Kingon, A. I. *Scanning Probe Microscopy: Characterization, Nanofabrication and Device Application of Functional Materials*; Nato Science Series II: (closed); Kluwer Academic Publishers, 2006.
- (5) Ghodssi, R.; Lin, P. *MEMS Materials and Processes Handbook*; MEMS Reference Shelf; Springer, 2011.
- (6) Pethrick, R. A. *Polymer Structure Characterization: From Nano to Macro Organization in Small Molecules and Polymers*; Royal Society of Chemistry, 2013.
- (7) Waser, R. *Nanoelectronics and Information Technology*; Wiley, 2012.
- (8) Driggers, R. G. *Encyclopedia of Optical Engineering*; Dekker Encyclopedias Series; Marcel Dekker, 2003.
- (9) Vijaya, S. *Piezoelectric Materials and Devices: Applications in Engineering and Medical Sciences*; Taylor & Francis, 2012.
- (10) Kasap, S.; Capper, P. *Springer Handbook of Electronic and Photonic Materials*; Springer Handbook of Electronic and Photonic Materials; Springer, 2007.
- (11) Bertotti, G.; Mayergoyz, I. D. *The Science of Hysteresis: Hysteresis in materials*; Elsevier Series in Electromagnetism; Academic, 2006.
- (12) Defaÿ, E. *Integration of Ferroelectric and Piezoelectric Thin Films: Concepts and Applications for Microsystems*; ISTE; Wiley, 2013.
- (13) Richerson, D.; Richerson, D. W.; Lee, W. E. *Modern Ceramic Engineering: Properties, Processing, and Use in Design, Third Edition*; Materials Engineering; Taylor & Francis, 2005.
- (14) Lang, S. B. *Sourcebook of Pyroelectricity*; Ferroelectrics and related phenomena; Gordon and Breach Science Publishers, 1974.

- (15) Rogalski, A. *Infrared Detectors*; Electrocomponent science monographs; Taylor & Francis, 2000.
- (16) Yoder, B. L. *Steric Effects in the Chemisorption of Vibrationally Excited Methane on Nickel*; Springer Theses; Springer, 2012.
- (17) Mandelis, A.; Christofides, C. *Physics, Chemistry and Technology of Solid State Gas Sensor Devices*; A Wiley Interscience publication; Wiley, 1993.
- (18) Abu-Faraj, Z. O. *Handbook of Research on Biomedical Engineering Education and Advanced Bioengineering Learning: Interdisciplinary Concepts: Interdisciplinary Concepts*; Medical Information Science Reference, 2012.
- (19) Erhart, J. *Phys. Educ.* **2013**, 48, 438.
- (20) Lyshevski, S. E. *Nano- and Micro-Electromechanical Systems: Fundamentals of Nano- and Microengineering, Second Edition*; Nano- and microscience; Taylor & Francis, 2005.
- (21) Kermani, M. R.; Moallem, M.; Patel, R. V. *Applied Vibration Suppression Using Piezoelectric Materials*; Nova Science Publishers, 2008.
- (22) Madou, M. J. *Fundamentals of Microfabrication: The Science of Miniaturization, Second Edition*; Taylor & Francis, 2002.
- (23) Wang, Z. L. *J. Phys. Condens. Matter* **2004**, 16, R829–R858.
- (24) Henrich, V. E.; Cox, P. A. *The Surface Science of Metal Oxides*; Cambridge University Press, 1994; p. 480.
- (25) Chen, H.; Brunswick, R. T. S. U. of N. J.-N. B. G. S.-N. *Dye Sensitized Solar Cells Using Zinc Oxide Nanotips and Gallium-doped Zinc Oxide Films*; Rutgers The State University of New Jersey - New Brunswick, 2008.
- (26) Briscoe, J.; Bilotti, E.; Dunn, S. *Appl. Phys. Lett.* **2012**, 101, 093902.
- (27) Brauer, G.; Anwand, W.; Grambole, D.; Grenzer, J.; Skorupa, W.; Čížek, J.; Kuriplach, J.; Procházka, I.; Ling, C. C.; So, C. K.; Schulz, D.; Klimm, D. *Phys. Rev. B* **2009**, 79, 115212.
- (28) Agrawal, R.; Espinosa, H. D. *Nano Lett.* **2011**, 11, 786–790.
- (29) Espinosa, H. D.; Bernal, R. A.; Minary-Jolandan, M. *Adv. Mater.* **2012**, 24, 4656–4675.
- (30) Xu, F.; Qin, Q.; Mishra, A.; Gu, Y.; Zhu, Y. *Nano Res.* **2010**, 3, 271–280.
- (31) Janotti, A.; Van de Walle, C. G. *Reports Prog. Phys.* **2009**, 72, 126501.

- (32) Hatch, S. M.; Briscoe, J.; Sapelkin, A.; Gillin, W. P.; Gilchrist, J. B.; Ryan, M. P.; Heutz, S.; Dunn, S. *J. Appl. Phys.* **2013**, *113*, 204501.
- (33) Jalali, N.; Woolliams, P.; Stewart, M.; Weaver, P. M.; Cain, M. G.; Dunn, S.; Briscoe, J. *J. Mater. Chem. A* **2014**, *2*, 10945.
- (34) Jalali, N.; Briscoe, J.; Woolliams, P.; Stewart, M.; Weaver, P. M.; Cain, M.; Dunn, S. *J. Phys. Conf. Ser.* **2013**, *476*, 012131.
- (35) Lv, Y.; Yao, W.; Ma, X.; Pan, C.; Zong, R.; Zhu, Y. *Catal. Sci. Technol.* **2013**.
- (36) Hu, Y.; Lin, L.; Zhang, Y.; Wang, Z. L. *Adv. Mater.* **2012**, *24*, 110–114.
- (37) Noei, H.; Qiu, H.; Wang, Y.; Löffler, E.; Wöll, C.; Muhler, M. *Phys. Chem. Chem. Phys.* **2008**, *10*, 7092–7097.
- (38) Jagadish, C.; Pearton, S. J. *Zinc Oxide Bulk, Thin Films and Nanostructures: Processing, Properties, and Applications*; Elsevier Science, 2011.
- (39) He, L.; Chen, F. *ECS Solid State Lett.* **2014**, *3*, P41–P44.
- (40) Bathe, K. J. *Computational Fluid and Solid Mechanics 2003*; Elsevier Science, 2003.
- (41) Bowen, C. R.; Kim, H. A.; Weaver, P. M.; Dunn, S. *Energy Environ. Sci.* **2014**, *7*, 25.
- (42) Yoon, J. Y. *Introduction to Biosensors: From Electric Circuits to Immunosensors*; Springer, 2012.
- (43) Lefeuvre, E.; Sebald, G.; Guyomar, D.; Lallart, M.; Richard, C. *J. Electroceramics* **2007**, *22*, 171–179.
- (44) Purcell, E. M.; Morin, D. J. *Electricity and Magnetism*; Electricity and Magnetism; Cambridge University Press, 2013.
- (45) Schmidt, R. M.; Press, S. R. M. I. O. S.; Schitter, G.; Rankers, A. *The Design of High Performance Mechatronics - 2nd Revised Edition: High-Tech Functionality by Multidisciplinary System Integration*; IOS Press, 2014.
- (46) Saggini, S.; Giro, S.; Ongaro, F.; Mattavelli, P. In *2010 IEEE 12th Workshop on Control and Modeling for Power Electronics (COMPEL)*; IEEE, 2010; pp. 1–6.
- (47) Bakshi, A. V. B. U. A. *Network Analysis And Synthesis*; Technical Publications, 2009.
- (48) Harris, P.; Bowen, C.; Kim, H. A.; web-support@bath.ac.uk. Manufacture and characterisation of piezoelectric broadband energy harvesters based on

asymmetrie bistable laminates. *29th Annual American Society for Composites Technical Conference*, 2014.

- (49) Lvovich, V. F. In *Impedance Spectroscopy*; John Wiley & Sons, Inc., 2012; pp. 319–331.
- (50) Von Meier, A. *Electric Power Systems: A Conceptual Introduction*; Wiley survival guides in engineering and science; Wiley, 2006.
- (51) Piprek, J. *Semiconductor Optoelectronic Devices: Introduction to Physics and Simulation*; Elsevier Science, 2003.
- (52) Luy, J. F. *Microwave Semiconductor Devices: Theory, Technology and Performance*; Reihe Technik; expert-Verlag, 2006.
- (53) Brennan, K. F. *The Physics of Semiconductors: With Applications to Optoelectronic Devices*; Cambridge University Press, 1999.
- (54) Briscoe, J.; Stewart, M.; Vopson, M.; Cain, M.; Weaver, P. M.; Dunn, S. *Adv. Energy Mater.* **2012**, 2, 1261–1268.
- (55) Ishiwara, H.; Okuyama, M.; Arimoto, Y. *Ferroelectric Random Access Memories: Fundamentals and Applications*; Topics in Applied Physics; Springer, 2004.
- (56) De Araujo, C. P.; Scott, J. F.; Taylor, G. W. *Ferroelectric Thin Films: Synthesis and Basic Properties*; Ferroelectricity and related phenomena; Gordon and Breach, 1996.
- (57) Wood, C.; Jena, D. *Polarization Effects in Semiconductors: From Ab Initio Theory to Device Applications*; Springer, 2007.
- (58) Bar-Cohen, Y. *High Temperature Materials and Mechanisms*; Taylor & Francis, 2014.
- (59) Shen, D.; Park, J.-H.; Ajitsaria, J.; Choe, S.-Y.; Wickle, H. C.; Kim, D.-J. *J. Micromechanics Microengineering* **2008**, 18, 055017.
- (60) Shen, D.; Choe, S.-Y.; Kim, D.-J. *Jpn. J. Appl. Phys.* **2007**, 46, 6755–6760.
- (61) Jiang, X.; Kim, J.; Kim, K. *Crystals* **2014**, 4, 351–376.
- (62) Kim, H. S.; Kim, J.-H.; Kim, J. *Int. J. Precis. Eng. Manuf.* **2011**, 12, 1129–1141.
- (63) Kim, H.; Priya, S. In *2008 17th IEEE International Symposium on the Applications of Ferroelectrics*; IEEE, 2008; Vol. 1, pp. 1–2.
- (64) Lefeuvre, E.; Audigier, D.; Richard, C.; Guyomar, D. *Power Electron. IEEE Trans.* **2007**, 22, 2018–2025.

- (65) Ottman, G. K.; Hofmann, H. F.; Bhatt, A. C.; Lesieutre, G. A. *Power Electron. IEEE Trans.* **2002**, *17*, 669–676.
- (66) Calìò, R.; Rongala, U. B.; Camboni, D.; Milazzo, M.; Stefanini, C.; de Petris, G.; Oddo, C. M. *Sensors* **2014**, *14*, 4755–4790.
- (67) Medical Design <http://medicaldesign.com/components/precision-piezo> (accessed Jan 10, 2015).
- (68) Kong, L. B.; Li, T.; Hng, H. H.; Boey, F.; Zhang, T.; Li, S. *Waste Energy Harvesting*; Lecture Notes in Energy; Springer Berlin Heidelberg: Berlin, Heidelberg, 2014; Vol. 24.
- (69) Richards, C. D.; Anderson, M. J.; Bahr, D. F.; Richards, R. F. *J. Micromechanics Microengineering* **2004**, *14*, 717–721.
- (70) Qi, Y.; McAlpine, M. C. *Energy Environ. Sci.* **2010**, *3*, 1275.
- (71) Tadigadapa, S.; Mateti, K. *Meas. Sci. Technol.* **2009**, *20*, 092001.
- (72) Kim, H. W.; Priya, S.; Uchino, K.; Newnham, R. E. *J. Electroceramics* **2005**, *15*, 27–34.
- (73) Kim, H.; Priya, S.; Stephanou, H.; Uchino, K. *IEEE Trans. Ultrason. Ferroelectr. Freq. Control* **2007**, *54*, 1851–1859.
- (74) Sodano, H. A.; Park, G.; Inman, D. J. *Mech. Syst. Signal Process.* **2004**, *18*, 683–697.
- (75) Sodano, H. A.; Inman, D. J.; Park, G. *J. Intell. Mater. Syst. Struct.* **2005**, *16*, 799–807.
- (76) Lee, H. J.; Zhang, S.; Bar-Cohen, Y.; Sherrit, S. *Sensors* **2014**, *14*, 14526–14552.
- (77) Wang, Z. L.; Song, J. *Science* **2006**, *312*, 242–246.
- (78) Vijay K. Varadan, K. J. Vinoy, S. G. Wiley: Smart Material Systems and MEMS: Design and Development Methodologies <http://eu.wiley.com/WileyCDA/WileyTitle/productCd-0470093617.html>.
- (79) Liu, J.; Fei, P.; Song, J.; Wang, X.; Lao, C.; Tummala, R.; Wang, Z. L. *Nano Lett.* **2008**, *8*, 328–332.
- (80) Lee, M.; Bae, J.; Lee, J.; Lee, C.-S.; Hong, S.; Wang, Z. L. *Energy Environ. Sci.* **2011**, *4*, 3359.
- (81) Xu, S.; Qin, Y.; Xu, C.; Wei, Y.; Yang, R.; Wang, Z. L. *Nat. Nanotechnol.* **2010**, *5*, 366–373.

- (82) Wang, X.; Jinhui, S.; Jin, L.; Zhong Lin, W. *Science* (80-.). **2007**, *316*, 102.
- (83) Zhu, G.; Yang, R.; Wang, S.; Wang, Z. L. *Nano Lett.* **2010**, *10*, 3151–3155.
- (84) Saeedkia, D. *Handbook of Terahertz Technology for Imaging, Sensing and Communications*; Woodhead Publishing Series in Electronic and Optical Materials; Elsevier Science, 2013.
- (85) Hu, Y.; Zhang, Y.; Xu, C.; Lin, L.; Snyder, R. L.; Wang, Z. L. *Nano Lett.* **2011**, *11*, 2572–2577.
- (86) Liu, W. Z.; Xu, H. Y.; Ma, J. G.; Liu, C. Y.; Liu, Y. X.; Liu, Y. C. *Appl. Phys. Lett.* **2012**, *100*, 203101.
- (87) Pham, T. T.; Lee, K. Y.; Lee, J.-H.; Kim, K.-H.; Shin, K.-S.; Gupta, M. K.; Kumar, B.; Kim, S.-W. *Energy Environ. Sci.* **2013**, *6*, 841.
- (88) Sohn, J. I.; Cha, S. N.; Song, B. G.; Lee, S.; Kim, S. M.; Ku, J.; Kim, H. J.; Park, Y. J.; Choi, B. L.; Wang, Z. L.; Kim, J. M.; Kim, K. *Energy Environ. Sci.* **2013**, *6*, 97.
- (89) Lee, S.; Lee, J.; Ko, W.; Cha, S.; Sohn, J.; Kim, J.; Park, J.; Park, Y.; Hong, J. *Nanoscale* **2013**, *5*, 9609–9614.
- (90) Ghosh, M.; Rao, M. G. *Mater. Express* **2013**, *3*, 319–327.
- (91) Riaz, M.; Song, J.; Nur, O.; Wang, Z. L.; Willander, M. *Adv. Funct. Mater.* **2011**, *21*, 628–633.
- (92) Scrymgeour, D. A.; Hsu, J. W. P. *Nano Lett.* **2008**, *8*, 2204–2209.
- (93) Zhao, M.-H.; Wang, Z.-L.; Mao, S. X. *Nano Lett.* **2004**, *4*, 587–590.
- (94) Zeyen, B.; Virwani, K.; Pittenger, B.; Turner, K. L. *Appl. Phys. Lett.* **2009**, *94*, 103507.
- (95) Hussain, M.; Abbasi, M. A.; Ibupoto, Z. H.; Nur, O.; Willander, M. *Phys. status solidi* **2014**, *211*, 455–459.
- (96) Sugunan, A.; Warad, H. C.; Boman, M.; Dutta, J. *J. Sol-Gel Sci. Technol.* **2006**, *39*, 49–56.
- (97) Liu, Y.; Tai, K.; Dillon, S. J. *Chem. Mater.* **2013**, *25*, 2927–2933.
- (98) Ashfold, M. N. R.; Doherty, R. P.; Ndifor-Angwafor, N. G.; Riley, D. J.; Sun, Y. *Thin Solid Films* **2007**, *515*, 8679–8683.

3. Experimental and Methodology

A basic schematic of an energy harvester is, ZnO nanorods sandwiched between two electrodes. The ITO, Ag and Zn served as the bottom electrodes. Basically, ZnO nanorods were synthesised on top of the bottom electrode. For this, adhesion between nanorod arrays and bottom electrode was imperative. Prior to nanorod growth, ZnO seed layer was deposited on the bottom electrode, which acts as the nucleation sites. Thereafter, ZnO nanorods were grown using aqueous solution growth method.

The tips of the ZnO nanorods were coated with layers of polymers which served as the top electrode. Two types of top electrode materials were used for the study: Poly(3,4-ethylenedioxythiophene):polystyrenesulfonic acid (PEDOT:PSS) and poly(methyl methacrylate) (PMMA). On the surface of top electrode, gold (Ag) electrode was deposited which served as device active area. After this, the device was wired and its mechanical structure was modified for a specific bend-release measurement.

This chapter presents the details of fabrication techniques of energy harvester, and the device groups which were fabricated by varying fabrication and material parameters such as: seeding techniques, nanorod growth techniques and top and bottom electrode materials.

3.1. ZnO Seed Layer Deposition on Bottom Electrode

The substrates used in the presented research work were polyethylene terephthalate (PET) coated with indium tin oxide (ITO) film, kapton polyimide coated with silver (Ag) film and zinc (Zn) metal foil. The conductive film on the substrate surface served as the device bottom electrode. The aim was to grow c-axis oriented vertical nanorod arrays on the films, where each film had its respective surface properties,

e.g. wettability and roughness, which affect ZnO nucleation. Moreover, in order to obtain well-oriented ZnO nanorods, the lattice of ZnO should match the lattice of the bottom electrode film ¹. Hence, a ZnO seed layer using either zinc salt or ZnO nanoparticles was deposited on top of the bottom electrode film; and this seed layer was considered to reduce the lattice mismatch ¹, provide low activation barrier for the nanorods growth ², and decrease the surface roughness of the conductive film ³. Therefore, as reported, well-aligned nanorod arrays were grown from the seeded ZnO nucleation sites, and their orientation depended on the seed layer grain crystallinity ^{4,5}. This section provides detailed description of the methods used to deposit the seed layer on flexible substrates.

Initially, attempts were made to deposit a seed layer using sol-gel method. In this regard, zinc acetate seed layer solution was first deposited on ITO-coated PET substrate. This seed layer deposition method did not provide sufficient ZnO coverage on the substrate. Therefore, for uniform coverage, ZnO seed layer was sputtered at an external institute, Cranfield University. With the sputtered substrates the fabrication experiments were initialised, whilst another sol-gel deposition method of ZnO nanoparticle seed layer was under development.

3.1.1. Substrate Cleaning

All substrate types, which include indium tin oxide (ITO)-coated polyethylene terephthalate (PET) (Aldrich, surface resistivity 60 Ω per square), Ag-coated kapton polyimide and zinc foil, were cleaned with isopropanol (IPA) and acetone. For this, the substrate(s) was inserted in a substrate holder which was immersed in a beaker filled with IPA and kept in an ultrasonic bath for 15 minutes. Thereafter, the substrate was removed from the IPA bath and immersed in the same way into an acetone filled beaker and kept inside the ultrasonic bath for 15 minutes.

3.1.2. Zinc Acetate-Based Seed Solution Deposition

Sol-gel based method, reported by Choi et al. (2010) ⁶ and Choi et al. (2009) ⁷, was used to obtain seed layer on 2 x 1 cm² ITO-coated substrate. Before seed layer deposition, 0.3 x 1 cm² of the area from the edge of the substrate was masked with kapton polyimide tape (Figure 29), to avoid ZnO growth on it; this area was later used to prepare the device electrodes. 0.01 M zinc acetate dehydrate seed solution in

ethanol was prepared and a pipetted out. 3 drops of solution were spread on the substrate surface and spin-coated at 1000 rpm for 60 seconds. The substrates were heated on the hot plate at 100°C for 10 minutes. The spin-casting and heating steps were repeated six times.

The substrates prepared using this technique were ITO-coated PET and they were arranged in a group called ITO ZnAc (Table 1).

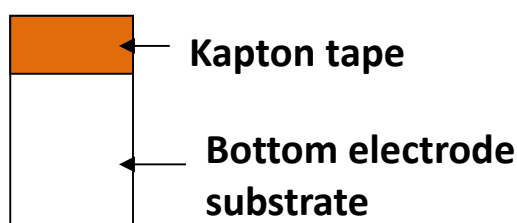


Figure 29. $0.3 \times 1 \text{ cm}^2$ of the area from the edge of the substrate was masked with kapton polyimide tape.

3.1.2.1. Substrate Pre-Treatment for Seed Layer

This method was adopted to improve the adhesion and coverage of the zinc acetate-based seed layer on the ITO substrate. The ITO substrate was dipped inside ethanol and ultrasonicated for 5 minutes. Thereafter, the method of zinc acetate seed layer deposition was implemented; according to which, 0.01 M zinc acetate dehydrate seed solution was spin-deposited six times on the pre-treated substrate.

The substrates prepared using this technique were ITO-coated PET and they were arranged in a group called ITO ZnAc* (Table 1).

3.1.3. Sputter Deposition

The sputtered ZnO seed layer was initially used as a substitute to zinc acetate-based seed seed layer. Prior to sputtering, the substrates were cleaned with IPA and acetone. Following the cleaning process, ZnO seed layer of 200 nm thickness was sputtered on ITO substrates using Balzer sputtering system at an external institution, Cranfield University.

The substrates prepared using this technique were ITO-coated PET and they were arranged in a group called ITO Sp and ITO Sp* (Table 1).

3.1.4. ZnO Nanoparticle Seed Deposition

The ZnO nanoparticle seed solution was prepared by the method described by Liu & Kelly (2014) ⁸ and was used to deposit seed layer on ITO-coated PET, Ag coated kapton polyimide and zinc foil. 13.4 mM of zinc acetate dehydrate in methanol and 23 mM of KOH in methanol were prepared. The zinc acetate solution was heated to 65°C with simultaneous stirring. When the temperature of the solution reached 65°C, the stirring was continued and KOH solution was dropped into it at a rate of 1 ml per minute. The mixture turned translucent after 10 min and it was left to stir for 2.5 hours at 65°C. Thereafter, it was left to cool for another hour. Precipitates were formed and they settled to the bottom of the container. The solution along with the precipitate was centrifuged for 5 min at 4000 rpm. The supernatant was drained and the precipitate was cleaned with methanol; the cleaning step involved dispersing of precipitate in methanol and centrifuging it for 5 min at 4000 rpm. The cleaning process was repeated three times and then the precipitate was dispersed in 1-butanol, methanol and chloroform in the ratio 14:1:1 to obtain the final ZnO nanoparticle solution concentration of 6 mg/ml. This solution was left to settle for 15 min and then it was filtered using 0.45 µm polytetrafluoroethylene (PTFE) filter to remove the precipitate residue. The filtered suspension carried ZnO nanoparticles which were spray-coated onto cleaned conductive substrates using pneumatic micro-spray gun ⁹. The substrates, with conductive surfaces facing up, were placed on a 45° angled hotplate set at 100°C. The reservoir of the spray gun was filled with the seed solution and the substrates were sprayed using side-to-side motion of the gun. One complete coat comprised of back and forth spraying on the substrates for 12 seconds and total 20 coats were sprayed on the substrates.

The substrates prepared using the nanoparticle seeding technique were ITO-coated PET, zinc foil and Ag-coated kapton and they were arranged in groups called ITO NP, Zn NP and Ag NP respectively (Table 1).

Table 1. Group names of the ITO, zinc and silver substrates seeded using various methods.

Group Names of Seeded Samples	Description
ITO ZnAc	ITO-coated PET substrate coated with zinc acetate-based seed solution.
ITO ZnAc*	ITO-coated PET substrate pre-treated with ethanol and then coated with zinc acetate-based seed solution.
ITO Sp	ITO-coated PET substrate sputtered with ZnO seed layer
ITO Sp*	ITO-coated PET substrate sputtered with ZnO seed layer
ITO NP	ITO-coated PET substrate seeded with ZnO nanoparticle seed solution.
Zn NP	Zinc foil substrate seeded with ZnO nanoparticle seed solution.
Ag NP	Ag-coated kapton polyimide substrate seeded with ZnO nanoparticle seed solution.

3.2. Nanorods Growth on Bottom Electrode: Aqueous Solution Growth Technique

3.2.1. 25 mM Equimolar Solution Growth Condition

In the presented work, ZnO nanorod arrays were synthesised on seeded substrates using aqueous solution growth technique reported by Greene et al. (2003)¹⁰. The substrates used were: polyethylene terephthalate (PET) coated with indium tin oxide (Aldrich, surface resistivity 60 Ω per square), silver coated kapton polyimide and zinc foil. Aqueous solutions of zinc nitrate hexahydrate $\text{Zn}(\text{NO}_3)_2 \cdot 6\text{H}_2\text{O}$ (Alfa Aesar, 99%) and Hexamethylenetetramine HMT (Alfa Aesar, 99+%) in 25 mM equimolar concentration were used as the precursor solutions. 25 M equimolar concentration of aqueous solutions of $\text{Zn}(\text{NO}_3)_2$ and HMT were prepared; 25 ml of each was added to 200 ml of DI water in a jar to obtain the final precursor concentration of 25 mM. The seeded substrates were adhered onto the flat surface of a rectangular glass slab with the conductive seeded side facing upward. The slab had wires wound around the smaller two sides in order to hang it in the solution. The slab along with the substrates was immersed inside the solution and the flat surface with substrates was facing downwards (Figure 29). It was kept off from touching the base of the jar and the attached wires were hooked onto the wall edge of the jar. The lid of the jar was closed and the solution was kept inside a pre-heated oven at 90°C for 2.5 hours. Thereafter, the substrate subjected to 1 synthesis, was rinsed with DI water. The cleaning step removes the adhered homogeneously nucleated nanorods from heterogeneously nanorods surface. The solution was refreshed and the synthesis process was repeated six times to obtain nanorods with 2 μm length and 70 nm width.

Using 25 mM equimolar solution growth condition, the nanorods were synthesised on ITO ZnAc, ITO ZnAc* and ITO Sp seeded-substrates (seeded substrates Table 1); after nanorods growth on the mentioned samples, they were named as ITO ZnAc(25), ITO ZnAc*(25) and ITO Sp(25), respectively (Table 2).

3.2.2. 50 mM Equimolar Solution Growth Condition

In this growth condition, the final solution concentration of $\text{Zn}(\text{NO}_3)_2$ and HMT was 50 mM each. 25 mM aqueous solutions of $\text{Zn}(\text{NO}_3)_2$ and HMT were prepared; 50 ml of each solution was dissolved in 150 ml of DI water to obtain the final solution concentration of 50 mM for each precursor. The substrates were placed inside the jar and allowed to suspend in the solution. One synthesis was carried out for 4 hours.

Using 50 mM equimolar solution growth condition, the nanorods were synthesised on ITO Sp*, ITO NP, Zn NP and Ag NP seeded-substrates (seeded substrates Table 1); after nanorods growth on the mentioned samples, they were named as ITO Sp*(50), ITO NP(50), Zn NP(50) and Ag NP(50), respectively (Table 2).

Table 2. ZnO nanorods grown using different final solution concentrations and on various substrates. These nanorod samples were grouped as follows:

Group Names of Nanorod Samples	Description
ITO ZnAc(25)	25 mM equimolar solutions of $\text{Zn}(\text{NO}_3)_2$ and HMT used for nanorod synthesis on ITO ZnAc sample. Nanorod synthesis steps were repeated six times. Each step had a duration of 2.5 hours.
ITO ZnAc*(25)	25 mM equimolar solutions of $\text{Zn}(\text{NO}_3)_2$ and HMT used for nanorod synthesis on ITO ZnAc* sample. Nanorod synthesis steps were repeated six times. Each step had a duration of 2.5 hours.
ITO Sp(25)	25 mM equimolar solutions of $\text{Zn}(\text{NO}_3)_2$ and HMT used for nanorod synthesis on ITO Sp sample. Nanorod synthesis steps were repeated six times. Each step had a duration of 2.5 hours.
ITO Sp*(50)	50 mM equimolar solutions of $\text{Zn}(\text{NO}_3)_2$ and HMT used for nanorod synthesis on ITO Sp* sample. One nanorod synthesis was performed for 4 hours.
ITO NP(50)	50 mM equimolar solutions of $\text{Zn}(\text{NO}_3)_2$ and HMT used for nanorod synthesis on ITO NP sample. One nanorod synthesis was performed for 4 hours.
Zn NP(50)	50 mM equimolar solutions of $\text{Zn}(\text{NO}_3)_2$ and HMT used for nanorod synthesis on Zn NP sample. One nanorod synthesis was

performed for 4 hours.

Ag NP(50)

50 mM equimolar solutions of $\text{Zn}(\text{NO}_3)_2$ and HMT used for nanorod synthesis on Ag NP sample. One nanorod synthesis was performed for 4 hours.

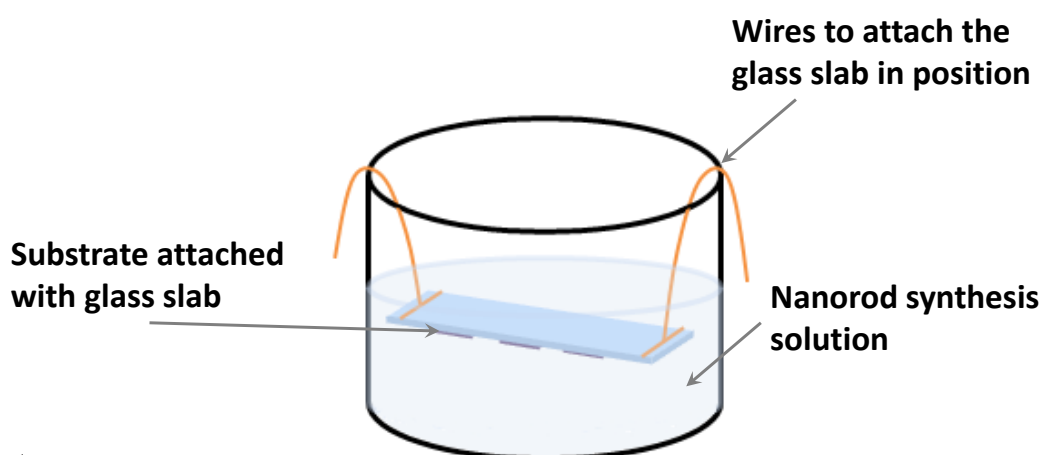


Figure 30. Substrate attached to the surface of a glass slab and immersed facing down in a jar containing precursor solution.

3.3. Surface Passivation of ZnO Nanorods

In the reported research work, analysis was performed on effects of ZnO surface modification or surface passivation on PEDOT:PSS-based energy harvester's performance. In this method, the surface-states of ZnO were modified for device performance optimisation. For this, a nanometre-ranged ceramic material layer was coated on the synthesised nanorods surface. The performance of these coated nanorod-based devices was compared with devices in which surface passivation was not performed (non-coated nanorods).

The surface of ZnO nanorods was modified using copper thiocyanate (CuSCN) spray-deposition. In surface modified ZnO devices, this process was carried out after the growth of nanorods. For the non-coated (as grown) nanorod-based devices, this process was not performed.

3.3.1. CuSCN Passivation

The surface of the ZnO nanorods was modified using CuSCN deposition. 0.15 M CuSCN (Aldrich, 99%) solution in dipropyl sulphide (Alfa Aesar, 98+%) was sprayed on the nanorods surface using pneumatic micro-spray gun. The nanorod substrates were fastened on a hotplate, which was angled at approximately 45° and set at 50°C. 2, 10 and 20 coats were sprayed on ITO Sp(25) nanorod samples. For each coat, 0.5 ml of CuSCN was filled in the spray gun reservoir and the spraying was performed in a side-to-side motion of the gun⁹.

After the spray-deposition of CuSCN on the ITO Sp(25) samples, the device top electrode was fabricated. Thereafter, the gold electrode deposition, device wiring and mounting was performed. The devices fabricated with 2, 10 and 20 coats of CuSCN modifier were grouped as CuSCN-2, CuSCN-10, CuSCN-20 (Table 3).

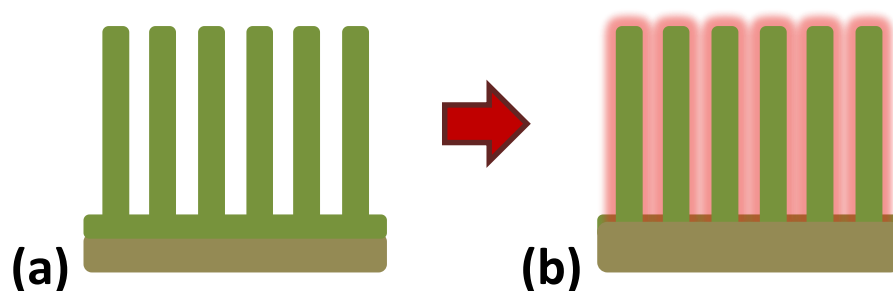


Figure 31. (a) As-grown ZnO nanorods, (b) CuSCN solution spray-coated on the surface of ZnO nanorods.

3.4. Top Electrode Fabrication

Two types of top electrodes were fabricated, PEDOT:PSS-based and PMMA-based. These top electrodes were deposited on top of both CuSCN-coated and non-coated nanorods.

3.4.1. Spin Coating of PEDOT:PSS

There were two different speeds at which PEDOT:PSS was spin-coated over the nanorods substrates:

3.4.1.1. 2000 RPM

ZnO nanorods were synthesised on seeded $2 \times 1 \text{ cm}^2$ ITO, silver and zinc coated polymer substrates. Each of the ITO, silver and zinc served as a bottom electrode and in p-n junction-based devices the top electrode comprised of Poly(3,4-ethylenedioxythiophene):polystyrenesulfonic acid (PEDOT:PSS). PEDOT:PSS is an organic p-type semiconducting and flexible polymer. The deposition of PEDOT:PSS (Aldrich, 1.3 wt% in water, conductive grade) was carried out using spin-coating technique. The ZnO nanorod substrate was fastened onto the spin-coater disk and 0.5 ml of PEDOT:PSS was dropped onto the surface of nanorods and spun at 2000 rpm for 30 seconds. For 5 minutes, the substrate was kept on a hotplate set at 100°C for the layer to dry. Thereafter, another layer of PEDOT:PSS was spin-coated at 2000 rpm for 30 seconds, and dried in the similar way. In this way, 2 layers of PEDOT:PSS were deposited onto the nanorods (Figure 32).

The devices whose top electrodes were prepared with above outlined method were arranged into groups, as outlined in Table 3.

3.4.1.2. 1000 RPM

This method of PEDOT:PSS electrode fabrication was specifically applied for devices grouped in PDOT-1K. In this method, the nanorods were coated with 2 layers of PEDOT:PSS spin-deposited at 1000 rpm. This method was performed in the similar manner as 2000 rpm deposition with the spin-coater speed changed to 1000 rpm.

The devices fabricated with PEDOT:PSS deposited at 1000 rpm were grouped as PDOT-1K (Table 4).

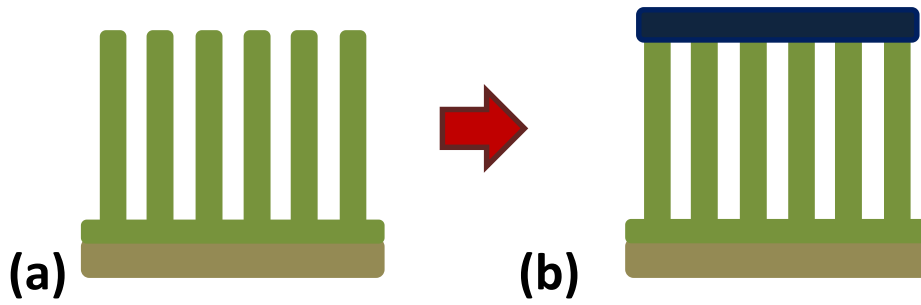


Figure 32. (a) ZnO nanorods before top electrode, (b) Top electrode spin-deposited on top of the nanorods.

3.4.2. Spin Coating of PMMA

3.4.2.1. 2000 RPM

The PMMA-based top electrode was fabricated using 10 wt % solution of poly(methyl methacrylate) (PMMA, Aldrich, 850,000 average M_w) in methoxybenzene (Anisole, Sigma-Aldrich, 99%). The deposition of PMMA solution was carried out using spin-coating technique. The ZnO nanorod substrate was attached onto the spin-coater disk. Using a pipette, 0.5 ml of PMMA solution was dropped onto the surface of nanorods and the coater was spun at 2000 rpm for 30 seconds. The substrate was kept for 5 minutes on a hotplate set at 100°C, and layer was dried. Thereafter, another layer of PMMA was spin-coated at 2000 rpm for 30 seconds, and dried in the similar way. In this way, 2 layers of PMMA were deposited onto the nanorods.

The devices whose top electrodes were prepared with above outlined method were arranged in a group named PMA-2K (Table 4).

3.4.2.2. 3000 RPM

In case of 3000 rpm spin-speed PMMA deposition, the 2 layers of PMMA were coated on top of the nanorods in the same way as the 2000 RPM deposition. The nanorod sample was attached on the disk of the spin-coater. 0.5ml of PMMA solution was dropped on top of the rods and the spin-coating was performed at 3000 rpm. The layer was dried at 100°C on a hotplate. The second layer of PMMA was also deposited at 3000 rpm and dried at 100°C.

The devices whose top electrodes were prepared with PMMA deposition at 3000 rpm were grouped as PMA-3K (Table 4).

Table 3. PEDOT:PSS-based device groups based on the top electrode fabrication method, bottom electrode and nanorod fabrication method and surface modification.

Top Electrode Fabrication	Bottom Electrode & Nanorod Fabrication (Table 2)	Surface Modification	Group Names
PEDOT:PSS @ 2000 rpm	ITO Sp(25)	No	PDOT-2K/A
PEDOT:PSS @ 2000 rpm	ITO Sp(25)	No	PDOT-2K/B
PEDOT:PSS @ 2000 rpm	ITO Sp(25)	No	PDOT-Shorted
PEDOT:PSS @ 1000 rpm	ITO Sp(25)	No	PDOT-1K
PEDOT:PSS @ 2000 rpm	ITO Sp(25)	No	PDOT-EM
PEDOT:PSS @ 2000 rpm	ITO Sp*(50)	No	PDOT-Sm
PEDOT:PSS @ 2000 rpm	Zn NP*(50)	No	PDOT-Zn
PEDOT:PSS @ 2000 rpm	Ag NP*(50)	No	PDOT-Ag
PEDOT:PSS @ 2000 rpm	ITO Sp(25)	2 coats of CuSCN	CuSCN-2
PEDOT:PSS @ 2000 rpm	ITO Sp(25)	10 coats of CuSCN	CuSCN-10
PEDOT:PSS @ 2000 rpm	ITO Sp(25)	20 coats of CuSCN	CuSCN-20

Table 4. PMMA-based device groups based on the top electrode fabrication method, bottom electrode and nanorod fabrication method and surface modification.

Top Electrode Fabrication	Bottom Electrode & Nanorod Fabrication (Table 2)	Surface Modification	Group Names
PMMA @ 2000 rpm	ITO Sp(25)	No	PMA-2K
PMMA @ 3000 rpm	ITO Sp(25)	No	PMA-3K

3.5. Wiring Device Terminals and Fabrication of Mechanical Structure Suitable for Bend-Release Test

After fabrication of the top electrode, an active device area was made using gold sputtering. For deposition of gold on a controlled area, the top electrode surface was masked. The gold electrode and bottom electrodes were thereafter connected with wires. The $2 \times 1 \text{ cm}^2$ device substrate was adhered on a $5.5 \times 2.5 \text{ cm}^2$ base substrate. In this manner the final device dimensions were increased. The increased dimension increased the device bending curvature, which was essential for a specific bend-release test designed for output performance of the devices (measurement set up described in section 3.6).

3.5.1. Masking and Electrode Sputtering

The gold layer was deposited on the top electrode using Agar Auto Sputter Coater. This gold electrode served as an active area which can be wired. As shown in Figure 33(e), half of the $0.3 \times 2 \text{ cm}^2$ area without having nanorods grown on it, was coated with epoxy and left to dry for 2-3 hours. This insulated area allowed the gold electrode on top of the PEDOT:PSS to be extended to the edge of the device for further wiring. The edge of the epoxy coat which meets the non-coated-ITO area was masked with a narrow kapton polyimide (Figure 33(f)), in order to avoid the shorting of bottom ITO electrode with gold electrode. The surface of the PEDOT:PSS was masked to allow electrode deposition in only a confined area called effective area or active area (Figure 33(f)). The effective area allows the selection of an area with homogenously and evenly coated PEDOT:PSS, therefore it avoids short-circuiting of device and related leakage losses. The average effective area of the devices was 0.17 cm^2 . By carefully defining the electrode area using a mask, the gold was sputtered on the effective PEDOT:PSS area, extended onto the top of epoxy-coated area and the ITO electrode area (Figure 33 (g)). The aluminium mask and the kapton polyimide spacer between the ITO and gold electrodes were removed.

The masked substrates were kept inside Agar sputter coater and six coats of gold were coated at 0.1 mbar pressure on the defined electrode area.

3.5.2. Wiring and Mounting of Device on Base Substrate

As discussed earlier, the gold electrode was extended up to the edge of the substrate. By partially coating the ITO contact with epoxy, the top and bottom electrodes were made to lie on the same edge of the substrate but well-separated from each other. This configuration assisted the wiring attached to the gold and ITO contact: the wires remained on one side of the device while the other end was free to bend without moving them. Flat copper wires were adhered on the gold and ITO electrodes using silver dag and it was left to dry for 1 hour. After this, the wire contacts bonded with silver dag were reinforced using epoxy and left to dry for 1 hour (Figure 33(h)).

The $2 \times 1 \text{ cm}^2$ device was mounted on top of a $5.5 \times 2.5 \text{ cm}^2$ and $500 \text{ }\mu\text{m}$ thick PET base substrate. For this, the 2 cm long device was adhered 0.5 cm away from the edge of the thicker substrate, and the remaining area of the base substrate was reserved for laying the wires for further reinforcement. The copper wires extending from the main device to the base substrate, were embedded in epoxy; this reduced the movement of wires during bending tests. The copper wires were further extended by soldering aluminium wires with them. The soldered contact was carefully bonded to the base substrate using epoxy and a glass slab of $1 \times 0.5 \text{ cm}^2$ was fastened on top of it. This glass slab assisted in gripping the device with the clamp holder (Figure 33(i)).

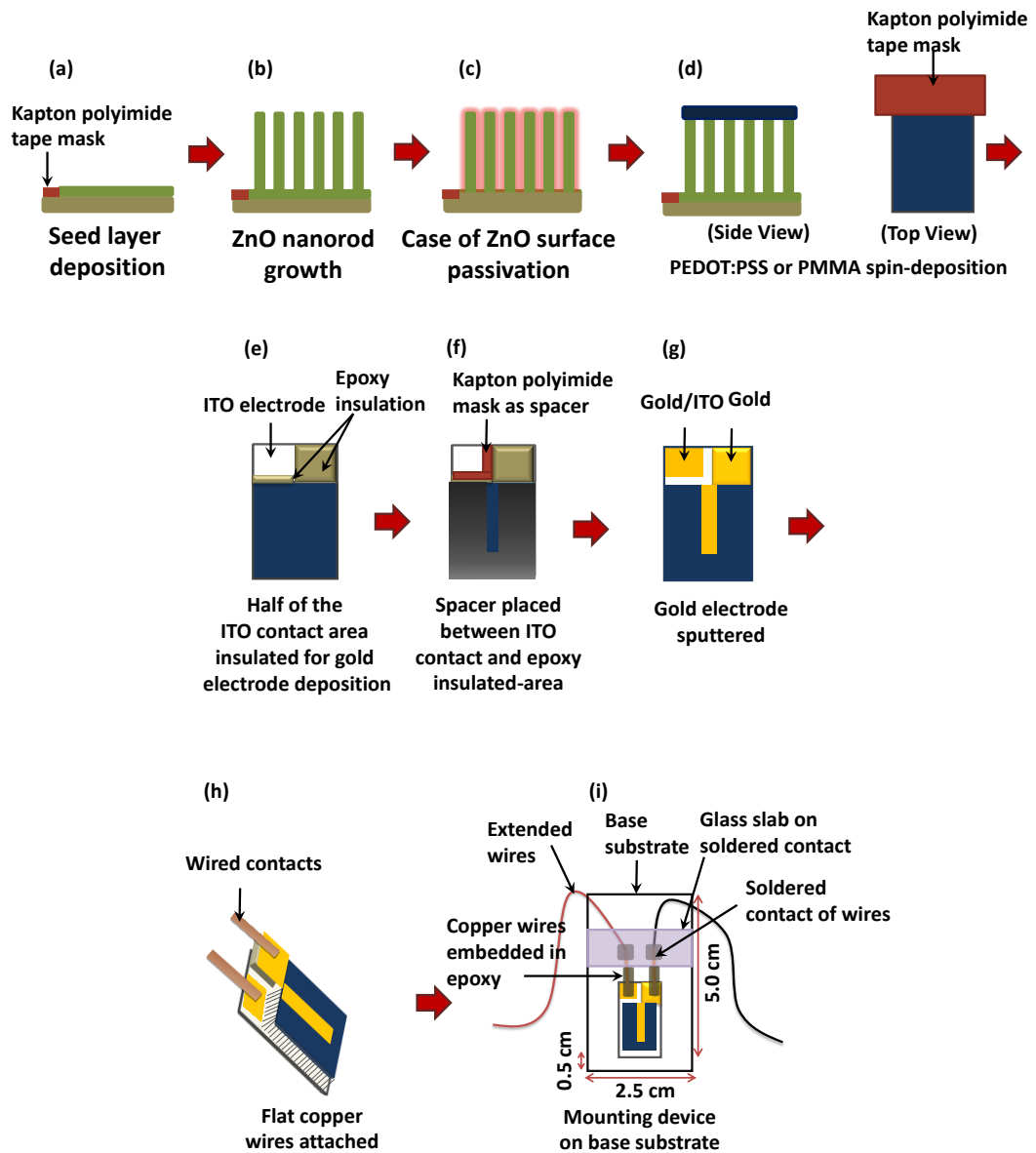


Figure 33. Step by step processes involved in the fabrication of ZnO energy harvester.

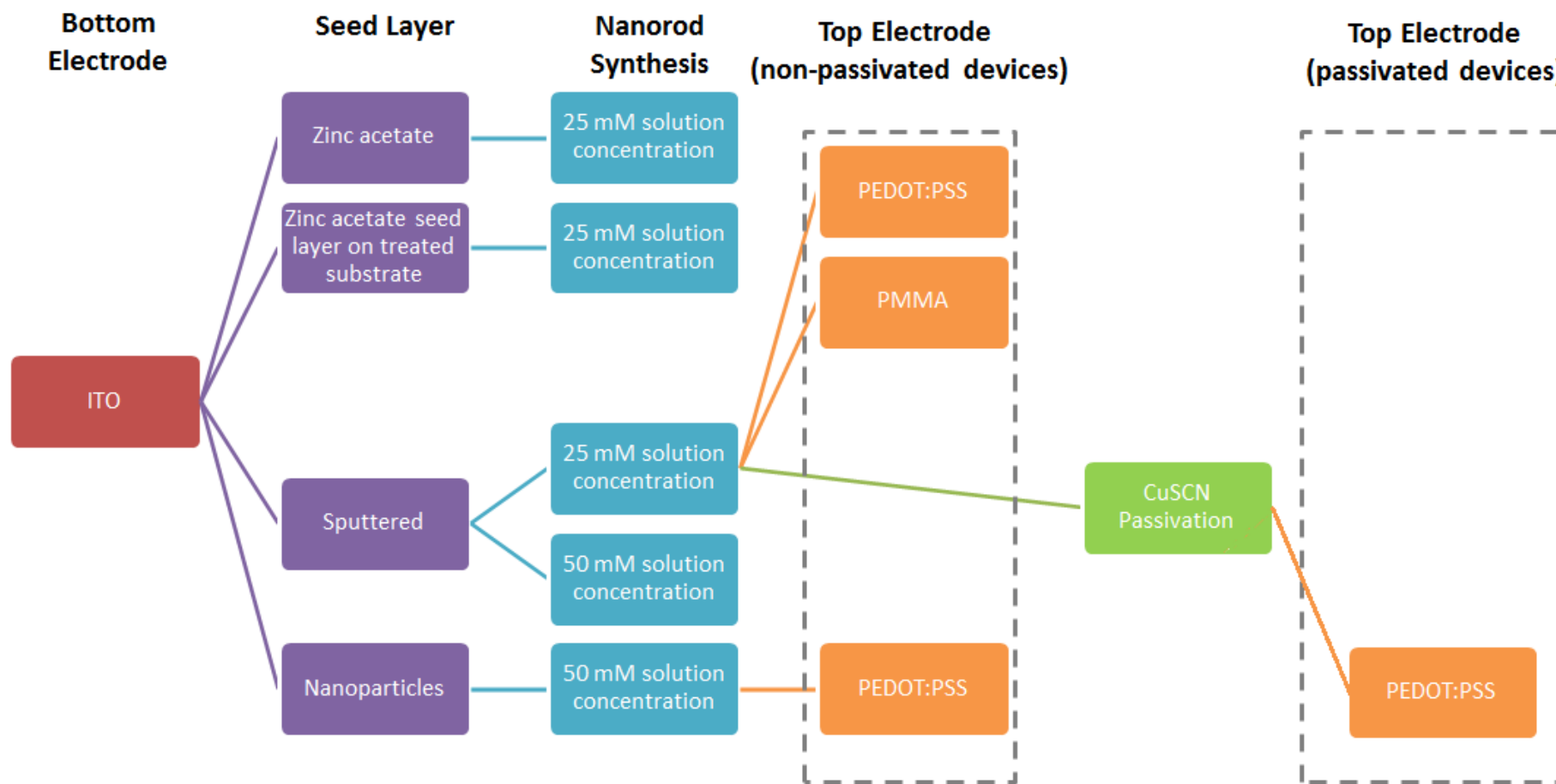


Figure 34. Block diagram of experimentations carried out on ITO substrates to fabricate ITO-based devices.

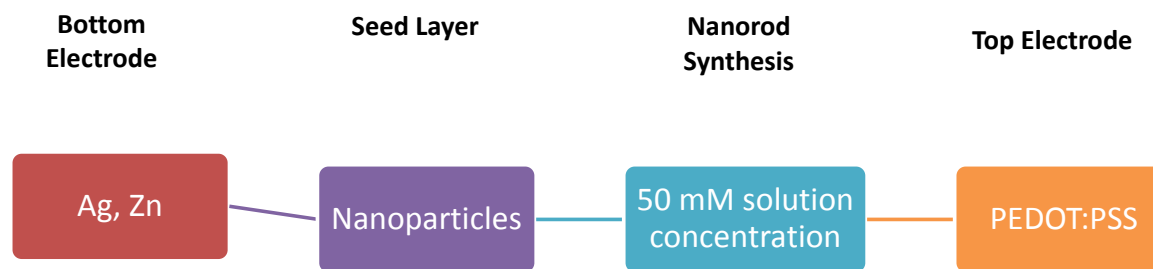


Figure 35. Block diagram of experimentations carried out on Ag and Zn substrates to fabricate ITO-based devices.

3.6. Bend Release Measurements

The bend release measurements were performed on the devices using a mechanical set up prepared by the hardware technician team at Queen Mary University of London. The detailed set up is demonstrated in Figure 36. The sample holder was attached to a handle whose height was adjustable by moving it in z-axis against a scale. Opposite to the sample holder, a rotational motor was attached to an x and y-axis moveable base. The motor had its shaft connected with a cam which served as the main source of mechanical excitation to the device at 1 Hz. The oval shaped cam had a 2 cm long protruded edge which was used to mechanically displace the device upward and release.

3.7. Measurement of Device Output

The open-circuit voltage output peaks of the device were recorded using data acquisition module National Instruments NI PXI-4461 (24-bit ADC) on the NI PXIe-1062Q chassis, which was operated through Labview program. Similarly, a Low-Noise Current Preamplifier SR570 was connected with the NI PXI-4461 (24-bit ADC) module and operated by a Labview program to record the short-circuit current density peaks. The terminals of the device were connected in parallel to a resistive decade box, Meatest M602 programmable decade box, which was connected with the PXI-4461 module for data acquisition. A Labview program controlled the resistive sweep of the decade box and also recorded the output of the device across the sweep of load resistance.

The impedance analysis was performed from 40 Hz – 110 MHz at oscillator level of 500 mV using Agilent 4294a Precision Impedance Analyzer. Short-circuit and open-circuit compensation was performed prior to all measurements.

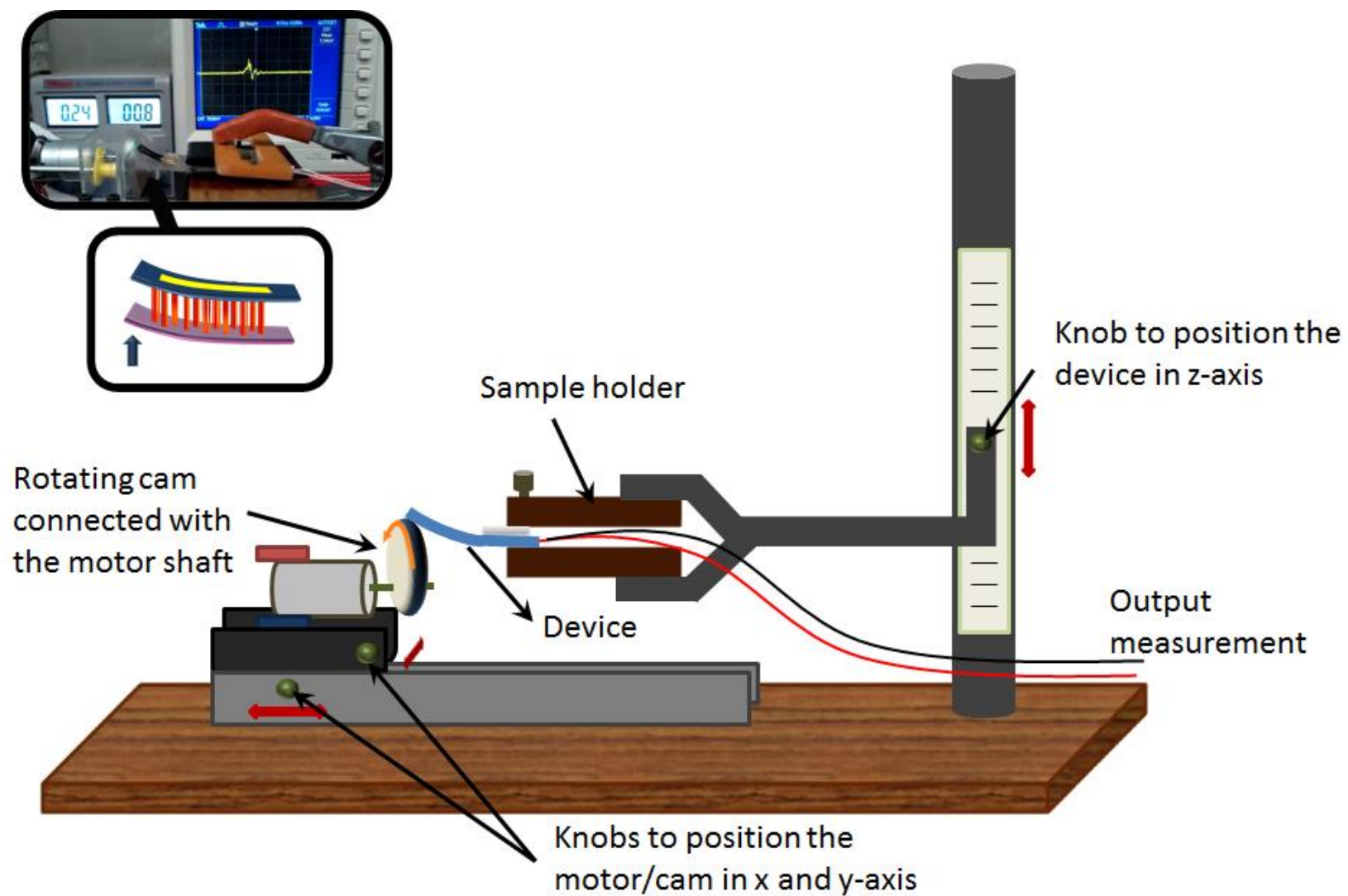


Figure 36. Bend-release measurement kit with motor/cam assembly used to bend the device.

3.8. References

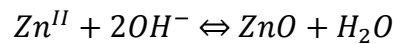
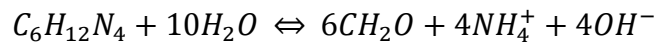
- (1) Li, C.; Fang, G.; Li, J.; Ai, L.; Dong, B.; Zhao, X. *J. Phys. Chem. C* **2008**, *112*, 990–995.
- (2) Sugunan, A.; Warad, H. C.; Boman, M.; Dutta, J. *J. Sol-Gel Sci. Technol.* **2006**, *39*, 49–56.
- (3) Dong, J.-J.; Zhen, C.-Y.; Hao, H.-Y.; Xing, J.; Zhang, Z.-L.; Zheng, Z.-Y.; Zhang, X.-W. *Nanoscale Res. Lett.* **2013**, *8*, 378.
- (4) Ghayour, H.; Rezaie, H. R.; Mirdamadi, S.; Nourbakhsh, A. A. *Vacuum* **2011**, *86*, 101–105.
- (5) Ji, L.-W.; Peng, S.-M.; Wu, J.-S.; Shih, W.-S.; Wu, C.-Z.; Tang, I.-T. *J. Phys. Chem. Solids* **2009**, *70*, 1359–1362.
- (6) Choi, D.; Choi, M.-Y.; Shin, H.-J.; Yoon, S.-M.; Seo, J.-S.; Choi, J.-Y.; Lee, S. Y.; Kim, J. M.; Kim, S.-W. *J. Phys. Chem. C* **2010**, *114*, 1379–1384.
- (7) Choi, M.-Y.; Choi, D.; Jin, M.-J.; Kim, I.; Kim, S.-H.; Choi, J.-Y.; Lee, S. Y.; Kim, J. M.; Kim, S.-W. *Adv. Mater.* **2009**, *21*, 2185–2189.
- (8) Liu, D.; Kelly, T. L. *Nat Phot.* **2014**, *8*, 133–138.
- (9) Hatch, S. M.; Briscoe, J.; Dunn, S. *Thin Solid Films* **2013**, *531*, 404–407.
- (10) Greene, L. E.; Law, M.; Goldberger, J.; Kim, F.; Johnson, J. C.; Zhang, Y.; Saykally, R. J.; Yang, P. *Angew. Chem. Int. Ed. Engl.* **2003**, *42*, 3031–3034.

4. Nucleation and Growth of ZnO Nanorod Arrays

The first step in the fabrication of energy harvester was synthesis of columnar ZnO nanostructure arrays called nanorods. These nanostructures were fabricated using aqueous solution growth technique reported by Greene et al. (2003) ¹. This section describes the trials to deposit seed layer on various bottom electrode substrates and addresses the issues of seed layer adhesion. Moreover, it discusses the dimensions and orientations of nanorods grown using solution growth technique with different precursor solution concentrations.

4.1. Aqueous Solution Growth Technique

ZnO is widely grown at temperature range of 55 – 95 °C ² using chemical bath synthesis method, with the aqueous solutions of Zn salt and amine salt. The reaction of the chemicals cause dissociation of Zn^{+2} ions from the zinc salt and amine hydrolyses to release hydroxide ions ³. Commonly used chemicals are $Zn(NO_3)_2$ ² as zinc salt and Hexamethylenetetramine (HMT) ^{2,3} as amine salt. HMT has been described to be solution pH buffer: as the pH of the solution increases due to OH^- generation, the rate of hydrolysis of HMT decreases ⁴. The key reactions which take place to form ZnO are as follows ⁴:



As evident from the reaction equations, HMT hydrolyses to release OH^- ions that react with Zn^{+2} ions to form ZnO ⁴.

Prior to the growth of ZnO nanorods, ZnO seed layer is deposited on the substrate which provides low activation barrier ² and lattice matched ⁵ nucleation sites for ZnO to grow in columnar rod-like structures. The presence of seed layer ensures growth

of well-oriented nanostructures. The seeded substrate samples discussed and demonstrated in this chapter are shown in Table 5.

Table 5. Group names of the ITO-coated PET, zinc foil and silver (Ag)-coated kapton substrates seeded using various methods.

Group Names of Seeded Samples	Description
ITO ZnAc	ITO-coated PET substrate coated with zinc acetate-based seed solution.
ITO ZnAc*	ITO-coated PET substrate pre-treated with ethanol and then coated with zinc acetate-based seed solution.
ITO Sp	ITO-coated PET substrate sputtered with ZnO seed layer
ITO Sp*	ITO-coated PET substrate sputtered with ZnO seed layer
ITO NP	ITO-coated PET substrate seeded with ZnO nanoparticle seed solution.
Zn NP	Zinc foil substrate seeded with ZnO nanoparticle seed solution.
Ag NP	Ag-coated kapton polyimide substrate seeded with ZnO nanoparticle seed solution.

4.1.1. ZnO Nanorods Grown on Zinc Acetate-Based Seed Layer

The sol-gel seed solution comprised of zinc acetate salt solution in ethanol. This solution was spin-deposited six times on ITO-coated PET substrate. After each step of spin-coating, the substrate was heated at 100°C in order to allow the zinc acetate salt to adhere on to the ITO surface. The seeded substrate was grouped as ITO ZnAc (Table 5). After six coats of the seed layer, the nanorods were grown on ITO ZnAc using the solution growth technique. Six synthesis for nanorods growth were carried out at 90 °C, using 25 mM equimolar final solution concentration of $\text{Zn}(\text{NO}_3)_2$ and HMT in DI water. The resulting nanorods samples were grouped as ITO ZnAc(25).

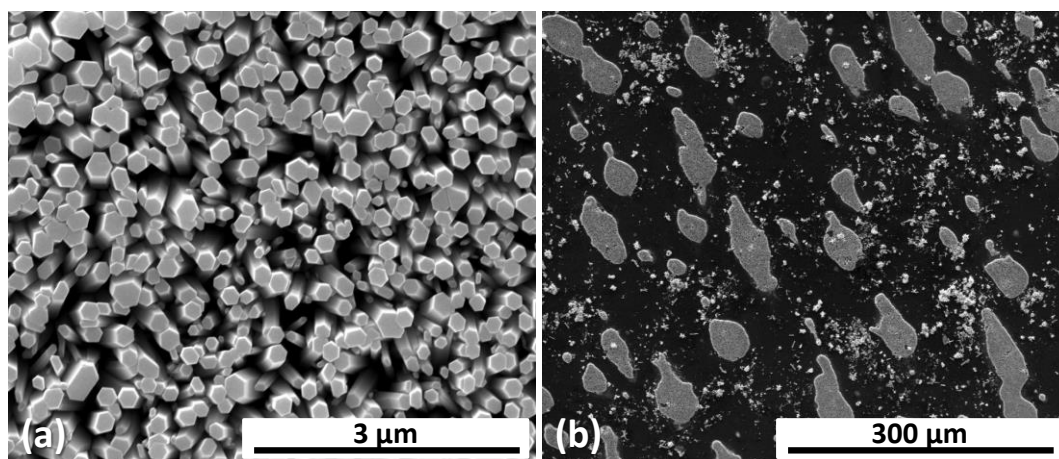


Figure 37. (a) 187 nm wide densely packed nanorods grown on ITO substrate spin-coated with zinc acetate-based seed solution. (b) Uneven coverage of the seed layer on ITO forming island-like patches where nanorods grew.

The ITO ZnAc(25) nanorods samples was observed under the SEM; the nanorods had nucleated from island-like patches on the substrate (Figure 37(b)). This result indicated that the seed layer adhered only at random areas on the ITO and there were areas left uncovered where nanorods did not grow. The nanorods were ~187 nm in diameter and densely packed as shown in Figure 37(a). It was considered that the lack of ITO surface wettability inhibited dispersion of the seed solution, which reduced its coverage on the substrate. Therefore, the seed layer was cohered only to random island-like patched locations having higher surface energy. Hence the nanorods only grew on the randomly distribution island-like seed layer patches. The hydrophobicity of the areas surrounding the seeded patches was believed to cause the

seed solution droplets to come into closer contact, which formed dense layers. Therefore, in these dense nucleation sites, the nanorods grew in a closely packed fashion.

4.1.1.1. Substrate Pre-treatment with Ethanol

For an energy harvester to function efficiently, an even coverage of ZnO nanorods on ITO surface was required. This required even coverage of seed layer on the substrate by improving ITO surface wettability. In order to improve the surface wettability of ITO for ethanol-based seed solution, the substrate was treated with ethanol and then the zinc acetate seed solution was deposited. These substrate samples were grouped as ITO ZnAc*. The nanorods were grown on these treated substrates using 25 mM equimolar final solution concentration of $\text{Zn}(\text{NO}_3)_2$ and HMT. Six syntheses were performed at 90 °C and the nanorods samples were grouped as ITO ZnAc*(25). The SEM images showed improved coverage of nanorods on the ITO surface. This indicated increase in ITO surface wettability due to ethanol treatment which therefore increased the seed layer adhesion and coverage (Figure 38(b)). The results were confirmed by measuring contact angles of water droplets on the substrates using sessile drop method (Figure 39 (a) and (b)); the water droplets formed angles of 78.8° and 58.7° with non-treated and ethanol-treated ITO substrates respectively. However, this did not fully resolve the problem, since there were non-seeded voids and gaps still present where nanorods did not grow. In order to address this issue, seeding solution and deposition method were optimised and for this ZnO nanoparticles seed solution was developed.

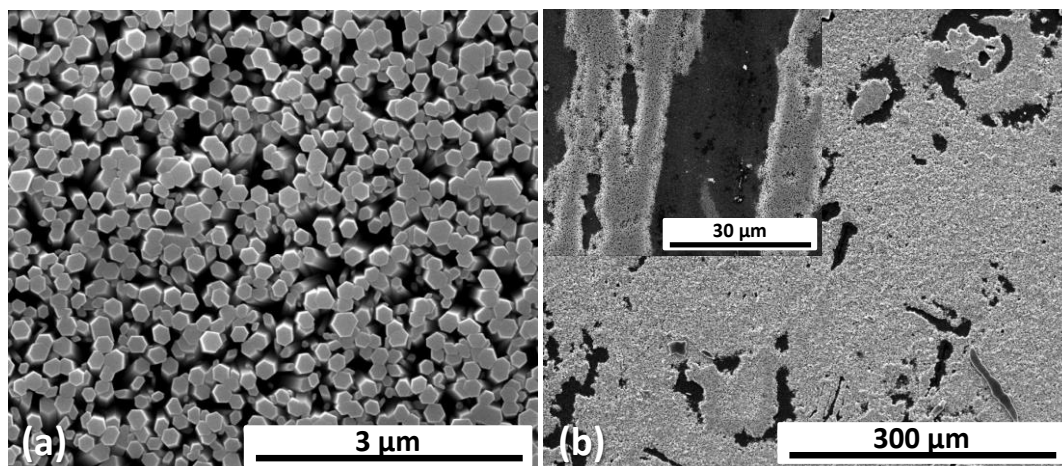


Figure 38. Zinc acetate seed layer spin-deposition on ethanol-treated ITO substrate: (a) nanorods grew in densely packed fashion similar to the rods on non-treated ITO (b) The coverage of the seed layer on ethanol treated-ITO improved when compared to non-treated ITO but non-seeded voids and gaps were present.

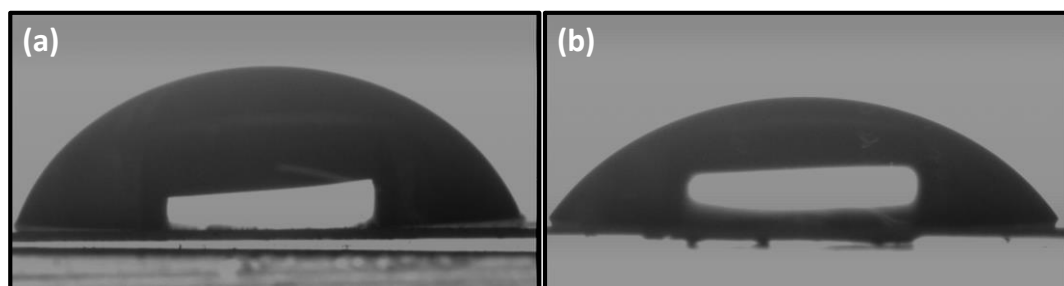


Figure 39. Contact angle of water droplets measured using sessile method: (a) 78.8° contact angle on non-treated ITO substrate, (b) 58.7° contact angle on ethanol-treated ITO surface

4.1.2. ZnO Nanorods on Sputtered ITO

On the sputter seeded substrates, grouped as ITO Sp (Table 5), the nanorods were synthesised using 25 mM equimolar concentration of aqueous $\text{Zn}(\text{NO}_3)_2$ and HMT solutions (Chapter 3, section 3.2.1). These nanorod samples were grouped as ITO Sp(25). The seed layer and synthesised nanorods were analysed using SEM. Figure 40(a) demonstrates the conductive ITO surface without ZnO seed layer and Figure 40(b) shows ITO surface coated with sputtered ZnO seed layer. The seeded substrate shows deposited ZnO crystals which act as nucleation sites for the growth of c-axis oriented ZnO nanorods. The sputtered seed layer on the ITO had covered

the ITO surface sufficiently and the non-seeded gaps and voids were negligible (Figure 41(b)).

The nanorods grown from the sputtered ZnO seed layer ITO Sp(25), are shown in Figure 41. The 25° tilted top view of the 2 μm long nanorods; the hexagonally indexed nanorods were observed to have 70 nm diameter.

Similar to ITO Sp, ITO Sp* seeded substrate group was also prepared. The nanorods on these substrates were grown using 50 mM equimolar concentration of aqueous $\text{Zn}(\text{NO}_3)_2$ and HMT solutions (Chapter 3, section 3.2.2). These nanorods were c-axis oriented having diameter of 40 nm and length of 1 μm (Figure 42).

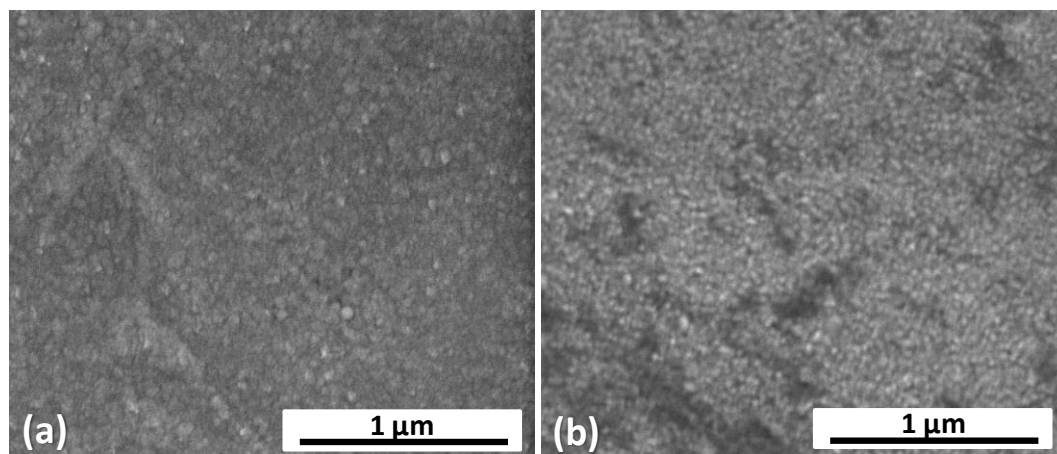


Figure 40. (a) Surface of ITO coated on PET substrate. (b) ZnO seed layer sputtered onto ITO.

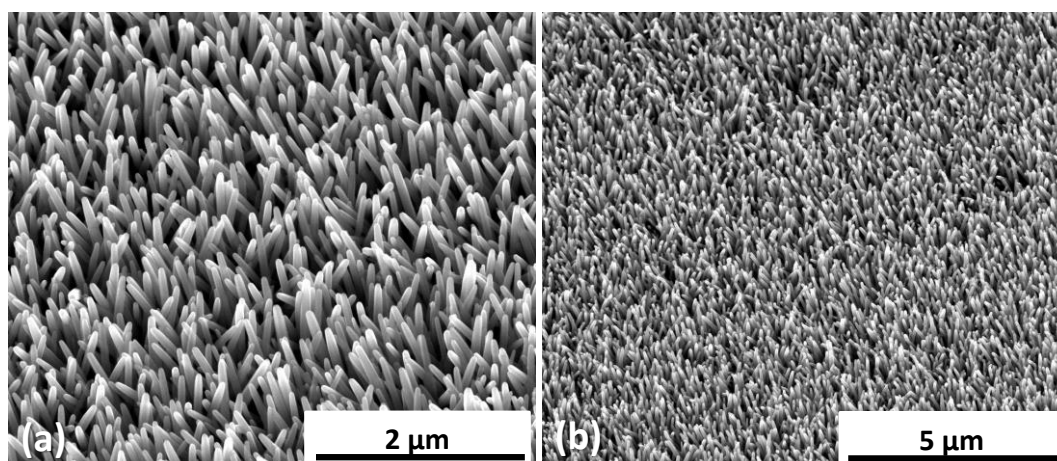


Figure 41. (a) ZnO nanorods grown on sputtered ITO-coated PET substrate using 25 mM precursor solution concentration. (b) 5 μm magnification image showing even coverage of nanorods on ITO surface.

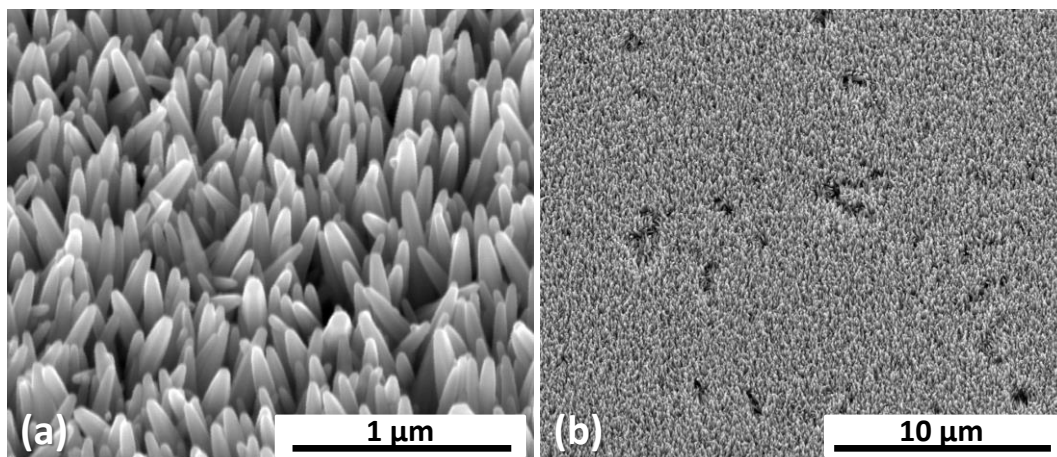


Figure 42. (a) ZnO nanorods grown on sputtered ITO-coated PET substrate using 50 mM precursor solution concentration. (b) 10 μm magnification image showing even coverage of nanorods on ITO surface.

4.1.3. ZnO Nanorods Grown from Nanoparticles Seed Layer

Attempts to deposit seed layer using zinc acetate seed layer solution were unsuccessful because of lack of adhesion between seed solution and ITO surface. The approach to adhere seed solution with ITO substrate was modified and ZnO nanoparticle-based seed solution was considered for deposition. The zinc salt-based seed layer was previously spin-coated on the ITO substrate and heated to 100°C for adhesion. The ZnO nanoparticle-based seed solution was, however, spray-coated on to ITO-coated PET at 100°C to form seed layer. Being nanostructured, the surface energy of ZnO nanoparticles was considered to be higher than powdered zinc salt. Therefore, it was believed that the ZnO nanoparticles would adhere better than the previous zinc acetate seed solution.

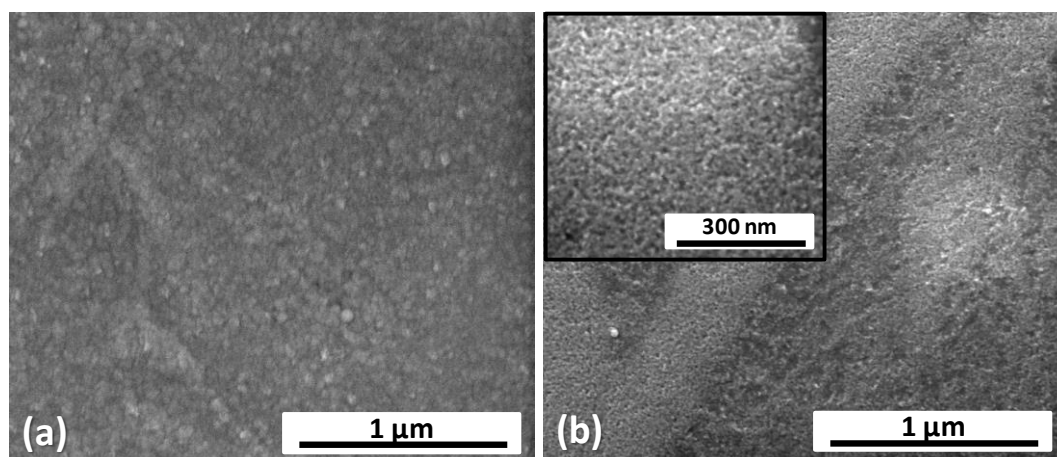


Figure 43. (a) Surface of ITO coated on PET substrate. (b) ZnO nanoparticle seed layer spray-coated onto ITO.

For coating a surface using spin-deposition, the surface is required to be sufficiently wet to allow its contact with the seed solution. Therefore, the nanoparticle seed solution was sprayed onto the substrate which has advantages over spin-coating method: the spray-coating ensures landing of seed solution from the nozzle over the area it is travelled on the substrate. Hence, spray-coating improved the contact of seed solution with the surface without any surface treatment for wettability. The 20-step spray-deposition covered the entire $2 \times 1 \text{ cm}^2$ substrate with the seed layer. Moreover, in the spin-deposition method, the substrate was heated at 100°C after each step deposition. However, in case of spray-coating, the heating of the substrate was performed simultaneously with spray-coating which reduced the number of processes.

The ITO substrates seeded with nanoparticles seed solution were grouped as ITO NP (Table 5). Figure 43 (a) and (b) show non-coated ITO surface and surface of ITO coated with nanoparticle seed solution. The seeded ZnO crystals had sufficiently covered the ITO surface. However, due to manual spray-deposition, the seeded crystals were dense in some areas.

The ITO NP substrates were used for the synthesis of nanorods using 50 mM equimolar solution concentrations of $\text{Zn}(\text{NO}_3)_2$ and HMT. The growth was carried out for 4 hours at 90°C and only one synthesis was performed. The ITO samples prepared using this growth condition were grouped as ITO NP(50). The synthesised nanorods were $\sim 1.5 \text{ }\mu\text{m}$ long and $\sim 80 \text{ nm}$ wide (Figure 44(a)).

The reason for increasing the final solution molar concentration to 50 mM and increasing the growth duration to 4 hours was to fabricate micro-meter ranged nanorods in less than six synthesis steps. By cutting the synthesis duration shorter, more time was spent in analysing the seed layer issues and developing the nanoparticle seeding method

Similarly, the nanoparticles-based seed solution was also coated on silver (Ag)-coated and Zn foil substrates and the resultant substrates were grouped as Ag NP and Zn NP respectively (Table 5). The nanorod growth was carried out using 50 mM equimolar final solutions concentration of $\text{Zn}(\text{NO}_3)_2$ and HMT, for 4 hours. The fabricated nanorod samples on Ag and Zn substrates were grouped as Ag NP(50) and Zn NP(50). On the silver (Ag) substrate, $\sim 1\ \mu\text{m}$ long and $\sim 66\ \text{nm}$ wide nanorods were obtained (Figure 45(a)) and $\sim 600\ \text{nm}$ long and $\sim 50\ \text{nm}$ wide nanorods were grown on the Zn foil (Figure 46(a)). Figure 45(b) and Figure 46(b) shows that, the nanorods covered the substrate evenly and there were fewer areas with pin-holes and growth retardation. Hence, the spray-coated nanoparticles-based seed deposition was an effective method to grow evenly covered ZnO nanorods on flexible substrates, without requiring substrate pre-treatment.

XRD analysis was performed on the ZnO nanorods grown on ITO, Ag and Zn and the indices were annotated for the wurzite ZnO structure from ICDD 36-1451. The results demonstrated a prominent 002 peak of ZnO, having the highest intensity and positioned at 34.4° . This peak confirmed the c-axis oriented vertical axis growth of ZnO nanorods.

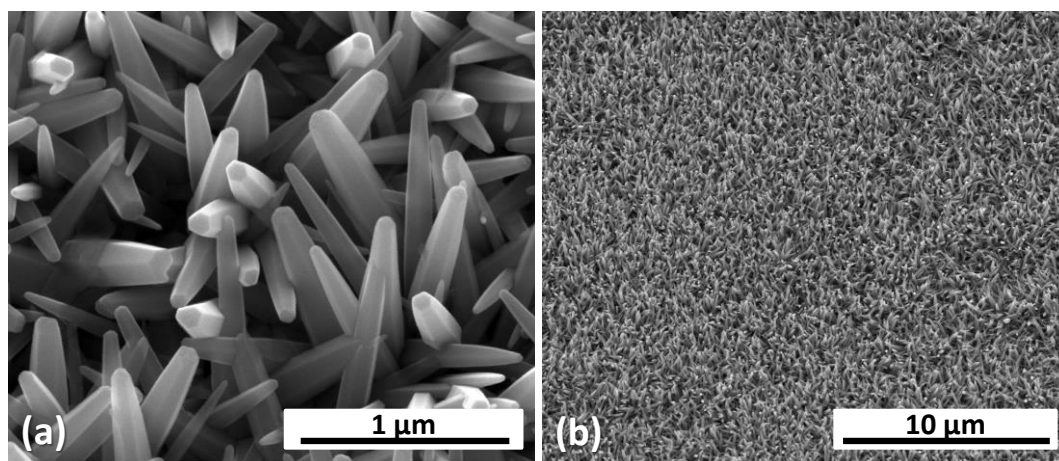


Figure 44. (a) C-axis oriented nanroods grown from spray-coated nanoparticle seeds on ITO-coated PET substrate. (b) 10 μm magnified image confirming the even coverage of the seed layer and nanorods on the substrate.

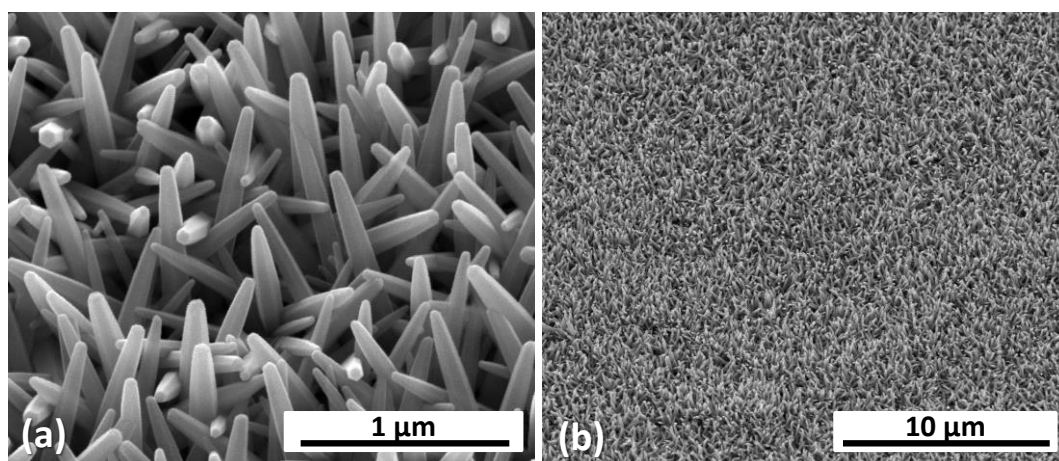


Figure 45(a) C-axis oriented nanroods grown from spray-coated nanoparticle seeds on Ag-coated kapton polyimide substrate. (b) 10 μm magnified image confirming the even coverage of the seed layer and nanorods on the substrate.

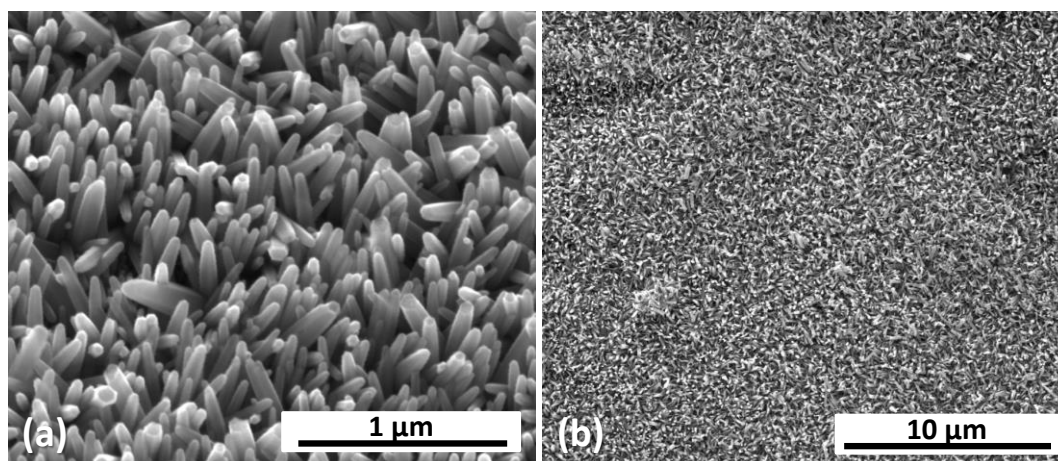


Figure 46. (a) C-axis oriented nanorods grown from spray-coated nanoparticle seeds on Zn foil substrate. (b) 10 μm magnified image confirming the even coverage of the seed layer and nanorods on the substrate.

The aspect ratio of ZnO nanorods depend on the growth parameters, seed layer conditions and bottom electrode lattice. To exemplify the growth parameters, let us take the example of 25 mM and 50 mM equimolar final solution concentrations of $\text{Zn}(\text{NO}_3)_2$ and HMT in this research work. In case of 25 mM solution condition, the syntheses were carried out six times, for 2.5 hours each to obtain 2 μm long and 70 nm wide nanorods. However, for the case of 50 mM solution condition, the concentration of solution and the duration of synthesis were increased to 4 hours and 1 μm and 40 nm wide nanorods were grown. This indicated that the rate of growth of ZnO nanorods was increased with the increase in precursor solution concentration and growth time. These results were studied in the light of research work reported by other authors. It was explained by Zhao et al. (2009)⁶ that, due to increase in precursor solution concentration, the concentration gradient between solution and substrate increases. As a result, there are more precursor near substrate per unit time and hence the diffusion rate of Zn and O from precursors to substrate increases. This accelerates the growth of nanorods. Similarly as reported by Guo et al. (2005)⁷, an increase in growth time also increases the Zn and O dissociation which increases ZnO growth. Hence, the growth rate of ZnO nanorods grown using 50 mM final concentration was higher than that of the 25 mM final concentration solution.

For the case of various substrates seeded with nanoparticle seed solution, such as ITO NP (50), Ag NP(50), Zn NP(50), the nanorods were growth under similar

growth conditions. However, for each substrate, the length and diameter of ZnO nanorods were different. This dissimilarity has been discussed by previous studies⁸⁻¹⁰ to be attributed to substrate lattice, defects and surface energy.

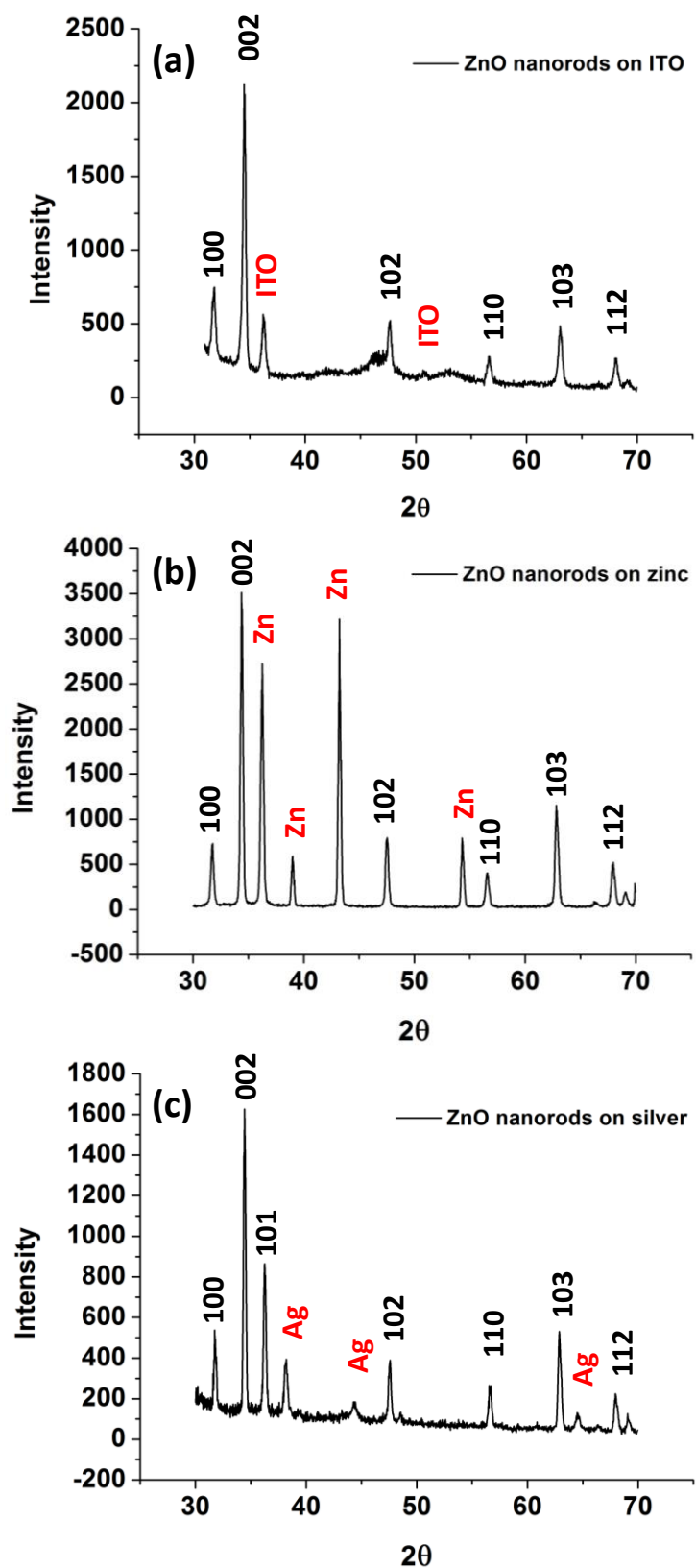


Figure 47. XRD analysis of ZnO on various substrates showing 002 peak positioned at 34.4° . ZnO nanorods grown on (a) ITO, (b) zinc foil and (c) Ag (silver).

4.2. Summary

The surface wettability of conductive layer on the substrate and the adhesion of ZnO seed layer on it were the key issues which required to be addressed for seeding the substrates using sol-gel technique. Zinc acetate-based seed solution was spin-coated on the substrates but the surface of the ITO was not sufficiently wet to allow seed solution contact with the substrate. Consequently, the seed layer only cohered with random locations forming island-like patterns on ITO where ZnO nanorod arrays grew. Attempts were made to improve ITO surface wettability using ethanol pre-treatment, which did not fully resolve the issue. Hence, the deposition technique and the seed solution were both modified to improve the coverage of ZnO on the substrates. ZnO nanoparticle-based seed solution was developed, which as compared to zinc salt-based seed solution had better adhesion properties with the substrate. Secondly, it was spray-coated which did not require the pre-treatment of the substrate to improve its wettability. Instead, the spray-coating allowed adhesion of seed layer on the substrate areas where the nozzle was travelled. The spray-deposition technique was developed to allow maximum coverage of the entire $2 \times 1 \text{ cm}^2$ substrate.

The nanorods were grown from the seeded ZnO nanoparticles on ITO and Ag coated flexible substrates and Zn foil. 50 mM equimolar final concentration of precursor solution was taken for the nanorods growth for 4 hours and the results were observed using SEM imaging. On the ITO substrate, 1.5 μm long and 80 nm wide rods were grown. Similarly, on the Ag substrate 1 μm long rod with 66 nm width were observed and 600 nm long rods with 50 nm width were grown on the Zn foil. Maximum coverage of the seed layer on the substrate was obtained and the pin-holes were reduced.

The ZnO nanorods were also grown on sputtered seed layer. The growth of nanorods was carried out using 25 mM final solution concentration of $\text{Zn}(\text{NO}_3)_2$ and HMT and was repeated six time to yield 2 μm long rods with 70 nm diameter. The coverage of the rods was even and there were negligible gaps and pin-holes which was desired for device fabrication. Moreover, 50 mM final solution concentration of $\text{Zn}(\text{NO}_3)_2$ and HMT yielded 1 μm long and 40 nm wide ZnO nanorods in one synthesis for 4 hours.

Nucleation and Growth of ZnO Nanorod Arrays

Hence, various seeding techniques were implemented to grow highly oriented and uniformly covered ZnO nanorods, of controlled length and diameter, on various substrate. For the development of devices, the nanorods growth obtained from spray-coated nanoparticles as well as sputtered seed deposition were suitable.

4.3. References

- ((1) Greene, L. E.; Law, M.; Goldberger, J.; Kim, F.; Johnson, J. C.; Zhang, Y.; Saykally, R. J.; Yang, P. *Angew. Chem. Int. Ed. Engl.* **2003**, *42*, 3031–3034.
- (2) Sugunan, A.; Warad, H. C.; Boman, M.; Dutta, J. *J. Sol-Gel Sci. Technol.* **2006**, *39*, 49–56.
- (3) Liu, Y.; Tai, K.; Dillon, S. J. *Chem. Mater.* **2013**, *25*, 2927–2933.
- (4) Ashfold, M. N. R.; Doherty, R. P.; Ndifor-Angwafor, N. G.; Riley, D. J.; Sun, Y. *Thin Solid Films* **2007**, *515*, 8679–8683.
- (5) Li, C.; Fang, G.; Li, J.; Ai, L.; Dong, B.; Zhao, X. *J. Phys. Chem. C* **2008**, *112*, 990–995.
- (6) Zhao, X.; Lee, J. Y.; Kim, C.-R.; Heo, J.; Shin, C. M.; Leem, J.-Y.; Ryu, H.; Chang, J.-H.; Lee, H. C.; Jung, W.-G. *Phys. E Low-dimensional Syst. Nanostructures* **2009**, *41*, 1423–1426.
- (7) Guo, M.; Diao, P.; Cai, S. *J. Solid State Chem.* **2005**, *178*, 1864–1873.
- (8) Nandi, R.; Joshi, P.; Singh, D.; Mohanta, P.; Srinivasa, R. S.; Major, S. S. *Thin Solid Films* **2014**, *555*, 122–125.
- (9) Nayak, J.; Sahu, S. N.; Kasuya, J.; Nozaki, S. *J. Phys. D. Appl. Phys.* **2008**, *41*, 115303.
- (10) Yang, J.; Zheng, J.; Zhai, H.; Yang, X.; Yang, L.; Liu, Y.; Lang, J.; Gao, M. *J. Alloys Compd.* **2010**, *489*, 51–55.

5. Analysis of Mechanical and Electrical Performance Parameters of Devices

For piezoelectric devices, electrical and mechanical characterisation is an important requirement for development of knowledge on their operation and output performance evaluation. The fabricated ZnO nanorods-based devices were mechanically displaced using a cam attached to a motor shaft and their piezoelectric response was recorded. For electrical output analysis, it was necessary to analyse the mechanical behaviour of devices when they were subjected to a particular bend-release strain from the rotating cam. Therefore, a device's displacement profile was characterised and its velocity and acceleration of motion were also calculated and analysed. In addition to the analysis of the device motion, interesting results related to strain-dependent piezoelectric behaviour of the fabricated devices were studied.

Evaluation of ZnO nanorods-devices' performance parameters, such as open-circuit voltage, short-circuit current density, power density and impedance were performed using measurement techniques which were standardised for microelectromechanical systems (MEMS) ¹. Along with development of the measurement techniques, it was also necessary to analyse measured output results and device-to-device performance variation. In this regard, factors were studied which affect the device performance such as, series resistance (R_s) and shunt resistance (R_{sh}).

5.1. Analysis of Electromechanical Response

The strain-induced piezoelectric polarisation in an energy harvester was studied by bending a device, and simultaneously recording its displacement and open-circuit voltage output. The analysis of device voltage output response and its dependence on the subjected displacement rate were studied.

5.1.1. Simultaneous Voltage and Displacement Measurements

A ZnO piezoelectric energy harvester based on PEDOT:PSS top electrode and ITO bottom electrode, labelled as PDOT-EM (Chapter 3, Table 3), was studied for its electrical response to mechanical excitation. The device was mechanically bent using a rotating cam set up (described in Chapter 3, section 3.6) and its z-axis displacement profile was measured using a MEL M5 laser triangulation sensor². Simultaneously, the bending-induced piezoelectric response of the device was recorded using data acquisition module National Instruments NI PXI-4461 (24-bit ADC) on the NI PXIe-1062Q chassis. This concurrent recording of device's bending profile and generated voltage output signal assisted in analysing the instant of output generation and its dependence on displacement rate. Figure 48 shows the displacement profile when PDOT-EM was bent and released using the cam. This profile was recorded using the NI PXIe-1062Q chassis on National Instruments NI PXI-4461. The highest z-axis displacement was ~6 mm which was attained in 0.10 seconds. After 0.125 seconds, the cam released the device and at 0.15 seconds it reached its initial position. However, due to natural resonance of the plastic base substrate, the device oscillated before it reached at rest at 0.275 seconds.

The generated voltage by the PDOT-EM and its subjected mechanical excitation were recorded simultaneously. Figure 49 demonstrates the bend-release displacement simultaneous with the voltage output generation plot³. As observed from the plot, the device generated an output pulse when it was released from ~6 mm² bending displacement at 0.125 seconds. The displacement-voltage plot in Figure 48 was converted to strain rate-voltage plot (Figure 50) by taking time derivative of the displacement profile $\frac{\partial s}{\partial t}$. As observed from Figure 50, the device was bent at 0.05 m/sec, which did not sufficiently excite ZnO nanorods and hence a measurable voltage output response was not obtained. Contrariwise, when the device was released, its strain rate increased until it attained a maximum of 1.5 m/sec and acceleration of 50 g (480 m/s²)², which sufficiently strained the ZnO nanorods causing a peak open-circuit voltage of 125 mV to be generated^{2,3}.

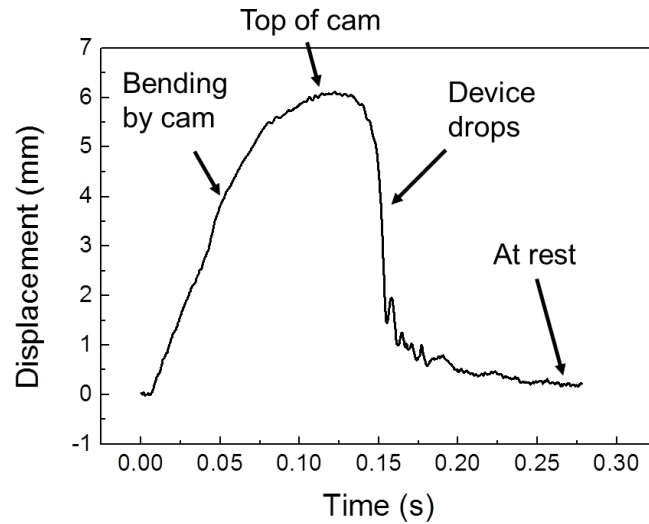


Figure 48. Displacement profile of device showing bend and release of the device by the cam rotating at 1 Hz².

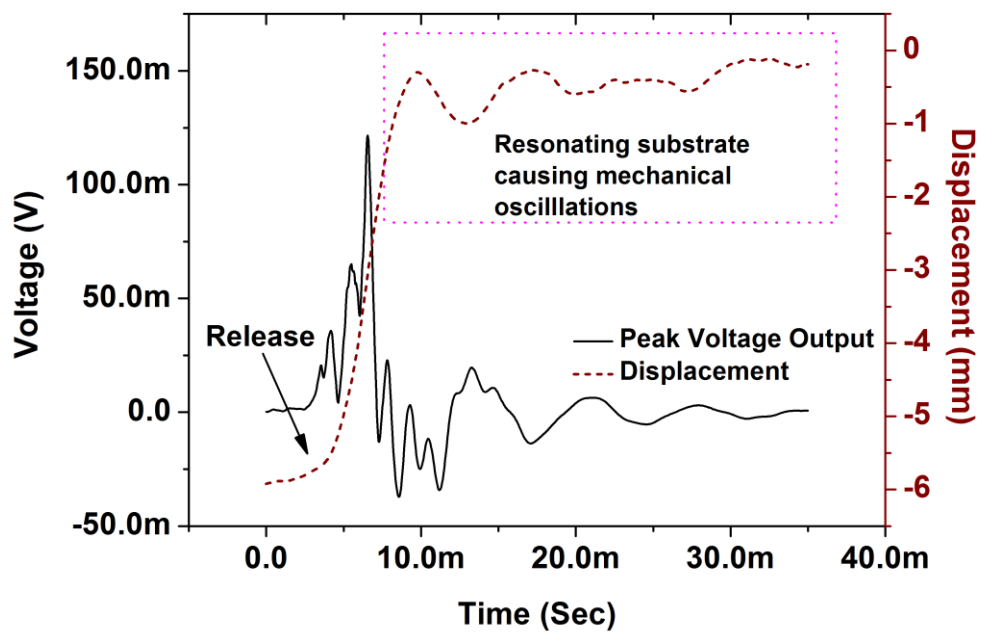


Figure 49. Peak open-circuit voltage of the device measured along with its displacement, showing generation of voltage signal when the device was released

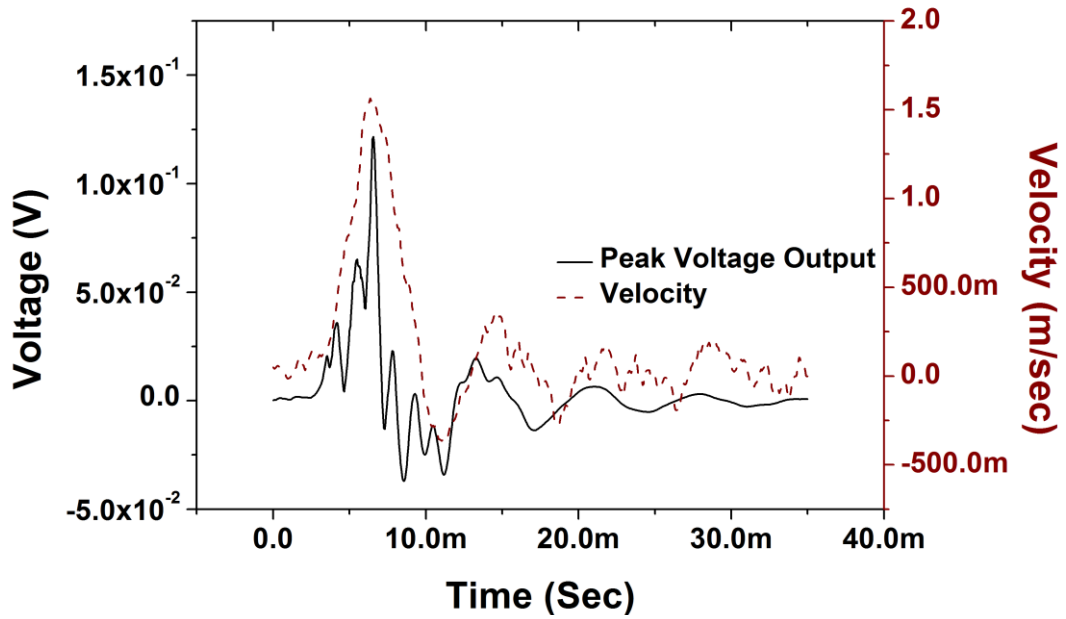


Figure 50. The displacement plot in Figure 49 was time derivated to obtain device's velocity profile. When the cam released the device, its output voltage attained a peak value of 125 mV at a peak motion velocity of 1.5 m/sec.

The results obtained from simultaneous displacement-voltage measurement were analysed in the light of piezoelectric effect and its mathematical equations. An ideal piezoelectric source behaves as a parallel plate capacitor in which the generated voltage output is directly related to the applied stress on it (Equation 3). This relationship is explained as below.

In a direct piezoelectric effect, a material develops electric charge as a response to stress applied to it, which is given as ^{4,5}:

$$D = \epsilon E \quad \text{Equation 3}$$

D= Electric Displacement

ϵ = Dielectric constant

E = Electric field

The electromechanical effect of charge displacement in response to applied stress is given as ^{4,5}:

$$D = \sigma d \quad \text{Equation 4}$$

D = Electric Displacement

σ = Applied Stress

d = Strain coefficient

Dielectric displacement is defined as surface charge density and so Equation 2 becomes:

$$\frac{Q}{A} = \sigma d$$

$$\frac{CV}{A} = \sigma d$$

Equation 5

Hence, according to equation 3, an ideal piezoelectric source behaves as a parallel plate capacitor in which the generated voltage output is directly related to the applied stress on it. However for the case of ZnO-energy harvesters this differs because the device behaves as a lossy capacitor. According to Briscoe et al. (2012) ⁶, for ZnO-energy harvesters, the voltage generation is dependent on the applied stress as well as the internal and external screening free charge carriers which flow due to semiconducting properties of ZnO. This can be explained using the screening model of ZnO energy harvesters: when the energy harvester is strained, the polarisation increases over a finite time and attains a maximum value, after which screening occurs. According to this theory, the attainment of maximum polarisation and its screening is time dependent. Therefore, if the strain rate is increased, the polarisation can attain its maximum at a rate faster than the screening rate. This situation occurred during the bend-release test when during its release, the device attained strain rate of 1.5 m/sec (during release at time interval 0.125 seconds). As compared to 0.05 m/sec strain rate when device was bent, the release rate was 30 times faster. As a consequence of which, the generated voltage during release motion was higher than the minimum voltage generated when device was bent upwards. Hence, during its release motion, the generated voltage from piezoelectric PDOT-EM device increased with increasing device strain rate. In addition, when the strain rate attained its maximum of 1.5 m/sec (50 g acceleration), a peak voltage of 125 mV occurred (Figure 50).

The displacement-voltage and velocity-voltage profile in Figure 49 and Figure 50 also demonstrated that, ripple-like oscillating voltage signals were generated due to mechanical resonance of the plastic base substrate. The width of each oscillation was ≈ 7.6 ms and therefore the oscillating frequency was ≈ 130 Hz. The negative half cycle of the primary voltage signal of 125 mV amplitude (caused by 50 g acceleration) was overlapped by the signals generated through these 130 Hz substrate vibrations. Therefore, the reverse half-cycle voltages of the devices could not be analysed. The device came to rest when these oscillations were decayed.

Another interesting analysis on device voltage generation was obtained from the measurement in Figure 50: after the device attained a voltage peak of 125 mV at 6.5 msec, its output voltage profile did not follow the velocity profile for the next 4.45 msec. Subsequent to its attainment of voltage peak, the output signal falling edge occurred which did not follow the device velocity profile and dropped to zero in 0.75 milliseconds. It was believed that screening effect of piezoelectric polarisation caused this sudden drop in output signal's falling edge. Screening of bound polarised charges in a piezoelectric material occurs due to the flow of mobile charges through it. The flow of mobile charges creates an electric field, called screening field, which opposes the electric field of polarised bound charges ^{3,6}.

The screening phenomenon in piezoelectric ZnO can be described by using a screening model demonstrated by Briscoe et al. (2012) ⁶ shown in Figure 51. When polarisation is induced in a piezoelectric material (ZnO) through the application of stress, an electric field called depolarisation field is developed. This field allows the movement of free-charge carriers, which are either within the material or enter from external contacts. These free-charge carriers compensate the depolarisation field and cause it to drop to zero. This effect is called internal screening when free-charge carriers present in the material compensate the depolarisation field; whereas, if free-charges from an external contact cause this compensation then the effect is called external screening ^{3,6-8}. In piezoelectric devices, the polarisation field is therefore always screened out completely within a given time. Hence, the measured piezoelectric voltage output was the potential difference developed within the duration till the depolarisation field is persisting, after which it is compensated and voltage output drops to zero ⁶. Hence the measured device in Figure 50, attained its peak voltage of 125 mV before the depolarisation was completely screened.

Thereafter, when the depolarisation field was compensated by free-charge carriers, it was dropped to zero within 0.75 milliseconds. Hence for piezoelectric devices, the peak output voltage was not only dependent on the bending rate but also dependent on the screening *rate*.

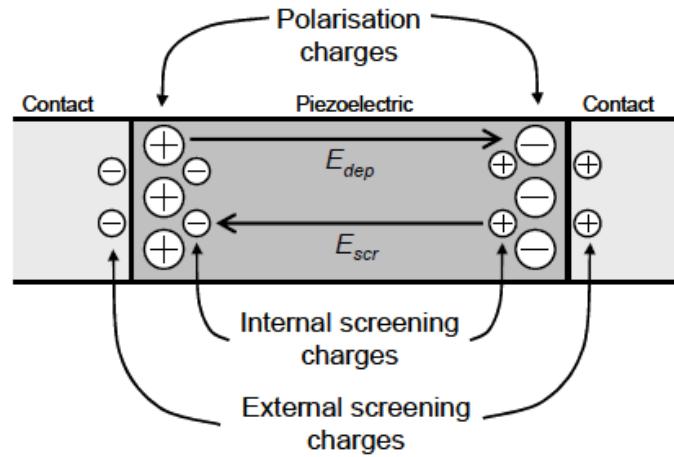


Figure 51. Screening model in a polarised piezoelectric material, showing bound charges screened out by the flow of mobile free-charge carriers⁶.

For further analysis, the voltage measurement was taken when a p-n junction device labelled as 'PDOT-A4' was bent at a higher displacement rate. For this, the rotation frequency of the cam was increased from 1 Hz to 2 Hz and 3 Hz and consequent voltage was recorded using National Instruments NI PXI-4461 (24-bit ADC) on the NI PXIe-1062Q chassis. Figure 52 compares the peak open-circuit voltage output when the cam rotating at 1 Hz, 2 Hz and 3 Hz bent and released the energy harvester. Due to increase in input frequency, the device bending rate was increased which also increased the rate at which it was released. Consequently, the peak open-circuit voltage of the device was increased from 90 mV at 1 Hz to 100 and 115 mV at 2 and 3 Hz. The generated voltage cycles attained their peak voltage output and thereafter dropped to zero within 2 milliseconds. This phenomenon can also be explained using the screening model by Briscoe (2012)⁶. When the device was bent at a higher frequency, the rate of charge displacement in piezoelectric ZnO increased which increased the depolarisation field and hence the measured piezoelectric voltage output was increased. However, after attaining the peak voltage value, the

depolarisation field was compensated by the screening field and therefore, the voltage peak dropped to zero.

Hence, the results and analysis on strain rate-dependent device voltage output elucidated the electromechanical response of the devices and also confirmed that the voltage was generated when strain-induced polarisation was developed across ZnO nanorods.

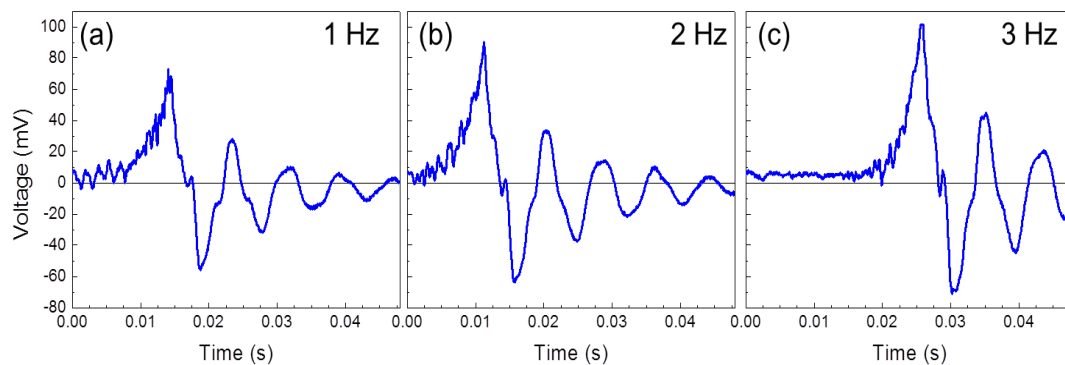


Figure 52. Measurement of peak open circuit voltage of PDOT-A4 when bent and released by a cam rotating at (a) 1 Hz, (b) 2 Hz and (c) 3 Hz

2.

5.2. Analysis of Electrical Parameters

The evaluation of a device's performance requires analysis of the electrical losses affecting its output, such as parasitic effects of series (R_s) and shunt resistance (R_{sh}). In this regard, ZnO nanorods-based devices were measured for their electrical output and the electrical losses affecting device-to-device variation in performance were studied in detail. For this study, twelve fabricated devices comprising of PEDOT:PSS top electrode and ITO bottom electrode were selected and for analysis they were divided into groups of four. The groups were based on device-to-device variations and difference in fabrication techniques. The group names and their devices are listed as follows:

Table 6. Group names and electrode fabrication method (from Chapter 3) for PEDOT:PSS-based devices, used in this chapter for analysis of electrical losses, characterisation and performance evaluation.

Group Names	Top Electrode Fabrication	Bottom Electrode & Nanorod Fabrication		Devices
PDOT-2K/A [†]	PEDOT:PSS @ 2000 rpm	ITO Sp(25)		PDOT-A1, PDOT-A2, PDOT-A3, PDOT-A4
PDOT-2K/B	PEDOT:PSS @ 2000 rpm	ITO Sp(25)		PDOT-B1, PDOT-B2, PDOT-B3
PDOT-1K	PEDOT:PSS @ 1000 rpm	ITO Sp(25)		PDOT-1K-1, PDOT-1K-2, PDOT-1K-3
PDOT-Shorted	PEDOT:PSS @ 2000 rpm	ITO Sp(25)		PDOT-Sh-1, PDOT-Sh-2, PDOT-Sh-3

The ITO Sp(25) electrode fabrication, nanorod synthesis and PEDOT:PSS electrode fabrication techniques are described in section 3.1.3 and 3.2.1 of Chapter 3.

[†] The devices in groups PDOT-2K/A, PDOT-2K/B and PDOT-Shorted were fabricated in a similar manner. However, based on device-to-device variation in electrical performances, they were divided into separate groups.

5.2.1. Series (R_s) and Shunt Resistances (R_{sh})

The fabricated devices in groups PDOT-2K/A, PDOT-2K/B, PDOT-1K and PDOT-Shorted were composed of n-type ZnO nanorods connected with p-type hole conducting polymer PEDOT:PSS⁹ (band gap 1.5-1.6 eV)¹⁰ to form a p-n junction as illustrated in Figure 53. The formation of p-n junction at ZnO/PEDOT:PSS interface has been studied previously using DC J-V (Current density-voltage) characterisation¹¹. Similarly, using Keithley 4200 source meter, J-V characterisation was carried out on our fabricated devices to confirm their non-linear diode behaviour. Figure 54 shows the J-V characteristic curve of PDOT-A2 device from -2 V to +2 V, which was non-linear due to its forward current increasing exponentially with the operating voltage¹². The current rectification ratio (defined as the ratio between forward current and reverse current) was 12 at ± 2 V¹¹. The diode turn-on voltage and the reverse leakage current were found to be 0.5 V and 1.3 mA cm^{-2} . Thus, the rectifying non-linear J-V characteristic curve indicated a p-n junction between n-type ZnO nanorods and p-type PEDOT:PSS¹¹.

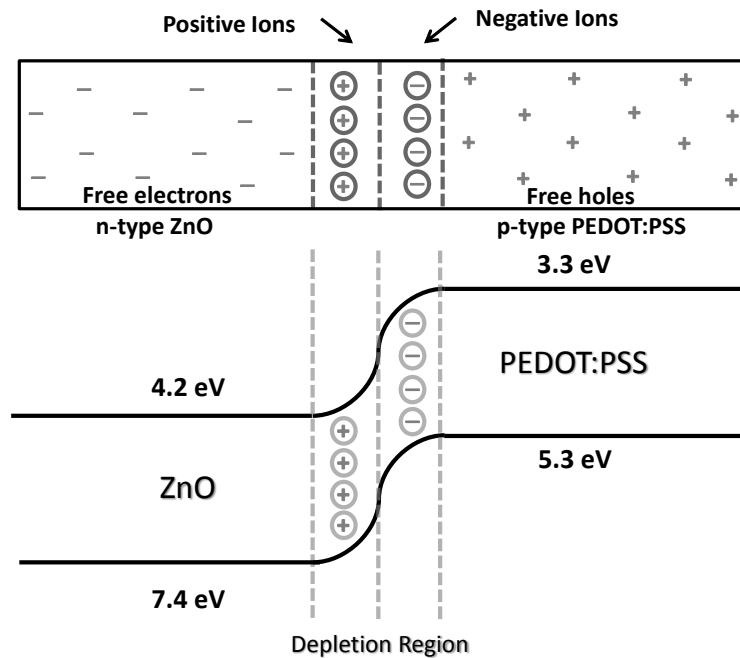


Figure 53. Band diagram showing p-n junction formation between n-type ZnO and p-type PEDOT:PSS.

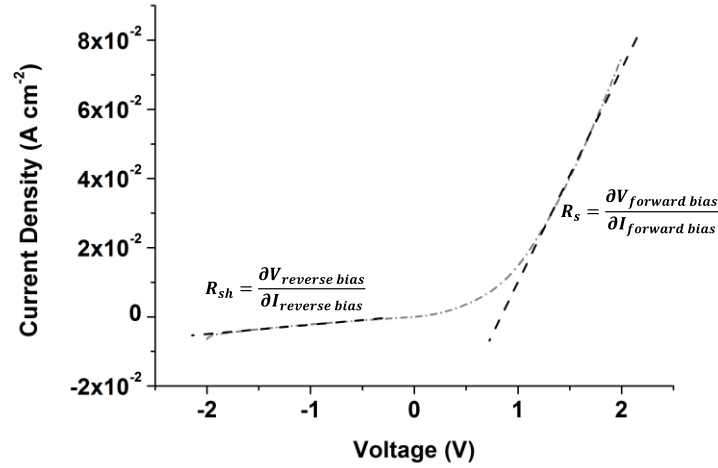


Figure 54. J-V characteristic plot of PDOT-A2 device demonstrating non-linear diode curve due to formation of p-n junction between ZnO and PEDOT:PSS. The inverse slope of forward bias and reverse bias region determines the R_s and R_{sh} , respectively.

The benefit of using PEDOT:PSS-based p-n junction-type devices over Schottky-type devices (with metal/ZnO contact) was described using a free charge screening model by Briscoe et al. (2012)⁶. According to this model (Figure 51), when a piezoelectric material is stressed, a depolarisation field is produced which is compensated by the movement of free-charge carriers both from within the material or from external contacts. The screening of polarisation is determined by the rate of flow of free charge carriers. In the case of a ZnO contact with p-type material or with metal of higher work function (> 4.26 eV), an energy barrier exists at the p-type/ZnO or metal/ZnO Schottky junction. This energy barrier reduces the transport of carriers across the junction¹³. Hence, it assists in reducing the external screening *rate*. The external screening cannot be fully avoided, because mobile carriers tunnel through barriers or accumulate at junctions causing screening of polarisation charges. In which case, if we compare metal electrode with semiconducting PEDOT:PSS electrode; then the 10^{22} cm^{-3} ranged carrier concentration of metal, compared with 10^{19} cm^{-3} for PEDOT:PSS, is considered to allow higher flow of free-charge carriers through ZnO. Hence, it was studied by that Briscoe et al. (2012)⁶ a p-type contact would allow slower screening *rate* and improve the device voltage output.

Device characterisation, which involves measuring its current as a function of an applied DC voltage, is also useful to determine its losses: for a diode, the J-V

characterisation is an effective way to determine series (R_s) and shunt resistances (R_{sh}). The series resistance (R_s) in heterojunction devices had been explained to be dependent on electrode contact resistance^{14,15}, electrode sheet resistivity^{16,17} and material dimensions¹⁸. The shunt resistance is related to a low resistance path in a device circuit which allows a flow of leakage current¹⁹. It is, therefore, related with those parameters which cause device short circuits. These parameters include, for example, pinholes^{19,20} in ZnO nanorod arrays that allow PEDOT:PSS electrode to come in contact with bottom electrode. Hence, techniques were implemented to extract the series (R_s) and shunt resistance (R_{sh}) from the J-V characteristic curves of the devices in groups PDOT-2K/A, PDOT-2K/B and PDOT-1K to determine the effects of losses on device performance, and to study the possible sources of losses.

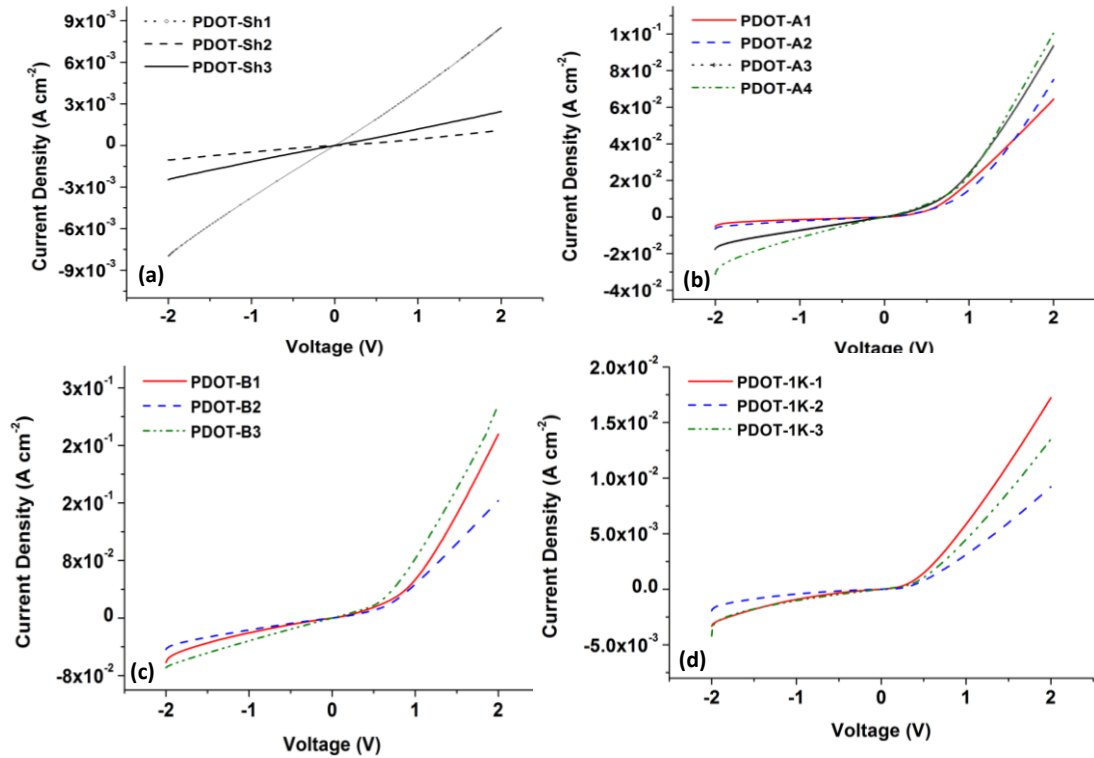


Figure 55. J-V characteristic curves of devices in groups: (a) PDOT-Shorted, (b) PDOT-2K/A, (c) PDOT-2K/B and (d) PDOT-1K.

Figure 55 shows the J-V characteristic plots of the devices in groups PDOT-2K/A, PDOT-2K/B and PDOT-1K. The R_s and R_{sh} of the devices in these groups were extracted by calculating the inverse slope

$R = \frac{\partial V}{\partial I}$ of the plots in the forward and reverse biased regions, respectively (as shown in Figure 54):²¹

Table 7 shows the extracted values of the R_s and R_{sh} from each device. The devices fabricated with two layers of PEDOT:PSS, spin-coated at 2000 rpm each (groups PDOT-2K/A and PDOT-2K/B) had R_s in range of 0.05 – 0.17 k Ω ; which was 3 - 6 times lower than 0.34 – 0.63 k Ω ranged R_s of devices fabricated with 2 layers of PEDOT:PSS spin-coated at 1000 rpm each (group PDOT-1K). The reason of this R_s difference was linked with the thickness of PEDOT:PSS layer. Figure 56 shows the final thicknesses of the dried PEDOT:PSS layers spin-deposited onto the nanorods at 1000 RPM and 2000 RPM. The final thickness of PEDOT:PSS layers deposited at 1000 RPM was 3 μm which was three times higher than that of the PEDOT:PSS layers spin-coated at 2000 RPM. Due to this, the R_s of the PDOT-1K devices was 3 – 6 times higher than that of the PDOT-2K/A and PDOT-2K/B devices. This effect can be further elaborated by considering the schematic of ITO/ZnO nanorod/PEDOT:PSS heterojunction (Figure 57), demonstrating the materials as connected in series. That is to say, the individual resistance offered by ITO, ZnO and PEDOT:PSS were arranged in series. In the case of increase in PEDOT:PSS thickness, the resistance R offered by the layer increased, because $R = \rho \frac{L}{A}$ ²². Hence, it was deduced that the increase in PEDOT:PSS layer thickness increased the overall R_s of the device. This effect of increase in R_s due to increase in electrode thickness has also been demonstrated on other heterojunction-based and diode-based devices (e.g., solar cells)^{16,23}. It was shown by Baglio et al. (2011)¹⁸, that the R_s of a solar cell increased 1.5 times when its top electrode thickness increased from 10 μm to 14 μm . On another account, Góes et al. (2011)²⁴ reported that with an increase in electrode thickness in solar cells from 50 nm to 120 nm, the R_s of the cell increased by 5 times.

Table 7. Calculated series (R_s) and shunt (R_{sh}) resistances of devices in groups (a) PDOT-2K/A, (b) PDOT-2K/B and PDOT-1K

Group	Device Name	Series Resistance	Shunt Resistance
		R_s (k Ω)	R_{sh} (k Ω)
PDOT-2K/A	PDOT-A1	0.17	1.65
	PDOT-A2	0.10	1.00
	PDOT-A3	0.08	0.50
	PDOT-A4	0.13	0.45
PDOT-2K/B	PDOT-B1	0.07	0.34
	PDOT-B2	0.09	0.33
	PDOT-B3	0.05	0.24
PDOT-1K	PDOT-1K-1	0.42	1.69
	PDOT-1K-2	0.63	2.30
	PDOT-1K-3	0.34	1.51

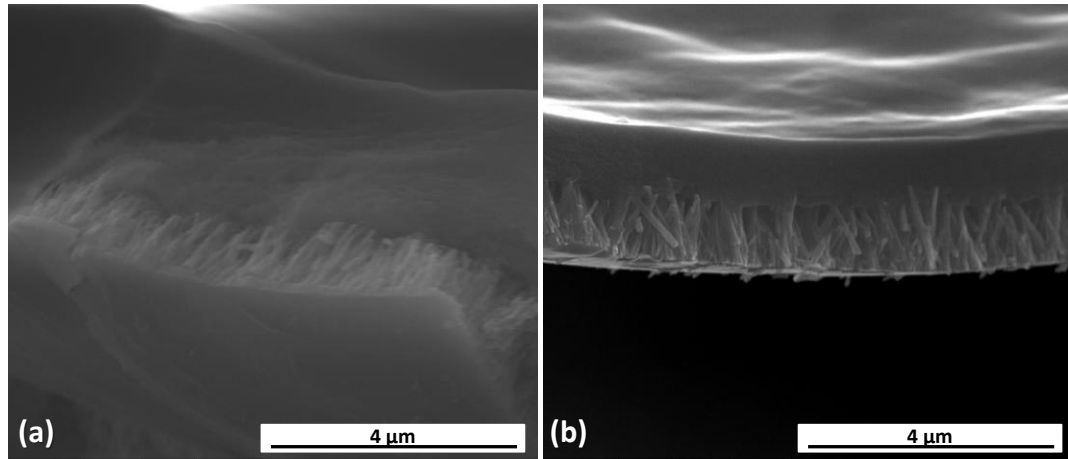


Figure 56. Cross-section images showing PEDOT:PSS layers coated onto ZnO nanorods at (a) 1000 RPM and forming 3 μm thick final layer (b) 2000 RPM and forming 1 μm thick final layer.

In addition to the series resistance (R_s), shunt resistance (R_{sh}) has also been described as an important parameter which affects the performance of heterojunction-based and diode-based devices. The shunt resistance relates to a path which, if decreased in magnitude, allows flow of leakage current, causing loss of electrons ²⁵. In ZnO heterojunction-based and diode-based devices, R_{sh} is widely studied in context to its effect on device performance. In addition, these research works have explained possible sources of lower R_{sh} . Berne`de et al. (2008) ²⁶ reported reduction of R_{sh} due to pinholes-induced short-circuits in ZnO film in a heterojunction-based solar cell.

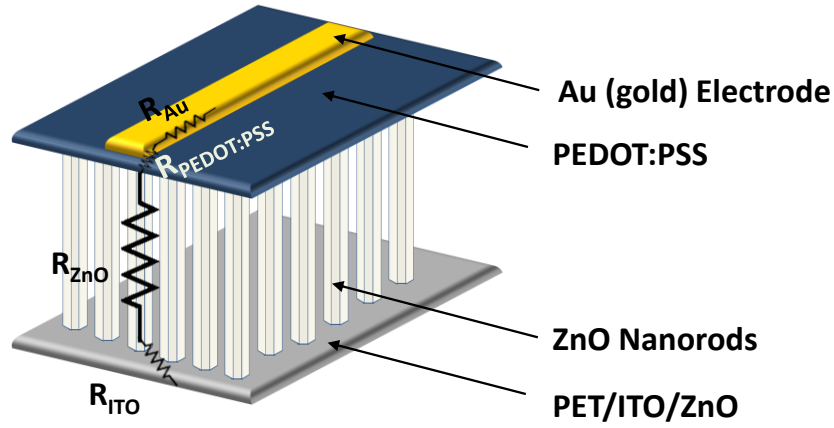


Figure 57. Schematic of ITO/ZnO/PEDOT:PSS/Au heterojunction, showing the series connection among the stacked materials.

The fabricated devices in PDOT-2K/A, PDOT-2K/B, PDOT-1K and PDOT-Shorted devices were analysed for their respective R_{sh} and possible factors affecting R_{sh} were studied in detail. Figure 55(a) shows the J-V characteristic plot of PDOT-Shorted devices. The J-V relationship for these devices was linear. The reason for this linearity was analysed in context to explanation provided by Rockett (2007)²⁷: for diodes with a decrease in shunt resistance, the linearity of reverse bias current-voltage plot increases (Figure 58(b)). In addition, in non-ideal diodes, series resistance²³ causes linearity in the forward bias region (Figure 58(a)). Hence, the overall effect of reduced R_{sh} appears as linear current-voltage relationship and it demonstrates the device to be more resistive than being rectifying (Figure 58).

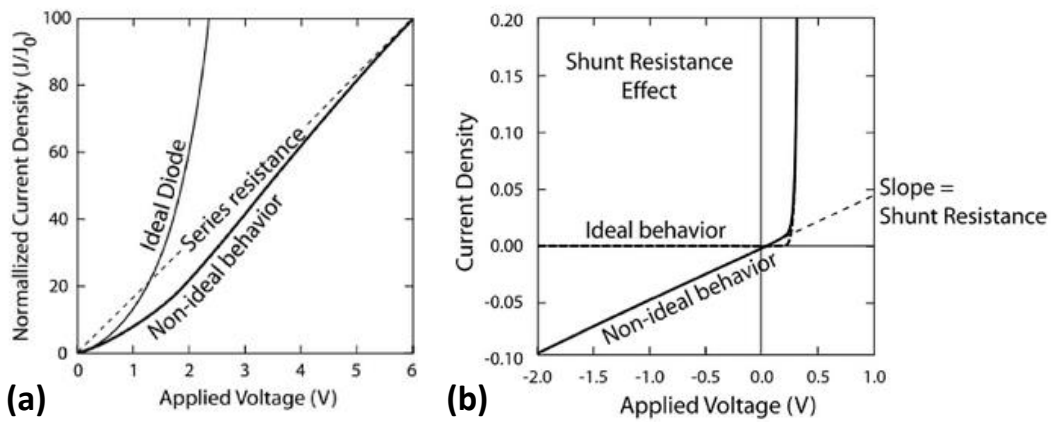


Figure 58. Non-ideal diode characteristic curve having (a) linearity in the forward bias region due to series resistance and (b) linearity in the reverse bias region due to shunt resistance²⁷.

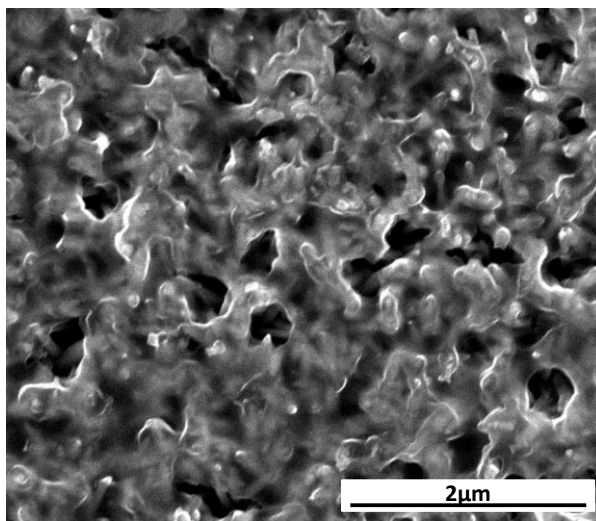


Figure 59. SEM image of PDOT-Sh1 device showing areas of PEDOT:PSS having voids and gaps which caused short-circuits in the device.

In heterojunction-based devices, the main cause of low shunt resistance-induced leakage loss is short-circuiting between top electrode and bottom electrode. The magnitude of leakage current flow through R_{sh} affects the device performance. In the case of PDOT-Shorted devices, the magnitude of leakage current flow was (such as, 8 mA cm^{-2} at -2 V in PDOT-Sh1) sufficiently high to cause the device to be dysfunctional and the J-V characteristic plot to be linear. In PDOT-Shorted devices, it was considered that the heterojunction of ITO/ZnO/PEDOT:PSS/Au(gold) was affected by short-circuits causing contacts between: ITO and PEDOT:PSS, and ITO and gold. Therefore SEM analysis was performed on the PDOT-Shorted devices and there were voids and gaps found in the PEDOT:PSS layer. Non-uniform coverage of PEDOT:PSS layer formed these gaps in the polymer layer and allowed underlying nanorods to be exposed and caused short-circuits in the device (Figure 59). This non-uniformity in polymer layer coverage was caused due to spin-deposition: the centrifugal forces around the edges of the substrate pulled on the PEDOT:PSS outward, and the attractive forces within the PEDOT:PSS pulled on the PEDOT:PSS near the centre of the substrate, where the centrifugal forces were smaller²⁸. This caused thinner layer of PEDOT:PSS near the edges of the substrate; and in some cases, the tips of the nanorods were not fully coated (Figure 61 and Figure 59). The subsequent gold electrode deposition on these non-coated nanorods caused short-

circuited connection between the gold electrode and bottom electrode. Hence in PEDOT-Shorted devices under bias, the short-circuit condition shown in Figure 60(a) caused the current to leak through a low resistance path. As a result, the J-V relationship of the device was linear, indicating that the device was not rectifying and it behaved like a resistor.

On another account, the cause of short-circuiting has been explained to be patches, pin-holes in ZnO nanorod arrays. The patches and pinholes in nanorod arrays are areas where nanorods did not grow either due to non-adhesion of ZnO seed layer or growth-hindering dirt particles settled on the substrate. Therefore, nanorods arrays always contained pinholes and discontinuities which caused the PEDOT:PSS layer to directly contact the bottom ITO electrode, causing a short-circuit. Hence, it was believed that the R_{sh} of PDOT-Shorted devices were also affected by ZnO pin-holes.

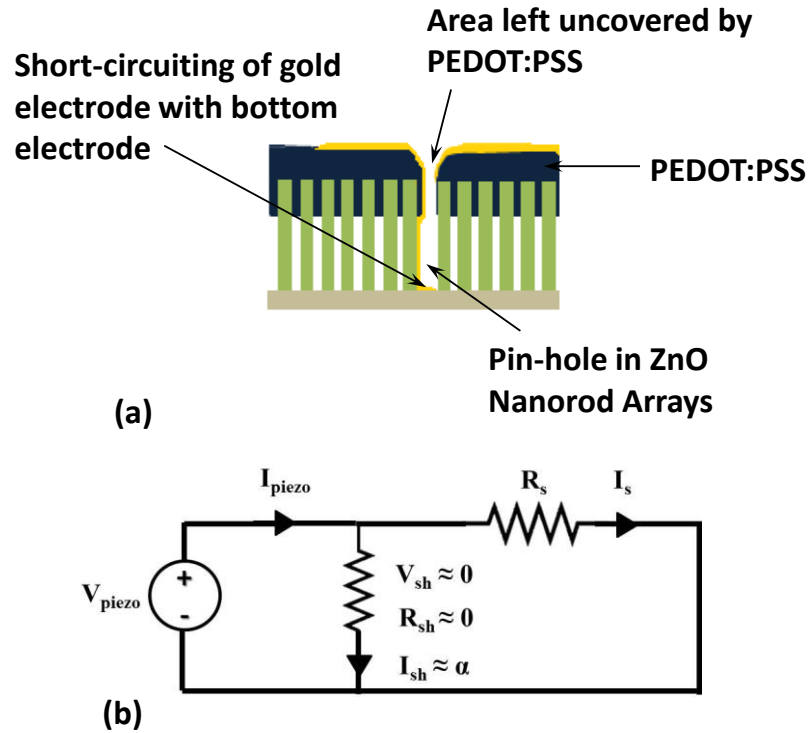


Figure 60. (a) Schematic showing short-circuit condition due to pin-holes, voids or gaps in PEDOT:PSS layer and ZnO nanorod arrays. (b) Resistive circuit model showing short-circuit fault ($R_{sh} \approx 0$) causing output voltage to drop.

For PDOT-2K/B devices, the reverse current density was in the range of 44 – 70 mA cm⁻², which indicated their R_{sh} to be lower when compared to PDOT-2K/A

devices having reverse current density of $5 - 25 \text{ mA cm}^{-2}$. The lowest reverse current density was $1.5 - 3 \text{ mA cm}^{-2}$ as obtained for PDOT-1K devices. By comparing the reverse current densities, it was confirmed that the PDOT-2K/B devices had the lowest R_{sh} of $0.2 - 0.3 \text{ k}\Omega$. The PDOT-2K/A devices had R_{sh} from $0.5 - 1.65 \text{ k}\Omega$ which was higher than PDOT-2K/B, but lower than PDOT-1K with R_{sh} from $1.5 - 1.7 \text{ k}\Omega$. It was indicative that among groups PDOT-2K/A, PDOT-2K/B and PDOT-1K, PDOT-2K/B were devices most affected by short-circuits. The short-circuits had reduced the R_{sh} of PDOT-2K/B devices but, their R_{sh} was not as low as the PDOT-Shorted devices, indicating their lesser short-circuits than PDOT-Shorted. As a consequence of lesser short-circuits the PDOT-2K/B had rectification ratios of 4-5 in their J-V characteristic curves.

In order to investigate the causes of short-circuits in devices, PDOT-2K/A, PDOT-2K/B, PDOT-1K devices were observed under the SEM. It was found that due to spin-deposition, the PDOT-2K/B and PDOT-2K/A devices had PEDOT:PSS layers around the substrate edges to be thinner than the substrate centre. Therefore, it had left the nanorods uncoated in areas near the edges and caused short-circuits when gold electrode was sputtered on them. It was believed that thinner PEDOT:PSS layers around the edges had also reduced the overall R_s of PDOT-2K/B devices to $0.04 - 0.09 \text{ k}\Omega$ when compared with $0.08 - 0.17 \text{ k}\Omega$ for PDOT-2K/A devices. In addition to the non-coated nanorods, another source of short-circuits were the homogenously nucleated microrods in the growth solution of $\text{Zn}(\text{NO}_3)_2$ and HMT²⁹. These microrods were randomly grown in the solution and they were longer than $5 - 6 \mu\text{m}$. They adhered with the non-homogenously nucleated nanorods because of high surface energy. During nanorods synthesis, the substrates were rinsed with DI water to get rid of adhered microrods. However, were not cleaned and the PEDOT:PSS layer, being $1 \mu\text{m}$ thick, did not coat these microrods (Figure 62(b)). Consequently, they caused short-circuits in the device.

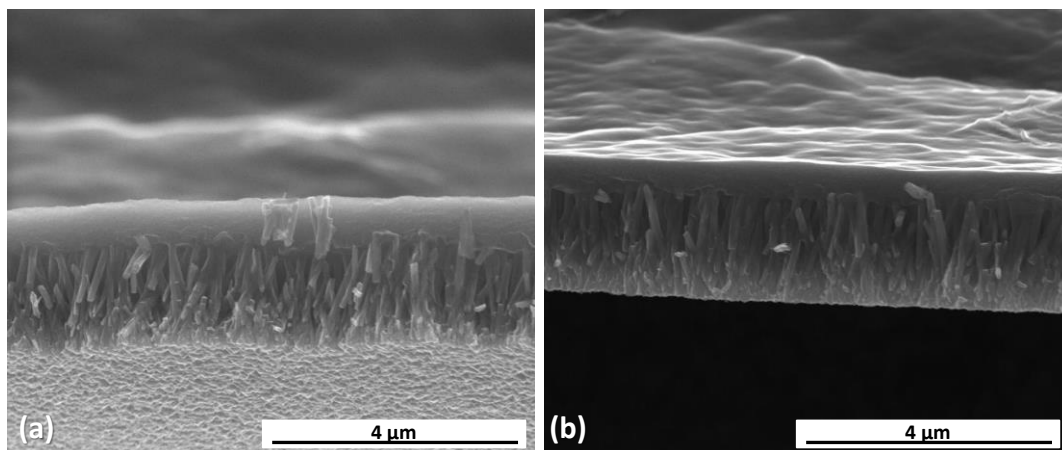


Figure 61. SEM image showing the thickness of PEDOT:PSS near the edges of the substrate to be as low as 300 nm – 500 nm.

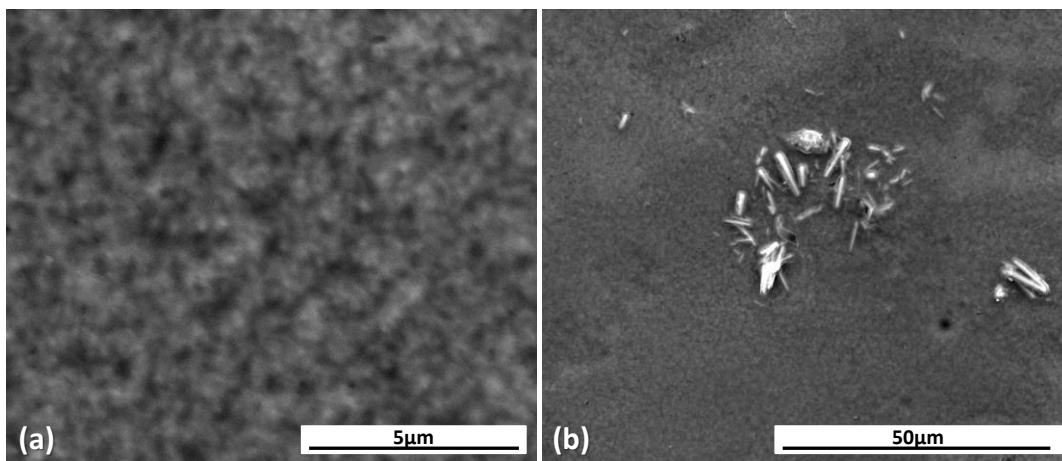


Figure 62. (a) Insufficient PEDOT:PSS layer thickness causing underlying nanorods to be exposed, (b) Homogeneously nucleated ZnO microrods settled on the surface of heterogeneously nucleated nanorods during synthesis. These microrods are 5 – 10 μm long and 2-4 μm wide, due to which they are not fully coated by 1 μm thick PEDOT:PSS layer.

Another source of shorts in the devices was linked with peeling off of PEDOT:PSS during gold deposition. The gold sputter deposition took place under 0.1 mbar vacuum conditions, which often caused patches of ZnO/PEDOT:PSS to crack and peel off and allowed the gold electrode to short-circuit with the bottom ITO electrode (Figure 64). Thus, the electrical parameters such as R_s and R_{sh} of the PEDOT:PSS-based devices were affected by lossy short-circuits. Although the PDOT-2K/A, PDOT-2K/B and PDOT-Shorted devices were fabricated using the same experimental conditions and methodology; but due to sample-to-sample

variations they had different ranges of R_s and R_{sh} and therefore, they were divided into separate groups.

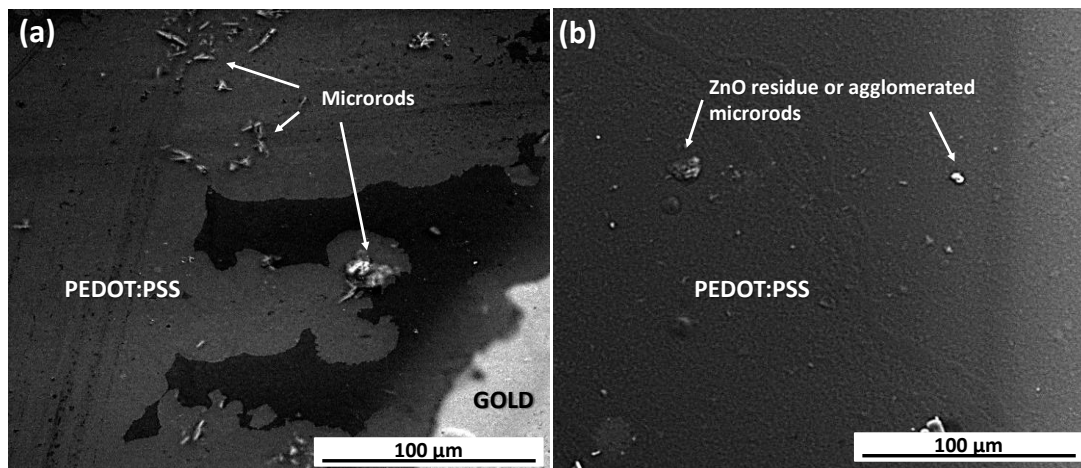


Figure 63. SEM image of PEDOT:PSS coated on nanorods at 2000 RPM and 1000 RPM. (a) PDOT-B3 device having microrods and ZnO residue not coated sufficiently by 1 μm thick PEDOT:PSS coated at 2000 RPM. (b) PDOT-1K device having lesser exposed microrods and ZnO residue than PDOT-B3. This demonstrated that 3 μm PEDOT:PSS coating at 1000 RPM had better coverage of the non-homogenously nucleated matter.

It was considered that due to lesser occurrences of short-circuits caused by better PEDOT:PSS coverage, the PDOT-2K/A devices had higher R_{sh} higher than the PDOT-2K/B devices. Nevertheless, the highest R_{sh} was obtained for PDOT-1K devices, which was in the range of 1.5 – 1.7 kΩ. The PEDOT:PSS coatings in these devices were observed under the SEM and they were found to have higher nanorod-tip coverage than the PDOT-2K/A and PDOT-2K/B devices. The coat thickness was sufficient around the substrate edges, where the centrifugal forces caused by spin-coating were high. It was, therefore, attributed to the 1000 RPM spinning of PEDOT:PSS which ensured a thicker coating on top of the nanorods, causing the PEDOT:PSS gaps and device short-circuits to be lower than the devices coated with PEDOT:PSS at 2000 RPM. Hence, the increased thickness of PEDOT:PSS layer caused the R_{sh} to increase and therefore, the PEDOT:PSS thickness and R_{sh} can be said to be correlated.

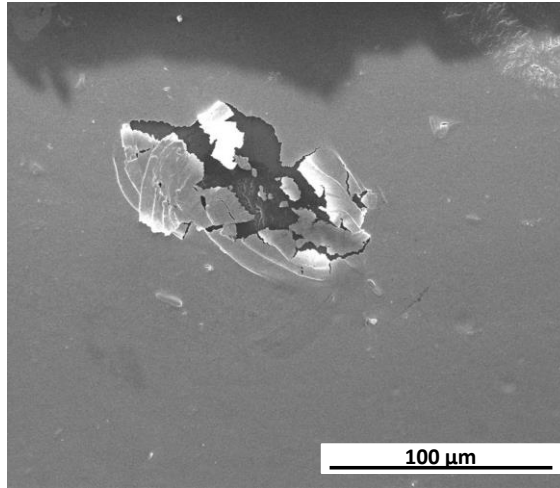


Figure 64. Cracking-off of PEDOT:PSS layer during gold sputtering process in vacuum.

To sum up, when compared with PDOT-2K/A and PDOT-2K/B devices, the PDOT-1K devices with PEDOT:PSS thickness of 3 μm had the highest R_s and R_{sh} of 0.3 – 0.6 $\text{k}\Omega$ and 1.5 – 1.7 $\text{k}\Omega$, respectively. The increased R_s was linked with 3 times thicker PEDOT:PSS layer than in PDOT-2K/A and PDOT-2K/B devices. The PDOT-2K/A devices had the R_s and R_{sh} of 0.08 – 0.17 $\text{k}\Omega$ and 0.5 – 1.65 $\text{k}\Omega$, which was intermediate between PDOT-2K/B and PDOT-1K devices. This was linked with 1 μm thick PEDOT:PSS layer, which had reduced the overall R_s . However in these devices, coating of nanorod-tips near substrate edges was insufficient which reduced the R_{sh} and caused short-circuits. For PDOT-2K/B, the fabrication conditions and methodology were similar to the PDOT-2K/A devices but, due to sample-to-sample variations, these devices had lower R_{sh} from 0.2 – 0.3 $\text{k}\Omega$ caused by higher occurrences of short-circuits. Similarly, the PDOT-Shorted devices were also fabricated using similar methodology as PDOT-2K/A and PDOT-2K/B but, the occurrences of short-circuits in these devices were the highest which caused the highest leakage current flow (8 mA cm^{-2} at -2 V) and linear J-V characteristic plot.

5.3. Analysis of Electrical Output

Evaluation of R_s and R_{sh} of the p-n junction-type devices provided an insight on connection discrepancies in a stacked heterojunction of ITO/ZnO/PEDOT:PSS/Au(gold). Moreover, it provided an understanding of parasitic losses in devices and their possible sources. Further to R_s and R_{sh} analysis,

output characterisation of devices were carried out using: open-circuit voltage measurement (V_{oc}), short-circuit current measurement (I_{sc}), power density calculation (P_L) and impedance analysis in order to investigate the effects of losses on the p-n junction-type device performance parameters. The output performance of devices in groups PDOT-2K/A, PDOT-2K/B and PDOT-1K were measured as shown in Figure 65 and Figure 66. All output measurements were performed when devices were mechanically excited using a 1 Hz rotating cam connected to shaft of a motor. Each device was clamped to a sample holder and its one end was fixed. The cam bent the subject device upward to ~6 mm and released at 50 g acceleration. At this acceleration, each device generated output response which was captured using NI PXI-4461 (24-bit ADC) on the NI PXIe-1062Q chassis. The open-circuit voltage output peaks of the device were directly recorded using NI PXI-4461 (24-bit ADC) on the NI PXIe-1062Q chassis, which was operated through Labview program. Similarly, a Low-Noise Current Preamplifier SR570 was connected with the NI PXI-4461 (24-bit ADC) module and operated by a Labview program to record the short-circuit current density peaks. The terminals of the device were connected in parallel to a resistive decade box, Meatest M602 programmable decade box, which was connected with the PXI-4461 module for data acquisition. A Labview program controlled the resistive sweep of the decade box and also recorded the output of the device across the sweep of load resistance.

For devices in groups PDOT-2K/B, the short-circuit measurement were carried out by capturing voltage signal across 50 Ω and 100 Ω resistors due to unavailability of Low-Noise Current Preamplifier SR570. In case of PDOT-1K devices, due to unavailability of Meatest M602 programmable decade box and Low-Noise Current Preamplifier SR570, the resistive load matching was performed manually using breadboards and ceramic resistors. The wired contacts of device labelled PDOT-A3 device were broken during bend-release measurements for short-circuit current density and resistive load matching, therefore, this device was only used for the analysis of open-circuit voltage.

The impedance analysis of devices was performed from 40 Hz – 110 MHz at oscillator level of 500 mV using Agilent 4294a Precision Impedance Analyzer. Short-circuit and open-circuit compensation was performed prior to all measurements.

5.3.1. Peak Open-Circuit Voltage (V_{oc}) and Peak Short-Circuit Current Density (J_{sc})

The peak open-circuit voltage (V_{oc}) of a device is the voltage generated when a load is not connected across it and hence no current is drawn from the device. In group PDOT-2K/A, the PDOT-A1, PDOT-A2 devices having the highest shunt resistance, generated V_{oc} of 225 mV and 212 mV; which was two times higher than the 98 mV and 90 mV generated by the PDOT-A3 and PDOT-A4 devices (Table 10). The R_{sh} for both PDOT-A3 and PDOT-A4 was 0.5 k Ω , whereas the PDOT-A1 and PDOT-A2 devices had R_{sh} of 1 k Ω and 1.65 k Ω . The effect of R_{sh} on V_{oc} of electronic devices has been studied extensively^{30–32}. Basically, the shunt resistance represents a path through which current flows under an applied electric field, in the absence of stress-induced electric field. Due to its characteristics of leakage resistance, shunt resistance is represented as a parallel resistor in electrical circuits^{30,31}. In Figure 60, the electrical model of ZnO-piezoelectric energy harvester is presented having the shunt resistance R_{sh} in parallel to the piezoelectric voltage source (V_{piezo}). Ideally, a short-circuit fault arises when $R_{sh} \approx 0$, which causes the voltage across R_{sh} to be $V_{sh} \approx 0$. Consequently, infinite (ideally, $I_{sh} \rightarrow \infty$) current flows through the R_{sh} and the potential difference across the device drops^{30,33}. Hence, low shunt resistance causes the potential difference between device terminals to drop; and in case of devices in group PDOT-2K/A, the PDOT-A3 and PDOT-A4 having lower shunt resistance than the PDOT-A1 and PDOT-A2, generated twice as low V_{oc} . Similarly, the PDOT-B1 and PDOT-B2 and PDOT-B3 devices, having R_{sh} of 0.34 k Ω , 0.33 k Ω and 0.23 k Ω , generated V_{oc} of 60 mV, 56 mV and 22 mV, which were 5 – 10 times lower than the PDOT-A1 device with 1.65 k Ω R_{sh} . Hence, the parasitic effect of reduced R_{sh} decreased the V_{oc} of energy harvesters.

Being of dielectric nature, piezoelectric materials are widely analogised with a capacitor or a capacitive voltage source³⁴. As defined by Fischer-Cripps (2012)³⁵, a piezoelectric material provides an electric output due to relative displacement in the negative and positive charges. Thus, charge displacement causes a potential difference to develop across the piezoelectric material which drives a current through a device. Current output of a piezoelectric device, therefore, depends on the magnitude of voltage generated by its piezoelectric source material. However,

studies on electronic devices have shown that current output also depends on the series resistance R_s of devices. It was reported extensively for ZnO nanorod-based solar cells that increased R_s caused the J_{sc} of device to decrease and therefore it reduced the overall efficiency of the system^{36–38}.

Table 8. Peak open-circuit voltage and short-circuit current density of fabricated devices.

Device Name	Peak Open-Circuit Voltage	Peak Short-Circuit Current Density	Remarks
	V_{oc} (mV)	J_{sc} (mA/cm ²)	
PDOT-A1	225	0.800	Measured
PDOT-A2	212	0.715	Measured
PDOT-A3	98	-	Device Broken
PDOT-A4	90	0.600	Measured
PDOT-B1	60	0.830	Calculated across 100 Ω
PDOT-B2	56	0.706	Calculated across 50 Ω
PDOT-B3	22	0.493	Calculated across 100 Ω
PDOT-1K-1	38	0.027	Calculated across 1 k Ω
PDOT-1K-2	36	0.016	Calculated across 1 k Ω
PDOT-1K-3	40	-	Not Performed

In the presented case of fabricated p-n junction devices, PDOT-A1, A2, A3 generated peak current densities (J_{sc}) of 0.8 mA cm⁻², 0.7 mA cm⁻², 0.6 mA cm⁻². However the PDOT-B1 and B2 devices, whose V_{oc} was 4-5 times lower than the PDOT-A1 and A2 devices, produced J_{sc} of 0.8 and 0.7 mA cm⁻²; which was similar in magnitude as that of the PDOT-A1 and A2 devices (Table 10). The device PDOT-B3 generated the lowest J_{sc} of 0.5 mA cm⁻² and device PDOT-A4 was excluded from this discussion because of its disintegration during bend-release measurement for J_{sc} and power density. Unlike their V_{oc} , the J_{sc} of PDOT-2K/A devices was not higher than that of the PDOT-B1 and B2 devices. For understanding the magnitudes of J_{sc} in PDOT-2K/A and PDOT-2K/B devices, here we consider devices' R_s and R_{sh} and their dependence on PEDOT:PSS thickness and coverage. As explained above, the thinner and insufficient PEDOT:PSS coverage near the device edges caused the overall R_s of PDOT-2K/A (R_s : 0.08 – 0.17 k Ω) and PDOT-2K/B devices (R_s : 0.04 – 0.09 k Ω) to reduce. Additionally, the occurrence of short-circuits in PDOT-2K/B devices was higher and their R_s was one order of magnitude lower than the PDOT-2K/A devices. This indicated that PDOT-2K/B devices had more areas of lower PEDOT:PSS coverage which reduced their overall R_s . Hence, it was considered that

the drop of current across R_s of PDOT-2K/B devices was lower than that of the PDOT-2K/A devices. To elaborate, we use the Ohm's law³⁹ according to which, the magnitude of current has been defined to depend on the resistance through which it flows ($I = \frac{V}{R}$)³⁹; therefore, it was considered that the magnitude of current dropped across 0.07 – 0.086 k Ω R_s of PDOT-B1 and B2 was lower when compared to the current dropped across 0.12 – 0.17 k Ω R_s of PDOT-2K/A devices. Therefore, although the PDOT-A1, A2 devices generated 4-5 times higher V_{oc} than the PDOT-B1 and B2 devices but, their voltage-driven current was dropped across R_s which was one order of magnitude higher than that of PDOT-2K/B. Consequently, the measured J_{sc} of PDOT-2K/A devices, unlike their V_{oc} , was not higher than J_{sc} of PDOT-B1 and B2. For PDOT-B1 and B2 devices, the J_{sc} was 0.83 mA cm⁻² and 0.71 mA cm⁻², and for B3 device it was the lowest 0.5 mA cm⁻² because it generated the lowest V_{oc} of 22 mV (Table 10).

In addition to decrease in J_{sc} , further effects of R_s have been studied extensively in ZnO nanorod-based sensing and photovoltaic devices and reportedly^{15,40–42}, an increase in R_s increases the I^2R_s ¹⁵ power losses which decreases power density and V_{oc} . Therefore for the presented work, the effects of R_s were studied in context of V_{oc} in piezoelectric energy harvesters. Table 7 shows that, when in the range of 0.05 – 0.1 k Ω for PDOT-2K/A and B devices, the effect of R_s on device V_{oc} was not pronounced; instead the R_{sh} had prominently affected the device V_{oc} . However, for PDOT-1K devices with R_s in the ranges of 0.4 – 0.6 k Ω , the V_{oc} was measured to be in the range of 30 – 40 mV which was 6 – 10 times lower than the PDOT-A1 device. In addition, their current densities measured across 1 k Ω resistor were also two orders of magnitude lower than the J_{sc} of PDOT-2K/A and PDOT-2K/B devices; which indicated that the overall J_{sc} of PDOT-1K devices was dropped across R_s . Hence, this effect of decrease in V_{oc} and J_{sc} in devices having 6 – 8 times higher R_s can be described as I^2R_s power dissipation (heat loss) across the series resistance. To elaborate, we consider the Kirchoff's Voltage Law⁴³ which states that, in a series resistive circuit the sum of voltage drop across each resistance is equal to the supply voltage⁴³. However, it is known that resistance causes heat dissipation and therefore if R_s is increased then conduction loss (heat dissipation) increase⁴⁴, which causes the current across R_s to decrease, causing the V_{oc} . Thus, it was inferred that V_{oc} and current density of PDOT-1K devices was one and two orders of magnitude lower

than the PDOT-2K/A and PDOT-2K/B devices, which was attributed to their 6 – 8 times higher R_s (Table 8).

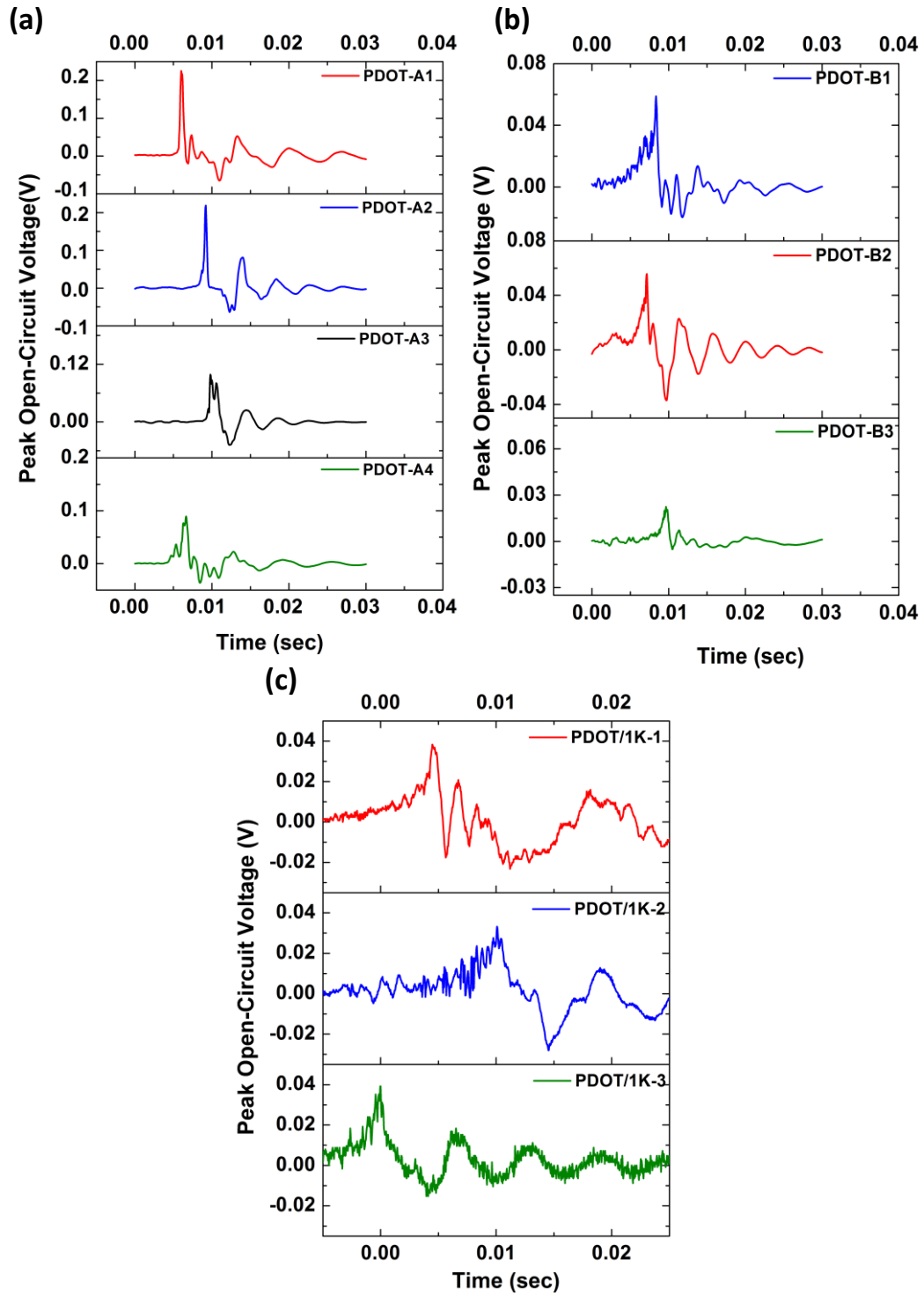


Figure 65. Measured peak open-circuit voltage plots of devices in groups: (a) PDOT-2K/A, (b) PDOT-2K/B and (c) PDOT-1K.

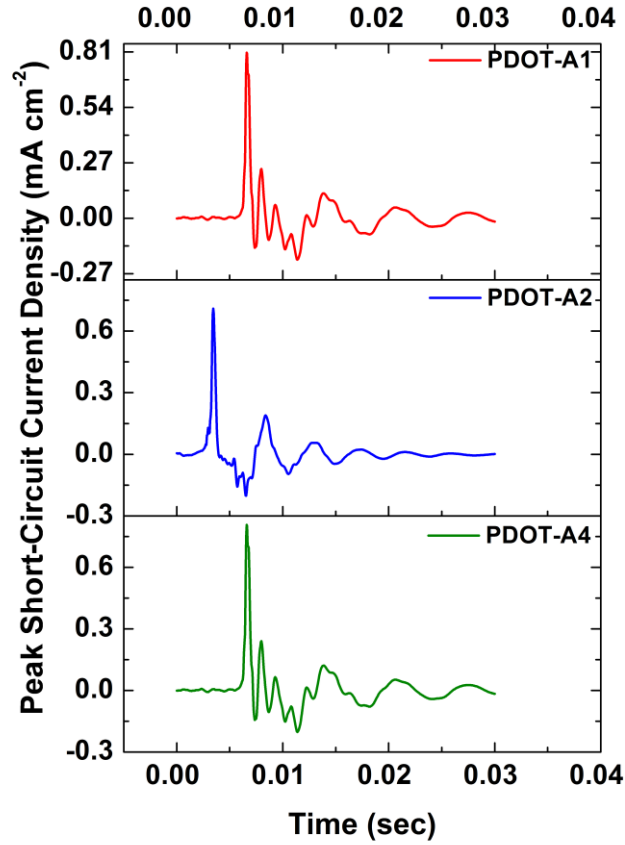


Figure 66. Measured peak short-circuit current plots of devices in groups PDOT-2K/A.

5.3.2. Peak Power Delivered to the Load (P_L) and Electrical Impedance Spectroscopy

Resistive load matching was performed to analyse maximum peak-power densities (P_L) delivered by the p-n junction type devices in PDOT-2K/A, PDOT-2K/B and PDOT-1K to their respective optimum load resistances. For each device, peak-voltage output across a sweep of resistive loads from $50\ \Omega$ to $100\ \text{k}\Omega$ were recorded and power delivered to each load resistance was calculated. The power delivered to a resistive load is defined as a product of voltage and current across it:

$$P = VI \quad \text{Equation 6}$$

According to Ohm's Law,

$$I = \frac{V}{R} \quad \text{Equation 7}$$

Therefore, after substituting Equation 8 in Equation 9, the power delivered to a resistive load becomes:

$$P = \frac{V^2}{R} \quad \text{Equation 10}$$

Table 9. Peak power density, optimum load and resistive impedance of fabricated devices.

Device Name	Peak Power Density	Load Resistance	Real Impedance
	$P_L (\mu\text{W}/\text{cm}^2)$	$R_L (\text{k}\Omega)$	$R_{\text{int}} (\text{k}\Omega)$
PDOT-A1	54 Decade Box	2.019	2
PDOT-A2	41.07 Decade Box	1.387	1.28
PDOT-A3	- Device Broken	- Device Broken	0.857
PDOT-A4	36.01 Decade Box	1.387	0.974
PDOT-B1	16.45 Decade Box	0.827	0.664
PDOT-B2	12.62 Decade Box	0.603	0.6
PDOT-B3	2.4 Decade Box	0.493	- Not Performed
PDOT-1K-1	0.20 - 0.25 Manual	2k Ω < Load < 5k Ω	- Not Performed
PDOT-1K-2	0.22- 0.25 Manual	3k Ω < Load < 6k Ω	- Not Performed
PDOT-1K-3	- Not Performed	- Not Performed	- Not Performed

Hence, for a sweep of resistances, the peak-voltage drop V across each resistor R was used to calculate the peak-power density delivered. Figure 67 demonstrates the resistive load matching plot for all fabricated devices. For devices in group PDOT-1K, the R_s loss induced reduction in V_{oc} and J_{sc} had caused the calculated P_L of 0.20 – 0.25 $\mu\text{W cm}^{-2}$ to be two orders of magnitude lower than the other device groups. Due to high R_s , their optimum load resistance (R_L) was in the range of 2 – 6 k Ω . The calculated P_L for PDOT-A1, A2, A4 devices were 54 $\mu\text{W cm}^{-2}$, 41 $\mu\text{W cm}^{-2}$ and 36 $\mu\text{W cm}^{-2}$ across optimum load resistances of 2.02 k Ω , 1.4 k Ω and 1.4 k Ω ; whereas the calculated P_L for PDOT-B1, B2 and B3 devices were 16.45 $\mu\text{W cm}^{-2}$, 12.62 $\mu\text{W cm}^{-2}$ and 2.4 $\mu\text{W cm}^{-2}$ across optimum load resistances of 0.83 k Ω , 0.6 k Ω and 0.5 k Ω . The reason behind improved P_L for PDOT-2K/A devices when compared to that of PDOT-2K/B devices was attributed to their 5 – 10 times higher V_{oc} , caused by higher R_{sh} . It was also observed for PDOT-2K/A and

PDOT-2K/B that, with the increase in power density (P_L) the optimum load resistance (R_L) of devices was also increased. However, in case of PDOT-1K devices, the optimum load resistance was the highest (2 – 5 k Ω) but the P_L , in the range of 0.20 – 0.25 $\mu\text{W cm}^{-2}$, was the lowest (Table 9). Reportedly, this effect was related to the internal impedance³⁹ of devices and in order to understand it, impedance analysis was performed.

Impedance analysis results were represented as Nyquist plots and devices' internal resistance was obtained from the real-axis diameter of these plots^{2,3,45}. The resistive internal impedance (R_{int}) values of the devices in groups PDOT-2K/A and PDOT-2K/B were observed to be close to the device optimum load resistance (R_L) (Table 10). This satisfied the maximum power transfer theorem³⁹; which states that, the maximum power transfer occurs when the impedance of a connected load is equal to the internal impedance of the source. Therefore, as per the theorem, the R_{int} was associated with the R_L across which maximum power was transferred by the devices. As described above, the increase in P_L was linked with the increase in optimum load resistance of devices. This was caused due to increase in R_{int} of devices. In case of devices with highest P_L (PDOT-2K/A devices), increase in R_{int} and R_L was most preferably caused by the increase in R_{sh} . However in case of PDOT-1K devices, the R_L was increased to the highest value of 2 – 5 k Ω . This was considered to be increased by the increase in R_s , which had increased the R_L , and assumably the R_{int} , as well. Hence, the voltage and current output of these devices were dropped across the R_s losses and consequently the P_L was also decreased.

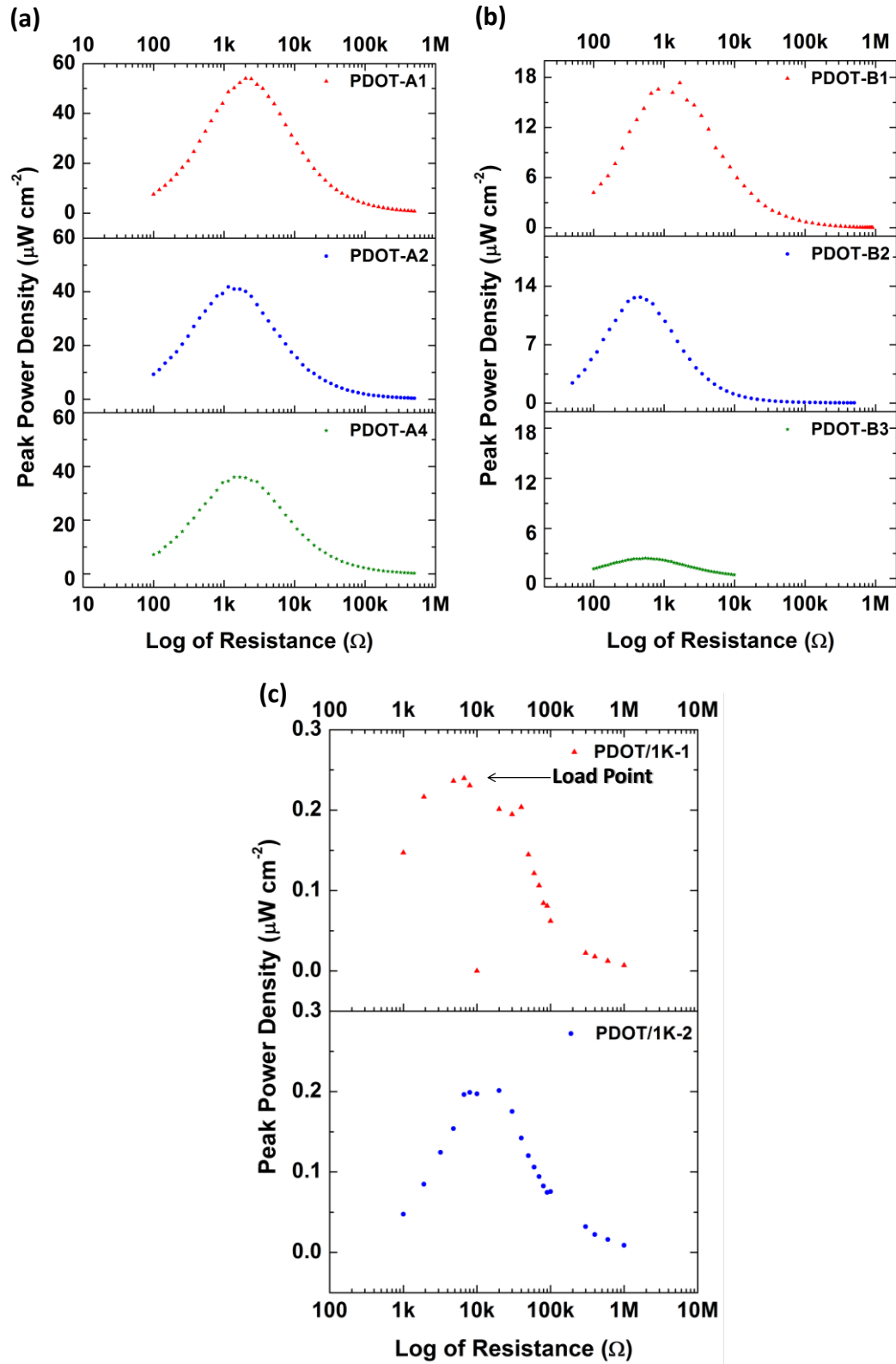


Figure 67. Resistive load matching plots for devices in groups: (a) PDOT-2K/A, (b) PDOT-2K/B and (c) PDOT-1K.

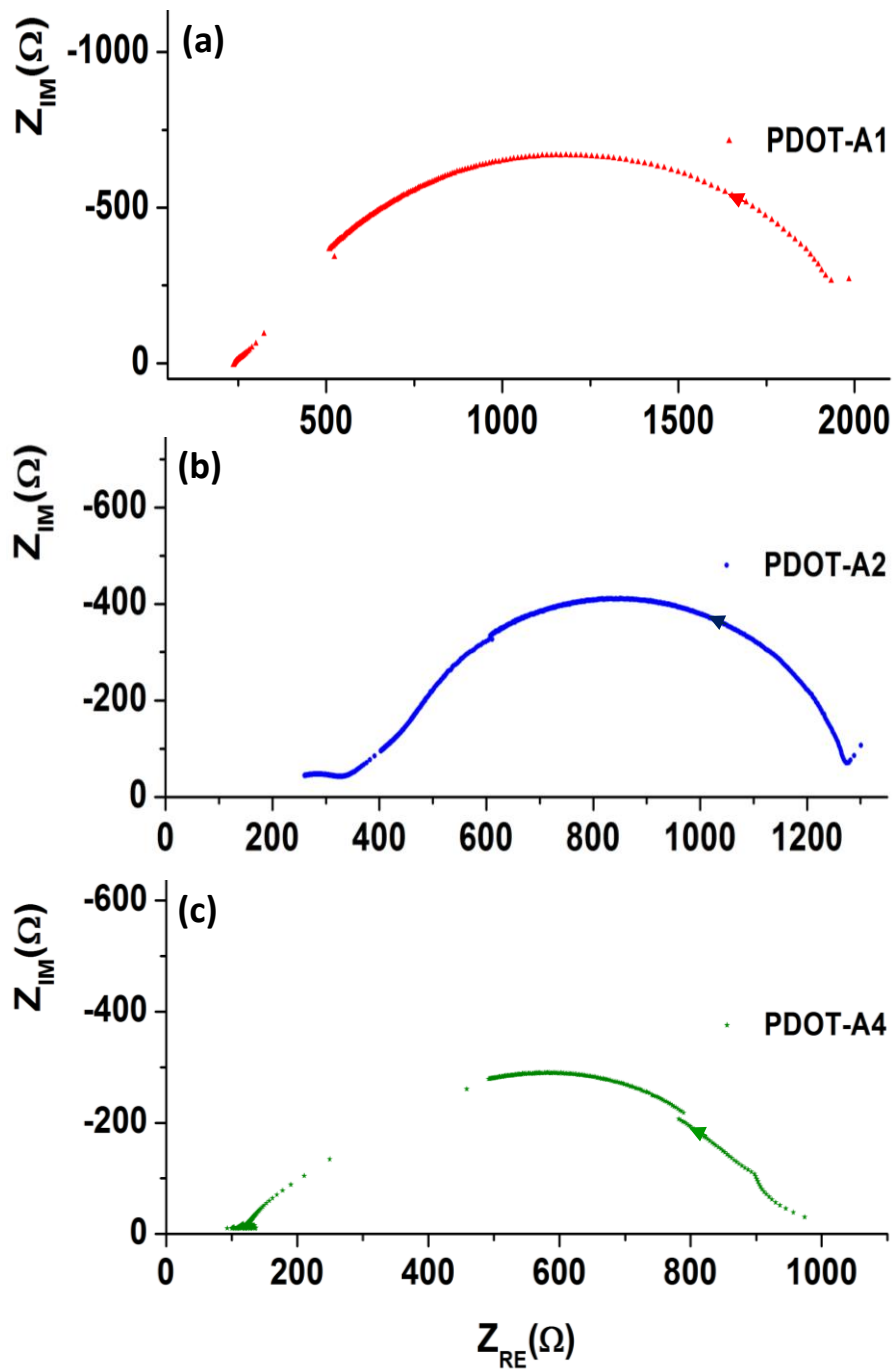


Figure 68. Impedance plots for devices in groups PDOT-2K/A.

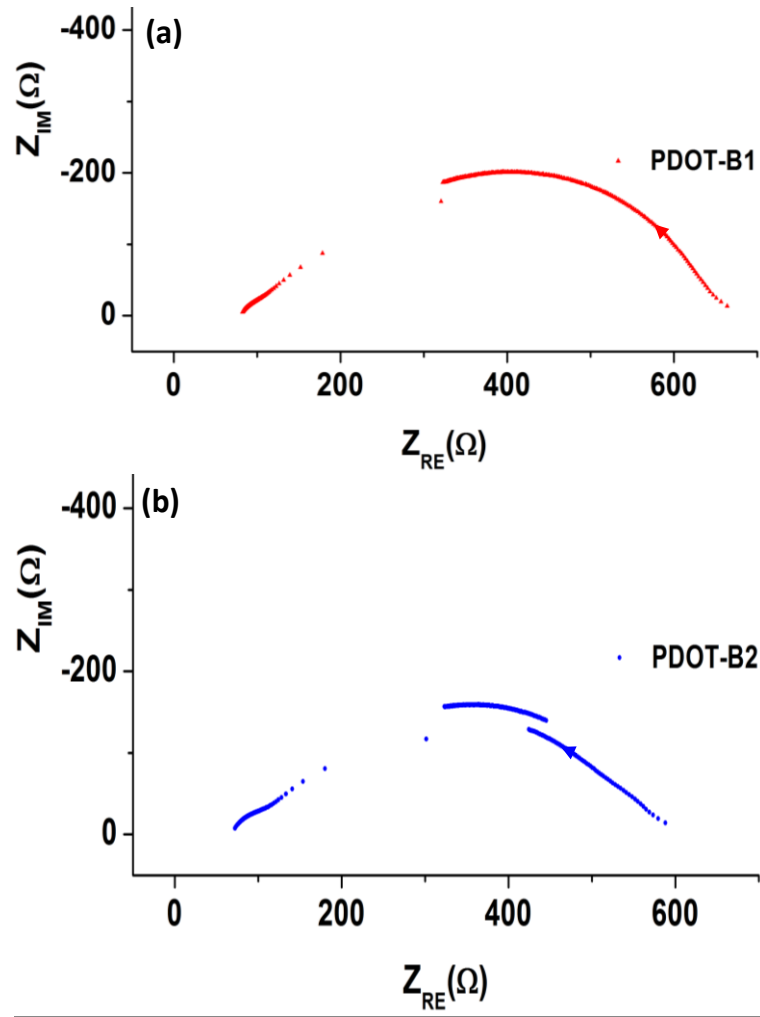


Figure 69. Impedance plots for devices in groups PDOT-2K/B.

5.3.3. Energy Delivered (E_L) to the Load

The resistive load matching of the energy harvester assisted in calculating maximum peak power density across an optimum load resistance. However, the power delivered to the load was dependent on the strain rate, since the maximum peak output voltage can be increased by increasing the strain rate. Therefore, a more reliable way to estimate device performance was to calculate the power delivered to the load over the period of peak voltage cycle. Thus, the output voltage cycle across the optimum load was recorded (Figure 71) and the power delivered to the load was integrated over the period of voltage cycle t_1 to t_2 , to obtain the energy delivered to the load, given by:

$$E = \int_{t_1}^{t_2} \frac{V(t)^2}{R} dt \quad \text{Equation 11}$$

Owing to its highest V_{oc} and J_{sc} output, the energy delivered to the load resistance by the PDOT-A1 devices was 37 nJ cm^{-2} , which was also the highest when compared to all other devices. PDOT-A2 device delivered 22 nJ cm^{-2} whereas, PDOT-B1 and B2 devices delivered 2.47 and 2.5 nJ cm^{-2} . Similar to V_{oc} , J_{sc} and P_L , the energy delivered across load resistance was also affected by the parasitic effects (Table 10).

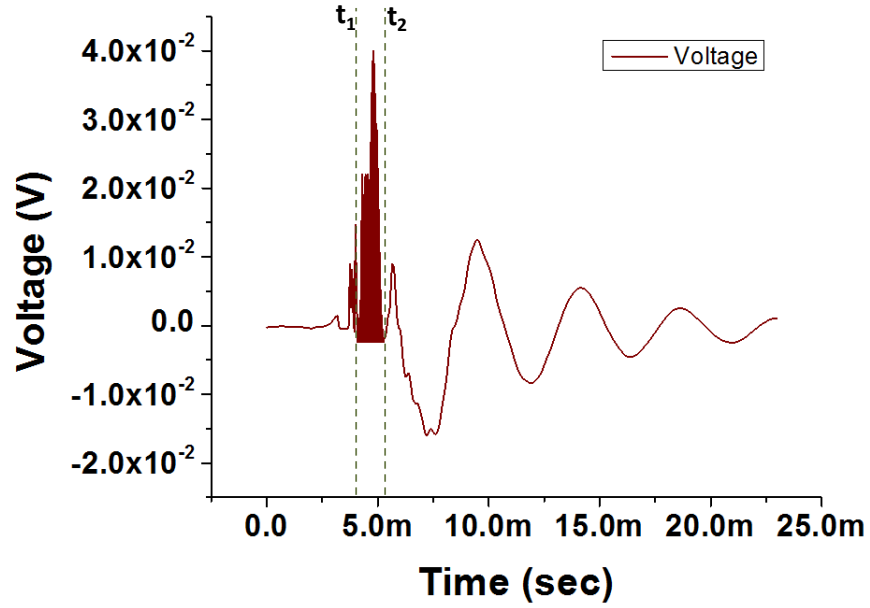


Figure 70. Device PDOT-A4 output voltage cycle measured across its optimum load.

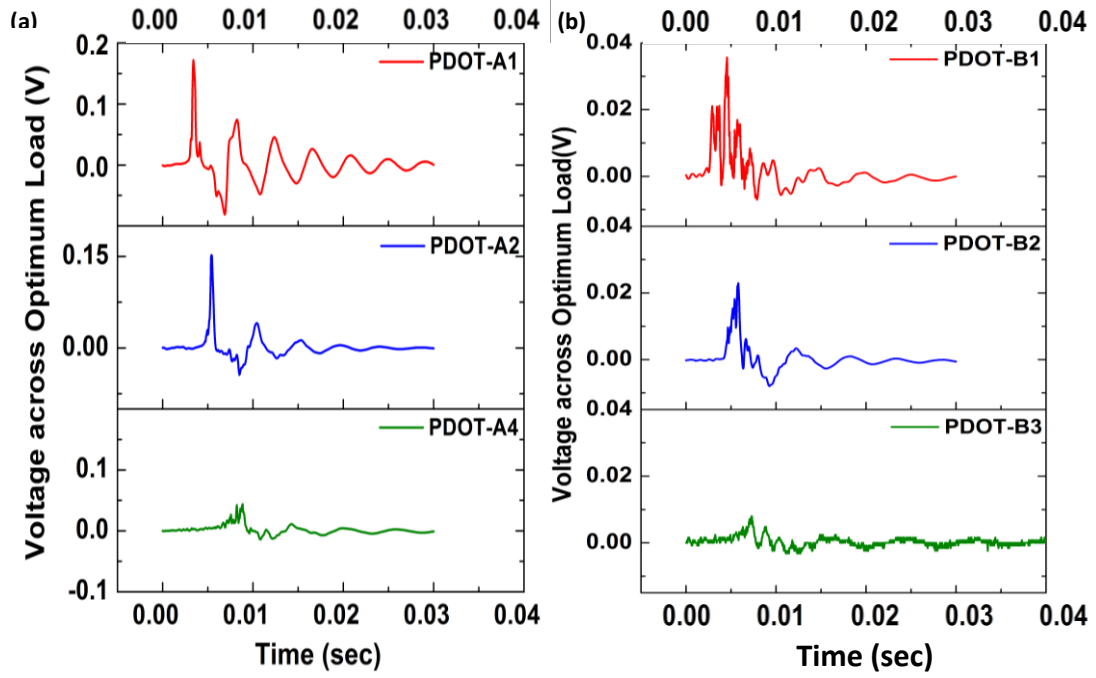


Figure 71. Measured voltage across optimum load (R_L) for devices in groups: (a) PDOT-2K/A, (b) PDOT-2K/B.

5.3.4. Charge Transferred (Q_L) to the Load

The analysis of the charge displaced is useful in estimating the charge delivered to a storage medium (e.g. battery) over a duration of time. In this analysis, the current delivered to the optimum load was integrated over the cycle period t_1 to t_2 , to obtain charge transferred to the load, given by:

$$Q = \int_{t_1}^{t_2} I dt = \int_{t_1}^{t_2} \frac{V}{R} dt \quad \text{Equation 12}$$

Similar as the energy delivered to load, the charge displaced across load resistor was also affected by the device parasitic parameters such as R_s and R_{sh} . Therefore, the highest charge across load resistor was displaced by PDOT-A1 device, which was 247 nC cm^{-2} . In addition, PDOT-A2 and PDOT-A3 devices displaced 236 and $178.85 \text{ nC cm}^{-2}$. The PDOT-B1 and PDOT-B2 devices had about 1.5 – 2 times lower charge displacement results, which were 178.85 and $140.63 \text{ nC cm}^{-2}$ (Table 10).

Analysis of Mechanical and Electrical Performance Parameters

Table 10. Overall performance parameters of all the fabricated devices in groups: PDOT-2K/A and PDOT 2K/B.

Device Name	Peak Open-Circuit Voltage	Peak Short-Circuit Current Density	Peak Power Density	Load Resistance	Energy Density	Charge Displaced	Series Resistance	Shunt Resistance	Real Impedance
	V_{oc} (mV)	J_{sc} (mA/cm ²)	P_L (μW/cm ²)	R_L (kΩ)	E_L (nJ/cm ²)	Q_L (nC/cm ²)	R_s (kΩ)	R_{sh} (kΩ)	R_{int} (kΩ)
		Measured/Calculated	Manual/Decade Box						Performed/Not Performed
PDOT-A1	225	0.800	54	2.019	37	355	0.172	1.650	2.00
REMARKS		Measured	Decade Box						
PDOT-A2	212	0.715	41.07	1.387	22	236	0.100	1.00	1.28
REMARKS		Measured	Decade Box						
PDOT-A3	98	-	-	-	-	-	0.081	0.50	0.857
REMARKS		Device Broken	Device Broken	Device Broken	Device Broken	Device Broken			
PDOT-A4	90	0.600	36.01	1.387	5.19	173.85	0.126	0.45	0.974
REMARKS		Measured	Decade Box						
PDOT-B1	60	0.830	16.45	0.827	2.5	158	0.073	0.34	0.664
REMARKS		Calculated across 100 Ω	Device Broken						
PDOT-B2	56	0.706	12.62	0.603	2.47	140.63	0.086	0.33	0.600
REMARKS		Calculated across 50 Ω	Device Broken						
PDOT-B3	22	0.493	2.4	0.493	0.82	155.15	0.049	0.24	-
REMARKS		Calculated across 100 Ω	Device Broken						Not Performed

Table 11. Overall performance parameters of all the fabricated devices in group PDOT-1K.

Device Name	Peak Open-Circuit Voltage	Peak Short-Circuit Current Density	Peak Power Density	Load Resistance	Energy Density	Charge Displaced	Series Resistance	Shunt Resistance	Real Impedance
	V_{oc} (mV)	J_{sc} (mA/cm ²)	P_L (μW/cm ²)	R_L (kΩ)	EL (nJ/cm ²)	Q_L (nC/cm ²)	R_s (kΩ)	R_{sh} (kΩ)	R_{int} (kΩ)
		Measured/Calculated	Manual/Decade Box						Performed/Not Performed
PDOT-1K-1	38	0.027	0.20 - 0.25	2kΩ < Load < 5kΩ	-	-	0.422	1.69	-
REMARKS		Calculated across 1 kΩ	Manual						Not Performed
PDOT-1K-2	36	0.016	0.22- 0.25	3kΩ < Load < 6kΩ	-	-	0.627	2.30	-
REMARKS		Calculated across 1 kΩ	Manual						Not Performed
PDOT-1K-3	40	-	-	-	-	-	0.341	1.51	-
REMARKS									Not Performed

5.4. Repeatability of Device Output and Long-term Stability

5.4.1. Measurement Repeatability

During bend-release measurement, the devices were subjected to stable and repeatable mechanical stress. The consequent device voltage generation was also repeatable, stable and reliable. The measurements of all devices were performed over a number of mechanical cycles and the output voltage and current peaks were observed for their repeatability. For an instance, the measurement repeatability of V_{oc} of a PEDOT:PSS-based CuSCN-20-1 device is shown in Figure 72. The output was measured over 10 cycles of bend-release test and the device demonstrated stable V_{oc} generation³.

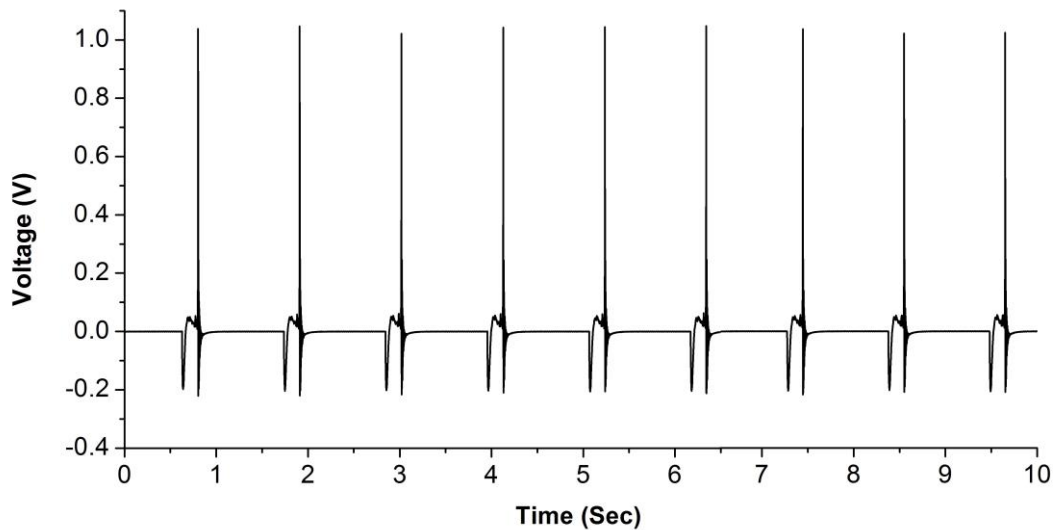


Figure 72. peak open-circuit voltage output of PEDOT:PSS-based device named CuSCN-20-1, recorded for 10 cycles of mechanical excitation³.

5.4.1. Long-term Stability

The long-term performance stability was studied for a PDOT-A4 device. The resistive load matching curves are presented in Figure 73 which demonstrates the variation in device P_L across optimum resistive load (R_L) over a period of 40 days. An initial measurement was carried out after fabrication and the calculated peak power density of $35 \mu\text{Wcm}^{-2}$ was obtained. The device was stored and measured in

the similar way after an interval of 30 days and the observed performance did not vary significantly. However, after another 10 days (total 40 days), the performance of the device degraded and its peak power density reduced from $35 \mu\text{Wcm}^{-2}$ to $20 \mu\text{Wcm}^{-2}$. This was linked to the environmental degradation effects on the PEDOT:PSS top layer and ZnO nanorods. This problem can be resolved by encapsulating the device using flexible polymer layer³.

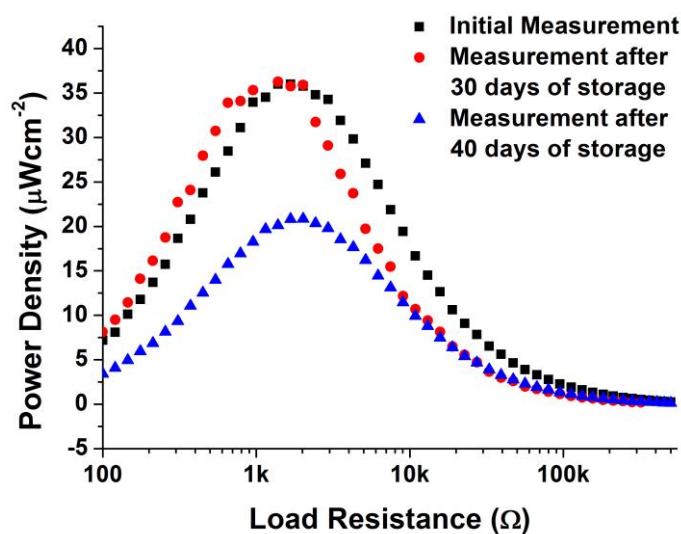


Figure 73. Long-term performance stability test on PDOT-A4 device³.

5.5. Summary

The measurement and characterisation techniques discussed in this chapter were important development steps in the field of ZnO energy harvesters. Previous research on this topic from 2006-2012 was focussed on the device fabrication techniques and optimisation to obtain increase in peak open-circuit voltage output. However, it was necessary to establish a fundamental understanding of the electrical and mechanical properties of these devices, in order to carry out its performance evaluation.

The device bend-release displacement profile provided an insight on its electromechanical behaviour, such as dependency of piezoelectric output on the strain rate. Further to this, the piezoelectric nature of the device output was confirmed by the displacement rate-dependent voltage output. Hence, it was confirmed that the electromechanical piezoelectric device was reliable and stable in output performance.

The electrical analysis provided a detailed insight on the dependence of devices' performance on its R_s and R_{sh} . Four groups of samples, each having devices of a certain range of R_s and R_{sh} were evaluated and analysed for their electrical performance. It was concluded that the most efficient devices in group PDOT-2K/A had R_s and R_{sh} of 0.08 – 0.17 k Ω and 0.5 – 1.65 k Ω , which were higher than the PDOT-2K/B devices but lower than the PDOT-1K devices. The PDOT-2K/B, affected by lower R_{sh} 0.2 – 0.3 k Ω , generated V_{oc} from 22 – 60 mV; whereas, the PDOT-1K devices, affected by their higher R_s 0.3 – 0.6 k, generated V_{oc} of 33 – 40 mV. Due to this, the power densities (P_L) of these devices were significantly dropped. In case of PDOT-2K/A devices, the R_{sh} was sufficiently high to allow less occurrences of short-circuits and R_s losses did not significantly affect the output of devices. Therefore, these devices had the peak power densities across load (P_L) of 36 - 54 $\mu\text{W cm}^{-2}$, which was higher than 2.5 – 16 $\mu\text{W cm}^{-2}$ generated by PDOT-2K/B and 0.2 – 0.25 $\mu\text{W cm}^{-2}$ generated by PDOT-1K.

In previous work on ZnO energy harvesters⁴⁶, the energy harvester peak open-circuit voltage output and peak short-circuit current density were measured and multiplied to calculate the peak power density. However, from the discussion presented in this chapter, it is clear that the power is delivered to a load and

therefore, the calculation using voltage and current density across unloaded energy harvester was not appropriate. Similarly, the analysis of the voltage cycle provided energy density and charge transfer to an optimum load over a time duration. Further to this, the impedance analysis of the device is an essential tool to understand it as an electrical circuit, to examine its electrical behaviour as a parallel RC system and to determine its time constant. In later chapters, the impedance analysis facilitated in expanding the concept on internal screening of polarisation charges in ZnO nanorods.

References

- (1) Anton, S. R.; Sodano, H. A. *Smart Mater. Struct.* **2007**, *16*, R1–R21.
- (2) Briscoe, J.; Jalali, N.; Woolliams, P.; Stewart, M.; Weaver, P. M.; Cain, M.; Dunn, S. *Energy Environ. Sci.* **2013**, *6*, 3035.
- (3) Jalali, N.; Woolliams, P.; Stewart, M.; Weaver, P. M.; Cain, M. G.; Dunn, S.; Briscoe, J. *J. Mater. Chem. A* **2014**, *2*, 10945.
- (4) Phillips, J. R. *CTS Wirel. Components* **2000**, 4800.
- (5) Priya, S.; Inman, D. J. *Energy Harvesting Technologies*; Springer, 2008.
- (6) Briscoe, J.; Stewart, M.; Vopson, M.; Cain, M.; Weaver, P. M.; Dunn, S. *Adv. Energy Mater.* **2012**, *2*, 1261–1268.
- (7) Jalali, N.; Briscoe, J.; Woolliams, P.; Stewart, M.; Weaver, P. M.; Cain, M.; Dunn, S. *J. Phys. Conf. Ser.* **2013**, *476*, 012131.
- (8) Jalali, N.; Briscoe, J.; Tan, Y. Z.; Woolliams, P.; Stewart, M.; Weaver, P. M.; Cain, M. G.; Dunn, S. *J. Sol-Gel Sci. Technol.* **2014**.
- (9) Kim, H.; Lee, J.; Ok, S.; Choe, Y. *Nanoscale Res. Lett.* **2012**, *7*, 5.
- (10) Wang, Y. *J. Phys. Conf. Ser.* **2009**, *152*, 012023.
- (11) Zakirov, A. S.; Yuldashev, S. U.; Lee, J. C.; KANG, T. W.; Cho, H. D. *J. Korean Phys. Soc.* **2011**, *59*, 482–484.
- (12) Neeraj, M. *Applied Physics for Engineers*; PHI Learning Pvt. Ltd.
- (13) KUMAR, B.; JAIN, S. B. *ELECTRONIC DEVICES AND CIRCUITS*; PHI Learning, 2014.
- (14) Cheng, C.-E.; Lin, C.-Y.; Shan, C.-H.; Tsai, S.-Y.; Lin, K.-W.; Chang, C.-S.; Shih-Sen Chien, F. *J. Appl. Phys.* **2013**, *114*, 014503.
- (15) Paulescu, M.; Paulescu, E.; Gravila, P.; Badescu, V. *Weather Modeling and Forecasting of PV Systems Operation*; Green Energy and Technology; Springer, 2012.
- (16) Brabec, C.; Scherf, U.; Dyakonov, V. *Organic Photovoltaics: Materials, Device Physics, and Manufacturing Technologies*; Wiley, 2011.
- (17) Kim, J.-H.; Lee, K.-J.; Roh, J.-H.; Song, S.-W.; Park, J.-H.; Yer, I.-H.; Moon, B.-M. *Nanoscale Res. Lett.* **2012**, *7*, 11.

- (18) V. Baglio, M. Girolamo, V. Antonucci, A. S. A. *Int. J. Electrochem. Sci.* **2011**, 6, 3375.
- (19) Beeby, S.; White, N. *Energy Harvesting for Autonomous Systems*; Artech House, Incorporated, 2010.
- (20) Law, M.; Greene, L. E.; Johnson, J. C.; Saykally, R.; Yang, P. *Nat. Mater.* **2005**, 4, 455–459.
- (21) Chavez, M. A. R.; Eng, T. U. of T. at E. P. E. *Fabrication and Analysis of Patterned and Planar Cadmium Telluride-based Solar Cells*; University of Texas at El Paso, 2008.
- (22) Viridi, S. *Construction Science and Materials*; Wiley, 2012.
- (23) C. Kamalakannan, L. P. S. S. S. D. B. K. P. *Power Electronics and Renewable Energy Systems*; Springer India, New Delhi.
- (24) Góes, M. S.; Joanni, E.; Muniz, E. C.; Savu, R.; Habeck, T. R.; Bueno, P. R.; Fabregat-Santiago, F. *J. Phys. Chem. C* **2012**, 116, 12415–12421.
- (25) Steim, R. *The Impact of Interfaces on the Performance of Organic Photovoltaic Cells*; KIT Scientific Publ., 2010.
- (26) Bernède, J. C.; Cattin, L.; Morsli, M.; Berredjem, Y. *Sol. Energy Mater. Sol. Cells* **2008**, 92, 1508–1515.
- (27) Rockett, A. *The Materials Science of Semiconductors*; Springer ebook collection / Chemistry and Materials Science 2005-2008; Springer, 2007.
- (28) Levinson, H. J. *Principles of Lithography*; Press Monographs; SPIE Press, 2005.
- (29) Ridhuan, N. S.; Razak, K. A.; Lockman, Z.; Abdul Aziz, A. *PLoS One* **2012**, 7, e50405.
- (30) Solanki. *Solar Photovoltaics: Fundamentals Technologies And Applications*; PHI Learning Pvt. Ltd., 2009; p. 478.
- (31) Kyaw, H. H.; Bora, T.; Dutta, J. *IEEE Trans. Nanotechnol.* **2012**, 11, 763–768.
- (32) Prakash, G.; Garg, H. P. *Solar Energy: Fundamentals and Applications*; Tata McGraw-Hill Publishing Company, 2000.
- (33) Mehta, V. K.; Mehta, R. *Principle Of Elect.Engg. & Electronics (M.E.)*; S. Chand Limited, 2006.
- (34) Smallman, R. E.; Ngan, A. H. W. *Physical Metallurgy and Advanced Materials*; Elsevier Science, 2011.

- (35) Fischer-Cripps, T. *Newnes Interfacing Companion: Computers, Transducers, Instrumentation and Signal Processing*; Elsevier Science, 2002.
- (36) Pietruszka, R.; Witkowski, B. S.; Luka, G.; Wachnicki, L.; Gieraltowska, S.; Kopalko, K.; Zielony, E.; Bieganski, P.; Placzek-Popko, E.; Godlewski, M. *Beilstein J. Nanotechnol.* **2014**, 5, 173–179.
- (37) Lai, M.-H.; Tubtimtae, A.; Lee, M.-W.; Wang, G.-J. *Int. J. Photoenergy* **2010**, 2010.
- (38) Bora, T.; Kyaw, H. H.; Sarkar, S.; Pal, S. K.; Dutta, J. *Beilstein J. Nanotechnol.* **2011**, 2, 681–690.
- (39) Meade, R. L. *Foundations of Electronics*; Delmar Cengage Learning, 2002.
- (40) Liao, H.-C.; Lin, C.-C.; Chen, Y.-W.; Liu, T.-C.; Chen, S.-Y. *J. Mater. Chem.* **2010**, 20, 5429.
- (41) Luan, C.; Vaneski, A.; Susha, A. S.; Xu, X.; Wang, H.-E.; Chen, X.; Xu, J.; Zhang, W.; Lee, C.-S.; Rogach, A. L.; Zapien, J. A. *Nanoscale Res. Lett.* **2011**, 6, 340.
- (42) Agrawal, B.; Tiwari, G. N. *Building Integrated Photovoltaic Thermal Systems: For Sustainable Developments*; RSC energy series; Royal Society of Chemistry, 2010.
- (43) Waygood, A. *An Introduction to Electrical Science*; Taylor & Francis, 2013.
- (44) Golio, M. *The RF and Microwave Handbook*; Electrical Engineering Handbook; CRC Press, 2010.
- (45) Lvovich, V. F. In *Impedance Spectroscopy*; John Wiley & Sons, Inc., 2012; pp. 319–331.
- (46) Hu, Y.; Lin, L.; Zhang, Y.; Wang, Z. L. *Adv. Mater.* **2012**, 24, 110–114.

6. Effects of Electrode Materials on Device Performance

The simplest assembly of a piezoelectric energy harvester comprises of the piezoelectric material, whether thin film, bulk or nanostructured, sandwiched between two electrodes. The electrodes connected to the base and tips of ZnO nanorods are commonly termed as “bottom electrode” and “top electrode”, respectively. They serve as the terminals across which potential difference is created. Prototypes of energy harvesters were made by varying the top and bottom electrodes and their performances were evaluated and analyses was performed based on their differences in mechanical to electrical energy conversion.

The device electrodes play an important role in affecting the piezoelectric polarisation, this phenomenon has been commonly explained as external screening effect ¹. In previous chapter, devices were studied which had their performance affected by the presence of ITO bottom electrode. In this chapter, two more bottom electrodes comprising of silver (Ag) and zinc were chosen and incorporated into devices. The performance of all device types was evaluated and through appropriate comparison, the screening effect of electrode on device performance was studied.

The top electrode materials most commonly used since 2011 ² were insulators called *poly(methyl methacrylate)* PMMA and *poly(dimethylsiloxane)* PDMS ³. PEDOT:PSS was the p-type polymer which was first used in 2012 ¹ as a semiconducting top electrode for ZnO-based piezoelectric energy harvester. Research on PMMA-based and PEDOT:PSS-based devices had established that external screening effects are minimum in both types of electrodes.

However, a suitable analysis was necessary to understand the fundamental differences between electrodes with different conductivities. Therefore, in order to bridge this gap, this report compares the electromechanical performance of PEDOT:PSS-based devices with the electromechanical response of PMMA-based

devices. In this way, an interesting analysis was performed on the effects of top electrode external screening on the performance parameters of ZnO-based piezoelectric energy harvesters. It was observed that, the energy delivered to an external load is not only affected by screening losses but also by the internal impedance of the energy harvester.

6.1. Effects of Bottom Electrode Materials

In Chapter 5, ITO-based bottom electrode devices PDOT-2K/A and PDOT-2K/B were observed to have R_s in the range of 0.05-0.2 k Ω (Table 7). The motivation was to further reduce the R_s , so that the I^2R_s losses of the devices reduce. Therefore, metal electrodes were chosen because of their lower sheet resistivity than ITO. In addition to reduction in R_s , our aim was to obtain an Ohmic contact (Figure 74(b)) between the bottom electrode and ZnO; because, the Ohmic contact was considered to be least resistance path for electron conduction ⁴ which would reduce device losses. To accomplish this, the electrode material work function (ϕ_M) was either required to be lower than or equal to ZnO. In the presented case, electrode materials with work function closest to ZnO (4.2 eV) were chosen: silver (Ag) of 4.26 ⁵ and Zn metal foil of 4.3 ⁶ eV. These materials were assumed to mitigate energy barrier at ZnO/electrode interface, which would otherwise be formed if ZnO contacted a metal with higher work function (Schottky Contact) (Figure 74(a)).

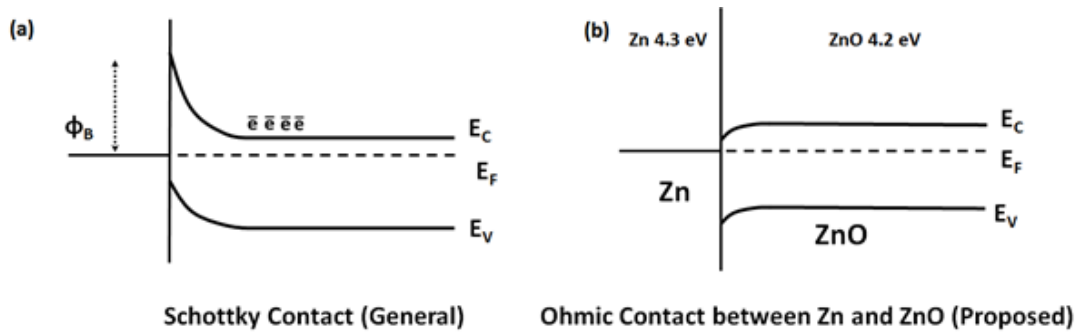


Figure 74. (a) Schottky contact between n-type semiconductor and metal when work function of metal (ϕ_M) is higher than work function of semiconductor (ϕ_s). (b) Proposed Ohmic contact between Zn metal and ZnO, when Zn of marginally higher ϕ_M of 4.3 eV ϕ_M is contacted with ZnO having 4.2 eV ϕ_M .

Schottky contact based energy harvesters were previously described to cause high external screening^{1,7}. In Schottky contacts, ZnO is commonly interfaced with metal such as Pt and Au, which have higher work function than ZnO. This causes Schottky barrier formation, because Fermi energies must become the same when two materials of dissimilar free energies are contacted^{8,9} (Figure 74(a)). Let us take an example of a device with Au bottom electrode forming a Schottky contact with ZnO. It was considered that, when ZnO is polarised, the depleted region in the Schottky barrier allows electrons from Au to accumulate at the ZnO/Au interface and eventually tunnel through the barrier. These accumulated and mobile charges from the external contacts cause screening of the polarisation charges in ZnO¹. Thus, an Ohmic contact between ZnO and bottom electrode was considered for study in terms of series losses as well as screening losses.

In the presented chapter, the bottom electrodes Ag and ZnO were compared with ITO which has a work function of 4.6 eV. The device group with Ag electrode were called PDOT-Ag and the same with Zn metal were called PDOT-Zn.

Table 12. Calculated series (R_s) and shunt (R_{sh}) resistances of devices in groups (a) PDOT-2K/A, (b) PDOT-2K/B and PDOT-1K

Group	Device Name	Series Resistance	Shunt Resistance
		$k\Omega$	$k\Omega$
PDOT-2K/A	PDOT-A1	0.17	1.65
	PDOT-A2	0.10	1.00
	PDOT-A3	0.08	0.50
	PDOT-A4	0.13	0.45
PDOT-2K/B	PDOT-B1	0.07	0.34
	PDOT-B2	0.09	0.33
	PDOT-B3	0.05	0.24

6.1.1. Overview of Device types based on Bottom Electrode Materials

Three types of bottom electrodes were analysed in terms of their performance in ZnO-based energy harvesters. All devices had common top electrode which was fabricated with PEDOT:PSS. PDOT-2K/A, PDOT-Sm were devices based on ITO bottom electrode, whereas, PDOT-Ag and PDOT-Zn were based on Ag (silver) and Zn bottom electrodes. To study the effects of varying bottom electrode materials, all devices were fabricated using similar methods and conditions. The fabrication methods of these devices were discussed in detail in the experimental and methodology chapter (Chapter 3) and is additionally summarised in Table 13.

Table 13. Group names and electrode fabrication method (from Chapter 3) for the ITO, zinc and silver based device used for the analysis of bottom electrode screening effects.

Group Names	Top Electrode Fabrication	Bottom Electrode & Nanorod Fabrication	Devices
PDOT-Sm	PEDOT:PSS @ 2000 rpm	ITO Sp*(50)	PDOT-Sm1, PDOT-Sm-2
PDOT-Ag	PEDOT:PSS @ 2000 rpm	Ag NP(50)	PDOT-Ag-1, PDOT-Ag-2, PDOT-Ag-3
PDOT-Zn	PEDOT:PSS @ 2000 rpm	Zn NP(50)	PDOT-Zn-1, PDOT-Zn-2, PDOT-Zn-3

6.1.1.1. ITO-based Devices

These devices were based on ZnO nanorods grown on ITO bottom electrode. The nanorods were 1 μm long and 40 nm wide (ITO Sp*(50)) as shown in Figure 75. Figure 76 shows the JV characteristic curve of the PDOT-Sm devices from -2 V to +2 V, which was non-linear due to its forward current increasing exponentially with the operating voltage ¹⁰. The current rectification ratio (defined as the ratio between forward current and reverse current) was 5 and 2 for PDOT-Sm-1 and Sm-2 respectively at ± 2 V ¹¹. The diode turn-on voltages were found to be 0.6 V and 0.8 V for PDOT-Sm-1 and Sm-2. Thus, the rectifying non-linear J-V characteristic curve indicated a p-n junction between n-type ZnO nanorods and p-type PEDOT:PSS ¹¹.

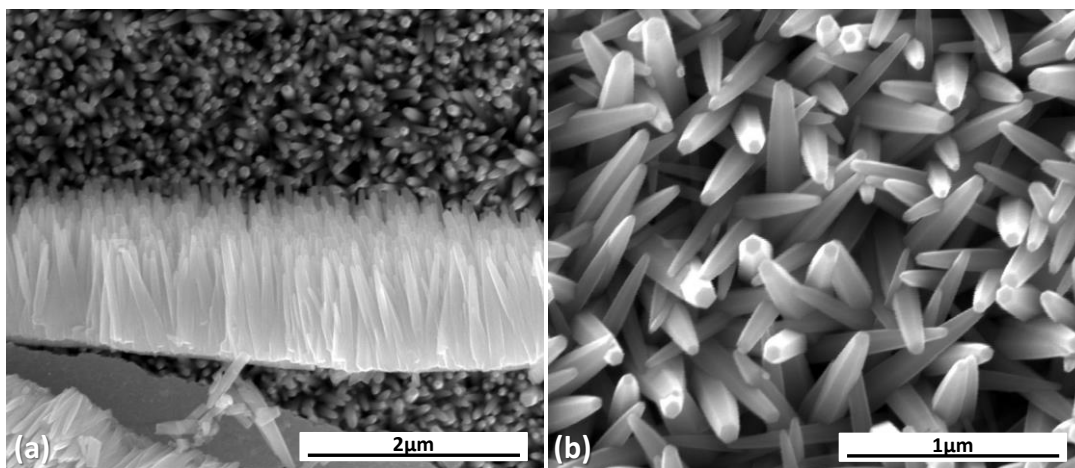


Figure 75. SEM images of nanorods grown on ITO: (a) Cross-section view, (b) top view.

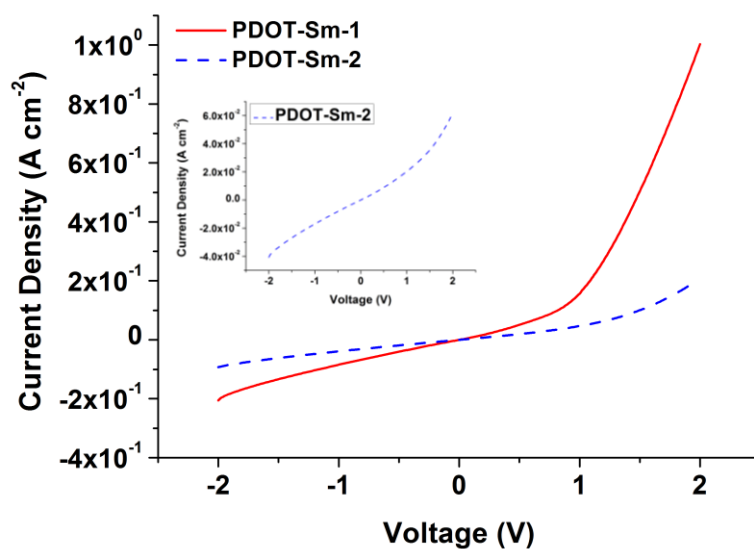


Figure 76. J-V characteristic curve of PDOT-Sm devices. Inset: JV curve of PDOT-Sm-2, for clarity.

A corner on the edge of the PDOT-Sm-2 device substrate was flicked with finger and its voltage response (inset of Figure 77) to mechanical vibration was recorded using an oscilloscope. Thereafter, both PDOT-Sm1 and PDOT-Sm2 were mechanically excited using a 1 Hz rotating cam connected to shaft of a motor. Each device was clamped to a sample holder and its one end was fixed. The cam bent the subject device upward to ~6 mm and released at 50 g acceleration. At this acceleration, each device generated output response which was captured using NI PXI-4461 (24-bit

ADC) on the NI PXIe-1062Q chassis. The open-circuit voltage output peaks of the device were directly recorded using NI PXI-4461 (24-bit ADC) on the NI PXIe-1062Q chassis, which was operated through Labview program.

Peak open-circuit voltage output (V_{oc}) obtained for PDOT-Sm-1 and Sm-2 were 65 V and 60 mV respectively. When compared with PDOT-2K/A devices, which generated 90 – 225 mV (Table 14), the PDOT-Sm devices generated lower voltages in the range of 50 – 65 mV. It was because these devices were fabricated with 1 μm long and 40 nm wide nanorods and that the PDOT-2K/A devices were fabricated with 2 μm long and 70 nm wide nanorods. For longer piezoelectric nanorods, as in case of PDOT-2K/A, bending radius of the nanorods was greater than PDOT-Sm devices. Hence, it was considered that their bending displacement for given strain was higher. Since, the piezoelectric response depends on the displacement of source material, therefore the higher bending displacement in PDOT-2K/A devices' nanorods increased their voltage output.

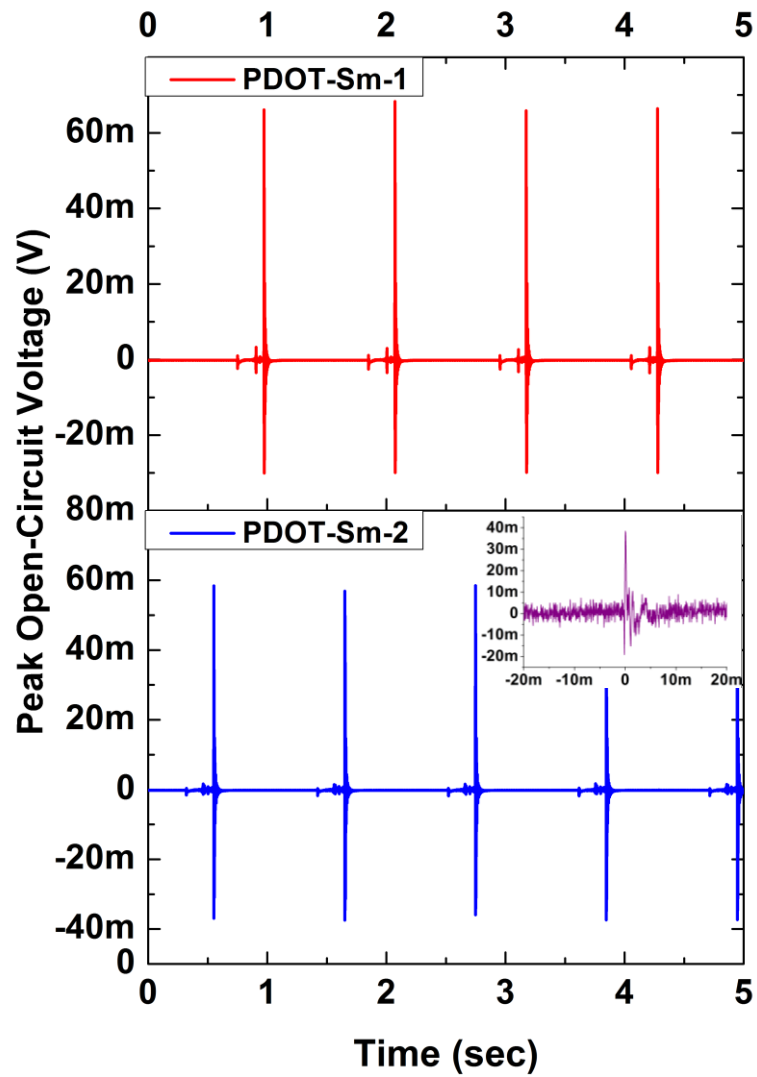


Figure 77. Open-Circuit voltage output of PDOT-Sm devices.

Table 14. Comparison between PDOT-2K/A and PDOT-Sm devices.

Device Name	Peak Open-Circuit Voltage V_{oc} (mV)
PDOT-Sm-1	65
PDOT-Sm-2	60
PDOT-A1	225
PDOT-A2	212
PDOT-A3	98
PDOT-A4	90

6.1.1.2. Ag-based Devices

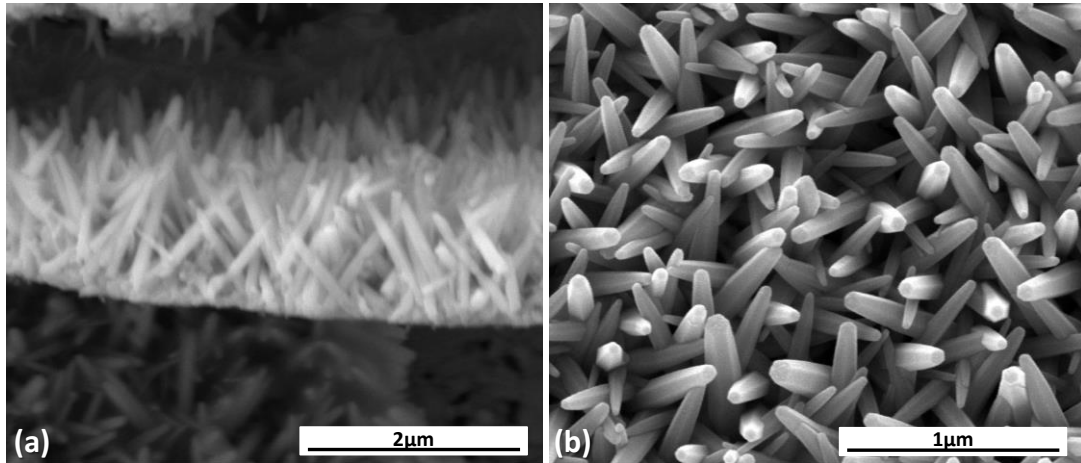


Figure 78. SEM images of nanorods grown on Ag electrode: (a) Cross-section view, (b) top view.

For the PDOT-Ag devices, the nanorods were grown on Ag-coated kapton substrates. They were 1 μm and 66 nm wide as shown in Figure 78. These devices had a problem of adhesion between ZnO nanorods and Ag (Silver). Therefore, when PEDOT:PSS was coated on the tip of the rods and dried at 100 $^{\circ}\text{C}$ then for most of the samples, the ZnO nanorods delaminated from the Ag substrate. This was due to weaker bonding between Ag and ZnO seed layer. Resultantly, when PEDOT:PSS expanded upon drying then the surface-induced stress caused the nanorods to delaminate from their roots (Figure 79). Some of the devices which were successfully coated with PEDOT:PSS encountered further problems during gold sputter coating. At low sputtering pressure (0.1 mbar), patches of ZnO/PEDOT:PSS peeled off and the devices had short-circuit paths between Au (gold) and Ag (silver). As explained by Mittal (2005)¹², adhesion between two surfaces results from mechanical, chemical and electrostatic contributions. For two materials to bond, their surface micro-roughness plays an essential role in their mechanical interlocking. In addition, it also depends on the chemical interaction between materials; for instance, Chromium forms metal-organo compounds with polyimide and immediately bonds with it upon deposition¹². For the presented case of ZnO seed layer and silver (Ag), it was established that the surface smoothness of silver (Ag) was not suitable to allow its adhesion with ZnO seed layer. Hence, the ZnO seed layer delamination occurred frequently during fabrication procedures.

Therefore, the JV characteristic curve of the PDOT-Ag devices showed an Ohmic response, and the forward current to reverse current ratio was ≈ 1 .

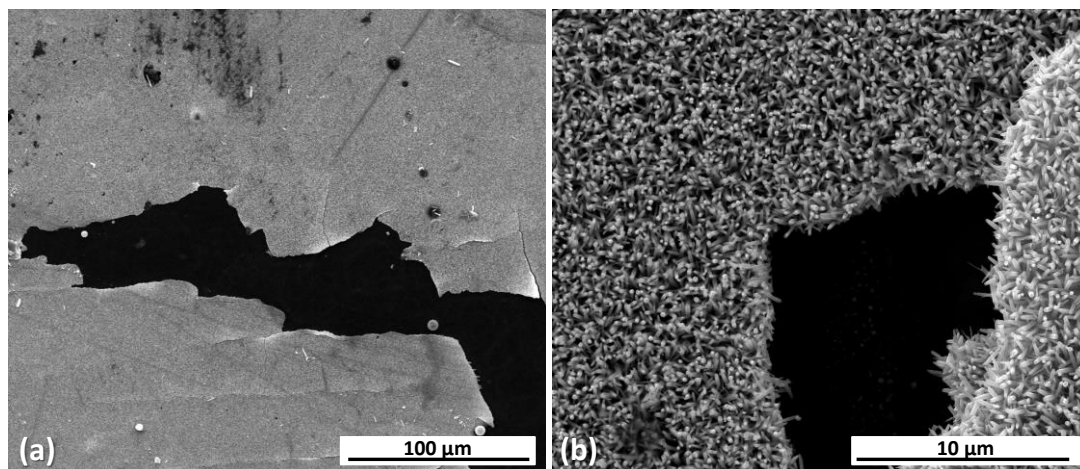


Figure 79. Delamination of ZnO nanorods from Ag electrode due to insufficient adhesion between electrode and ZnO seed layer.

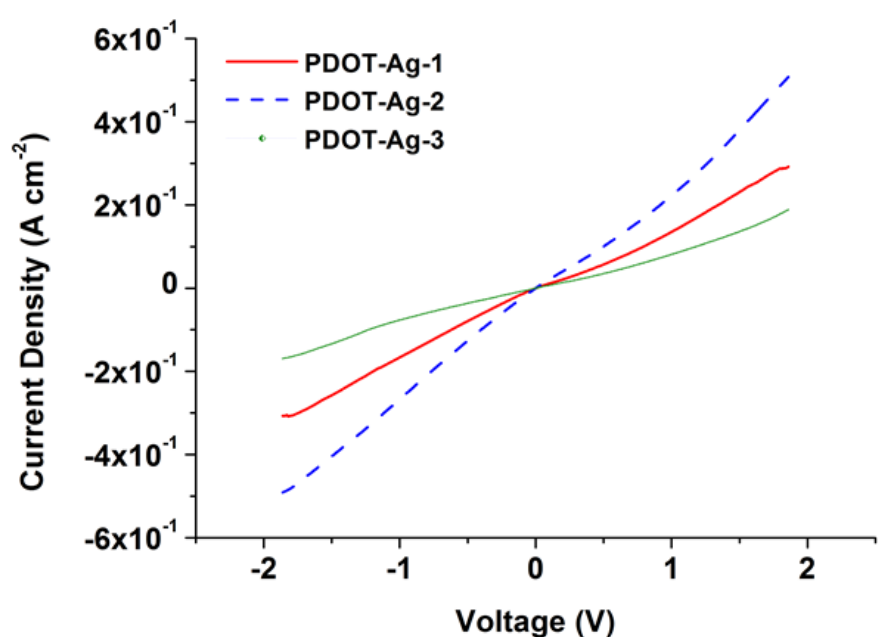


Figure 80. (a) J-V characteristic curve of PDOT-Ag devices. (b) J-V characteristic curve of PDOT-Ag-1, plotted to highlight the non-linear curves.

A corner on the edge of base substrate of these devices was flicked with fingers for mechanical vibration. However, they did not generate a voltage signal. The reason

for this discrepancy was studied in the light of devices' parasitic effects and explained later in section 6.2 of this chapter.

6.1.1.3. Zn-based Devices

Similar to Ag (silver) and ITO substrates, the ZnO nanorods grown on zinc foil nanorods were also fabricated into a device. These nanorods were 600 nm long and 80 nm wide (Figure 81). The J-V characteristic curve demonstrated rectifying current-voltage relationship with estimated series and shunt resistance of 0.028 – 0.185 k Ω 0.128 – 0.156 k Ω (Figure 82). The devices PDOT-Zn-1 and Zn-2 had series resistance two orders of magnitude lower than the PDOT-2K/A devices due to 5 orders of magnitude lower sheet resistance of zinc foil substrate.

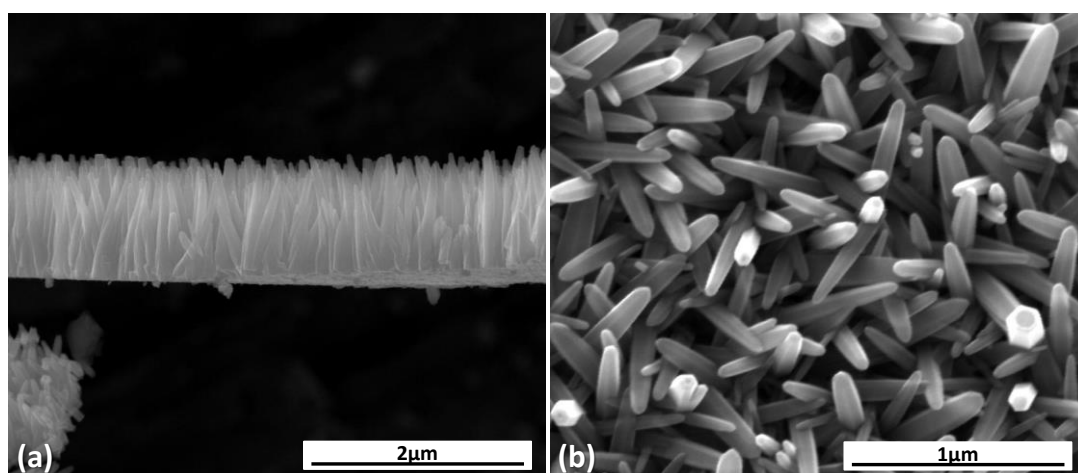


Figure 81. SEM images of nanorods grown on Zinc metal electrode: (a) Cross-section view, (b) top view.

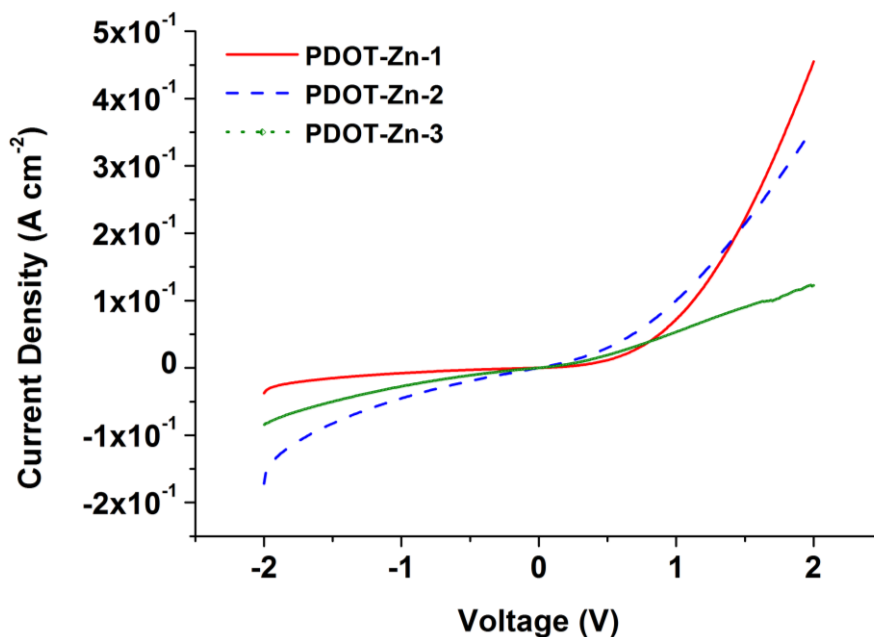


Figure 82. J-V characteristic curves of PDOT-Zn devices.

The PDOT-Zn devices were connected across oscilloscope to test their voltage output response to mechanical excitation. For a quick observation, the device was flicked with fingers and it did not provide any measurable voltage response. Since, the oscilloscope had the minimum detection threshold of 2 mV per division¹³; therefore, it was assumed that the device output was not sufficient to be measured. Hence, the device peak open-circuit voltage output was measured using Keithley 2400 source meter unit, which can detect minimum voltage of $\pm 1 \mu\text{V}$ ¹⁴. Corners on the edges of devices' base substrates were flicked manually, and the peak-open circuit voltage of the device was measured (Figure 83, Table 15). Since the devices were flicked manually, the bending strain was not controlled and therefore each flick bent them differently. Hence, each flick generated different amplitude of V_{oc} . For each device, the highest measured V_{oc} from 5 to 6 flicks was considered for analysis (Table 15). Among the three devices, PDOT-Zn-1 generated the highest V_{oc} of 200 μV . This voltage output was three orders of magnitude lower than the PDOT-Sm devices. However, it should also be noted that during measurement, the strain applied on the PDOT-Zn devices was different from the PDOT-Sm devices. The PDOT-Zn was flicked using fingers and PDOT-Sm devices were measured on the 50 g source bend-released equipment. But, it has been observed that by flicking the PDOT-Sm devices, as shown in the inset of Figure 77, the generated voltage of

40 mV was only marginally lower than the 50 g excitation of rotating cam. Hence, the PDOT-Zn devices' output measured by flicking the devices can be relied for comparison with ITO device output measured on the 50 g source bend-release measurement equipment.

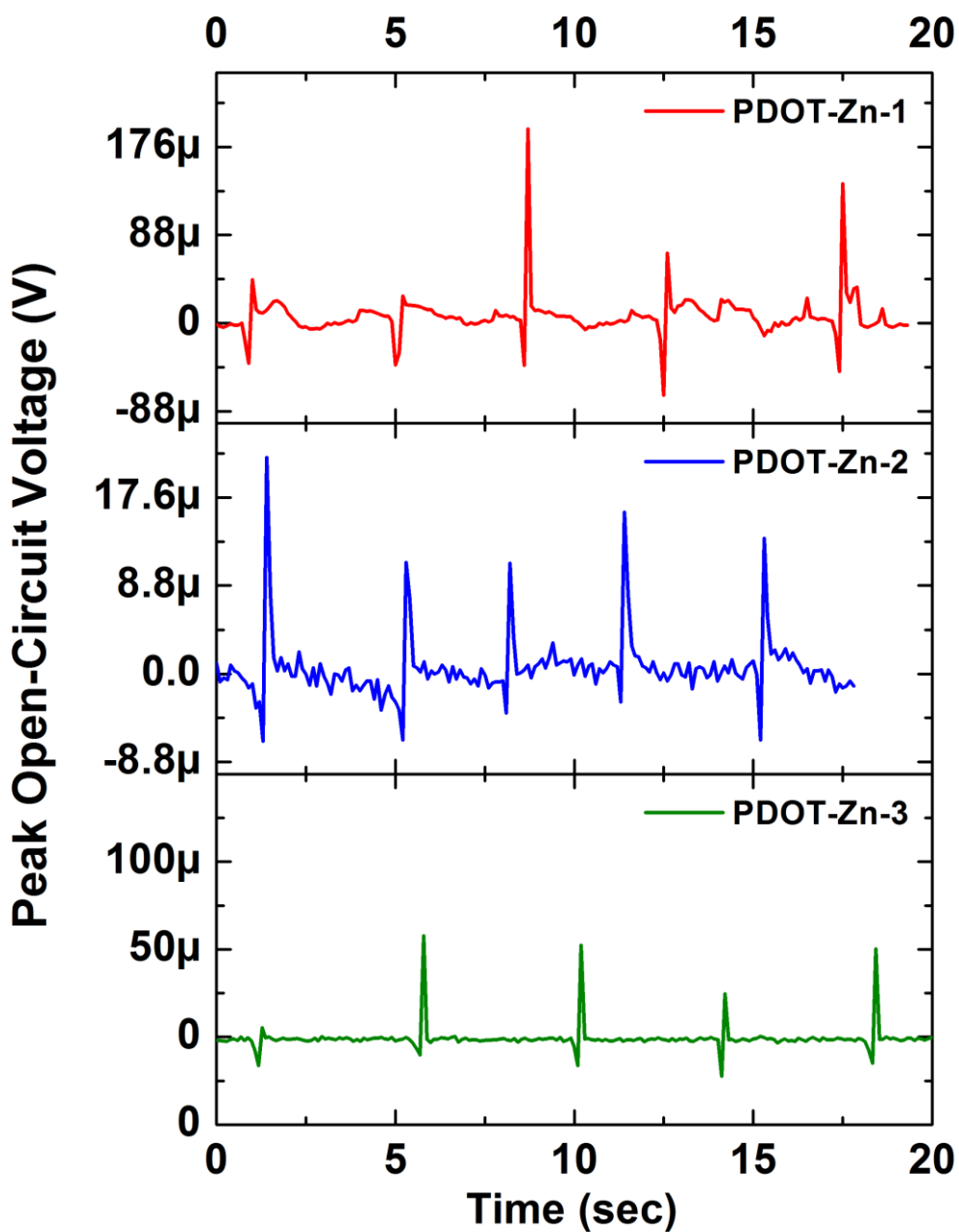


Figure 83. Open-circuit voltage output of PDOT-Zn devices.

Table 15. Calculated R_s and R_{sh} and measured V_{oc} of PDOT-Zn devices.

Group	Device Name	Series Resistance	Shunt Resistance	Peak Open-Circuit Voltage
		$k\Omega$	$k\Omega$	μV
PDOT-Zn	PDOT-Zn-1	0.028	0.128	200
	PDOT-Zn-2	0.037	0.0749	20
	PDOT-Zn-3	0.185	0.156	57

6.2. Comparative Analysis on the Bottom Electrode Materials

From the presented results of PDOT-Sm, PDOT-Ag and PDOT-Zn devices, it was observed that only two types of devices, PDOT-Zn and PDOT-Sm, generated desired piezoelectric response of voltage output to subjected mechanical excitation. For the case of PDOT-Ag devices, the J-V relationship was different from PDOT-Sm and PDOT-Zn devices. Firstly, PDOT-Ag's J-V relationship was studied. It was observed to be Ohmic response with rectification ratio of 1 (Figure 80(b)). The Ohmic response was caused by short-circuits in the device. These short-circuits were not completely avoidable in devices with material layers stacked over interspaced ZnO nanorod arrays. Some of the reasons for device short-circuits, as discussed earlier, were voids and pinholes in ZnO nanorod arrays which allowed PEDOT:PSS to come in contact with bottom electrode. In addition, uneven coverage of PEDOT:PSS exposed nanorod tips in areas where PEDOT:PSS coverage was low; this caused a short-circuit connection of ITO/ZnO/Au (gold). In case of PDOT-Ag devices, the short-circuits were majorly caused by delamination of ZnO nanorods, due to lack of sufficient bonding strength between Ag and ZnO nanorods. It was considered that ZnO delamination caused voids and gaps in the nanorod arrays (Figure 79) which allowed top electrode PEDOT:PSS to contact bottom Ag electrode and cause short-circuits. Therefore, when compared with PDOT-2K/A and PDOT-Sm, the lowered shunt resistance of the devices caused their malfunctioning.

For the case of PDOT-Zn devices, the JV relationship showed non-linear diode response. However, the highest generated voltage by these devices, being 200 μV for PDOT-Zn-1, was 300 times lower than that of the PDOT-Sm devices. The reason was studied firstly in the light of R_s and R_{sh} of the devices. The devices had their R_{sh}

in the range of 0.07 – 0.15 k Ω which was one to two order of magnitude lower than ITO devices. But, the lowered R_{sh} was not considered to be the cause of two orders of magnitude lower V_{oc} . The sheet resistivity of Zn foil was calculated to be 0.6 m Ω /sq, which was 5 orders of magnitude lower than ITO's 60 Ω /sq sheet resistivity. This caused the overall device internal impedance to reduce and hence the R_{sh} of the device reduced. Additionally, the PDOT-Zn devices showed non-linear diode behaviour in the J-V characterisation, which indicated that the device was not majorly affected by drop in R_{sh} induced by short-circuits.

Hence, the two orders of magnitude lower voltage output of PDOT-Zn foil was studied considering external screening effects of the bottom electrode. For this analysis, the band diagrams of ITO/ZnO (Figure 84) and Zn/ZnO (Figure 85) junction were hypothesised. Due to work function of 4.6 eV, the ITO was considered to form Schottky junction with ZnO (Figure 84(a)). Contrariwise, because of 4.3 eV of Zn and 4.26 eV of ZnO, the Zn/ZnO contact was considered to be Ohmic (Figure 85(a)).

In the case of ITO/ZnO, when ZnO was polarised under strain, a depolarisation field (E_{dep}) was developed, which allowed movement of internal free-charge carriers (Figure 84(b)). Moreover, the charges from ITO contact were accumulated near the depleted region of the ITO/ZnO junction. It was also considered that, mobile charges from ITO also tunnelled through the barrier and flowed through ZnO (Figure 84(b)). The accumulated charges at the interface and also the mobile charges which flowed through ZnO caused screening of polarisation charges ((Figure 84(c)). Similarly for Zn/ZnO contact, when ZnO was polarised under strain, the charges from Zn did not encounter a barrier at interface (Figure 85(b)). Therefore, they flowed easily into ZnO and caused screening of polarisation charges (Figure 85(c)). Because of lack of barrier between Zn/ZnO, the charges flowed more conveniently from Zn to ZnO than from ITO to ZnO. Additionally, the carrier concentration of metal Zn is considered to be greater than 10^{22} cm $^{-3}$; whereas for ITO which is an n-type semiconductor, the carrier concentration has been reported to be in the order of 10^{18} cm $^{-3}$ ¹⁵. Therefore, compared with ITO, the rate of flow of carriers through ZnO from higher carrier concentration Zn was considered to be more enhanced. Hence, due to lack of barrier and high carrier concentration, the Zn contact was believed to exhibit higher rate of

external screening of polarisation charges than ITO. Due to which, the V_{oc} of PDOT-Zn devices was two orders of magnitude lower than that of PDOT-Sm.

To conclude, the external screening effect of Zn foil electrode and the enhanced short-circuits in silver (Ag)-based devices did not allow the PDOT-Zn and PDOT-Ag devices to generate appreciable voltage output. Hence, the performance evaluation of the PDOT-Sm, PDOT-Zn and PDOT-Ag devices ascertained ITO to be a favourable electrode for ZnO-based piezoelectric energy harvester. Therefore, ITO was selected as a bench mark for further studies and for the fabrication of devices for all other analysis such as, top electrode study and ZnO surface passivation.

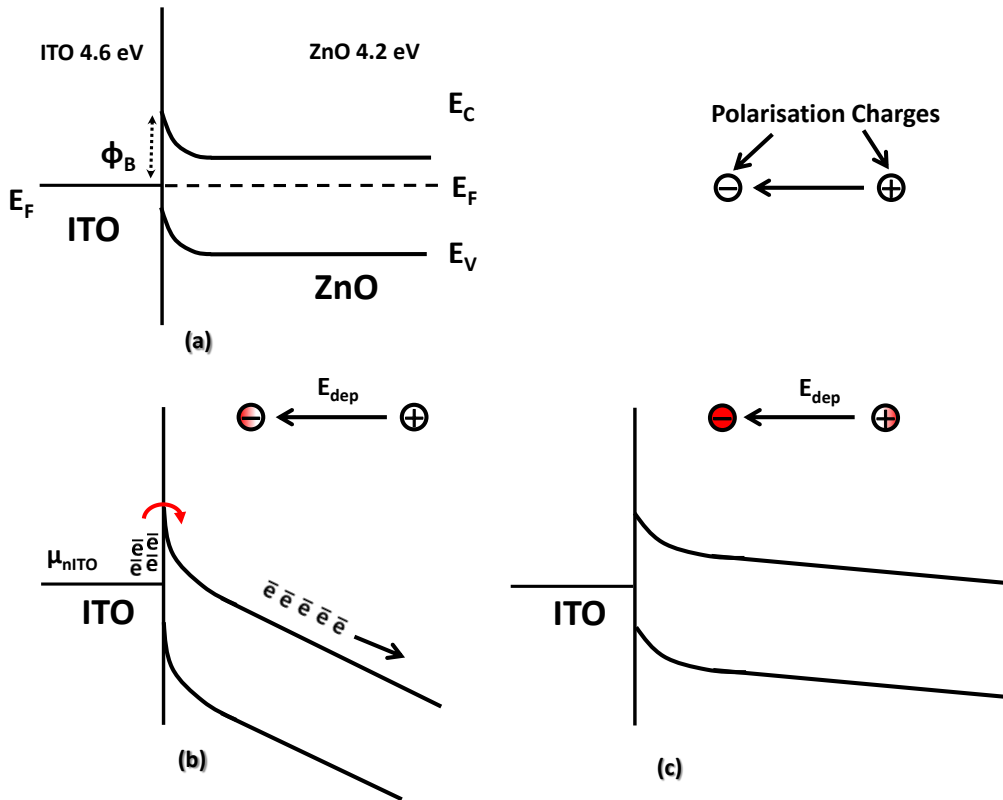


Figure 84. (a) Schottky contact between ITO and ZnO, having an Schottky barrier (ϕ_B) at the interface. (b) Polarised ZnO under strain, causing depolarisation field (E_{dep}) to develop and allow free-charge carriers to flow from within material and from the ITO contact. (c) The negative polarisation charges completely screening by the external and internal screening effect.

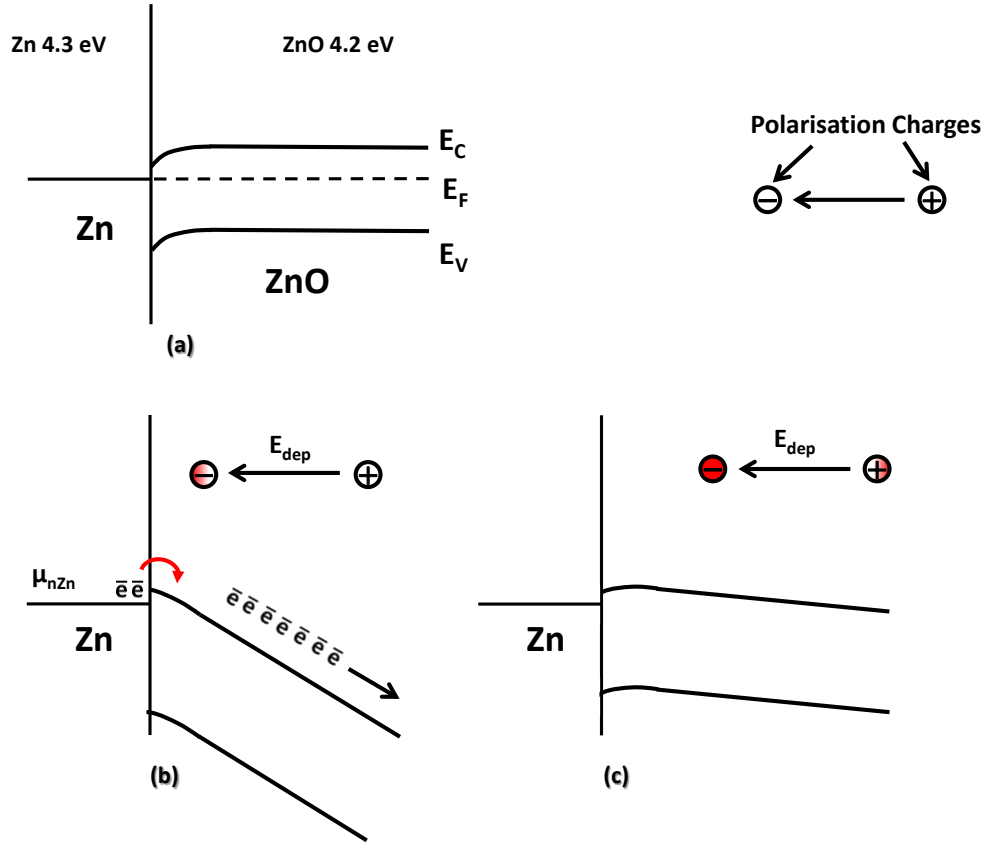


Figure 85. (a) Ohmic contact between Zn and ZnO, causing no energy barrier at the interface. (b) Polarised ZnO under strain, causing depolarisation field (E_{dep}) to develop and allow free-charge carriers from within material and from the ITO contact to flow. (c) The negative polarisation charges completely screening by the external and internal screening effect.

6.3. Effects of Top Electrode Materials

6.3.1. Overview of Device types based on Electrode Materials

As stated previously, electrode materials play a significant role in ZnO-based piezoelectric energy harvester performance, since they serve as terminals across which potential difference is created. An earlier study on bottom electrode materials elaborated effects of external screening on device performance and necessity of Schottky barrier to avoid screening of polarisation charges by interfacial charges. In addition to analysis of bottom electrode materials, study was carried out to understand the role of top electrode materials in the device performance. In this regard, the PEDOT:PSS (top electrode) and ITO (bottom electrode) based PDOT-

2K/A devices were observed and compared with PMMA (top electrode) and ITO (bottom electrode) based PMA-2K and PMA-3K devices.

6.3.1.1. Insulating Top electrodes

In 2011², PMMA was introduced as an insulating top electrode for ZnO-based energy harvester fabrication (Figure 86(a)). The main reason behind this was to mitigate the interfacial charge accumulation at ZnO/top electrode interface, which occurs when the electrode is conductive (Figure 86(b)). Therefore, the effects of external screening were reduced and the peak open-circuit voltage (V_{oc}) was improved⁷. This comparison of screening effects between insulator-type and Schottky-type device is further explained here using the hypothesised band diagrams in Figure 86. A Schottky-type contact between ZnO and gold electrode creates energy barrier and a depleted region in ZnO near ZnO/Au interface. When ZnO is polarised under strain (Figure 86(b)), the internal free-charge carriers (carriers within ZnO) flow toward the Au contact. Contrariwise, the free-charge carriers are attracted toward the depleted region in ZnO and accumulate at the ZnO/Au interface. These accumulated charges from Au, as well as the internally flowing carriers screen the polarisation charges in ZnO.

On the contrary, if insulating electrode, PMMA, is sandwiched between gold electrode and ZnO, an insulating barrier causes mitigation of interfacial charge accumulation at PMMA/ZnO. Therefore, the screening is considered to be caused by only the internal flow of charges. Hence, it was believed that the rate of screening of polarisation charges will be reduced for PMMA.

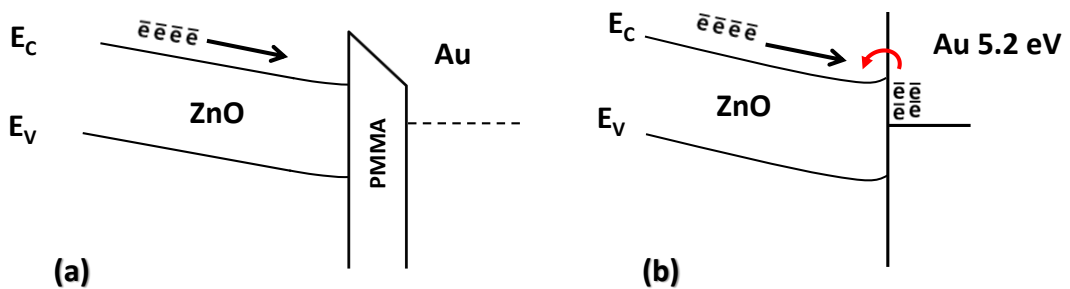


Figure 86. (a) Au/PMMA/ZnO metal-insulator semiconductor heterojunction. (b) Au/ZnO Schottky junction.

6.3.1.1. Semiconducting Top electrodes

The investigation of electrode material for ZnO-based energy harvester improvement was further expanded in 2012, when semiconductor PEDOT:PSS was used as a top electrode for ZnO-based piezoelectric energy harvester¹. Similar to insulating top electrode, the concept behind using a semiconducting top electrode was also related with reducing its external screening effects. The p-type PEDOT:PSS material in contact with n-type ZnO, was reported to form a p-n junction with a depletion region^{1,11}. The formation of depletion region was an essential element which acted as a barrier between p-type (free holes of PEDOT:PSS) and n-type material (free electrons of ZnO) (Figure 87). It was considered that compared with metal/n-type Schottky contact, a p-n junction material would reduce external screening effect. Because, PEDOT:PSS having carrier concentration (10^{19} cm^{-3}) lower than that of metal ($>10^{22} \text{ cm}^{-3}$), it will cause lesser movement of charges near the ZnO/top electrode interface. Hence, reportedly¹, the p-n junction device configuration reduced the external screening effects in the devices.

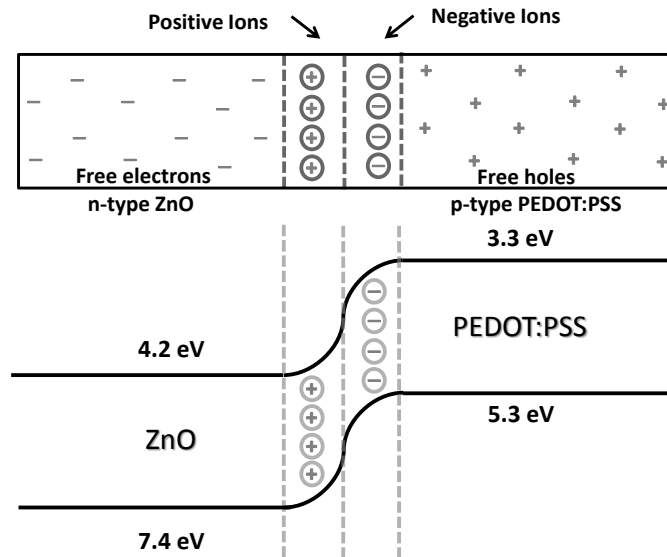


Figure 87. p-n junction between ZnO and PEDOT:PSS showing depletion region.

In order to compare the effects of insulating and semiconducting top electrodes on external screening of polarisation charges in ZnO-based energy harvester, it was

necessary to compare devices made with two top electrodes: PEDOT:PSS and PMMA. For this, devices were prepared using PEDOT:PSS and PMMA electrodes; in terms of fabrication, the only difference between the two types of devices lied in the manufacture of the top electrode. The rest of the processes related to nanorod synthesis, connecting the electrodes and mounting the device on base substrate were kept constant. In addition to this, the conditions for measurement and characterisation for both device types were kept constant. The PMMA devices were a heterojunction of ITO/ZnO nanorods/PMMA/Au(gold) and the same for PEDOT:PSS devices was ITO/ZnO nanorods/PEDOT:PSS/Au(gold). The devices prepared using PMMA as top electrode were grouped as PMA-2K and PMA-3K and devices prepared with PEDOT:PSS were grouped as PDOT-2K/A, PDOT-2K/B and PDOT-1K. The results of the PEDOT:PSS-based devices were previously presented in Chapter 5 and used here for comparison with PMMA-based devices. The devices with their respective groups and electrode fabrication methods are listed in Table 16.

Table 16. Group names and names of devices used for analysis on top electrode materials.

Group Names	Top Electrode Fabrication	Bottom Electrode & Nanorods Fabrication	
			Devices
PDOT-2K/A	PEDOT:PSS @ 2000 rpm	ITO Sp(25)	PDOT-A1, PDOT-A2, PDOT-A3, PDOT-A4
PDOT-2K/B	PEDOT:PSS @ 2000 rpm	ITO Sp(25)	PDOT-B1, PDOT-B2, PDOT-B3
PDOT-1K	PEDOT:PSS @ 1000 rpm	ITO Sp(25)	PDOT-1K-1, PDOT-1K-2, PDOT-1K-3
PMA-2K	PMMA @ 2000 rpm	ITO Sp(25)	PMA-2K-1, PMA-2K-2, PMA-2K-3
PMA-3K	PMMA @ 3000 rpm	ITO Sp(25)	PMA-3K-1, PMA-3K-2, PMA-3K-3

6.3.2. PEDOT:PSS-based p-n Junction-type Devices

This type of device comprised of spin-coated p-type PEDOT:PSS polymer layer on top of the n-type ZnO nanorod arrays, thus forming a p-n junction diode with PEDOT:PSS/ZnO. Flexibility of polymer-type electrode facilitated device bend-release measurements without forming cracks. Figure 88 shows 1 μm thick PEDOT:PSS layer coated on top of 2 μm long nanorods. PEDOT:PSS is a conjugated organic semiconducting polymer, having a carrier concentration of 10^{19} cm^{-3} ¹. The benefit of using PEDOT:PSS-based p-n junction-type devices over Schottky-type (higher work function metal contact) devices was described by Briscoe et al. (2012)¹ using a free charge screening model. According to this model, when a piezoelectric material is stressed, a depolarisation field arises which is compensated by the movement of free-charge carriers both from within the material or from external contacts¹. The rate of flow of free charge carriers determines the screening *rate*. In the case of ZnO contact with p-type material or metal with higher work function ($> 4.26 \text{ eV}$), an energy barrier exists at the p-type/ZnO or metal/ZnO junction which assists in reducing the rate of flow of carriers from external contacts into ZnO. Hence, it assists in reducing the external screening *rate*. However, external screening cannot be fully mitigated, because mobile carriers tunnel through barriers or accumulate at junctions causing screening of polarisation charges. In which case, if we compare any metallic electrode with PEDOT:PSS electrode; then the 10^{22} cm^{-3} ranged carrier concentration of metal, compared with 10^{19} cm^{-3} for PEDOT:PSS, is considered to allow higher flow of free-charge carriers through ZnO. Hence, it was established that a p-type contact would slow the screening process down and improve the device voltage output.

6.3.2.1. Electrical Characterisation and Performance Parameters

PEDOT:PSS-based devices have been analysed as devices with p-n junction between PEDOT:PSS and ZnO. Here we refer to the important findings in Chapter 5 based on the results of PDOT-2K/A, PDOT-2K/B and PDOT-1K devices and summarise them.

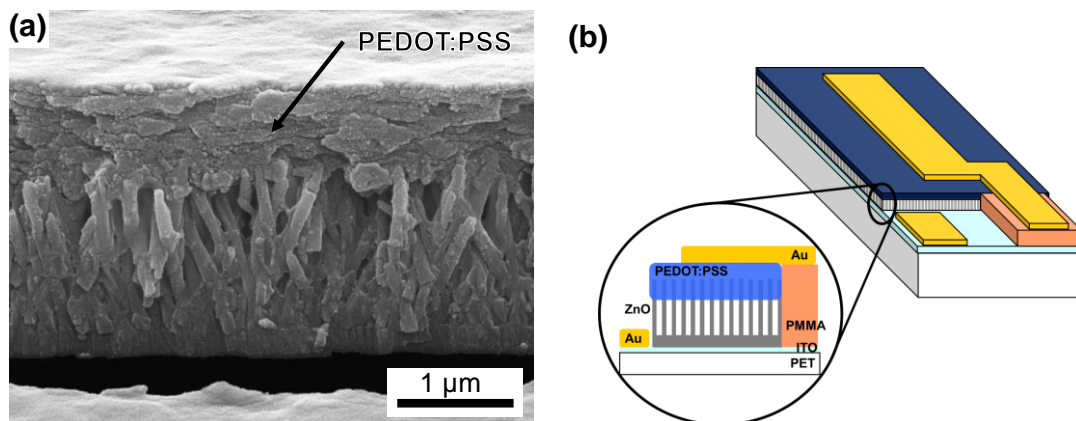


Figure 88. SEM image of 1 μm PEDOT:PSS layer coated on top of nanorods. (b) Schematic of ITO/ZnO/PEDOT:PSS/Au heterojunction

1.

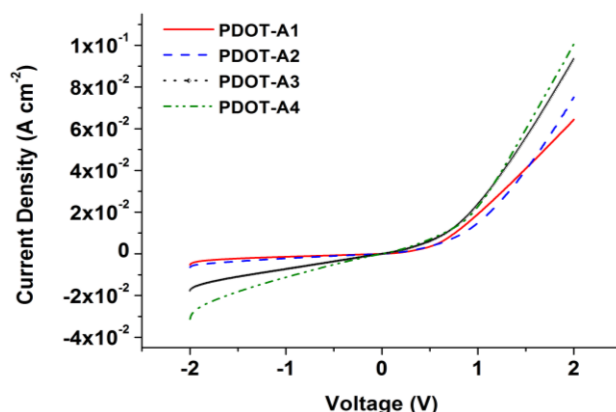


Figure 89. J-V characteristics curve of PDOT-2K/A devices

To elaborate the p-n junction between PEDOT:PSS and ZnO, Figure 89 shows the J-V characteristic curve of PDOT-2K/A devices from -2 V to +2 V, which were non-linear due to their forward current increasing exponentially with the operating voltage¹⁰. The current rectification ratios (defined as the ratio between forward current and reverse current) were 12, 12, 5 and 5 respectively at ± 2 V for PDOT-A1, A2, A3 and A4¹¹. The diode turn-on voltage was in the range of 0.3 – 0.5 V. Thus, the rectifying non-linear J-V characteristic curve indicated a p-n junction between n-type ZnO nanorods and p-type PEDOT:PSS¹¹. Figure 88 shows the SEM image of

the 1 μm thick PEDOT:PSS layer settled on top of the nanorods from the tips of the rods to a depth of 250 nm.

The DC J-V electrical characterisation had enabled to calculate the R_s and R_{sh} of devices in PDOT-2K/A, PDOT-2K/B and PDOT-1K groups. Further, the evaluation of output parameters of the devices was carried out by measuring device peak open-circuit voltage (V_{oc}), peak short-circuit current (J_{sc}) under unloaded device conditions. Moreover, the P_L of the devices was measured using resistive load matching across a sweep of resistances from 100 Ω to 100 k Ω . The device was bent 6 mm upwards by a rotating cam at 1 Hz and all measurements were recorded when it was released at an acceleration of 50 g. The impedance analysis on devices was performed from 40 Hz to 110 MHz input frequency and the results were converted into Nyquist plots to determine the real-axis based resistive internal impedance (R_{int}).

The performance parameters of the PDOT-2K/A, PDOT-2K/B and PDOT-1K devices were understood in the light of the parasitic effects of the R_s and R_{sh} on device performance. It was concluded that the most efficient devices in group PDOT-2K/A, with V_{oc} from 90 mV – 225 mV, had R_s and R_{sh} of 0.08 – 0.17 k Ω and 0.5 – 1.65 k Ω (Table 17), which were higher than the PDOT-2K/B devices but lower than the PDOT-1K devices. The PDOT-2K/B, affected by lower R_{sh} 0.2 – 0.3 k Ω , generated V_{oc} from 22 – 60 mV (Table 17); whereas, the PDOT-1K devices, affected by their higher R_s 0.3 – 0.6 k, generated V_{oc} of 33 – 40 mV (Table 18). Due to this, the power densities (P_L) of PDOT-2K/B and PDOT-1K devices were significantly dropped. In case of PDOT-2K/A devices, the R_{sh} was sufficiently high due to less occurrences of short-circuits and R_s losses did not significantly affect the output of devices. Therefore, these devices had the peak power densities across load (P_L) of 36 - 54 $\mu\text{W cm}^{-2}$, which was higher than 2.5 – 16 $\mu\text{W cm}^{-2}$ generated by PDOT-2K/B and 0.2 – 0.25 $\mu\text{W cm}^{-2}$ generated by PDOT-1K. The impedance analysis was performed on the p-n junction type device to evaluate its internal resistance, which were in the range of 0.6 k Ω - 2 k Ω .

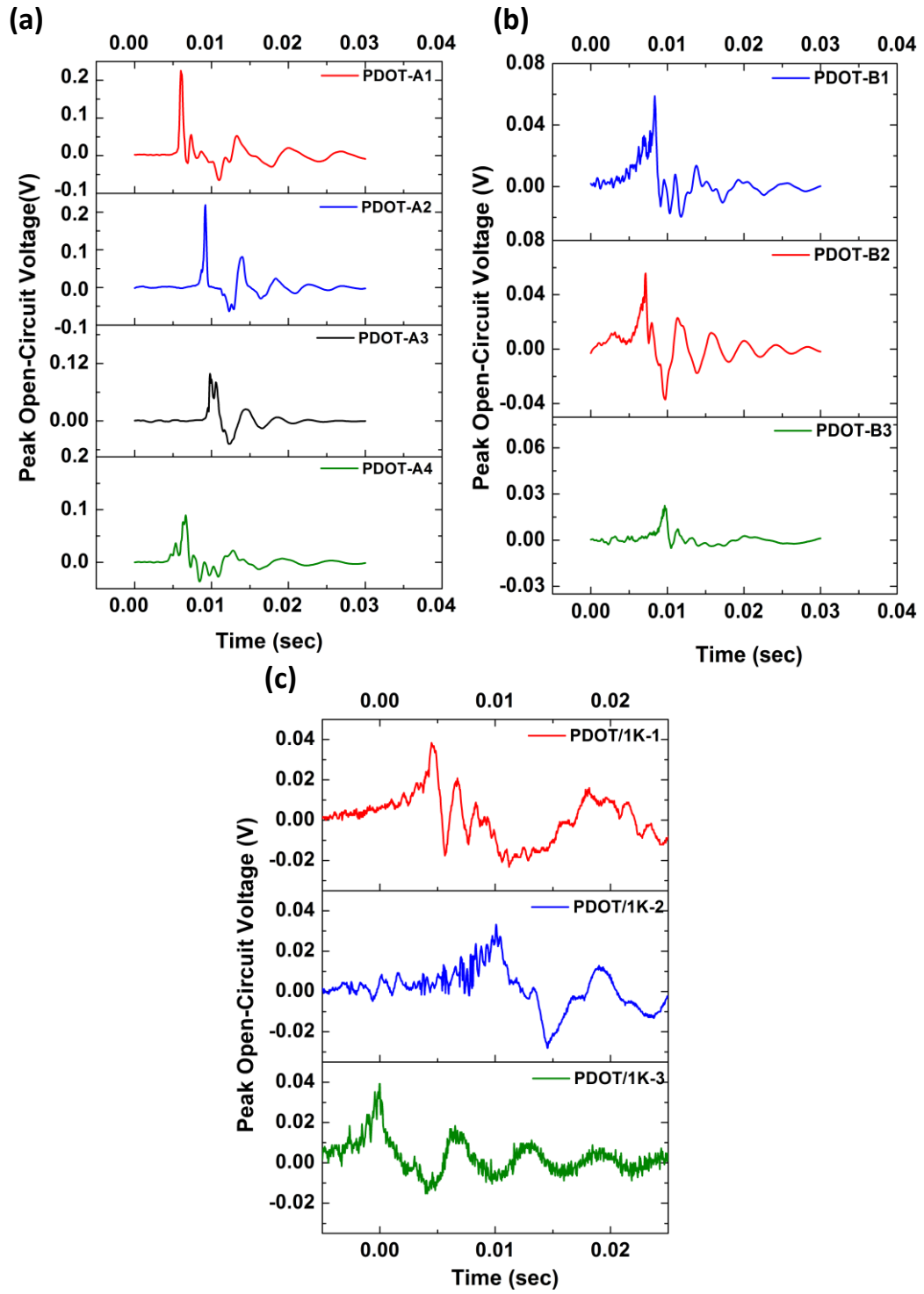


Figure 90. Measured peak open-circuit voltage plots of devices in groups: (a) PDOT-2K/A, (b) PDOT-2K/B and (c) PDOT-1K.

Figures from Chapter 5.

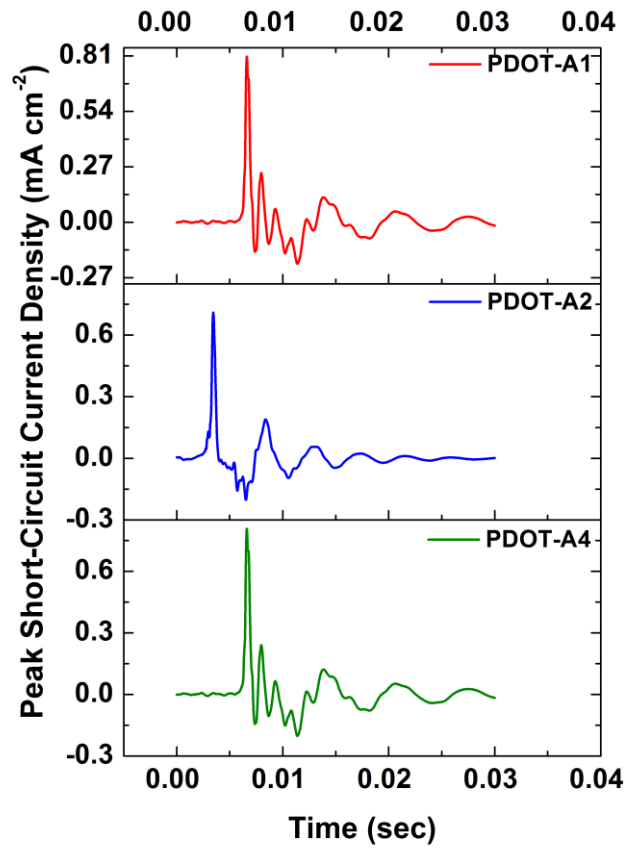


Figure 91. Measured peak short-circuit current plots of devices in groups: (a) PDOT-2K/A.
Figure from Chapter 5.

Table 17. Performance parameters of PDOT-2K/A and PDOT-2K/B devices from Chapter 5.

Device Name	Peak Open-Circuit Voltage	Peak Short-Circuit Current Density	Peak Power Density	Load Resistance	Energy Density	Charge Displaced	Series Resistance	Shunt Resistance	Real Impedance
	V_{oc} (mV)	J_{sc} (mA/cm ²)	P_L (μW/cm ²)	R_L (kΩ)	E_L (nJ/cm ²)	Q_L (nC/cm ²)	R_s (kΩ)	R_{sh} (kΩ)	R_{int} (kΩ)
		Measured/Calculated	Manual/Decade Box						Performed/Not Performed
PDOT-A1 REMARKS	225	0.800 Measured	54 Decade Box	2.019	37	355	0.172	1.650	2.00
PDOT-A2 REMARKS	212	0.715 Measured	41.07 Decade Box	1.387	22	236	0.100	1.00	1.28
PDOT-A3 REMARKS	98	- Device Broken	- Device Broken	- Device Broken	- Device Broken	- Device Broken	0.081	0.50	0.857
PDOT-A4 REMARKS	90	0.600 Measured	36.01 Decade Box	1.387	5.19	173.85	0.126	0.45	0.974
PDOT-B1 REMARKS	60	0.830 Calculated across 100 Ω	16.45 Device Broken	0.827	2.5	158	0.073	0.34	0.664
PDOT-B2 REMARKS	56	0.706 Calculated across 50 Ω	12.62 Device Broken	0.603	2.47	140.63	0.086	0.33	0.600
PDOT-B3 REMARKS	22	0.493 Calculated across 100 Ω	2.4 Device Broken	0.493	0.82	155.15	0.049	0.24	- Not Performed

Table 18. Performance parameters of PDOT-1K devices from Chapter 5.

Device Name	Peak Open-Circuit Voltage	Peak Short-Circuit Current Density	Peak Power Density	Load Resistance	Energy Density	Charge Displaced	Series Resistance	Shunt Resistance	Real Impedance
	V_{oc} (mV)	J_{sc} (mA/cm ²)	P_L (μW/cm ²)	R_L (kΩ)	EL (nJ/cm ²)	Q_L (nC/cm ²)	R_s (kΩ)	R_{sh} (kΩ)	R_{int} (kΩ)
		Measured/Calculated	Manual/Decade Box						Performed/Not Performed
PDOT-1K-1	38	0.027	0.20 - 0.25	2kΩ < Load < 5kΩ	-	-	0.422	1.69	-
REMARKS		Calculated across 1 kΩ	Manual						Not Performed
PDOT-1K-2	36	0.016	0.22- 0.25	3kΩ < Load < 6kΩ	-	-	0.627	2.30	-
REMARKS		Calculated across 1 kΩ	Manual						Not Performed
PDOT-1K-3	40	-	-	-	-	-	0.341	1.51	-
REMARKS									Not Performed

6.3.3. PMMA-based Insulator-type Device

This device was composed of a PMMA layer on top of the ZnO nanorods forming an insulator-semiconductor junction. The importance of this system lied in having an insulating PMMA electrode between gold and ZnO. Therefore, when in ideal contact with ZnO, PMMA would not allow band bending and reduce interfacial charges at ZnO/insulator and gold/insulator interface. However, in real systems, the presence of interface states at ZnO surface does not fully reduce interfacial band bending. It was also considered that, when ZnO and metal were connected with an external measurement system, their intermediate PMMA layer would not allow electric field to affect the band bending in ZnO. Hence, this metal-insulator-semiconductor (MIS) configuration was believed to reduce the carrier transport between ZnO and gold electrode, causing minimisation of the external screening effects. Devices in groups PMA-2K and PMA-3K were studied and analysed for their performances. In PMA-2K device, two layers of PMMA was spin-coated on top of nanorods at 2000 rpm whereas the same was done at 3000 rpm in PMA-3K devices. Figure 92 shows the cross-section image of 3.5 μm and 1 μm thick PMMA layers on PMA-2K-1 and PMA-3K-1 devices. The PMMA coated onto the nanorod tips and also filled in their interspaces ¹⁶. The fully configured devices were heterojunctions of ITO/ZnO nanorods/PMMA/Au (gold).

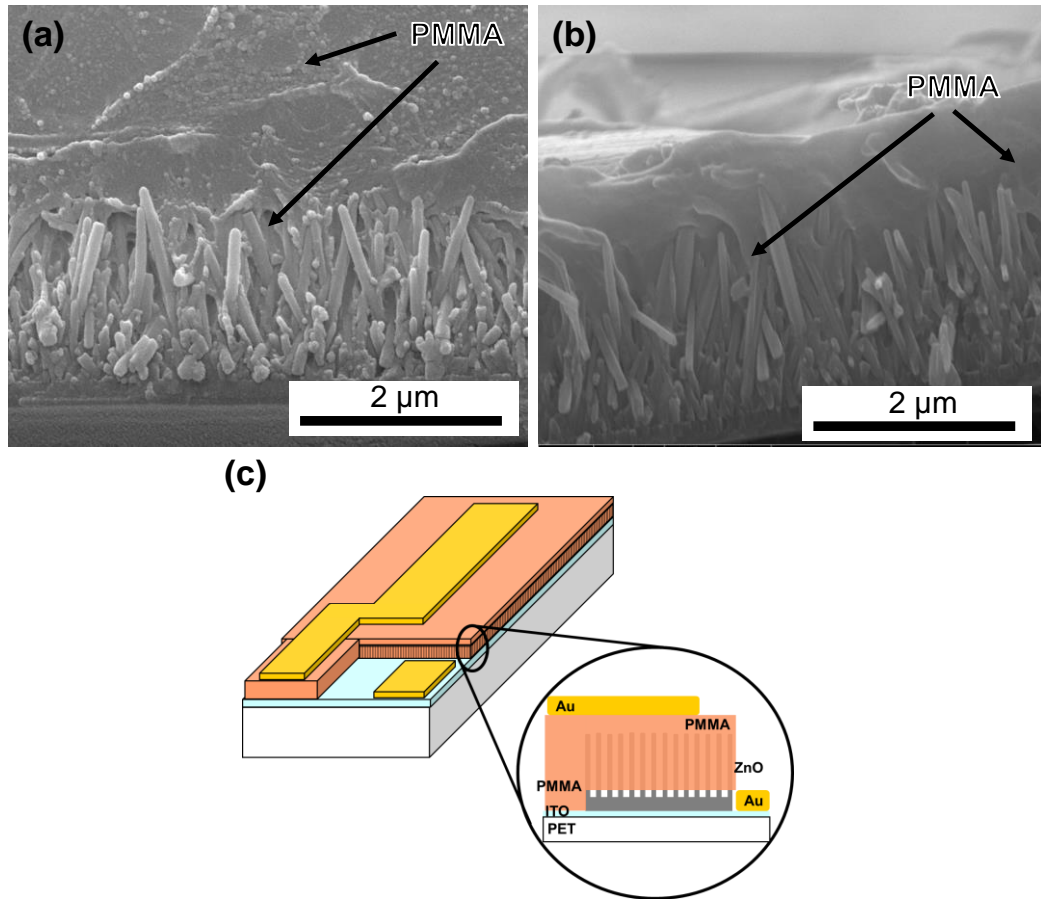


Figure 92. SEM images of (a) 3.5 μm thick PMMA layer coated on top of ZnO nanorods (b) 1 μm thick PMMA layer coated on top of ZnO nanorods. (c) Schematic of ITO/ZnO/PMMA/Au heterojunction device

16

6.3.3.1. Current-Voltage (J-V) Electrical Characterisation

An electric bias from -2 V to +2 V was applied across each device terminals using Keithley 4200 source meter, to measure its current-voltage relationship. The characteristic curve, shown in Figure 93, indicated a non-linear current-voltage relationship with rectification ratio (ratio between the forward current and the reverse current) of 0.5 – 1.2 for PMA-2K and 0.4 -0.6 for PMA-3K devices at ± 2 V. Upon application of an external bias across the device, there was a non-linear forward current was observed to flow. Figure 94 explains this non-linear forward current effect: when the metal was connected to positive and semiconductor to negative charge then excess of electrons were accumulated at the ZnO/PMMA junction which caused the bends to move downwards. Therefore, a non-linear

forward current flowed in order to accommodate the excess electron density (Figure 94(c)).

Similarly under reverse bias mode, when a positive potential was applied to the ZnO, there was some reverse leakage current observed to flow. This was caused by the depletion region created at ZnO/PMMA junction and it therefore small nA ranged currents flowed in the reverse direction (Figure 94(b)). Therefore, the J-V characteristic curve of devices showed a non-linear current-voltage relationship with rectification.

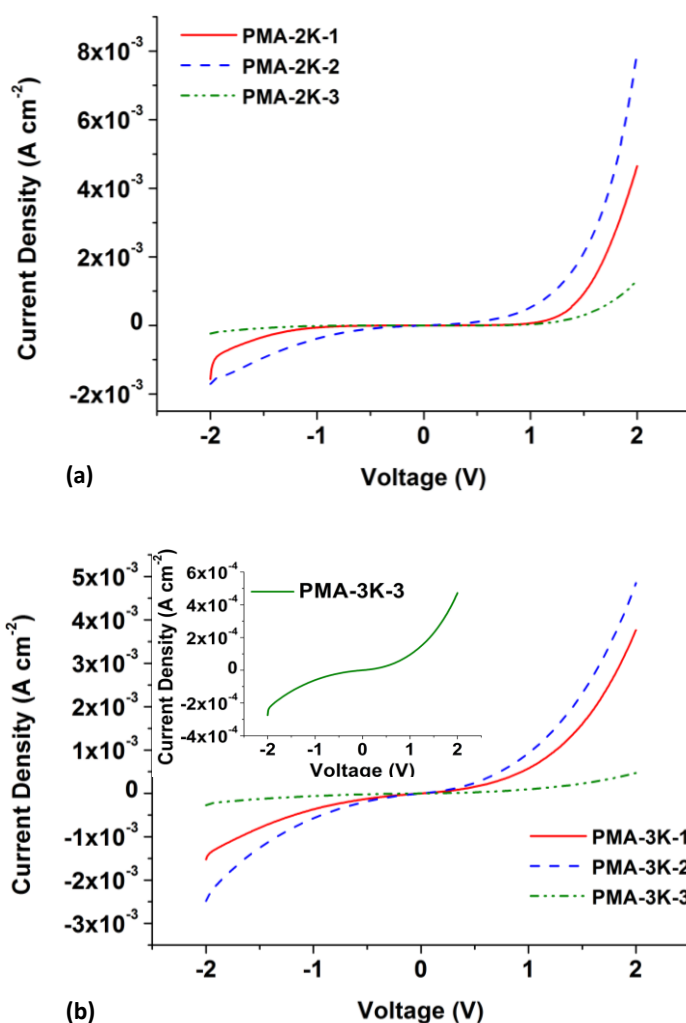


Figure 93. J-V characteristic curve of (a) PMA-2K and (b) PMA-3K devices. Inset showing J-V curve of PMA-3K-3 for clarity.

The series resistance (R_s) and shunt resistance (R_{sh}) of PMA-2K and PMA-3K devices were extracted by calculating the inverse slope $R = \frac{\partial V}{\partial I}$ of the plots in the forward and reverse biased regions, respectively.

Table 19 shows the calculated values of R_s and R_{sh} of the devices.

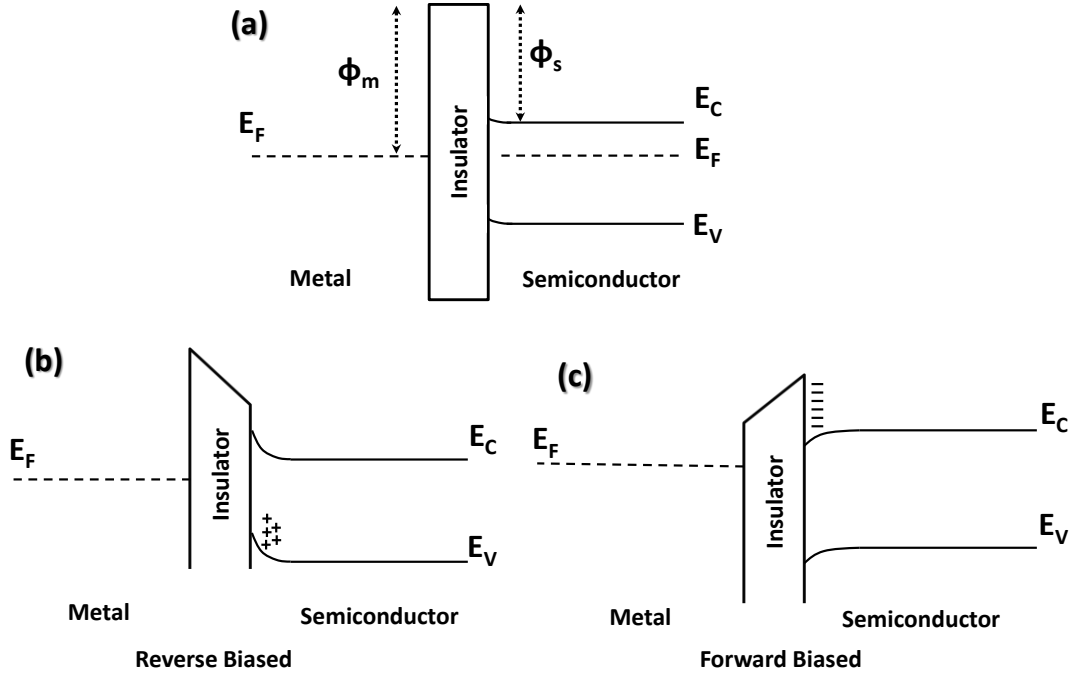


Figure 94. Metal insulator semiconductor (n-type) junction at (a) equilibrium, (b) under reverse bias condition, (c) under forward bias condition.

The values of R_s and R_{sh} obtained for heterojunction-based devices depend on the equilibrium state of their stacked materials. To elaborate, we take the example of the presented case of PMMA-based devices. The PMMA in these devices was dissolved in anisole solvent for spin-coating. It was considered that during its drying process at 100°C for 24 hours, the anisole solvent did not fully evaporate. This affected the device performance and their J-V characteristic curves. The devices mainly affected were the earliest fabricated batches, called as the PMA-2K devices. This was because: firstly, due to earlier phase of study, the effects of incomplete solvent evaporation were not known; secondly, due to initial fabrication trials, the thickness of PMMA layer was not optimised and being 3.5 μm thick it allowed more solvent to

be trapped. Figure 95 (a-c) shows J-V characteristic curve of devices right after fabrication completion. Figure 95 (d-f) shows that the J-V characteristic curve changed after one week of fabrication. Figure 95(a) showed no rectification ratio between forward and reverse current. Figure 95(b-c) demonstrated leakage current to be higher than forward current. From these results it was speculated that trapped solvent in PMMA could have ionised under the electric field caused by 1-2 V bias.

Table 19. Calculated R_s and R_{sh} of PMA-2K and PMA-3K devices.

Device Name	Series Resistance	Shunt Resistance
	R_s (kΩ)	R_{sh} (kΩ)
PMA-2K-1	0.7	81.5
REMARKS	Effected by Anisole (Solvent)	Effected by Anisole (Solvent)
PMA-2K-2	0.6	6.8
REMARKS	Effected by Anisole (Solvent)	Effected by Anisole (Solvent)
PMA-2K-3	0.65	46
REMARKS	Effected by Anisole (Solvent)	Effected by Anisole (Solvent)
PMA-3K-1	1.25	4.78
REMARKS		
PMA-3K-2	1.02	1.76
REMARKS		
PDOT-3K-3	10	10
REMARKS		

Therefore, this ionisation could have caused leakage current to flow. This in return, changed the J-V characteristic profile of the freshly prepared PMA-2K devices. The J-V characteristic curve was settled and had a diode-like non-linear profile after one week Figure 95 (d-f). This indicated that, the solvent was dried over the period of time. But, it was still improbable if the solvent had completely escaped from the deposited PMMA on PMA-2K devices.

The R_s and R_{sh} analysis was performed on the J-V characteristic data acquired one week after fabrication (Figure 95 (d-f)). However, the calculated R_s of PMA-2K devices, with 3.5 μm thick electrode, were in the range of 0.6 – 0.7 $\text{k}\Omega$; which after analysis were found to be lower than PMA-3K devices with 1 μm thick electrode (discussed later in this section). This result was contrary to other reports on the effect of electrode thickness on device R_s : as reported by Baglio et al. (2011)¹⁸ and Góes et al. (2011)¹⁹, increase in electrode thickness in heterojunction devices increased the overall internal resistance. Therefore, the calculated R_s of PMA-2K devices indicated that the solvent may have not completely escaped from the deposited PMMA. Due to this, the calculated R_s and R_{sh} from JV relationship of PMA-2K were not considered to be completely reliable.

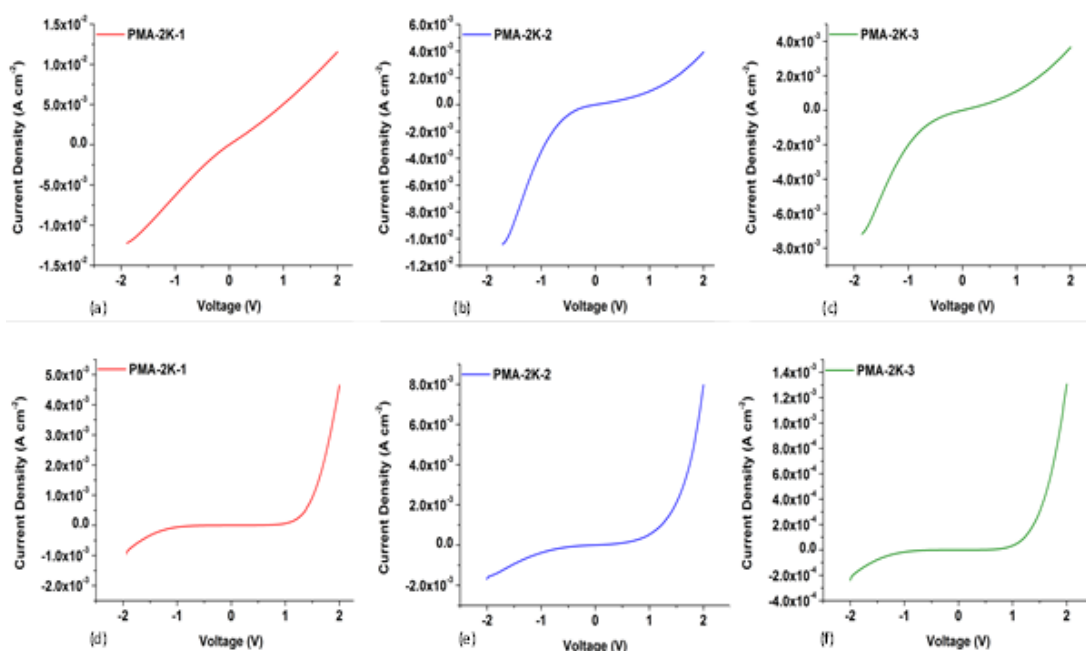


Figure 95. J-V characteristic curves of PMMA-based devices right after fabrication demonstrating the change in device characteristics due to incomplete evaporation of solvent. J-V characteristics of devices after 1 week of storage, showing change in behaviour after solvent evaporation.

To sum up, the R_s and R_{sh} of PMA-2K may have been higher than the calculated values (if the solvent had completely evaporated), but the incomplete solvent evaporation affected the result analysis. This effect of incomplete solvent was studied by Perlich²⁰ in spin-coated polystyrene (PS) dissolved in toluene. It was

found that the total remaining toluene content increased with increasing PS film thickness. Hence, in the presented case of PMMA dissolved in anisole, the remaining anisole content was considered to be higher in PMA-2K devices than in PMA-3K devices. Therefore, the reason behind fabricating PMA-3K devices, with 1 μm thick PMMA electrode, was to prevent the problem of solvent evaporation. The J-V plots of these devices were more stabilised, as compared to PMA-2K. However, the solvent of these devices was not completely dried since problems were occurred during output measurement of these devices. Figure 96 shows the J-V characteristic curve of PMA-3K devices right after fabrication completion. The extracted values of R_s and R_{sh} from the J-V plots were ranged as 1.02 – 10 $k\Omega$ and 1.76 – 10 $k\Omega$, respectively. The resistive impedance (R_{int}) of PMA-2K devices were higher than the 0.36 – 0.6 $k\Omega$ and 3.23 – 4.14 $k\Omega$ R_s and R_{sh} of PMA-2K devices, because the effects of solvent in PMA-3K with thinner (1 μm) electrode were less pronounced.

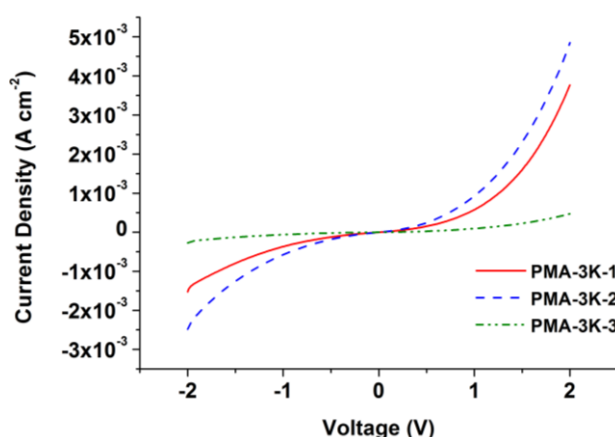


Figure 96. JV Characteristic curve of PMA-3K devices, right after fabrication.

The 1.02 – 10 $k\Omega$ and 1.76 – 10 $k\Omega$ ranged R_s and R_{sh} indicated a high sample-to-sample variations in PMA-3K devices. The reason behind these sample variations were, reduced PMMA coat thickness and sheet resistance of ITO. Firstly, the spinning of PMMA at 3000 rpm had caused deposition of 1 μm thick PMMA layer near in the centre of substrate and 30 nm thick (Figure 97 (b)) coating around the edges. This non-uniformity in polymer layer coverage was caused due to spin-deposition: the centrifugal forces around the edges of the substrate pulled on the PMMA outward, and the attractive forces within the PMMA pulled on the PMMA near the centre of the substrate, where the centrifugal forces were smaller²¹. Hence

the devices with electrodes closer to the edges had lower overall R_s . In addition, the lesser thickness around edges increased the chance of short-circuits. These short-circuits were more likely caused by the non-homogenously nucleated microrods in the synthesis solution. These microrods were randomly grown in the synthesis solution of $Zn(NO_3)_2$ and HMT and they were longer than 5-6 μm . They adhered with the non-homogenously nucleated nanorods because of high surface energy. The thinly coated edges of the substrate allow these microrods (Figure 97(a)) to be left uncovered with PMMA. Therefore, if these uncovered microrods are sputtered with gold, they cause short-circuit of Au (gold)/ZnO/ITO. In addition, for the case of PMA-3K-2 device, the lower PMMA thickness under the electrode and higher short-circuit had reduced its R_s and R_{sh} to 1.02 $k\Omega$ and 1.76 $k\Omega$. Its R_{sh} was 45 times lower when compared to PMA-3K-1 device.

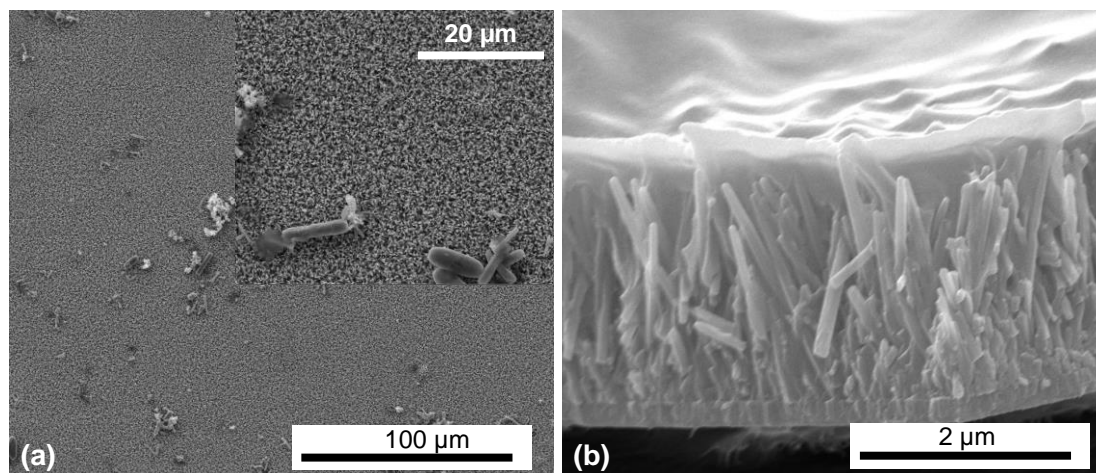


Figure 97. SEM images of (a) homogeneously nucleated nanorods adhered onto the surface of heterogeneously nucleated nanorods, (b) 30 nm PMMA coating on nanorods near the edge of the device substrate.

Secondly, higher ITO sheet resistance caused increase in device internal impedance. It is to be noted that due to process variations and discrepancies, the coated ITO resistance on PET cannot be homogenous throughout the sheet. Certain parameters such as increased PET substrate roughness or uneven structures cause the sputtered ITO particles to be rougher certain areas²². There are always chances that these rougher areas are incorporated into a device. Therefore, they reduce the conductivity of ITO electrode and cause overall internal impedance of the device to increase. This

case was observed in PMA-3K-3 device and was regarded to cause the highest internal resistive impedance comprising of $10\text{ k}\Omega R_s$ and $10\text{ k}\Omega R_{sh}$ in the device.

When compared with the PEDOT:PSS-based devices, the overall R_s and R_{sh} of PMMA-based devices was 1 to 2 orders of magnitude higher. The reason was the conductivity differences between the two materials. That is to say, PMMA being an insulating material has ideally infinite resistance. Due to which, its R_s was high and also the leakage losses due contact between top electrode and bottom electrode were minimised. To elaborate, in case of pin-holes or patched areas where ZnO nanorods did not grow, the PMMA layer contacted with ITO. However, due to insulating property of PMMA, the contact of PMMA/ITO did not cause device short-circuits.

6.3.3.2. Output Measurement and Performance Evaluation

The PMA-2K and PMA-3K devices were tested for their output performance. The output measurements were performed when devices were mechanically excited using a 1 Hz rotating cam connected to shaft of a motor (described in Chapter 3, section 3.6). Each device had its one end fixed and the other end was bent upwards to $\sim 6\text{ mm}$ by the cam and released at 50 g acceleration. At this acceleration, each device generated output response which was captured using NI PXI-4461 (24-bit ADC) on the NI PXIe-1062Q chassis. The open-circuit voltage output peaks of the device were recorded using Labview operated NI PXI-4461 (24-bit ADC) on the NI PXIe-1062Q chassis. The short-circuit current output peaks were recorded using Labview operated Low-Noise Current Preamplifier SR570 connected with the NI PXI-4461 (24-bit ADC) module. The resistive load curves were recorded using decade box, Meatest M602 programmable decade box, which was connected with the PXI-4461 module for data acquisition. A Labview program controlled the resistive sweep of the decade box and also recorded the output of the device across the sweep of load resistance.

The PMA-3K-2 device was disintegrated during bend-release measurement for power density. Therefore, the performance of this device could not be fully evaluated. For PMA-2K devices, the short-circuit measurement were carried out by capturing voltage signal across $40 - 50\text{ k}\Omega$ resistors due to unavailability of Low-Noise Current Preamplifier SR570. The reason of selecting $40 - 50\text{ k}\Omega$ resistors was

based on the internal impedance of these devices. To elaborate, short-circuit resistance is the resistance across which voltage output of a device is minimum (ideally 0) and its current is the highest (ideally $\rightarrow \infty$). In order to estimate the short-circuit resistance of the PMA-3K devices, resistors were connected in parallel with these devices and the voltage drop across them was recorded. For resistances lower than 40 k Ω , these devices did not generate any voltage, which meant that they were under short-circuited condition. At 40 k Ω , these devices generated the minimum voltage detectable by the measurement system. Hence, at this value of resistance, the short-circuit current density was estimated from the voltage peak ($I = \frac{V_R}{R}$). The impedance analysis of the devices was performed from 40 Hz to 110 MHz. The impedance response to the varying frequency input voltage signal was converted into Nyquist plot. From the real-axis diameter of the large semicircle in the Nyquist plot, the resistive internal impedance (R_{int}) of the devices was observed.

As discussed earlier, one of the major difficulties occurred during measurement of PMMA-based devices were caused by the incomplete anisole solvent evaporation from PMMA. This was linked with: thickness of PMMA which was the highest 3.5 μm in PMA-2K devices and PMMA's high molecular weight of 850,000 g/mol. Both factors have been found to trap a solvent in polymers²⁰. Due to this issue, problems were occurred mostly with resistive load matching. The resistive load matching is performed by measuring device voltage output across a sweep of resistances; but due to solvent trapping in the device, its electrical response was affected adversely and the voltage output of the device used to fluctuate. This had caused noise in the data set, which was reduced by taking average of 5 measurements for each device.

For understanding the effects of R_s and R_{sh} of PMMA-based devices on their performances, we took reference from the previously determined results of PDOT-2K/A, PDOT-2K/B and PDOT-1K devices. It was deduced from the analysis of results of these PEDOT:PSS-based devices that the real-axis resistive impedance (R_{int}) of an energy harvester increased with an increase in the optimal load resistance (R_L) of the device. This was in concordance with the maximum power theorem which states that, the maximum power transfer occurs when the impedance of a connected load is equal to the internal impedance of the source²³. Therefore it was

concluded experimentally that the real-axis load impedance was linked with the optimal load resistance (R_L) of the devices. In addition, it was also observed that increase in resistive (R_{int}) internal impedance or optimum load resistance (R_L) is caused either due to increase in device R_s or R_{sh} . Devices with increased R_{sh} had increased optimum R_L and P_L , because increased R_{sh} is linked with reduction in device leakage losses^{24–26}. On the contrary, devices with increased R_s had increased R_L but decreased P_L ^{27–29}; because increased R_s caused increase in I^2R_s ³⁰ and resistive losses in the device.

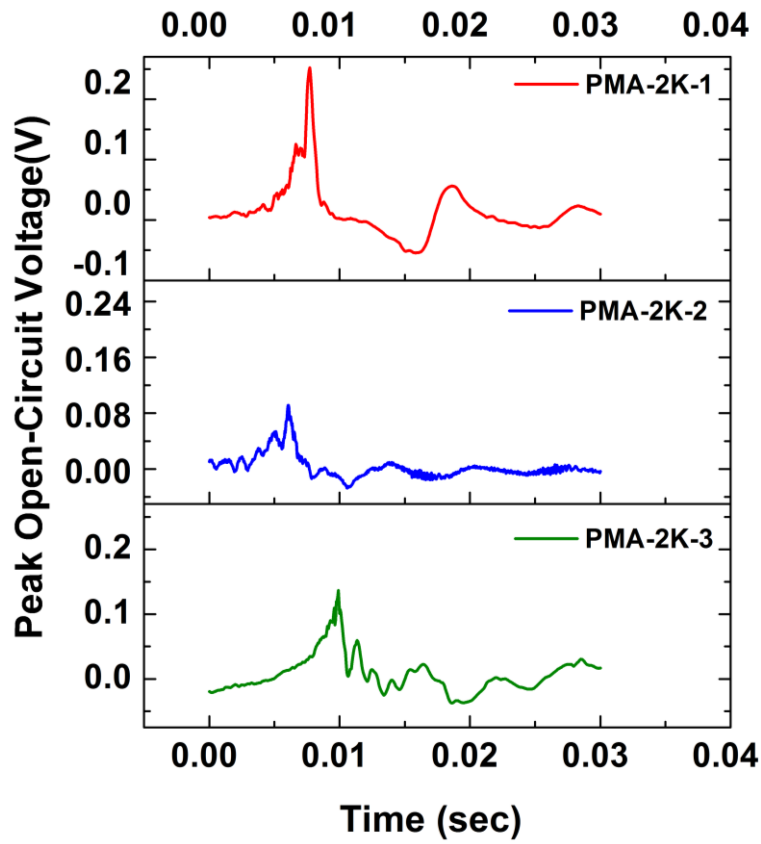


Figure 98. Measured peak open-circuit voltage output of PMA-2K devices.

Measurements performed for peak open-circuit voltage (V_{oc}) and peak short-circuit current density (J_{sc}) determined that among PMA-2K and PMA-3K devices, PMA-2K-1 generated the highest V_{oc} and J_{sc} of 250 mV and $3.2 \mu A cm^{-2}$ (Figure 98). The resistive load matching of the device assisted in analysis of its peak-power density (P_L) of $0.4 \mu W cm^{-2}$ across an optimum load of $363 k\Omega$ (Figure 99) (Table 20). The other devices in PMA-2K group such as PMA-2K-1 and PMA-2K-2 generated V_{oc}

of 90 mV and 140 mV with J_{sc} of $1.7 \mu A cm^{-2}$ and $2 \mu A cm^{-2}$. The lower V_{oc} and J_{sc} of the PMA-2K-2 and PMA-2K-3 devices were linked with the lower shunt resistance (R_{sh}) of these devices which were $6.8 k\Omega$ and $46 k\Omega$, respectively. Although it was understood that the J-V characteristic curve of PMA-2K devices was affected by incomplete solvent evaporation, which affected their R_s and R_{sh} . However, the effect of lower R_{sh} can also be inferred from optimum load resistance of PMA-2K-3 device; that is to say, the maximum P_L was generated as $0.1 \mu W cm^{-2}$ across $271 k\Omega$, which was 1.5 times lower than that of the PMA-2K-1 device. In addition, the R_{int} of PMA-2K-3 devices was $120 k\Omega$ which was 4 times lower than the $467 k\Omega$ R_{int} of the PMA-2K-1 device. It was determined previously that the real-axis resistive internal impedance (R_{int}) obtained from the Nyquist plots of an energy harvester increased with an increase in its shunt and series resistance. Therefore, the real-axis R_{int} in case of PMA-2K-3 device, its optimum load resistance (R_L) and calculated R_s from J-V curve were lower than that of the PMA-2K-1 device which indicated that the overall shunt resistance of the device was reduced.

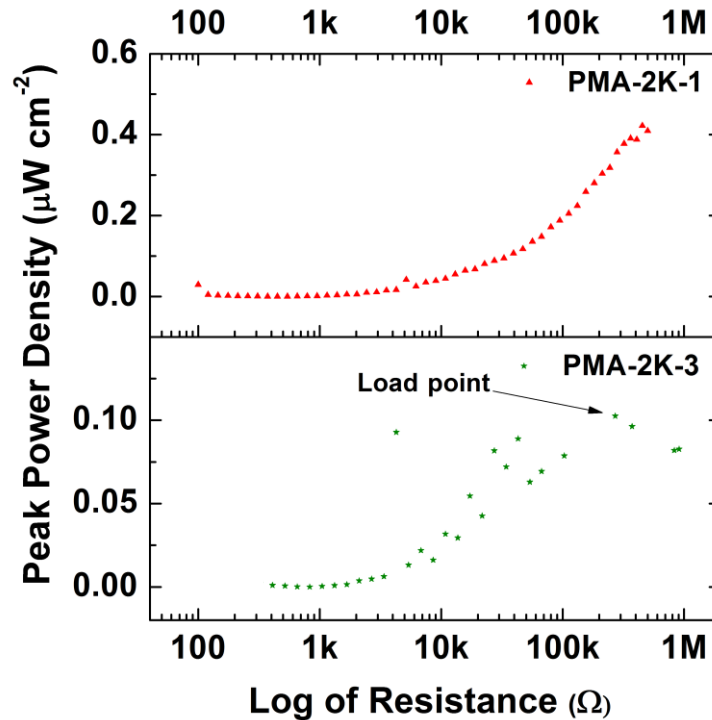


Figure 99. Resistive load matching for power density calculation of PMA-2K devices the impedance plot contained higher noise points near the optimum load resistance (R_L) (due to incomplete solvent evaporation effects). Therefore, the R_L is marked for clarity.

Effects of Electrode Materials on Device Performance

As a result of higher power density for PMA-2K-1 devices, its energy delivered to the load and charge displaced across load were 0.22 nJ cm^{-2} and 74.64 nC cm^{-2} which were higher than the rest of the devices in PMA-2K devices (Table 21).

Table 20. V_{oc} , J_{sc} and P_L of PMA-2K devices.

Device Name	Peak Open-Circuit Voltage	Peak Short-Circuit Current Density	Peak Power Density	Load Resistance
	V_{oc} (mV)	J_{sc} ($\mu\text{A}/\text{cm}^2$)	P_L ($\mu\text{W}/\text{cm}^2$)	R_L (k Ω)
		Measured/Calculated	Manual/Decade Box	
PMA-2K-1	250	3.2	0.4	363
REMARKS		Calculated across 50 k Ω	Decade Box	
PMA-2K-2	90	1.7	-	-
REMARKS		Calculated across 40 k Ω	Device Broken	Device Broken
PMA-2K-3	140	2.0	0.1	271
REMARKS		Calculated across 45 k Ω	Decade Box	

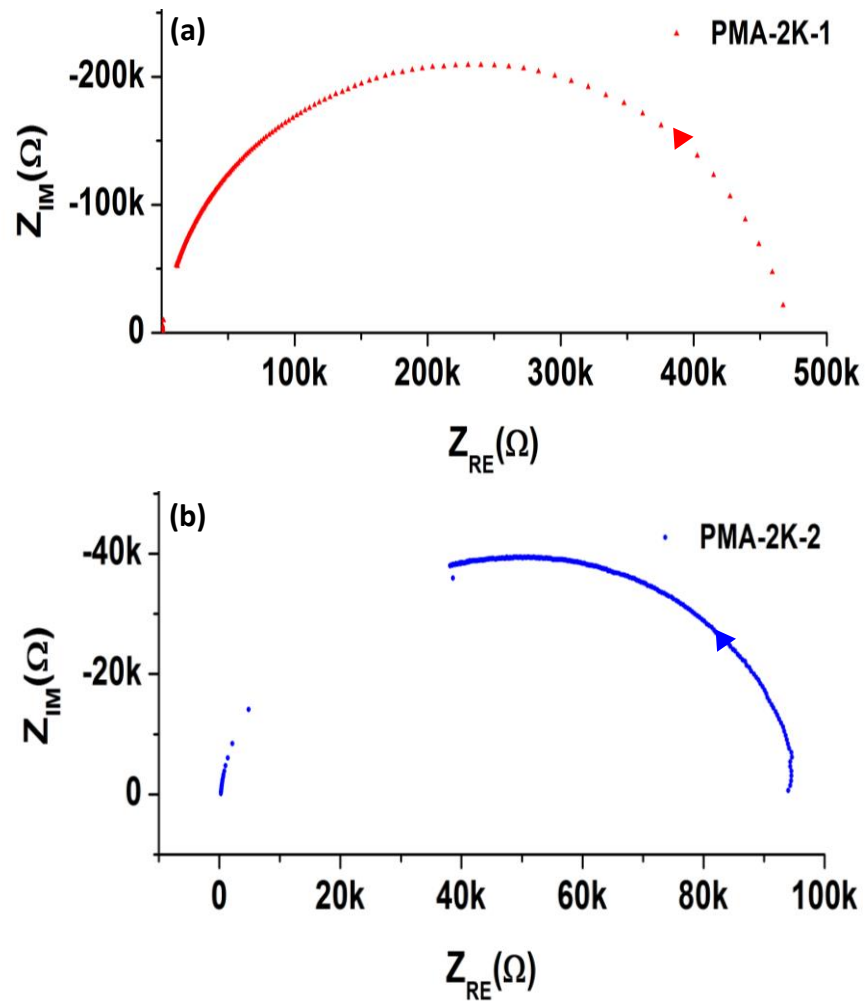


Figure 100. Nyquist plots from impedance analysis of PMA-2K devices.

Table 21. Performance parameters of PMA-2K devices.

Device Name	Peak Open-Circuit Voltage	Peak Short-Circuit Current Density	Peak Power Density	Load Resistance	Energy Density	Charge Displaced	Series Resistance	Shunt Resistance	Real Impedance
	V_{oc} (mV)	J_{sc} ($\mu A/cm^2$)	P_L ($\mu W/cm^2$)	R_L (k Ω)	E_L (nJ/cm 2)	Q_L (nC/cm 2)	R_s (k Ω)	R_{sh} (k Ω)	R_{int} (k Ω)
		Measured/Calculated	Manual/Decade Box						Performed/Not Performed
PMA-2K-1	250	3.2	0.4	363	0.13	1.65	0.70	81.5	467
REMARKS		Calculated across 50 k Ω	Decade Box				Effectuated by Anisole (Solvent)		
PMA-2K-2	90	1.7	-	-	-	-	0.60	6.8	-
REMARKS		Calculated across 40 k Ω	Device Broken	Device Broken	Device Broken	Device Broken	Effectuated by Anisole (Solvent)		Device Broken
PMA-2K-3	140	2.0	0.1	271	0.10	1.41	0.65	46	120
REMARKS		Calculated across 45 k Ω	Decade Box				Effectuated by Anisole (Solvent)		

The PMA-3K devices were analysed in the same manner as the PMA-2K devices. The device with highest P_L among PMA-3K devices was PMA-3K-1, which generated $0.27 \mu\text{W cm}^{-2}$ across $67 \text{ k}\Omega$ and the highest V_{oc} and J_{sc} of 100 mV and $8 \mu\text{A cm}^{-2}$. For PMA-3K-3 device, although due to its R_{sh} being 10 times higher than the PMA-3K-1 device, it generated 165 mV which was 1.6 times higher than PMA-3K-1 device. However, PMA-3K-3 had R_s twice as high as PMA-3K-1 device, which caused a drop of current density across R_s to be higher than that of the PMA-3K-1 device. Consequently, the J_{sc} of PMA-3K-3 device was $2.7 \mu\text{A cm}^{-2}$, which was 3 times lower than PMA-3K-1 (Figure 101). Consequently, the P_L , which was the product of current density and voltage across the optimum load (R_L), also decreased to $0.157 \mu\text{W cm}^{-2}$. The R_L of PMA-3K-3 was also indicative of its high resistive impedance, since it was $488 \text{ k}\Omega$ and 7 times higher than that of the PMA-1K-1 device. The real-axis resistive impedance (R_{int}), obtained from impedance analysis results of this device, was not of the same order of magnitude as its R_L . This was possibly occurred because of high overall R_s of the device, which caused it to be detected as an open-circuit by the impedance measurement system (Figure 102).

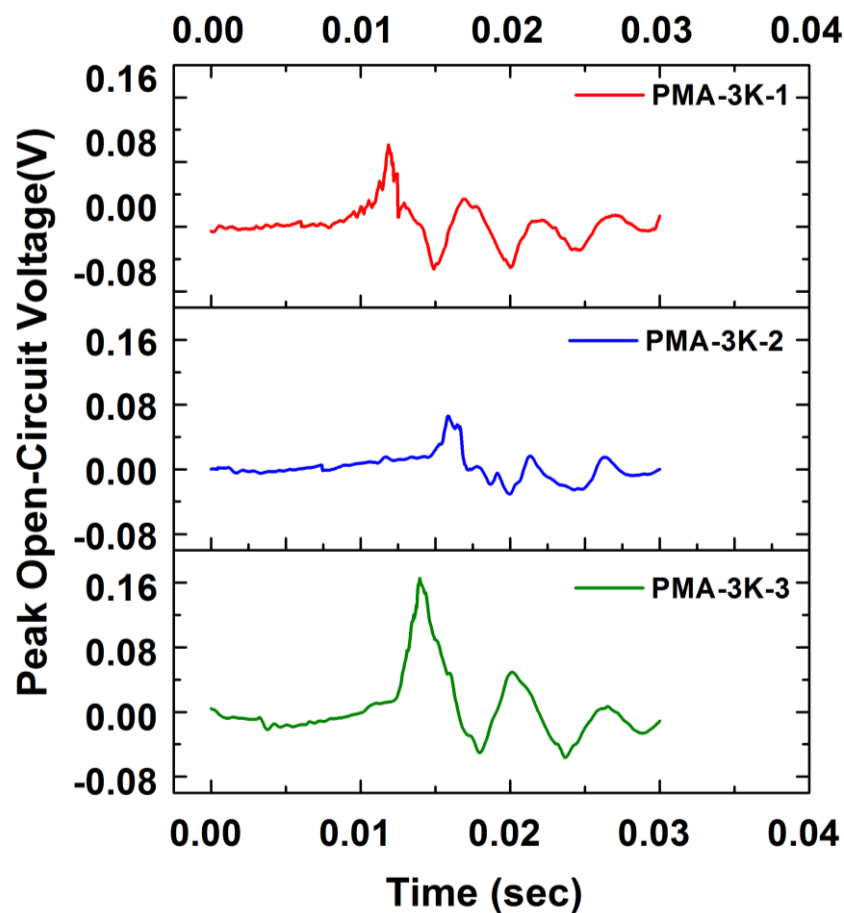


Figure 101. Measured peak open-circuit voltage of PMA-3K devices.

Table 22. J_{sc} and V_{oc} and P_L of PMA-3K devices.

Device Name	Peak Open-Circuit Voltage	Peak Short-Circuit Current Density	Peak Power Density	Load Resistance
	V_{oc} (mV)	J_{sc} ($\mu\text{A}/\text{cm}^2$)	P_L ($\mu\text{W}/\text{cm}^2$)	R_L (k Ω)
		Measured/Calculated	Manual/Decade Box	
PMA-3K-1	100	8.0	0.277	67.14
REMARKS		Measured	Decade Box	
PMA-3K-2	60	1.65	0.0199	43
REMARKS		Measured	Decade Box	
PDOT-3K-3	165	2.7	0.157	488
REMARKS		Measured	Decade Box	

Similarly the R_s and R_{sh} of PMA-3K-2 device was studied in the light of its output performance. This device comprised of the lowest R_{sh} of 1.76 k Ω and thus generated the lowest V_{oc} among the PMA-3K devices of 60 mV. This caused the voltage-driven J_{sc} of this device to reduce to 1.65 $\mu A cm^{-2}$ and hence the P_L of the devices was lowered to 0.02 $\mu W cm^{-2}$ across 43 k Ω .

The power density across optimum load (P_L) for the PMA-3K-1 device was the highest among PMA-3K devices, and its energy delivered and charge displaced across optimum load were 0.14 nJ cm^{-2} and 51.45 nC cm^{-2} ; which were also the highest among the rest of the devices (Figure 103).

To sum up, the P_L of overall PMMA-based devices was ranged between 0.02 $\mu W cm^{-2}$ to 0.4 $\mu W cm^{-2}$. In addition, their optimum load of maximum power transfer was ranged from 43 k Ω to 488 k Ω . These values of R_L were affected by the R_s and R_{sh} of devices. For the case of devices with high R_{sh} , an increase of R_L was associated with an increase in P_L . On the contrary, for devices with high R_s , the increase of R_L caused decrease in P_L . The device which was best in terms of overall V_{oc} , J_{sc} and P_L was PMA-2K-1. It generated V_{oc} and J_{sc} of 250 mV and 3.2 $\mu A cm^{-2}$. The P_L of the device was 0.4 $\mu W cm^{-2}$ generated across 363 k Ω R_L .

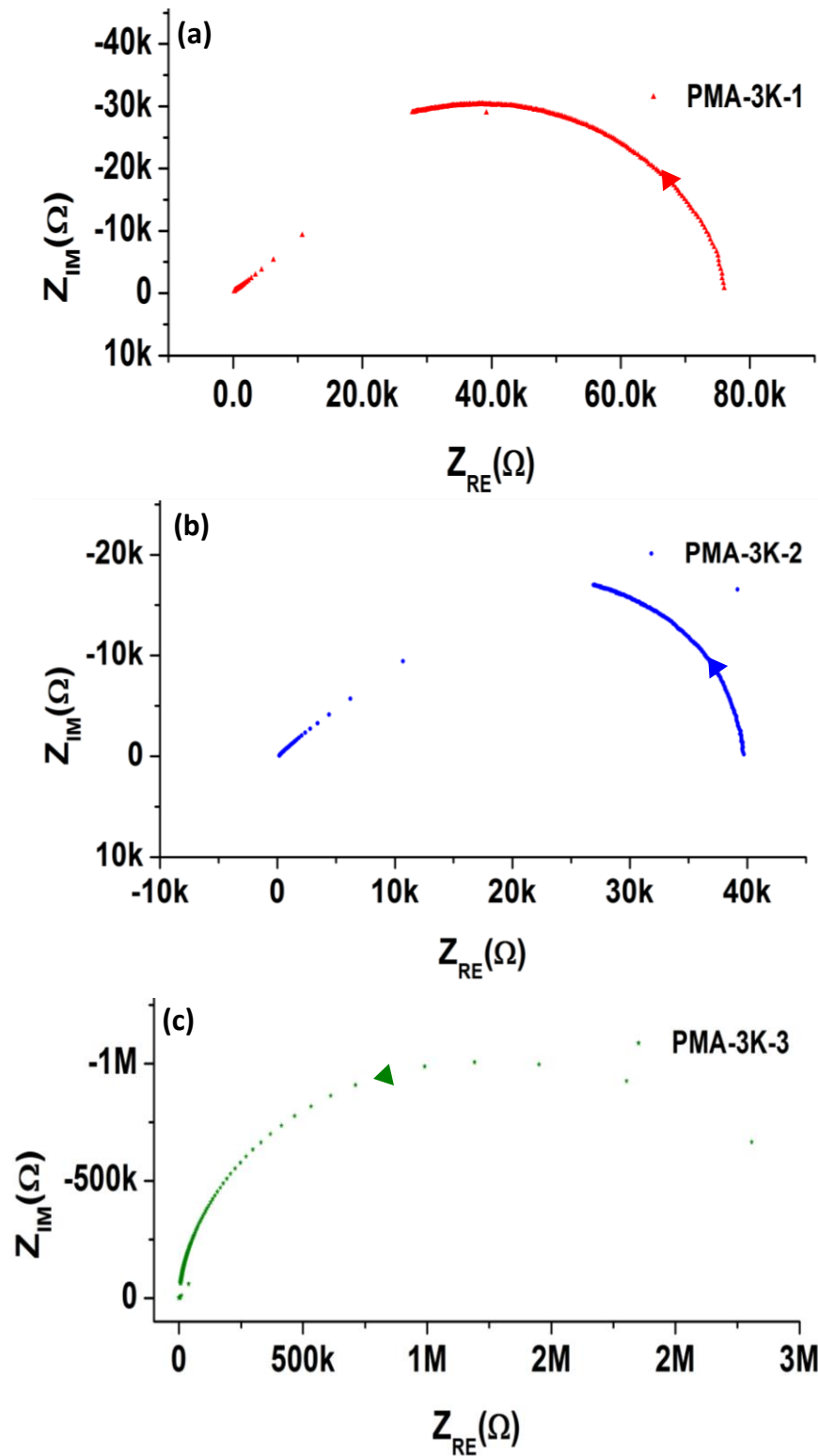


Figure 102. Nyquist plots from the impedance analysis of PMA-3K devices.

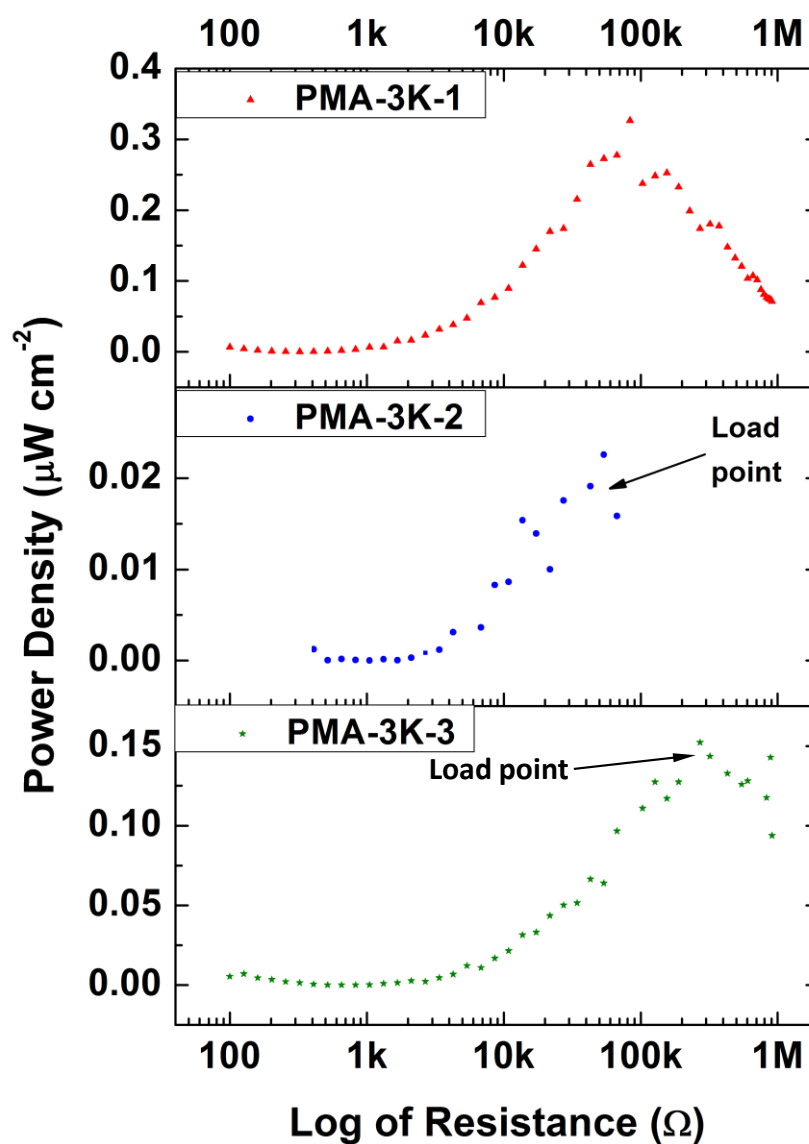


Figure 103. Resistive load matching for PMA-3K devices. For PMA-3K-2 and PMA-3K-3, the impedance plot contained higher noise points near the optimum load resistance (R_L) (due to incomplete solvent evaporation effects). Therefore, the R_L is marked for clarity.

Table 23. Performance parameters of PMA-3K devices.

Device Name	Peak Open-Circuit Voltage	Peak Short-Circuit Current Density	Peak Power Density	Load Resistance	Energy Density	Charge Displaced	Series Resistance	Shunt Resistance	Real Impedance
	V_{oc} (mV)	J_{sc} ($\mu A/cm^2$)	P_L ($\mu W/cm^2$)	R_L (k Ω)	E_L (nJ/cm 2)	Q_L (nC/cm 2)	R_s (k Ω)	R_{sh} (k Ω)	R_{int} (k Ω)
		Measured/Calculated	Manual/Decade Box						Performed/Not Performed
PMA-3K-1 REMARKS	100	8.0 Measured	0.277 Decade Box	67.14	0.09	2.29	1.25	4.78	76
PMA-3K-2 REMARKS	60	1.65 Measured	0.0199 Decade Box	43	0.07	3.00	1.02	1.76	40
PDOT-3K-3 REMARKS	165	2.7 Measured	0.157 Decade Box	488	0.02	0.53	10	10	3000

6.4. Comparative Analysis on the PEDOT:PSS-based and PMMA-based Devices

The electrical characterisation of devices was an essential step toward obtaining a complete profile on the device performance under the effect of different electrodes. The details thus obtained provided a useful comparison between insulator-type and p-n junction-type devices and assisted in understanding the differences in electromechanical efficiencies of the two systems. The aim of analysing the performance differences between PMMA and PEDOT:PSS, devices in groups PMA-2K, PMA-3K, PDOT-2K/A, PDOT-2K/B and PDOT-1K were considered. The two types of devices were used to analyse and compare the screening effects of different top electrode materials in piezoelectric energy harvesters. In addition, the effect of electrode material on the performance parameters of an energy harvester was also analysed.

Table 24. Measured and calculated performance parameters of the PMMA and PEDOT:PSS devices ¹⁶.

	PMMA Device PMA-2K-1	PEDOT:PSS Device PDOT-A1
Peak open-circuit voltage(mV)	250	225
Peak short-circuit density (mA cm^{-2})	0.003	0.8
Instantaneous peak power density (μWcm^{-2})	0.4	54
Energy Density (nJcm^{-2})	0.13	17
Approximate internal impedance, R_{int} (real, $\text{k}\Omega$)	467	2
Charge Transferred (nC cm^{-2})	1.65	247
Optimum load ($\text{k}\Omega$)	363	2.09
Calculated Series Resistance (R_s)	0.7	0.172
Calculated Shunt Resistance (R_{sh})	81.5	1.65

To begin with the analysis on comparison between PMMA and PEDOT:PSS-based devices, here we considered one best device, in terms of P_L , from each type: PDOT-A1 and PMA-2K-1. Table 24 compares the performance parameters of the PDOT-A1 and PMA-2K-1. The P_L of the PDOT-A1 was calculated to be two orders of magnitude higher than the PMA-1K-1 device. The 250 mV V_{oc} of PMA-2K-1 was although higher than 225 mV of PDOT-A1, but its J_{sc} was 2 orders of magnitude lower than 0.8 mA cm^{-2} of PDOT-A1. The resistive internal impedance (R_{int}) of

PDOT-A1 device was $2\text{ k}\Omega$ which was 180 times lower than the $363\text{ k}\Omega$ of PMA-2K-1 device. Moreover for PMA-2K-1, both the R_s and R_{sh} were 81 and 7 times higher than that of the PDOT-2K-1 device.

Therefore, it was observed that the internal impedance of the PMA-2K-1 device was higher than the PDOT-A1 device. The factor which dictated the differences in impedance of the two devices was the electrode conductivity. Being an insulator, the electrode resistivity of PMMA was considerably higher than the semiconducting PEDOT:PSS. Due to this, the overall R_{int} of PMMA-type devices was $40 - 500\text{ k}\Omega$ (Table 21 and Table 23); which was higher than the $0.5\text{ k}\Omega - 2\text{ k}\Omega$ (Table 17) R_{int} of PEDOT:PSS-based devices. Despite of higher internal impedance, the V_{oc} of PMA-2K-1 was higher than PDOT-A1. This was believed to be linked with lower screening rate caused by the insulating properties of PMMA. To elaborate the screening mechanisms, the energy band diagrams of PEDOT:PSS-based and PMMA-based devices were hypothesised and presented in Figure 104 and Figure 105. The PEDOT:PSS-based device comprised of p-n junction between ZnO and PEDOT:PSS (Figure 104). In Figure 104(b), the tilted bands represent polarised ZnO, and the depolarisation field (E_{dep}) allow movement of carriers within the material (Figure 104(b)). These carriers flow toward the positive potential of E_{dep} and accumulate at the positive charged zone of depletion region. Moreover, the positive potential of E_{dep} cause the holes in PEDOT:PSS to drift away from the depletion region. Hence, the accumulation of carriers in the depletion region and drift of holes away from depletion region caused complete screening of the positive polarisation.

Similarly, the screening mechanism in PMMA-based devices was studied. When ZnO was polarised, the free-carriers move toward the positive potential of E_{dep} (Figure 105(b)) and accumulate at the ZnO/PMMA interface (Figure 105(b)). Due to this accumulation, the screening of positive polarisation took place. However, unlike PEDOT:PSS, the insulating properties of PMMA would not exhibit screening effect. That is to say that, because PMMA is an insulator, it will not participate in transferring carriers into ZnO. Therefore, the rate of screening in case of PEDOT:PSS-based devices was believed to be faster than PMMA-based devices. Hence, the V_{oc} of PMA-2K-1 was higher than PDOT-A1.

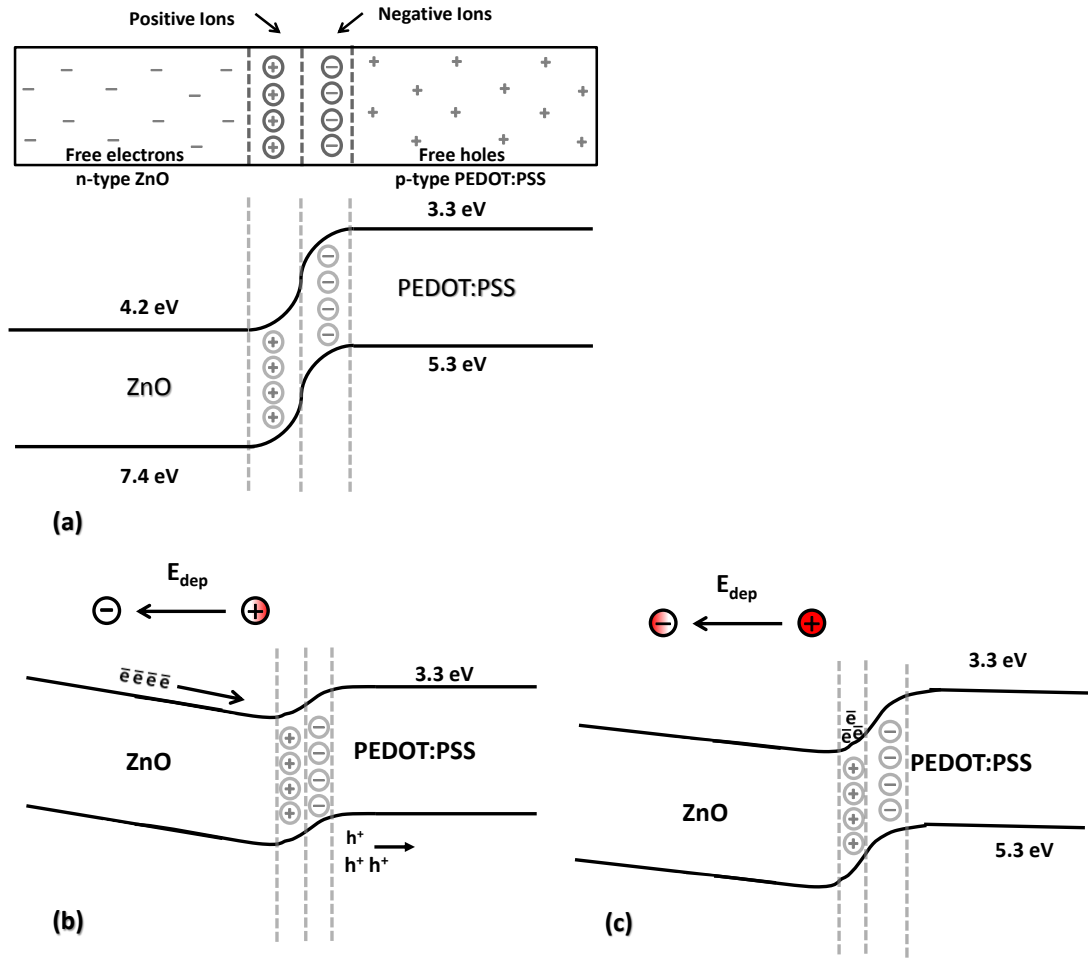


Figure 104. (a) PEDOT:PSS/ZnO p-n junction at equilibrium. (b) Polarised ZnO causing free carriers to move toward positive polarisation and holes in PEDOT:PSS drifting away from depletion region. (c) Complete screening of positive polarisation caused by accumulated charges at the junction and internal flow of carriers. Assumed partial screening of negative polarisation.

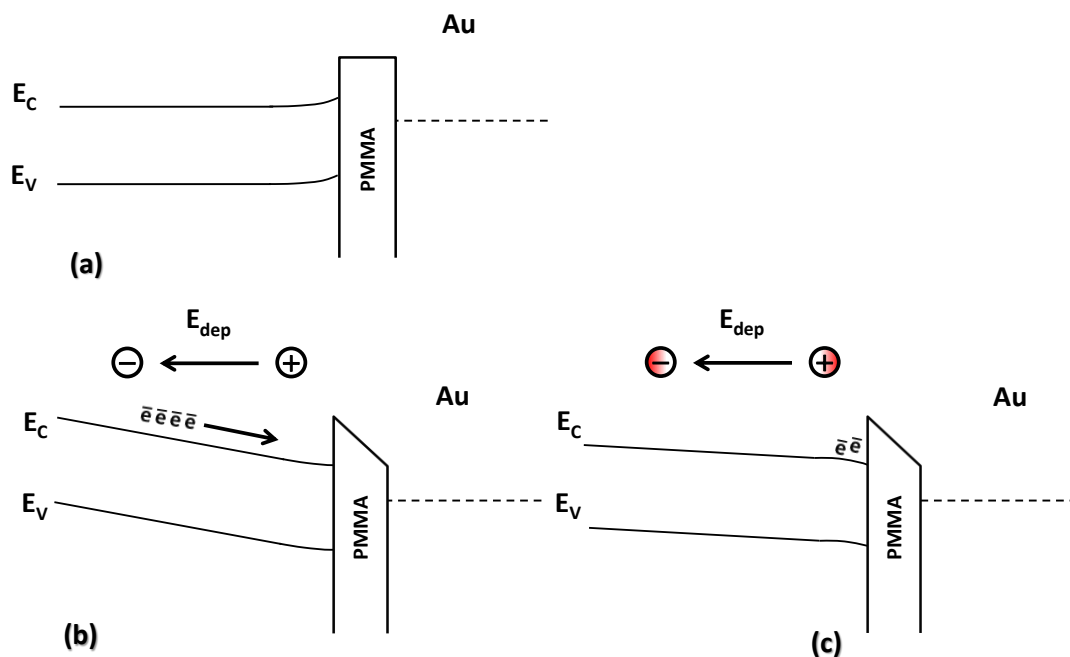


Figure 105. (a) Au (gold)/PMMA/ZnO metal-insulator-semiconductor junction at equilibrium. (b) Polarised ZnO causing free carriers to move toward positive polarisation (c) Partial screening (representing slower screening rate) of positive polarisation caused by accumulated internal carriers at the PMMA/ZnO junction only. Assumed partial screening of negative polarisation.

The overall R_{int} of PMMA-type devices of 40 – 500 k Ω was linked with the non-conductivity of PMMA. Due to this, the R_{sh} and R_s of PMMA-based devices were as high as 81.5 k Ω and 1 k Ω . At the same time, as described above, the non-conductivity of PMMA also caused lower external screening effects. Therefore, despite of higher R_s and I^2R_s losses, the average voltage generation from PMMA devices in group PMA-2K and PMA-3K was 135 mV and the average generation from PDOT-2K/A and PDOT-2K/B was 100 mV. In addition, the PMA-3K-2 device with an R_{sh} of 1.76 k Ω (which was lower than 2.3 k Ω of PDOT-1K-2 device) and R_s of 1.02 k Ω (which was higher than 0.6 k Ω of PDOT-1K-2), generated V_{oc} twice as high as PDOT-1K-2. This indicated that along with R_s and R_{sh} , the external screening effect was also affecting the device performances. Consequently, on average scale the V_{oc} of PMMA-based devices were higher than PEDOT:PSS-based devices, despite their higher I^2R_s losses considered across 0.6 k Ω to 1.25 k Ω R_s .

Thus, the lower external screening effect in PMMA-based device than the PEDOT:PSS-based device was maintaining the V_{oc} ranged 60 – 250 mV in PMA-2K

and PMA-3K device, which were higher than 22 mV – 225 mV ranged PDOT-2K/A and PDOT-2K/B devices. However, as mentioned previously, across R_s of PMA-2K and PMA-3K the drop of voltage-driven current was higher because of having higher overall R_s of 0.6 – 1.25 k Ω in PMA-2K and PMA-3K devices. Therefore, the J_{sc} was two orders of magnitude lower than PDOT-2K/A and PDOT-2K/B devices. This caused the P_L of these devices to decrease and the effect of 10 to 20 times higher R_s than PEDOT:PSS-based devices was observed in the high optimum load resistances of 43 – 488 k Ω .

In summary, having insulating top electrode was essential in keeping the electrode external screening effects to minimum. In case of PEDOT:PSS devices, which had semiconducting top electrode, the external screening was believed to adversely affect the polarisation field in ZnO. Consequently, the measured potential difference between the device terminals was reduced. Contrary to generating 60 – 250 mV which was higher than 22 – 225 mV of PEDOT:PSS devices; however, the P_L of 0.02 - 0.4 $\mu\text{W cm}^{-2}$ for PMMA devices, was one to two orders of magnitude lower than that of the PEDOT:PSS devices.

According to maximum power transfer theorem³¹, the optimum load depends on the internal impedance of the device. From the Nyquist plots, the internal impedance of the PEDOT:PSS device was 0.6 – 2 k Ω and that of the PMMA device was 43 - 488 k Ω . It was indicative that, the higher optimum load for PMMA device than the PEDOT:PSS device was possibly caused by high R_s of the insulating top electrode. Further to this, the J-V characteristic curves of the two devices also indicated that the series resistance of the PMMA devices were 10 to 20 times higher than PEDOT:PSS devices. Hence, the electrical characterisation indicated that the high internal impedance of the PMMA suppressed the current delivered to this load (since, $I = \frac{V}{R}$). For example, the calculated current density, across the optimum load, delivered by PMA-2K-1 device was 1.16 $\mu\text{A cm}^{-2}$ which was ~300 times lower than the PEDOT:PSS device. As a result of this, the calculated P_L of the device decreased by two orders of magnitude. This was also reflected in the calculated energy delivered by PMMA device to the load, which were reduced by two orders of magnitude when compared to PEDOT:PSS device¹⁶.

6.5. Summary

This chapter elaborates the sources of losses in ZnO piezoelectric polarisation which are introduced by electrode material type. For the bottom electrode three types of materials were chosen: silver, Zn and ITO. The materials Ag (silver) and zinc having work function of 4.26 and 4.3 eV were used to determine the role of Ohmic contacts in screening of polarisation charges. It was observed that metal Ohmic contacts of zinc with ZnO increased the rate of screening and it was not considered suitable for device operation. The reason for this increased rate of screening was related to low resistance Ohmic junction (non-rectifying), which allowed free-carriers to enter conveniently from zinc into ZnO. On the contrary, ITO which has a slightly higher work function than ZnO was considered to form a rectifying Schottky contact with ZnO. It was believed that having a Schottky contact between ZnO and ITO reduced the injection of free-carriers from ITO to ZnO. Thus the rate of screening was reduced. Consequently, the output voltage generated by ITO-based PDOT-Sm devices was two orders of magnitude higher than Zn foil-based PDOT-Zn devices.

In silver electrode devices, the shunt resistance was considerably low and therefore they were not suitable for output measurement and further analysis. The ITO-based devices generated measureable voltage output due to lower rate of screening effects. Therefore, ITO was used as bottom electrode for devices which were experimented for further studies and analysis.

The device top electrodes have obtained appreciable attention in terms of their screening effects on ZnO piezoelectric polarisation. However, most of the studies carried out in this regard were focussed on open-circuit voltage and short-circuit current measurement, which were not enough to portray the complete behaviour of top electrode material. The resistive load matching and impedance analysis were two important approaches adopted in this work which highlighted the effects of electrode conductivity on device performance. It was deduced from the results that, due to negligible external screening effects of the insulating PMMA electrode, the open-circuit voltage output ($V_{oc} = 250$ mV) of its device PMA-2K-1 was higher when compared to the PEDOT:PSS semiconducting top electrode-based device, PDOT-A1. However, due to high series resistance, the internal impedance of the PMA-2K-1 device was 180 times higher than the PDOT-A1 device and therefore, the current

delivered to the load by a PMMA device was two orders of magnitude lower than that of the PEDOT:PSS device. Therefore, the power delivered by the PMMA-based device dropped by two orders of magnitude to $0.4 \mu\text{W cm}^{-2}$ when compared with $54 \mu\text{W cm}^{-2}$ generated by PDOT-A1.

Hence, it was concluded that the analysis of electrode material electrical characteristics is essential for understanding the impact of its impedance losses on the devices. Similarly, the analysis of device operation under load is also important to obtain the realistic concept of its electromechanical conversion efficiency.

6.6. References

1. J. Briscoe, M. Stewart, M. Vopson, M. Cain, P. M. Weaver, and S. Dunn, *Adv. Energy Mater.*, 2012, **2**, 1261–1268.
2. Y. Hu, Y. Zhang, C. Xu, L. Lin, R. L. Snyder, and Z. L. Wang, *Nano Lett.*, 2011, **11**, 2572–7.
3. G.-H. Nam, S.-H. Baek, C.-H. Cho, and I.-K. Park, *Nanoscale*, 2014, **6**, 11653–11658.
4. V. S. Bagad, *Microwave Engineering-II*, Technical Publications, 2009.
5. T. Takahashi, T. Takenobu, J. Takeya, and Y. Iwasa, *Appl. Phys. Lett.*, 2006, **88**, 033505.
6. S.-I. Hsiu, J.-F. Huang, I.-W. Sun, C.-H. Yuan, and J. Shiea, *Electrochim. Acta*, 2002, **47**, 4367–4372.
7. Y. Hu, L. Lin, Y. Zhang, and Z. L. Wang, *Adv. Mater.*, 2012, **24**, 110–4.
8. A. Rockett, *The Materials Science of Semiconductors*, Springer, 2007.
9. L. W. Teo, V. T. Ho, M. S. Tay, Y. Lei, W. K. Choi, W. K. Chim, D. A. Antoniadis, and E. A. Fitzgerald, 2003.
10. M. Neeraj, *Applied Physics for Engineers*, PHI Learning Pvt. Ltd.
11. A. S. Zakirov, S. U. Yuldashev, J. C. Lee, T. W. KANG, and H. D. Cho, *J. Korean Phys. Soc.*, 2011, **59**, 482–484.
12. K. L. Mittal, *Polyimides and Other High Temperature Polymers: Synthesis, Characterization and Applications*, Taylor & Francis, 2005.
13. Tektronix. *TDS2000 Digital Storage Oscilloscopes 2015*. Available at: <http://www.tek.com/datasheet/tds2000/tds2000c-series-datasheet-0>. [Accessed 13 December 2014].
14. Keithley Instruments 2015. *Model 2400 SourceMeter & Instrument - Product Demo*. Available at: <http://www.keithley.com/events/proddemos/2400demo/2400.html>. [Accessed 14 December 2014].
15. M. Abb and O. L. Muskens, *Int. J. Opt.*, 2012, **2012**.
16. J. Briscoe, N. Jalali, P. Woolliams, M. Stewart, P. M. Weaver, M. Cain, and S. Dunn, *Energy Environ. Sci.*, 2013, **6**, 3035.
17. S. Imanaga, F. Nakamura, and H. Kawai, *Jpn. J. Appl. Phys.*, 2001, **40**, 1194.

18. A. S. A. V. Baglio, M. Girolamo, V. Antonucci, *Int. J. Electrochem. Sci.*, 2011, **6**, 3375.
19. M. S. Góes, E. Joanni, E. C. Muniz, R. Savu, T. R. Habeck, P. R. Bueno, and F. Fabregat-Santiago, *J. Phys. Chem. C*, 2012, **116**, 12415–12421.
20. J. Perlich, E. Metwalli, L. Schulz, R. Georgii, and P. Müller-Buschbaum, *Macromolecules*, 2008, **42**, 337–344.
21. H. J. Levinson, *Principles of Lithography*, SPIE Press, 2005.
22. W. C. Tien and A. K. Chu, *Opt. Express*, 2014, **22**, 3944–3949.
23. R. L. Meade, *Foundations of Electronics*, Delmar Cengage Learning, 2002.
24. Solanki, *Solar Photovoltaics: Fundamentals Technologies And Applications*, PHI Learning Pvt. Ltd., 2009.
25. H. H. Kyaw, T. Bora, and J. Dutta, *IEEE Trans. Nanotechnol.*, 2012, **11**, 763–768.
26. G. Prakash and H. P. Garg, *Solar Energy: Fundamentals and Applications*, Tata McGraw-Hill Publishing Company, 2000.
27. R. Pietruszka, B. S. Witkowski, G. Luka, L. Wachnicki, S. Gieraltowska, K. Kopalko, E. Zielony, P. Bieganski, E. Placzek-Popko, and M. Godlewski, *Beilstein J. Nanotechnol.*, 2014, **5**, 173–179.
28. M.-H. Lai, A. Tubtimtae, M.-W. Lee, and G.-J. Wang, *Int. J. Photoenergy*, 2010, **2010**.
29. T. Bora, H. H. Kyaw, S. Sarkar, S. K. Pal, and J. Dutta, *Beilstein J. Nanotechnol.*, 2011, **2**, 681–90.
30. M. Paulescu, E. Paulescu, P. Gravila, and V. Badescu, *Weather Modeling and Forecasting of PV Systems Operation*, Springer, 2012.
31. A. V. B. U. A. Bakshi, *Network Analysis And Synthesis*, Technical Publications, 2009.

7. Surface Modified ZnO-based Devices

From the analysis of electrode materials on piezoelectric energy harvester's performance, it was concluded that for optimum power generation semiconducting PEDOT:PSS was an essential material. In addition, ITO bottom electrode, having 4.6 eV work function that was higher than 4.3 eV of ZnO, was also suited for reduced external screening effects. Therefore, for further studies, the Au/PEDOT:PSS/ZnO/ITO heterojunction prototype was used. These p-n junction-type devices were optimised by using surface modified nanorods. For this, the surface of ZnO was passivated using p-type ceramic surface modifier, copper thiocyanate (CuSCN)^{1,2}. CuSCN was coated onto ZnO nanorods surface and incorporated into piezoelectric energy harvesters. Performance of coated-ZnO devices were analysed using no-load voltage and current output measurements, resistive load matching and impedance analysis. In addition, the performance of coated-ZnO-based devices was compared with non-coated ZnO nanorod-based devices. Thus, the difference between non-coated and CuSCN-coated devices' performance was analysed by considering internal screening effects on piezoelectric polarisation of ZnO.

7.1. CuSCN-coated Nanorod-Based Devices

When a piezoelectric material is stressed, the change in polarisation causes movement in internal charge carriers. These mobile free-charge carriers suppress the piezoelectric polarisation immobile charges, causing a phenomenon called screening effect. This effect is called internal screening when free-charge carriers present in the material compensate the depolarisation field¹⁻⁴; whereas, if free-charges from an external contact cause this compensation then the effect is called external screening^{1,2,4,5}. Therefore, rate of internal screening depends on the carrier concentration and conductivity of the piezoelectric material^{1,2,4}. ZnO is intrinsically an n-type

semiconductor and its conductivity is affected by unintentional doping from surface defects and environmentally adsorbed impurities^{1,2}. The most commonly reported native defects are oxygen vacancies, oxygen interstitials, zinc vacancies and zinc interstitials^{1,2,6-9}. The interaction of material surface with gases like CO₂, oxygen, hydrogen and moisture creates hydroxyl radical impurities on ZnO surface^{2,10}. In addition, the synthesis process is known to affect the stoichiometry of Zn and O atoms. In this regard, aqueous solution growth method reportedly yields excess of Zn atoms and oxygen vacancies^{11,12}. Several authors have studied the photoluminescence of ZnO nanostructures and associated the green, yellow, orange-red and blue emissions with surface defects and impurities^{13,14}.

The surface chemistry of ZnO is commonly modified to reduce its parasitic effects on electronic devices such as, transistors¹⁵, photo-detectors¹⁶ and piezoelectric energy harvesters^{2,9,17}. Surface coating techniques have previously been adopted for surface modification, in order to reduce the free carriers introduced by surface states in ZnO. For ZnO-based piezoelectric energy harvesters, the surface states-induced free mobile carriers adversely affect its performance^{4,9,17}. When ZnO is polarised, the free mobile carriers suppress the non-mobile polarisation charges causing a phenomenon called internal screening^{1,2,4,3}. It has been shown that, the surface of states of ZnO can be suppressed by using surface modification technique. This reduces the surface-induced carrier concentration and consequently decreases the rate of internal screening^{4,9,17,18}. Hence, the surface modification or surface passivation technique is essential to improve ZnO-based piezoelectric energy harvester's performance.

Previous studies on ZnO-based piezoelectric energy harvesters have employed a variety of surface modification techniques, such as oxygen plasma treatment, polymer layer coating and thermal annealing. Thermal annealing has been reported to reduce the native defects and impurities of ZnO nanostructures^{1,2,7,17,19,20}. It has been demonstrated that the carrier concentration of ZnO nanowires reduced by two orders of magnitude when annealed in air at 450 °C²¹; which was considered to be caused by mitigation of free carrier-injecting surface species. Moreover, due to the same reason, oxygen plasma treatment was reported to reduce the carrier concentration of ZnO nanowires by 8 to 12 times²² and 40 times in ZnO thin films

²³. In the presented research work, ZnO nanorods surface was coated with p-type ceramic material copper thiocyanate (CuSCN). Surface coating is considered to be more effective surface modification technique when compared with oxygen plasma treatment and thermal annealing, because the adhered chemicals prevent the surface interaction with the atmosphere and mitigate the re-adsorption ⁹ of surface species ^{1,2}.

ZnO nanorods array of 2 μm length and 70 nm width were spray-coated with 0.15 M CuSCN in steps of 2, 10 and 20. For each step, 0.5 ml of CuSCN solution was filled in the pneumatic micro-spray gun reservoir and sprayed onto the nanorods. The CuSCN-coated-ZnO devices prepared after 2, 10 and 20 steps of CuSCN spray-deposition were grouped as CuSCN-2, CuSCN-10 and CuSCN-20. These coated-ZnO devices were compared against the non-coated device group PDOT-2K/A, in order to study the effect of nanorod passivation.

Figure 106 shows the SEM image of the non-coated and coated-ZnO nanorods. The CuSCN layer was coated onto the surface of the nanorods along their lengths. The width of 100 coated and 100 non-coated nanorods was measured. The average width of non-coated nanorod was subtracted from the average width of coated nanorod to estimate the thickness of CuSCN passivation layer. It was observed that for CuSCN-10 and CuSCN-20 samples, 2 nm and 4 nm of CuSCN layer was coated onto the rods. For CuSCN-2 nanorod samples, having the least steps of CuSCN deposition, a change in nanorod width after deposition was not observed. The spray-coating was performed manually therefore the CuSCN coating was not completely uniform. As shown in Figure 107, there were some nanorods around which clusters of CuSCN were formed. Some areas had more coated-nanorods than the others. However, as an overall effect, the increase in CuSCN deposition steps had increased the surface coverage of ZnO ².

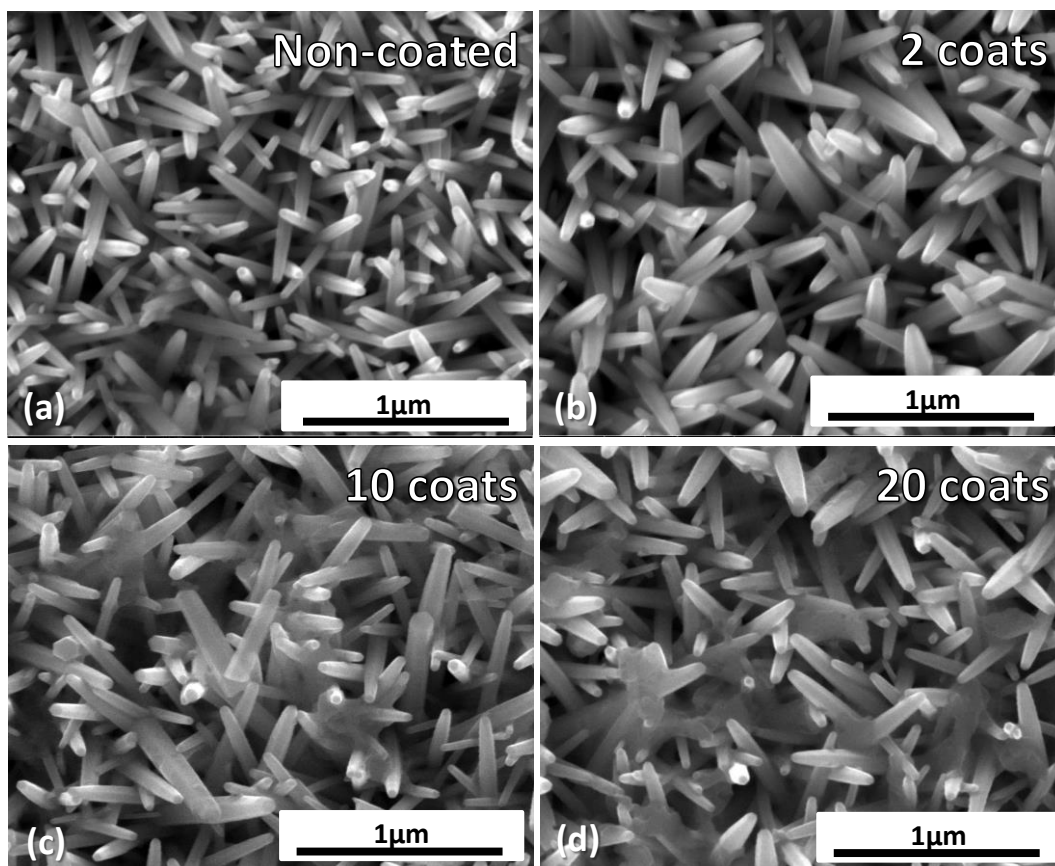


Figure 106. SEM image showing (a) non-coated and as-grown ZnO nanorods, (b) nanorods after 2 steps spray deposition of CuSCN, (c) nanorods after 10 steps spray deposition of CuSCN (d) nanorods after 20 steps spray deposition of CuSCN².

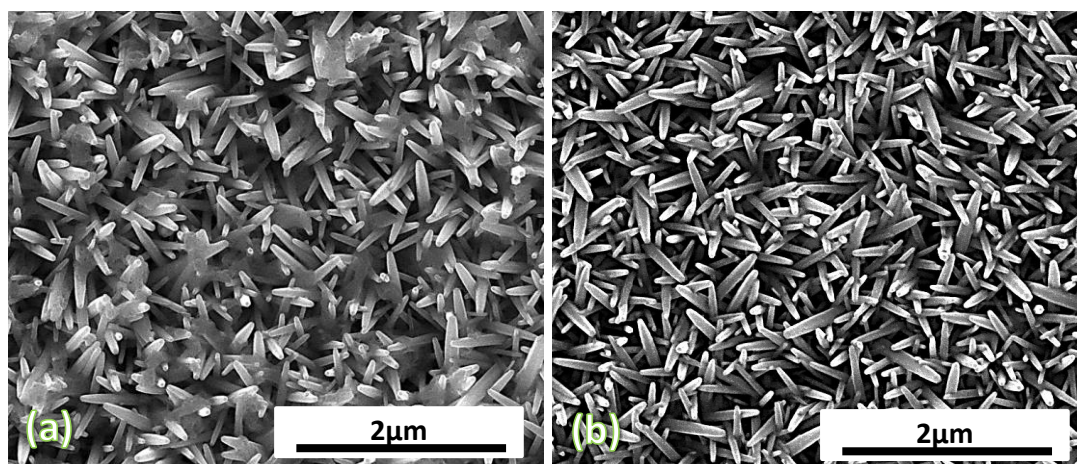


Figure 107. SEM image of nanorods in different regions of CuSCN-20-1 sample: (a) showing rods heavily coated with CuSCN, (b) showing area where rods were not thickly coated with CuSCN. (Images sharpened to observe details).

Table 25 defines the list of devices and their groups used for the surface passivation analysis.

Table 25. List of devices and their respective group titles, used for analysis on surface passivation.

Group Names	Top Electrode Fabrication	Bottom	Devices
		Electrode & Nanorod Fabrication	
PDOT-2K/A	PEDOT:PSS @ 2000 rpm	ITO Sp(25)	PDOT-A1, PDOT-A2
CuSCN-2	PEDOT:PSS @ 2000 rpm	ITO Sp(25)	CuSCN-2-1, CuSCN- 2-2
CuSCN-10	PEDOT:PSS @ 2000 rpm	ITO Sp(25)	CuSCN-10-1, CuSCN-10-2, CuSCN-10-3, CuSCN-10-4
CuSCN-20	PEDOT:PSS @ 2000 rpm	ITO Sp(25)	CuSCN-20-1, CuSCN-20-2, CuSCN-20-3, CuSCN-20-4

7.1.1. Current-Voltage Electrical Characterisation

All the coated and non-coated devices were fabricated using 1 μm thick p-type PEDOT:PSS layer (Figure 108) as the top electrode. Therefore, they were p-n junction-based devices. Additionally, Figure 109 shows CuSCN-full device which was a heterojunction of ITO/ZnO/CuSCN/Au. Therefore, this device had CuSCN, which is a p-type semiconductor ceramic, as the top electrode. Current-voltage J-V characterisation of CuSCN-coated, non-coated and CuSCN-full devices was carried out using Keithley 2400 source meter unit, to observe the diode characteristics between p-type PEDOT:PSS and n-type ZnO. J-V characterisation was an important technique to determine the series R_s and shunt resistance R_{sh} of a system. Therefore, it was considered as a means to analysing parasitic effects of R_s and R_{sh} on device performance, which caused device-to-device variation in specific groups. Figure 111 shows the J-V characteristic curve of the CuSCN-10, CuSCN-20 devices and Figure 110 shows the J-V characteristic curve of the non-coated PDOT-A1 and A2 devices and CuSCN-full device. The J-V relationship of PDOT-A1, A2 and CuSCN-full demonstrated rectifying devices that had a non-linear current-voltage relationship in the forward bias region. In addition, upon application of reverse bias voltage, leakage currents -6 mA cm^{-2} at -2 V for PDOT-A1 and A2 and 50 mA cm^{-2} at -2 V for CuSCN-full was observed, which was related with magnitude of each devices' shunt resistance R_{sh} . This non-linear forward current conduction in J-V characterisation was linked with formation of diode between p-type PEDOT:PSS and n-type ZnO for PDOT-A1 and A2 devices. For CuSCN-full device, a diode formed between p-type CuSCN and n-type ZnO also caused non-linear J-V relationship. As highlighted in the figures, the diode turn-on voltages for PDOT-A1, A2 and CuSCN-full devices was in the range of $0.35 - 0.4 \text{ V}$.

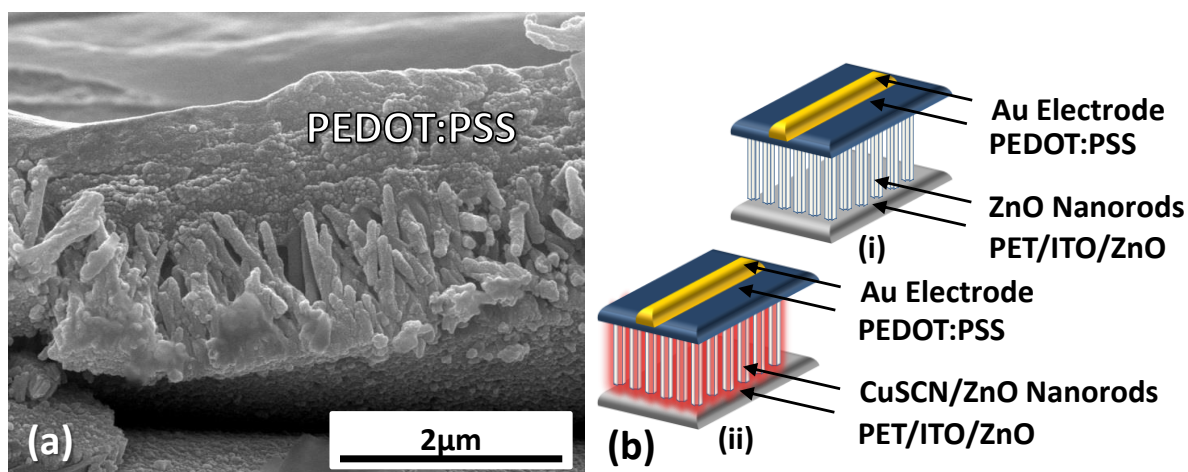


Figure 108. SEM image of PEDOT:PSS layer coated on top of nanorods. This type of top electrode configuration was chosen for both non-coated and CuSCN-coated nanorod devices. (b) Schematic of (i) non-coated PEDOT:PSS-based and (ii) CuSCN-coated PEDOT:PSS-based device.

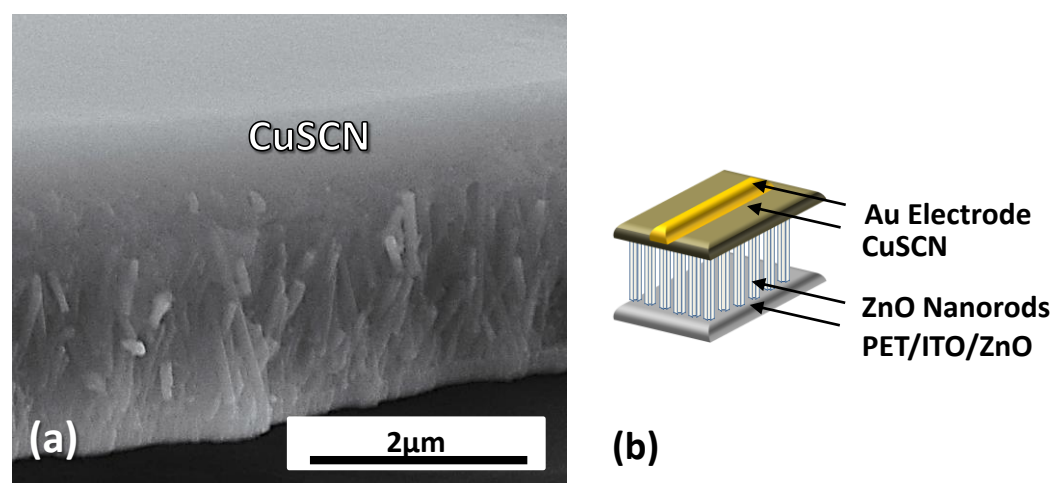


Figure 109. SEM image of CuSCN layer coated on top of nanorods in CuSCN-full device. (b) Schematic of (i) CuSCN-full device showing ITO/ZnO/CuSCN/Au heterojunction.

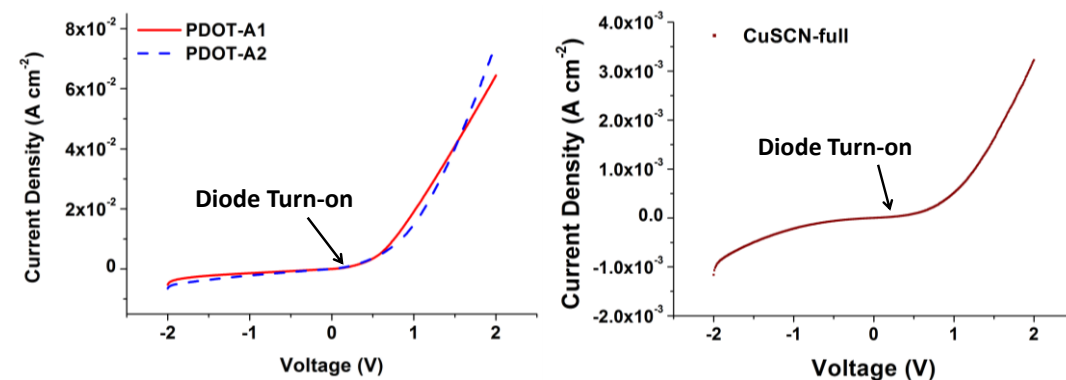


Figure 110. J-V characteristic curve of PDOT-A1, A2 and CuSCN-full devices.

However, the J-V characteristic curves of CuSCN-10 and CuSCN-20 devices were different from the PDOT A1, A2 and CuSCN-full devices. To elaborate, let us consider the J-V characteristic curves of CuSCN-20 devices (Figure 111(c)). The forward bias region from 0 to +2 V for CuSCN-20 was a non-linear current-voltage relationship like PDOT-A1, A2 and CuSCN-full devices, having diode turn-on voltage from 0.35 – 0.4 V; but in the reverse bias region, another diode was switched on at -0.5 V causing a non-linear J-V response. This response was analysed by considering the two types of p-n junction diodes in the presented CuSCN-coated PEDOT:PSS-based devices, which were: PEDOT:PSS/ZnO diode and CuSCN/ZnO diode. It was considered that the presence of these two diodes in one system caused the J-V behaviour to be different from a standard p-n junction diode. It was speculated that the resultant J-V characteristic curve of CuSCN-coated devices were composed of two overlapped responses of PEDOT:PSS/ZnO and CuSCN/ZnO diodes. Upon considering J-V relationship of CuSCN-2 devices, the overlap of CuSCN/ZnO diode response was negligible, since the number of spray steps in this system was the least. Therefore, the J-V characteristic profile of CuSCN-2 (Figure 111(a)) devices was similar to that of PDOT-A1 and A2 devices. Hence, with the increase in CuSCN deposition steps, the CuSCN/ZnO diode became elaborate in the J-V characteristic curve. The R_s and R_{sh} extraction method from J-V response is based on a single diode system; and due to complexity of ZnO/CuSCN/PEDOT:PSS system, the slope calculation method to determine R_s and R_{sh} could not be applied. Therefore, the R_s and R_{sh} could not be extracted for study on device-to-device

variation in a specific group. Instead, the performance variation of devices was studied by considering only the effects of CuSCN coating on internal screening.

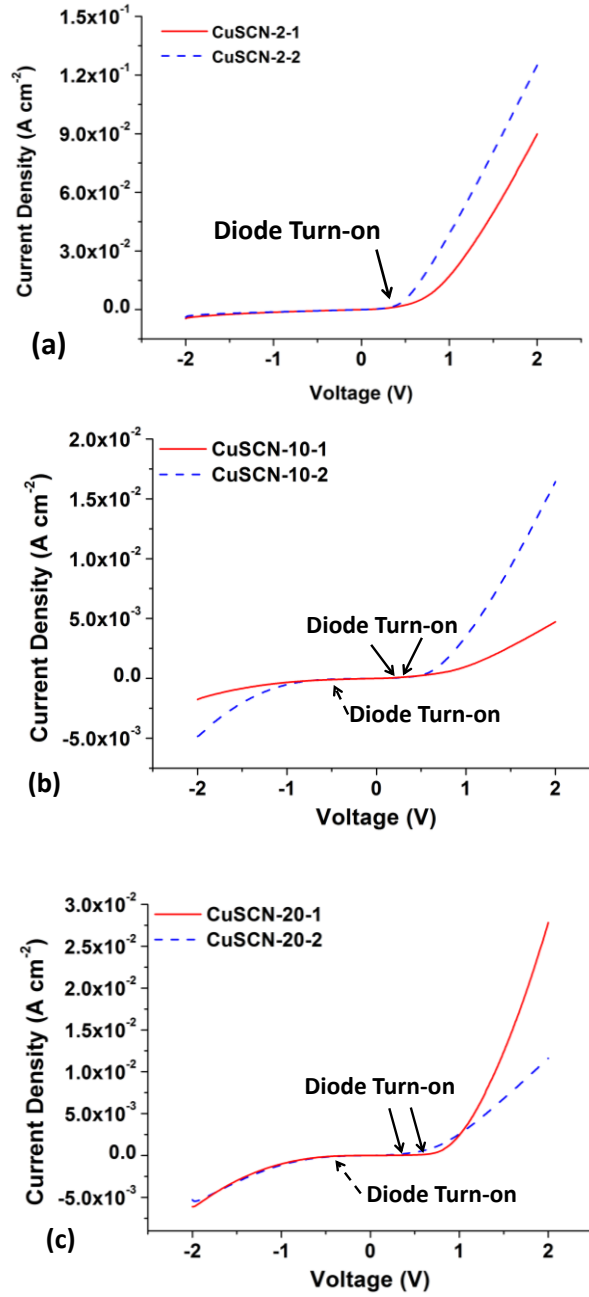


Figure 111. JV characteristic curves of (a) CuSCN-2, (b) CuSCN-10-1, 10-2 and (c) CuSCN-20-1, 20-2 devices.

7.1.2. Performance Evaluation and Comparison with non-coated Devices

The CuSCN-coated and non-coated ZnO-based devices were measured for their output performance using open-circuit voltage, short-circuit current and power density over optimum load which was determined using resistive load matching technique. For all devices, the output measurements were performed using the rotating cam and motor arrangement (described in Chapter 3, section 3.6). Each device was clamped to a sample holder and its one end was fixed. The other end of the device was bent upward to ~6 mm and released at 50 g acceleration by the cam rotating at 1 Hz. At the acceleration of 50 g, each device generated output response which was recorded using NI PXI-4461 (24-bit ADC) on the NI PXIe-1062Q chassis. The open-circuit voltage output V_{oc} peaks were recorded using NI PXI-4461 (24-bit ADC) on the NI PXIe-1062Q chassis. A Low-Noise Current Preamplifier SR570 was connected with the NI PXI-4461 (24-bit ADC) module to capture the short-circuit current density J_{sc} peaks. A resistive decade box, Meatest M602 programmable decade box, was connected with the PXI-4461 module for resistive load matching and peak power density measurement. All the equipment used for measurement and data acquisition were operated by Labview programs.

The measured peak open-circuit voltage (V_{oc}), peak short-circuit current density (J_{sc}) and calculated peak power density (P_L) of non-coated and CuSCN-coated devices are shown in Figure 112-Figure 114 and Table 26. An increase in peak open-circuit voltage output in CuSCN-coated devices was observed when compared with non-coated PDOT-2K/A devices. For PDOT-2K/A devices, the highest peak open-circuit voltage was measured as 225 mV from PDOT-A1. For CuSCN-2-1 and CuSCN-2-2 devices, the measured V_{oc} was increased to 260 and 330 mV. In addition, the voltage-driven J_{sc} was also increased to 1.2 mA cm^{-2} for both devices due to increase in their V_{oc} . Similarly when compared with the PDOT-A1 device, the P_L of CuSCN-2 devices being $115 \text{ } \mu\text{W cm}^{-2}$ and $140 \text{ } \mu\text{W cm}^{-2}$, were more than two times higher.

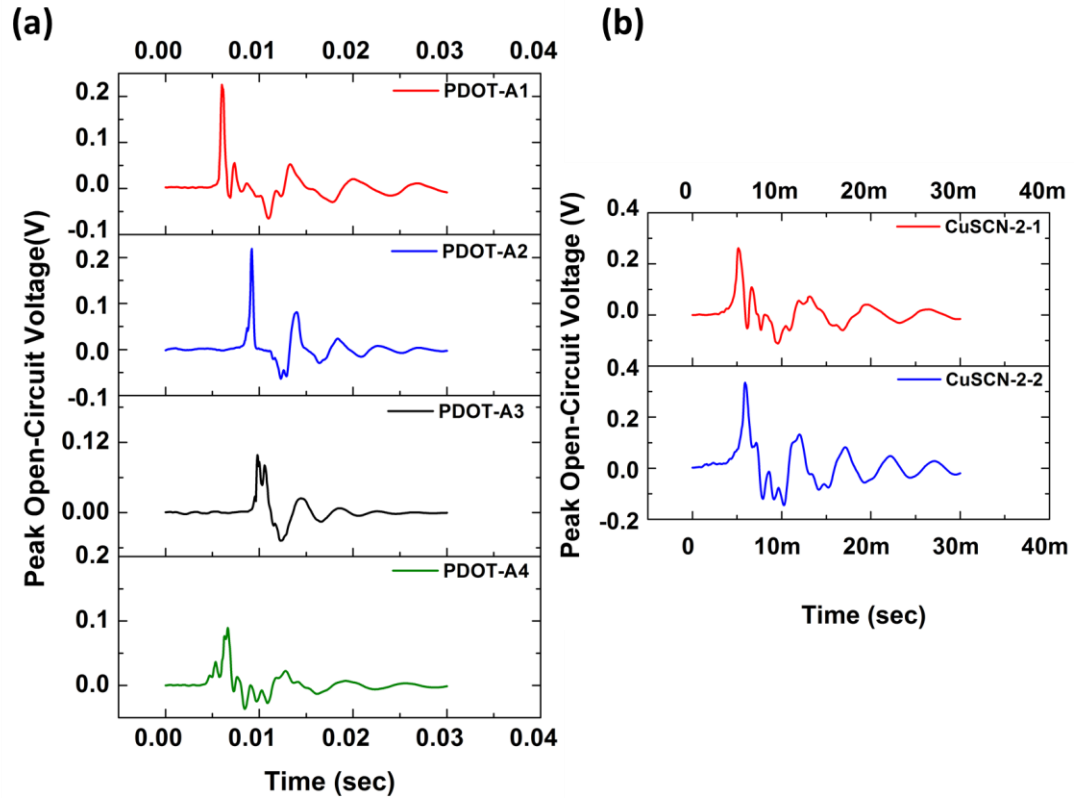


Figure 112. Measured peak open-circuit voltage output of (a) PDOT-2K/A and (b) CuSCN-2 devices.

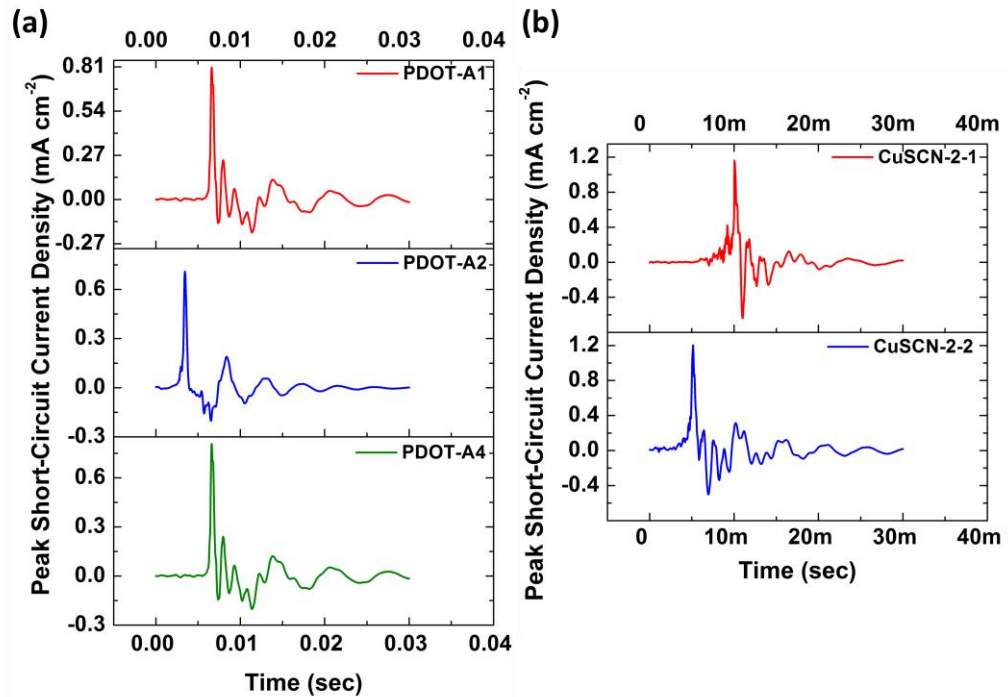


Figure 113. Measured peak short circuit current density of (a) PDOT-2K/A and (b) CuSCN-2 devices.

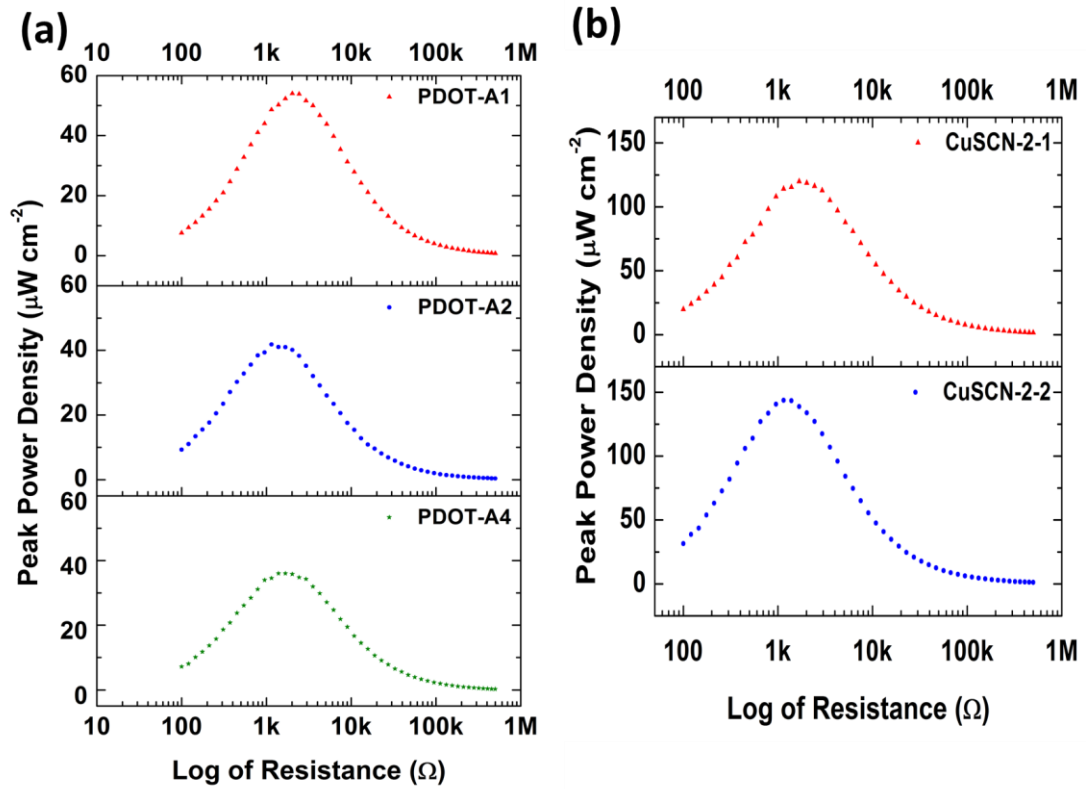


Figure 114. Resistive load matching of (a) PDOT-2K/A and (b) CuSCN-2 devices across optimum R_L .

Further to CuSCN-2 devices, the number of CuSCN coats was increased to 10 and 20 to fabricate CuSCN-10 and CuSCN-20 devices, which had demonstrated a further increase in V_{oc} . The average of V_{oc} generated by four CuSCN-10 and four CuSCN-20 devices was 660 mV and 790 mV (Table 26). This indicated that on average CuSCN-20 device performance was marginally higher than CuSCN-10 devices; which showed that the performance of devices increased with the increase in CuSCN coats until saturation was reached. Therefore, after this saturation point a further increase in CuSCN coating was not effective in increasing device V_{oc} . In addition, it was also proposed that the increase in loading of CuSCN from 2 coats to 10 and 20 coats actually increased the surface coverage of ZnO, due to which the CuSCN coverage on nanorods in CuSCN-20 and CuSCN-10 was higher than CuSCN-2. The increase in coats increased the ZnO surface coverage with CuSCN, which increased the suppression of active parasitic sites on ZnO surface. Therefore, it can also be stated that, although CuSCN thickness in CuSCN-20 nanorods was 4 nm which was twice as high as that of CuSCN-10; the surface coverage of CuSCN-10 and CuSCN-

20 was not varied significantly. As a consequence of which, on average the CuSCN-10 and CuSCN-20 generated similar ranges of V_{oc} , that is 454 – 900 mV for CuSCN-10 and 403 mV – 1.07 V for CuSCN-20 (Figure 115-Figure 117).

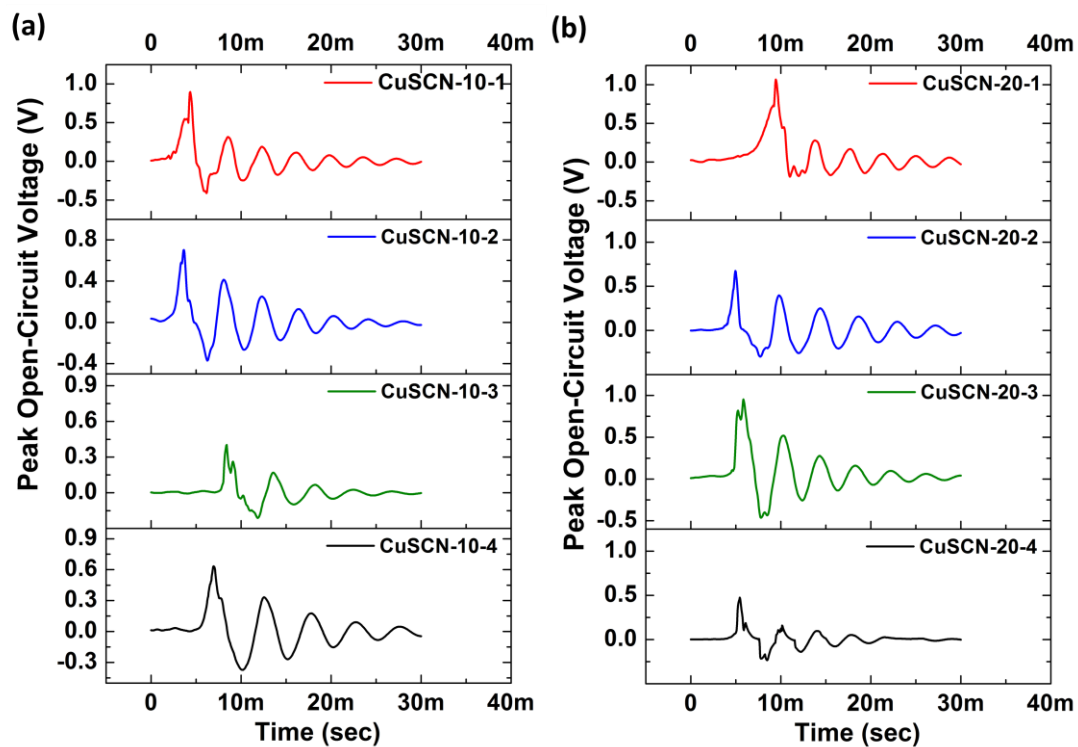


Figure 115. Measured peak open-circuit voltage output of (a) CuSCN-10 and (b) CuSCN-20 devices.

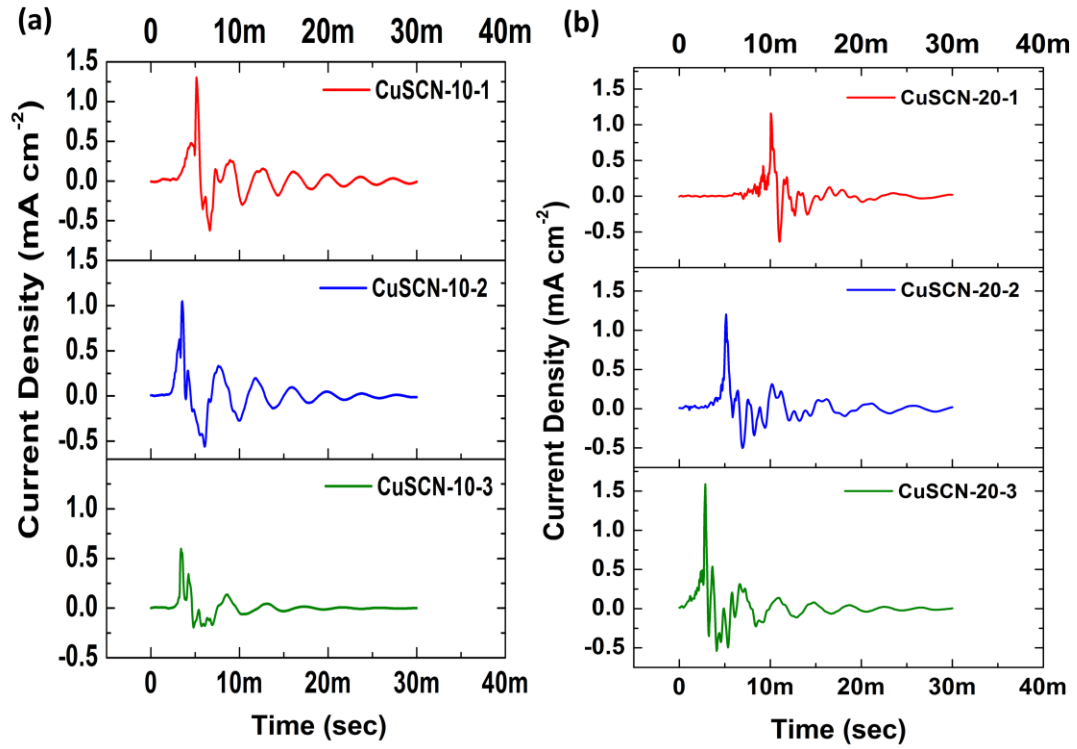


Figure 116. Measured peak short-circuit current density output of (a) CuSCN-10 and (b) CuSCN-20 devices.

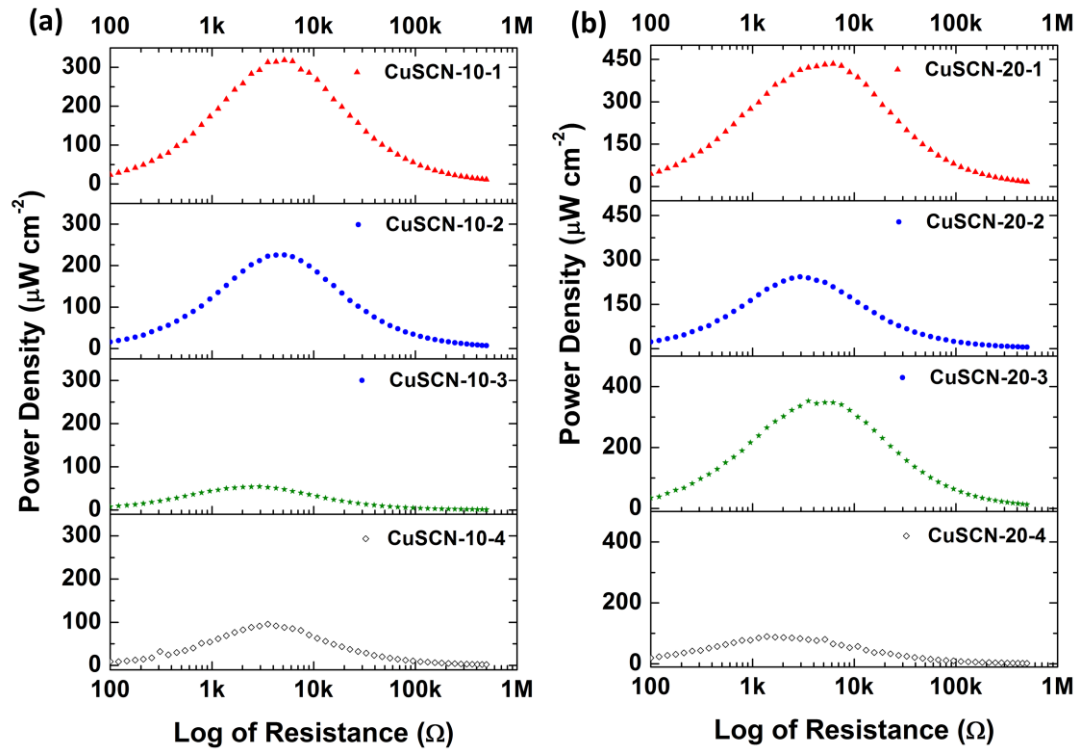


Figure 117. Resistive load matching across optimum load resistance for (a) CuSCN-10, (b) CuSCN-20 devices.

Table 26. V_{oc} , J_{sc} and P_L of PDOT-A1, A2, CuSCN-2, CuSCN-10 and CuSCN-20 devices.

Device Name	Peak Open-Circuit Voltage	Peak Short-Circuit Current Density	Peak Power Density	Load Resistance
	V_{oc} (mV)	J_{sc} (mA/cm ²)	P_L (μW/cm ²)	R_L (kΩ)
PDOT-A1	225	0.8	54	2.019
PDOT-A2	212	0.715	41.07	1.387
CuSCN-2-1	260	1.2	115	1.15
CuSCN-2-2	330	1.2	140	1.4
CuSCN-10-1	900	1.3	318.71	5.15
CuSCN-10-2	708	1.04	225.25	4.3
CuSCN-10-3	403	0.6	53	2.02
CuSCN-10-4	634	0.56	91.12	3.54
CuSCN-20-1	1070	1.88	434.33	6.22
CuSCN-20-2	675	1.1	242.68	2.94
CuSCN-20-3	952	1.6	344.5	4.3
CuSCN-20-4	454	1.02	87.8	1.67

The ranges of V_{oc} generated for both CuSCN-10 and CuSCN-20 was varied from 400 mV to 1 V which showed a significant device-to-device variation (Table 26). There were two possible causes of this: parasitic effects of R_s and R_{sh} and inadequate coverage of CuSCN coating. Firstly, the losses caused by R_s and R_{sh} were unavoidable and they had adversely affected devices in every device group studied in this thesis. But in the presented case, it was not possible to study the R_s and R_{sh} effects on CuSCN-coated devices' performance. This was because, as explained earlier, the J-V characteristic curves for these devices were different from standard p-n junction diode curve due to the presence of two diodes: CuSCN/ZnO diode and PEDOT:PSS/ZnO diode. Hence, the R_s and R_{sh} calculation from two overlapping diode curves could be misleading. However at the same time, the reason of a wide device-to-device variation could also be linked with inadequate coverage or variation of coverage of CuSCN from sample to sample. The CuSCN spray-coating was performed manually therefore it was not completely uniform throughout each nanorod array sample. As shown in Figure 107, there were some nanorods around which clusters of CuSCN were formed and in some areas CuSCN coating was not apparent, which indicated non-uniform coverage. Therefore, the devices with lower V_{oc} (400 – 700 mV) could have also been affected by lower coverage of CuSCN on

their nanorods. Hence, in such case the internal screening in the non-coated rods was not suppressed, which caused a drop of V_{oc} and other performance parameters.

Table 27. Performance parameters of best selected devices from each group.

Device	PDOT-A1	CuSCN-2-2	CuSCN-10-1	CuSCN-20-1
Open Circuit Peak Voltage (mV)	225	330	897	1070
Short Circuit Peak Current Density (mA/cm²)	0.8	1.2	1.3	1.88
Load Resistance (kΩ)	2	1	5	6
Peak Power Density (μW/cm²)	54	140	319	434
Energy Density (nJ/cm²)	17	78	175	256
Charge Displaced (nC/cm²)	247	280	647	848
RC Time Constant (ms)	0.068	0.11	1.001	1.137

To explain the effects of CuSCN on device performance, the device-to-device variation was ignored and the best performance devices, CuSCN-2-2, CuSCN-10-1, CuSCN-20-1, were studied for surface passivation effects (Table 27). Similarly, for comparison with non-coated device PDOT-A1 device was also considered. As discussed earlier, the non-coated PDOT-A1 device generated 225 mV and $54 \mu\text{W cm}^{-2}$ across an optimum load of 2 k Ω . The V_{oc} and P_L were observed to increase to 330 mV and $140 \mu\text{W cm}^{-2}$ for 2 coats of CuSCN-based device CuSCN-2-2. Similarly, when the number of coats were further increased, the CuSCN-10-1 generated 900 mV but, the highest peak voltage observed was 5 times higher than the non-coated device, which was 1.07 V and generated by CuSCN-20-1 device. Similarly, an increase in the voltage-driven current density was also observed: from 0.8 mA cm^{-2} for PDOT-A1, the current density increased to 1.3 mA cm^{-2} and 1.88 mA cm^{-2} for CuSCN-10-1 and CuSCN-20-1 devices. Hence, the CuSCN-20 device generated the highest peak power density of $434 \mu\text{W cm}^{-2}$ across an optimal load of 6 k Ω which was 8 times higher than $54 \mu\text{W cm}^{-2}$ generated by the non-coated device across 2 k Ω . In addition, the calculated energy density of the CuSCN-20-1 device was also observed to be 10 times higher than that of the non-coated device.

Therefore, the results for non-coated and coated ZnO devices indicated that CuSCN loading had modified the surface properties of ZnO. It was believed that 2 nm - 4 nm

thick CuSCN loading suppressed the defect and impurity sites on ZnO. This in return reduced the surface-induced free-charge carrier concentration and hence the rate of internal screening of piezoelectric polarisation decreased. As a result, the peak voltage and current output of the devices increased. Therefore, the peak power density of the devices was also increased from $54 \mu\text{W cm}^{-2}$ for non-passivated device to 8 times with the highest loading of CuSCN. In addition, as explained earlier, the increase in loading of CuSCN from 2 coats to 10 and 20 coats actually increased the surface coverage of ZnO, which increased the suppression of active parasitic surface-states in CuSCN-10 and CuSCN-20. As a consequence, the surface-state induced carriers in ZnO reduced and the rate of flow of free-charge carriers in polarised ZnO. Consequently, the screening *rate* in CuSCN-coated devices decreased, causing an increase in their V_{oc} . This concept is further illustrated using the impedance analysis results in later sections of this chapter.

Jaffe et al. (2010) ²⁴ demonstrated through XPS analysis that, CuSCN is formed of Cu^+ ions ionically bonded to SCN^- ions ^{2,24}. The Cu^+ ions were identified to be present in both isolated CuSCN films ²⁴ and CuSCN coated onto TiO_2 in a similar fashion to the CuSCN coating on ZnO used in the presented work ²⁵. When considering the similar tetragonal bonding arrangement in ZnO ²⁴, it is likely that the bonding of CuSCN to the ZnO surface is ionic in nature. Hence CuSCN was considered to chemisorb and form new bonds on ZnO surface. This chemical bonding could have reduced the density of defects on the ZnO surface and therefore reduce the carrier concentration in the ZnO.

Another characteristic of CuSCN that can be suggested to be effective in reducing the carrier density of ZnO is its p-type nature. The p-type CuSCN and n-type ZnO based ITO/ZnO/CuSCN/Au device discussed in section 7.1.1 produced a diode with rectification ratio ²⁶, indicating the formation of a depletion region at the ZnO/CuSCN interface. The presence of depletion region on ZnO surface could have reduced the carrier transport from any surface species into ZnO. A similar surface modification work also confirmed the formation of depletion region at copper phthalocyanine (CuPc)/ZnO when 20 nm p-type CuPc was coated onto n-type ZnO nanowires ^{2,16}.

Optimum load resistance R_L , across which maximum power density was obtained, also increased for passivated-devices. For non-coated device PDOT-A1 the R_L was 2 k Ω , which further increased to 5 k Ω and 6 k Ω for CuSCN-10-1 and CuSCN-20-1 devices. Theoretically, as described by maximum power transfer theorem, this increase in optimum load R_L is linked with increase in device resistive internal impedance (R_{int})²⁷: the power output of a device (power generator) is optimised when the connected complex load is equal to its internal impedance. In the presented case, the connected load was not complex ($R + jX$), but the increase in R_L was considered to be associated with increase in R_{int} .

Therefore, for analysis on R_L and R_{int} , impedance analysis was performed on each device from 40 Hz – 110 MHz and represented as the Nyquist plots (Figure 118 - Figure 121) and R_{int} was calculated obtained from the real axis impedance on Nyquist plot. It was observed that, similar to R_L , the R_{int} of CuSCN-coated devices, was increased with increase in CuSCN layers in the device. For PDOT-A1 the internal impedance was 2 k Ω which increased to 12.5 k Ω and 12 k Ω for CuSCN-10-1 and CuSCN-20-1. This was linked with addition of layers of CuSCN which are speculated to increase the R_s of device. Hence, it was confirmed by the impedance analysis that the increase in R_L was associated with increase in R_{int} of CuSCN-coated devices.

It was also observed that the increase in R_s due to increase in CuSCN layers did not reduce the P_L of devices. This result was contrary to the results of PDOT-2K/A, PDOT-2K/B and PDOT-1K devices (Chapter 5): the devices whose R_{int} or R_L was increased due to R_s (for e.g. PDOT-1K devices) had undergone a decrease in P_L output. This was because the increase in R_s had increased the I^2R_s ²⁸ resistive losses in the device. For the presented case of CuSCN-coated devices, an increase in CuSCN layers was considered to increase the R_s of devices but it also increased the surface coverage of ZnO and reduced the screening *rate*. Resultantly, the V_{oc} , J_{sc} and P_L of devices improved to 320 $\mu\text{W cm}^{-2}$ (CuSCN-10-1) and 434 $\mu\text{W cm}^{-2}$ (CuSCN-20-1). Moreover, the increased R_s was reflected as increased R_L of 5 k Ω and 6 k Ω for CuSCN-10-1 and CuSCN-20-1.

For CuSCN-2 devices, the optimum load resistance R_L of 1.15 – 1.4 k Ω and internal impedance of 0.93 – 1 k Ω were lower than PDOT-A1 device (Table 26). This was

believed to be related with parasitic effects of R_s and R_{sh} ; since R_s and R_{sh} affect the resistive internal impedance as well as the R_L of devices. To elaborate, it was analysed from the previous results of PDOT-2K/A, PDOT-2K/B, PMA-2K and PMA-3K devices (Chapter 5 & 6) that the decrease in R_{int} or R_L was mainly caused by decrease in device R_{sh} . Hence, for CuSCN-2 devices, it was speculated that decrease in R_{sh} was linked with the reduction in its overall internal impedance. This reduced R_{sh} was considered to be the adverse effect of device short-circuits. However this decrease in R_L and R_{sh} hadn't adversely affected its P_L , because the effect of CuSCN-induced reduction in screening *rate* was more pronounced. Therefore, the CuSCN-2 devices although had lower R_L than PDOT-A1 but higher V_{oc} , J_{sc} and P_L .

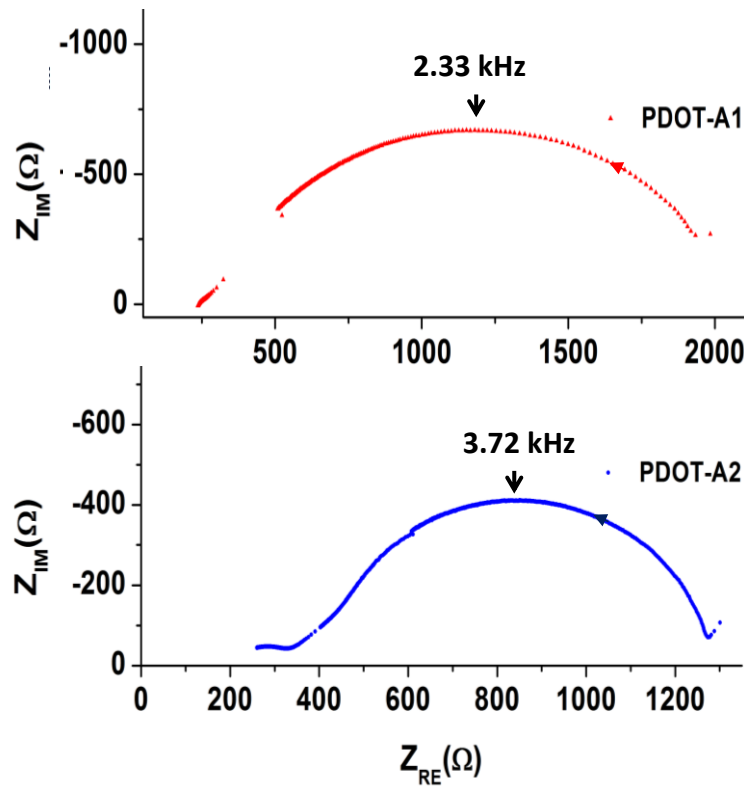


Figure 118. Nyquist plots of impedance analysis of PDOT-A1 and A2 devices.

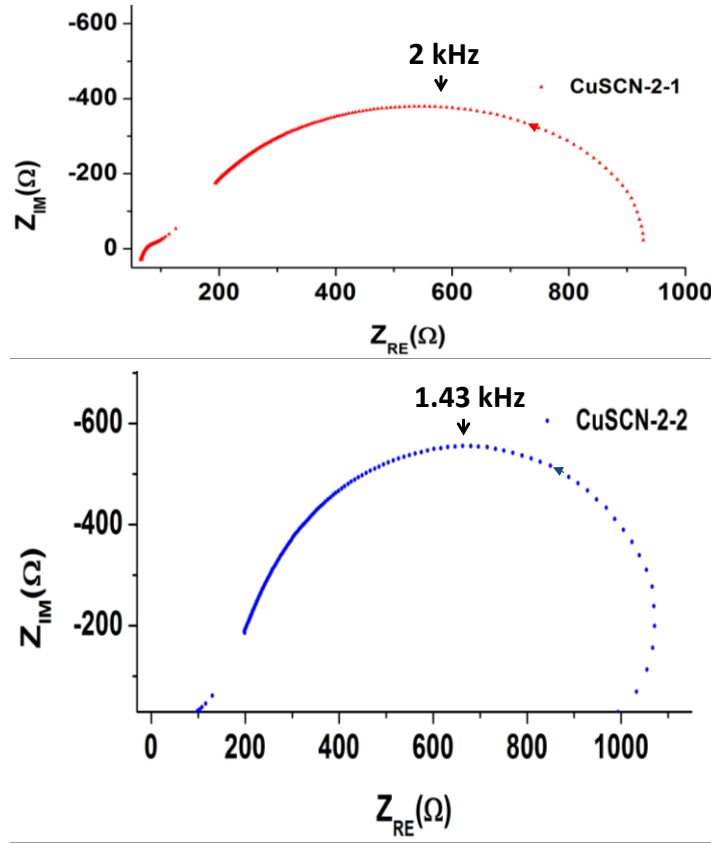


Figure 119. Nyquist plots of impedance analysis of CuSCN-2 devices.

In addition to resistive internal impedance, the Nyquist plots were also used to determine RC time constants (τ_{RC}) of the devices. This was obtained from the largest diameter arcs labelled with their resonant frequency (f_c) using the relation $\tau_{RC} = \frac{1}{2\pi f_c}$ ²⁹ (Figure 118 - Figure 121). In an RC circuit, at high frequencies ($f \rightarrow \infty$), the impedance is completely capacitive and at low frequencies ($f \rightarrow 0$), it is resistive. The RC time constant is associated with a characteristic frequency called ‘critical frequency’ f_c at which the impedance is both resistive and capacitive in nature. Therefore this critical frequency of a circuit determines the duration it takes for its capacitor to charge and discharge in the presence of resistive and reactive impedance. Therefore, at critical frequency the resistive and capacitive components of the circuit impedance are ideally in phase²⁹.

From the critical frequencies, the time constants for PDOT-A1, CuSCN-2-1, CuSCN-10-1 and CuSCN-20-1 were calculated as 0.068 ms, 0.11 ms, 1.001 ms and 1.14 ms respectively. It was therefore observed that, a step increase in the CuSCN deposition increased the device time constant as well as its V_{oc} . Since we know that,

due to surface passivation and suppression of ZnO surface states, the rate of ZnO internal screening associated with free-charge carrier flow reduced. Due to which, the duration of polarisation of strained-ZnO increased. Therefore it was proposed that this duration of retention of polarisation charges in ZnO was linked with devices' RC time constant. That is to say, the device RC time constants was associated with the rate of internal screening in ZnO. Thus, for non-passivated-ZnO device PDOT-A1, the RC time constant was two orders of magnitude lower than the passivated-ZnO devices; which indicated that the duration of retention of polarised immobile charges in ZnO was higher for CuSCN-2, CuSCN-10 and CuSCN-20 devices. Consequently, for CuSCN-coated devices the internal screening *rate* was lowered which caused their V_{oc} to increase. This concept has been further elaborated in section 7.2.

Table 28. Devices' critical frequency and time constants derived from their Nyquist plots.

Device Name	Peak Open-Circuit Voltage	Critical Frequency	Calculated Time Constant
	V_{oc} (mV)	f_c (Hz)	τ_{RC} (msec)
PDOT-A1	225	2.33 k	0.068
PDOT-A2	212	3.72 k	0.042
CuSCN-2-1	260	2.0 k	0.07
CuSCN-2-2	330	1.43 k	0.11
CuSCN-10-1	900	159	1
CuSCN-10-2	708	378	0.42
CuSCN-10-3	403	837	0.19
CuSCN-10-4	634	438	0.36
CuSCN-20-1	1070	140	1.14
CuSCN-20-2	675	717	0.22
CuSCN-20-3	952	199	0.8
CuSCN-20-4	454	438	0.36

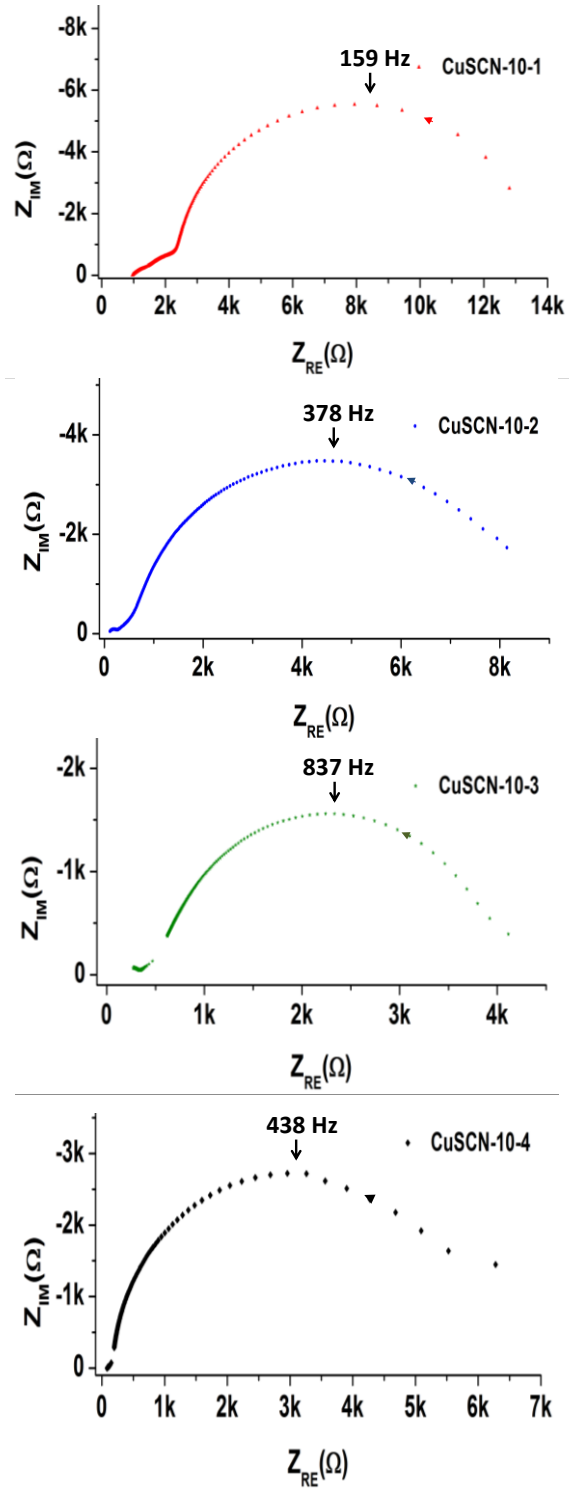


Figure 120. Nyquist plots of impedance analysis of CuSCN-10 devices.

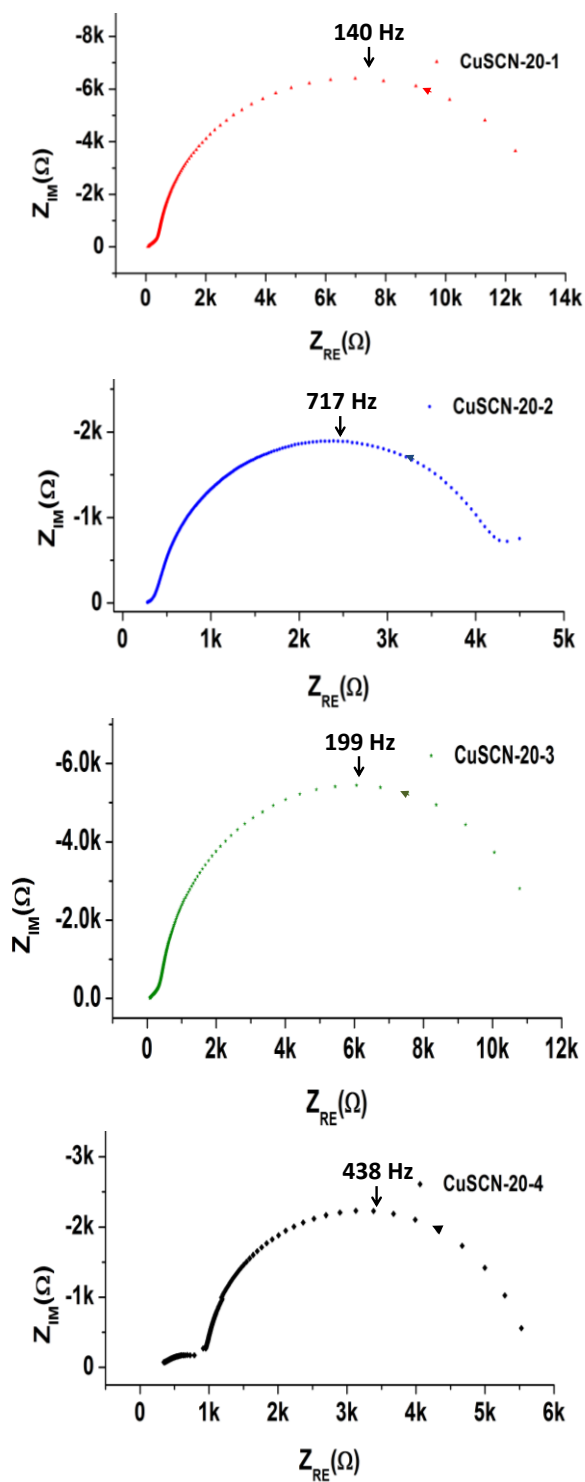


Figure 121. Nyquist plots of impedance analysis of CuSCN-20 devices.

Table 29. Performance parameters of PDOT-A1, A2 and CuSCN-2 devices.

Device Name	Peak Open-Circuit Voltage	Peak Short-Circuit Current Density	Peak Power Density	Load Resistance	Energy Density	Real Impedance
	V_{oc} (mV)	J_{sc} (mA/cm ²)	P_L (μW/cm ²)	R_L (kΩ)	E_L (nJ/cm ²)	R_{int} (kΩ)
		Measured/Calculated	Manual/Decade Box			Performed/Not Performed
PDOT-A1	225	0.8	54	2.019	17	2
REMARKS		Measured	Decade Box			
PDOT-A2	212	0.715	41.07	1.387	22	1.28
REMARKS		Measured	Decade Box			
CuSCN-2-1	260	1.2	115	1.15	64	0.93
REMARKS		Measured	Decade Box			
CuSCN-2-2	330	1.2	140	1.4	78	1
REMARKS		Measured	Decade Box			

Table 30. Performance parameters of CuSCN-10 and CuSCN-20 devices.

Device Name	Peak Open-Circuit Voltage	Peak Short-Circuit Current Density	Peak Power Density	Load Resistance	Energy Density	Real Impedance
	V_{oc} (mV)	J_{sc} (mA/cm ²) Measured/Calculated	P_L (μW/cm ²) Manual/Decade Box	R_L (kΩ)	E_L (nJ/cm ²)	R_{int} (kΩ) Performed/Not Performed
CuSCN-10-1 REMARKS	900	1.3 Measured	318.71 Decade Box	5.15	175	12.5
CuSCN-10-2 REMARKS	708	1.04 Measured	225.25 Decade Box	4.3	125	8.15
CuSCN-10-3 REMARKS	403	0.6 Measured	53 Decade Box	2.02	29	4
CuSCN-10-4 REMARKS	634	0.56 Calculated across 100Ω	91.12 Decade Box	3.54	50	6
CuSCN-20-1 REMARKS	1070	1.88 Measured	434.33 Decade Box	6.22	256	12
CuSCN-20-2 REMARKS	675	1.1 Measured	242.68 Decade Box	2.94	134	4.27
CuSCN-20-3 REMARKS	952	1.6 Measured	344.5 Decade Box	4.3	191	10.8
CuSCN-20-4 REMARKS	454	1.02 Calculated across 100Ω	87.8 Decade Box	1.67	49	5.5

7.2. A Theoretical Approach to Understand the Effect of ZnO Surface Passivation on Device Internal Screening

A piezoelectric material under strain-induced polarisation charges allows internal flow of free-charge carriers which suppress the field of polarisation. This compensation of immobile polarisation charges by mobile charges is referred to as internal polarisation screening. That is to say, the screening *rate*, which depends on the rate of flow of free-carriers, affects the retention of polarisation charges in ZnO. Therefore, in comparison with a faster screening *rate*, a slower rate is believed to allow voltage to develop to a higher peak value before it is screened to zero⁴. Owing to the presence of mobile carriers, screening effect in piezoelectric material is unavoidable; however, if the rate is slowed, the duration of polarisation of ZnO can be increased and therefore the measured peak voltage can be increased. Therefore, the carrier concentration in ZnO was reduced using surface passivation, which reduced the flow of mobile charges in polarised ZnO. As a result, the measured peak voltage output of the devices increased to 4 times with the maximum surface area coverage of surface modifier. The impedance analysis provided a measure of device RC time constants, which were believed to be related to the duration of retention of polarisation charges. Since, the device which generated the highest peak voltage had the highest duration of RC time constant. Therefore, the RC time constants were correlated with the device peak voltage output.

We demonstrate the screening concept using a lossy capacitor model, in which the dielectric material ZnO is represent as a lossless parallel plates capacitor in parallel with a leakage resistance. The leakage resistance is tuned by the conductivity of ZnO which means that it represents flow of free-charge carriers. The electric dipole caused by the separation of the polarisation charges result in the development of depolarisation field (E_{dep}). The depolarisation field strength depends on the retention of stored charges by the parallel plates of capacitor. Therefore, increase in depolarisation field causes increase in the developed potential difference. The field opposite in direction of depolarisation field is the screening field which depends on ZnO carrier concentration².

The surface state-induced carrier concentration affect the conductivity of ZnO which is represented by the leakage resistance. When ZnO is polarised, the strain-induced

dipole moment develops the depolarization field (E_{dep}). This causes the flow of internal charge carriers which cause screening of polarisation charges. This screening field is represented as E_{scr} and it is in a direction opposite to E_{dep} . In non-coated ZnO, the E_{scr} is enhanced due to the lowered leakage resistance and higher surface-induced conductivity (Figure 122(a)). This tends to screen the retained polarization charges at a higher rate when compared to coated-ZnO (Figure 122(b)). This means, the increase in screening *rate* reduces the duration of retention of polarisation charges. Therefore, as indicated by the time constant (τ_{RC}) results, due to lower screening *rate* the duration of retention of polarized charges of the coated ZnO devices ($\tau_{RC} = 1.001$ ms and 1.14 ms) was two orders of magnitude higher than the non-coated ZnO devices ($\tau_{RC} = 0.068$ ms). This had caused the voltage outputs of CuSCN-10-1 and CuSCN-20-1 devices were 900 mV and 1.07 V respectively, which were 4 times higher than the 225 mV measured from non-passivated ZnO devices ².

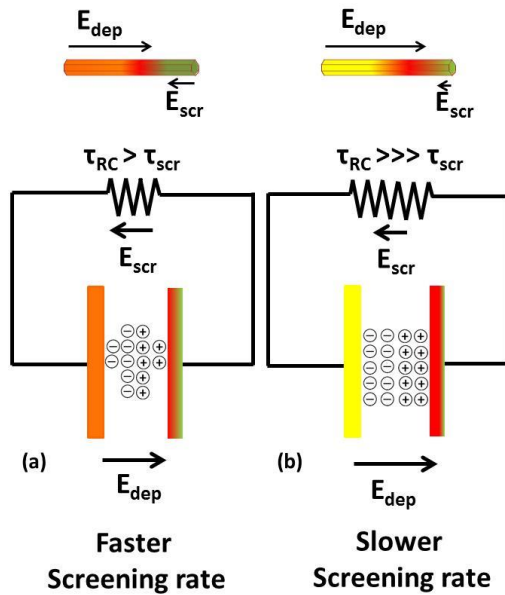


Figure 122. Modelling of piezoelectric voltage source.

Polarised ZnO nanorod is represented as a parallel plate capacitor and its internal impedance is modelled as a leakage resistor. The stored charges represent retention of polarisation charges which are affected by the screening field (E_{scr}). The retained charges reduce faster in (a) non-coated ZnO than (b) coated-ZnO ².

To sum up from the above-discussed results, the surface passivation of ZnO reduced the surface-induced free charge carrier concentration in ZnO as

represented in the schematics and band diagrams shown in Figure 123 (d) and (e). Due to this, the rate of screening of polarisation charges E_{scr} decreased and the polarised immobile charges retained for a longer duration as indicted by the time constants τ_{RC} (Figure 123 (a), (c), (e)). The tilted bands Figure 123(d) and (e) represent the electric field induced in ZnO upon polarisation. The higher rate of flow of internal carriers in non-coated devices caused the band tilt to decrease at a faster rate than that of the coated-devices. Therefore, the reduced band tilting in non-coated ZnO corresponds to lowered electric field; as a consequence of which lower peak output voltage is measured (Figure 123 (b)). This effect is elaborated by schematic of polarised non-coated nanorod, in which the potential difference along the length of the nanorod is low. On the contrary, the increased band tilting (Figure 123 (d)) represented higher electric field in CuSCN-coated ZnO device; as a consequence of which, higher voltage output is measured. This effect is elaborated by schematic of polarised CuSCN-coated nanorod, in which the potential difference along the length of the nanorod is high.

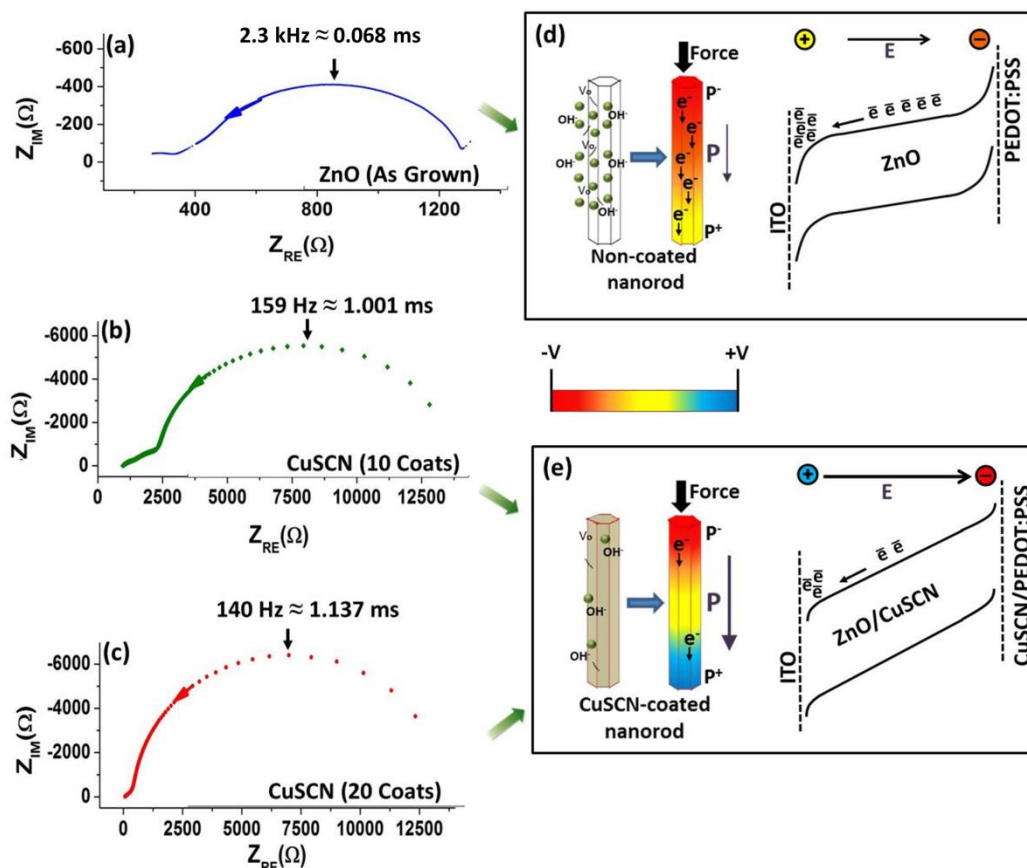


Figure 123. Correlation between device voltage output and its time constant (τ_{RC}). Nyquist plots of (a) non-coated, (b) CuSCN-10-1 and (c) CuSCN-20-1 devices with time constants of 0.068 ms, 1.001 ms and 1.137 ms as indicated on the plots. (d) Band diagrams showing higher rate of flow of free charge carriers in non-coated ZnO which caused electric field to decrease at a higher rate. Nanorod schematic demonstrated lower potential difference built-up across the length of the nanorod. (e) Band diagrams showing lower rate of flow of free charge carriers in CuSCN-coated ZnO which caused electric field to decrease at a lower rate. Nanorod schematic demonstrated higher potential difference built-up across the length of the nanorod².

7.3. Summary

The study presented in this chapter details the effects of carrier concentration of ZnO on the rate of internal screening of polarisation charges. A method of surface modification of ZnO using CuSCN was presented which increased the device power density by one order of magnitude. The study provided an in depth analysis on the reduction of internal screening *rate* due to suppression of parasitic sites on ZnO surface. It was established that due to modified ZnO surface, the surface-induced carrier concentration reduced and therefore the rate of internal screening reduced. Consequently, the peak voltage output of the devices increased from 225 mV for a

non-coated device to about 1 V for CuSCN-passivated. Using the impedance analysis the device RC time constants τ_{RC} were calculated and important correlation between the device voltage output and its RC time constant was obtained. To elaborate, the device RC constant was related to the duration of retention of piezoelectric polarisation charges in ZnO, therefore for devices with RC time constants τ_{RC} in the range of 1 ms, the peak voltage output generated was 900 mV – 1.07 V (CuSCN-10-1 and 20-1), which was 4 times higher than the devices with 0.04 – 0.07 ms time constant and lower voltage output of 220 - 225 mV (PDOT-A1 and A2). Hence, this analysis technique of RC time constant can be defined as a tool to understand the rate of screening of polarisation charges in piezoelectric material.

7.4. References

1. N. Jalali, J. Briscoe, P. Woolliams, M. Stewart, P. M. Weaver, M. Cain, and S. Dunn, *J. Phys. Conf. Ser.*, 2013, **476**, 012131.
2. N. Jalali, P. Woolliams, M. Stewart, P. M. Weaver, M. G. Cain, S. Dunn, and J. Briscoe, *J. Mater. Chem. A*, 2014, **2**, 10945.
3. J. Liu, P. Fei, J. Song, X. Wang, C. Lao, R. Tummala, and Z. L. Wang, *Nano Lett.*, 2008, **8**, 328–332.
4. J. Briscoe, M. Stewart, M. Vopson, M. Cain, P. M. Weaver, and S. Dunn, *Adv. Energy Mater.*, 2012, **2**, 1261–1268.
5. N. Jalali, J. Briscoe, Y. Z. Tan, P. Woolliams, M. Stewart, P. M. Weaver, M. G. Cain, and S. Dunn, *J. Sol-Gel Sci. Technol.*, 2014.
6. A. Janotti and C. G. Van de Walle, *Reports Prog. Phys.*, 2009, **72**, 126501.
7. S. M. Hatch, J. Briscoe, A. Sapelkin, W. P. Gillin, J. B. Gilchrist, M. P. Ryan, S. Heutz, and S. Dunn, *J. Appl. Phys.*, 2013, **113**, 204501.
8. Y. Lv, W. Yao, X. Ma, C. Pan, R. Zong, and Y. Zhu, *Catal. Sci. Technol.*, 2013.
9. Y. Hu, L. Lin, Y. Zhang, and Z. L. Wang, *Adv. Mater.*, 2012, **24**, 110–4.
10. H. Noei, H. Qiu, Y. Wang, E. Löffler, C. Wöll, and M. Muhler, *Phys. Chem. Chem. Phys.*, 2008, **10**, 7092–7.
11. N. S. Ridhuan, K. A. Razak, Z. Lockman, and A. Abdul Aziz, *PLoS One*, 2012, **7**, e50405.
12. L. H. Quang, S. J. Chua, K. Ping Loh, and E. Fitzgerald, *J. Cryst. Growth*, 2006, **287**, 157–161.
13. A. B. Djurišić, Y. H. Leung, K. H. Tam, Y. F. Hsu, L. Ding, W. K. Ge, Y. C. Zhong, K. S. Wong, W. K. Chan, H. L. Tam, K. W. Cheah, W. M. Kwok, and D. L. Phillips, *Nanotechnology*, 2007, **18**, 095702.
14. M. Willander, O. Nur, J. R. Sadaf, M. I. Qadir, S. Zaman, A. Zainelabdin, N. Bano, and I. Hussain, *Materials (Basel)*, 2010, **3**, 2643–2667.
15. W.-K. Hong, B.-J. Kim, T.-W. Kim, G. Jo, S. Song, S.-S. Kwon, A. Yoon, E. A. Stach, and T. Lee, *Colloids Surfaces A Physicochem. Eng. Asp.*, 2008, **313-314**, 378–382.
16. Q. Chen, H. Ding, Y. Wu, M. Sui, W. Lu, B. Wang, W. Su, Z. Cui, and L. Chen, *Nanoscale*, 2013, **5**, 4162–5.

17. T. T. Pham, K. Y. Lee, J.-H. Lee, K.-H. Kim, K.-S. Shin, M. K. Gupta, B. Kumar, and S.-W. Kim, *Energy Environ. Sci.*, 2013, **6**, 841.
18. W. Wu and Z. L. Wang, *Nano Lett.*, 2011, **11**, 2779–85.
19. F. Hai-Bo, Y. Shao-Yan, Z. Pan-Feng, W. Hong-Yuan, L. Xiang-Lin, J. Chun-Mei, Z. Qin-Sheng, C. Yong-Hai, and W. Zhan-Guo, *Chinese Phys. Lett.*, 2007, **24**, 2108–2111.
20. L. L. Yang, Q. X. Zhao, M. Willander, J. H. Yang, and I. Ivanov, *J. Appl. Phys.*, 2009, **105**, 053503.
21. I. Mora-Seró, F. Fabregat-Santiago, B. Denier, J. Bisquert, R. Tena-Zaera, J. Elias, and C. Lévy-Clément, *Appl. Phys. Lett.*, 2006, **89**, 203117.
22. H.-W. Ra, R. Khan, J. T. Kim, B. R. Kang, K. H. Bai, and Y. H. Im, *Mater. Lett.*, 2009, **63**, 2516–2519.
23. S. Lee, S. Bang, J. Park, S. Park, W. Jeong, and H. Jeon, *Phys. status solidi*, 2010, **207**, 1845–1849.
24. J. E. Jaffe, T. C. Kaspar, T. C. Droubay, T. Varga, M. E. Bowden, and G. J. Exarhos, *J. Phys. Chem. C*, 2010, **114**, 9111–9117.
25. L. Sun, Y. Huang, M. Anower Hossain, K. Li, S. Adams, and Q. Wang, *J. Electrochem. Soc.*, 2012, **159**, D323.
26. S. M. Hatch, J. Briscoe, and S. Dunn, *Thin Solid Films*, 2013, **531**, 404–407.
27. R. L. Meade, *Foundations of Electronics*, Delmar Cengage Learning, 2002.
28. M. Paulescu, E. Paulescu, P. Gravila, and V. Badescu, *Weather Modeling and Forecasting of PV Systems Operation*, Springer, 2012.
29. V. F. Lvovich, in *Impedance Spectroscopy*, John Wiley & Sons, Inc., 2012, pp. 319–331.

8. Conclusion

In this research work, nanostructured material-based energy harvesters were developed and their output performance was optimised. In addition, repeatable and reliable methods of measurements were implemented and quantitative analysis was undertaken to understand the effect of loss parameters such as, series resistance (R_s), shunt resistances (R_{sh}) and polarisation screening on device performance.

The development of ZnO nanorods-based energy harvester started from a basic PEDOT:PSS-based device, which was designed as a stacked heterojunction of ITO/ZnO/PEDOT:PSS/Au. These types of devices were used for establishing basic characterisation techniques such as determination of series and shunt resistance, impedance analysis and resistive load matching for power density calculation across optimum load. These basic analysis techniques were later implemented on other device prototypes and the performance of those devices was assessed in relation to their constituent material properties.

The detailed electrical analysis showed that the most efficient devices comprising of basic ITO/ZnO/PEDOT:PSS/Au structure were the PDOT-2K/A devices. These devices had R_s and R_{sh} in the range of 0.08 – 0.17 k Ω and 0.5 – 1.65 k Ω and they generated V_{oc} in the range of 90 – 225 mV. Along with PDOT-2K/A devices two other groups of devices, PDOT-2K/B and PDOT-1K, were also examined. These devices had higher losses than PDOT-2K/A devices. PDOT-2K/B devices were affected by lower R_{sh} of 0.2 – 0.3 k Ω which was caused by high occurrences of short-circuits and they generated V_{oc} from 22 – 60 mV. Similarly, the PDOT-1K devices were affected by their higher R_s 0.3 – 0.6 k Ω which was caused by 3 times higher thickness of the PEDOT:PSS top electrode and they generated V_{oc} of 33 – 40 mV. In case of PDOT-2K/A devices, the R_{sh} was sufficiently high caused by lesser occurrences of short-circuits and R_s losses did not significantly affect the output of devices. Therefore, these devices had the peak power densities across load (P_L) of 36 - 54 $\mu\text{W cm}^{-2}$, which was higher than 2.5 – 16 $\mu\text{W cm}^{-2}$ generated by PDOT-2K/B and 0.2 – 0.25 $\mu\text{W cm}^{-2}$ generated by PDOT-1K.

After establishing techniques to analyse electrical losses and evaluate performance parameters, the next target was to study the external screening effects which are caused by the electrical properties of the electrodes attached with ZnO. To elaborate, the higher conductivity of electrode allows free-charge carriers to flow through polarised ZnO and cause the induced electric field to reduce. To study screening effect, the bottom electrodes were varied and three different electrodes such as, ITO, zinc and silver (Ag) were used. The devices based on ITO electrode called PDOT-Sm generated the highest V_{oc} of 60 mV which was two orders of magnitude higher than the zinc foil based devices. This was attributed to lower external screening effects caused by the ITO contact. On the contrary, a contact with metal like zinc, allowed a higher rate of external free-charge carriers to flow through ZnO, which increased the screening of polarisation. Hence, the voltage output of the zinc-based devices dropped. Similarly, the top electrode materials were also varied and study was conducted to observe the differences between PEDOT:PSS and PMMA top contacts. It was analysed that PMMA, being an insulating material, caused reduction of external screening effects but contrariwise, it allowed the device series resistance (R_s) to increase. This caused a drop in the PMMA-based power density output. Therefore, the PMMA-based device generated $0.4 \mu\text{W cm}^{-2}$ which was two orders of magnitude by the $54 \mu\text{W cm}^{-2}$ generated by PEDOT:PSS-based device.

The last analysis was performed to understand the internal screening of polarisation caused by surface-states of ZnO. In this regard, ZnO surface was passivated using a surface modifier CuSCN and the performance was evaluated for both coated and non-coated devices. The results confirmed that the surface defects and impurities inject free-carriers into ZnO and cause the rate of internal screening to increase. When these surface species were modified by CuSCN, the peak open-circuit voltage output of the best performing device increased to 1.07 V from 225 mV generated by non-coated device. Similarly, the highest peak power density generated by this coated device was $434 \mu\text{W cm}^{-2}$, which was about 8 times higher than $54 \mu\text{W cm}^{-2}$ generated by the non-coated device.

This research work develops a nanostructured-ZnO based piezoelectric energy harvester with various prototypes and analyses their electrical characteristics through reliable and repeatable measurements. These characterisation techniques were the key to analyse the parasitic and lossy components in every device prototype; which

assisted in recognising the materials responsible for optimum device performance (in terms of power density). Hence, a further improvement of these optimum devices led to enhanced output generation.

8.1. Future Work

8.1.1. Surface Passivation

In the presented work, the surface of ZnO was modified using spray-coating of CuSCN. The spray-coating was performed manually, due to which the surface of ZnO was not evenly covered. Therefore, to improve the quality of results it shall be beneficial to automate the surface-coating technique. This can be achieved by using programmed robotic arm.

8.1.2. Impedance Matching

This research work used resistive impedance matching for the measurement of power density across optimum resistive load. It was observed that, for all prototype of devices that, the optimum resistive load (R_L) was linked with the resistive internal impedance of the device (R_{int}); where the R_{int} was obtained from the impedance analysis. However, for a more detailed profile on the effects of internal impedance on device power density, it is suggested for the load matching to be performed using real and complex impedance elements such as inductor ($R + jX_L$) and capacitors ($(R + jX_C)$). In this manner, impedance load matching using both real and complex impedance components would assist in examining the effect of reactive and resistive components of impedance on the energy harvesting efficiency of devices.

8.1.3. Doping of Nanorods

In addition to surface passivation, the carrier concentration of ZnO can also be reduced by doping it with suitable ions of lithium and silver. This work has been performed earlier in Schottky-based devices. However, it will be interesting to fabricate PEDOT:PSS-based devices with doped nanorods and to observe the effects of doping on electrical characterisation of devices. This will essentially be helpful to compare the doped-nanorod device performance with surface-passivated device performance.

8.1.4. Nanorods Aspect Ratio

Increasing the length of the nanorods increase their bending curvature and therefore, a higher strain can be induced into them. Therefore, the nanorods can generate higher voltage output and this can lead to increase in power density. Hence, it is suggested that the PEDOT:PSS-based device performance can be further enhanced by increasing the length of the nanorods.

8.1.1. p-n-p Device Design

A device design is suggested which is considered to reduce the external screening effects: p-n-p diode-based device. For this device, PEDOT:PSS is suggested to be bottom electrode as well as the top electrode i.e. PEDOT:PSS/ZnO/PEDOT:PSS. This device is assumed to form p-n junction on the top electrode/ZnO and bottom electrode/ZnO junction and reduce the flow of free-charge carriers through ZnO and hence improve device voltage output.